

Efficient Ray-Tracing Algorithms for Radio Wave Propagation in Urban Environments



Sajjad Hussain BSc. MSc.

Supervisor: Dr. Conor Brennan

School of Electronic Engineering
Dublin City University

This dissertation is submitted for the degree of
Doctor of Philosophy

September 2017

To my parents for their love and encouragement, my loving and supportive wife Akasha
for always standing beside me and our beautiful son Muhammad Hashir.

Declaration

I hereby certify that this material, which I now submit for assessment on the programme of study leading to the award of PhD is entirely my own work, and that I have exercised reasonable care to ensure that the work is original, and does not to the best of my knowledge breach any law of copyright, and has not been taken from the work of others save and to the extent that such work has been cited and acknowledged within the text of my work.

Signed:

A handwritten signature in black ink, appearing to read "Satiad", written over a horizontal line.

ID No.: 13212215

Date: 05/09/2017

Acknowledgements

I would like to express special appreciation and thanks to my supervisor, Dr. Conor Brennan, for his continuous support and confidence in my work. His patience and encouragement were invaluable to me throughout the course of my PhD. He pushed me to perform to the best of my abilities. I would also like to thank my examiners, Dr. Jean-Frédéric and Dr. Prince Anandarajah for their brilliant comments and suggestions that has really improved the quality of this thesis. I would especially like to thank my colleagues including Ian Kavanagh, Vinh Pham-Xuan and Dung Trinh-Xuan for their help and support.

I thank, from the bottom of my heart, those who have supported me throughout my stay at DCU through their true friendship and thoughtfulness. A special thanks to my family. Your prayer for me was what sustained me thus far. At the end, I would like to express appreciation to my beloved wife Akasha and our son Muhammad Hashir for their love, support and patience.

Table of Contents

List of Figures	viii
List of Tables	xii
1 Introduction	3
1.1 Motivation for Radio Channel Modeling	4
1.2 Contribution and Overview	4
2 Electromagnetic Theory	6
2.1 Constitutive Parameters	7
2.2 Types of Materials	7
2.3 Classification Of Media	8
2.4 Mathematical Formulation	9
2.5 Ray Properties	10
2.6 Ray Interaction with Surfaces	11
2.6.1 Reflection	12
2.6.2 Diffraction	14
2.7 Scattering	19
2.8 Application of UTD	20
2.8.1 2-D fields from a wedge	20
2.8.2 3-D fields from a cube	21
2.9 Conclusion	21
3 General Methods in Ray Tracing	24
3.1 Ray Tracing Techniques	25
3.1.1 Shooting and Bouncing Ray (SBR)	25
3.1.2 Image Method	26
3.1.3 Hybrid Method	26
3.2 Modeling of Objects	27
3.2.1 Buildings	27
3.2.2 Vegetation	29
3.2.3 Pedestrians and Vehicular Traffic	30
3.3 Visibility Algorithms	32

3.3.1	Dimensional Reduction Technique	33
3.3.2	BSP Algorithm	34
3.3.3	Polar Sweep Algorithm	38
3.4	Image-Tree	39
3.5	Ray-Object Intersection	40
3.6	Characterization of the Radio Channel	44
3.6.1	Path Loss	44
3.6.2	Channel Impulse Response (CIR)	45
3.6.3	Time Dispersion Parameters	45
3.6.4	Frequency Dispersion Parameters	46
3.7	Conclusion	47
4	Literature Review	48
4.1	Empirical Models	49
4.1.1	Okumura Model	50
4.1.2	Hata Model	51
4.1.3	Lee Model	52
4.1.4	Erceg Model	52
4.2	Vertical Plane Models	54
4.2.1	COST-231 Walfisch Ikegami Model	54
4.2.2	Vogler Model	57
4.2.3	Flat Edge Model	58
4.2.4	Saunders and Bonar Hybrid Model	59
4.2.5	Knife-Edge Diffraction Models	60
4.3	Ray Tracing Models	63
4.4	Efficient RT Techniques	64
4.4.1	Space Division Methods	64
4.4.2	Transmitter Dependant Methods	67
4.4.3	Receiver Dependant Methods	71
4.4.4	2-D/2.5-D Simplification Methods	72
4.4.5	Exhaustive Pre-Processing Methods	75
4.4.6	Hybrid Methods	77
4.4.7	Interpolation Methods	78
4.4.8	Parallel Computing and GPUs	80
4.4.9	Commercial Tools	81
4.4.10	Other Methods	83
4.5	Ray Tracing Limitations	83
4.6	Future Trends	84

5	Ray Tracing Acceleration for a Mobile Receiver	86
5.1	Introduction	87
5.2	Lit and Shadow Polygons	89
5.3	Fast Ray-Object Intersection Test	92
5.4	Performance of Initial Model	97
5.4.1	Measured Data	98
5.4.2	Initial Results	100
5.4.3	Analysis of Propagation Mechanisms	103
5.5	Mapping of Lit Polygons	110
5.5.1	Selection of Grid Resolution	116
5.5.2	Results	118
5.6	RT for a Mobile Route	119
5.6.1	Selection of Route Length	122
5.6.2	Results	126
5.7	Mapping of Shadow Polygons	126
5.7.1	Results	128
5.8	Summary of Acceleration Techniques	128
5.9	Conclusion	130
6	Ray Tracing Acceleration for a Mobile Transmitter	132
6.1	Introduction	133
6.2	Intra-Visibility Matrix	134
6.3	Initial Model	140
6.4	Ray tracing for a Mobile Transmitter	142
6.5	The Ray Tracing Algorithm	145
6.5.1	First order visible nodes	145
6.5.2	Visible nodes for wall reflection	147
6.5.3	Direction of the Mobile Transmitter	154
6.5.4	Visible nodes for edge diffraction	156
6.5.5	Image-tree computation	156
6.6	Results	161
6.6.1	Run Time Comparison	161
6.6.2	Results Validation	164
6.6.3	Selection of Transmitter Route Length	166
6.7	Conclusion	167
7	Conclusions and Future Work	168
7.1	Conclusions	168
7.2	Future Work	169
Bibliography		171

Appendix A Publications

184

List of Figures

2.1	A diverging astigmatic ray tube [11].	10
2.2	Incident and reflected ray at a point on a surface.	12
2.3	The planes of incidence and reflection in ray-fixed coordinate system.	13
2.4	Cone of diffracted rays [11].	15
2.5	Geometry for scattering from a wedge [11].	16
2.6	Edge fixed coordinate system for oblique incidence wedge diffraction [13].	17
2.7	Geometry of a wedge illuminated by a line source [21].	21
2.8	Comparison of electric field (dB) along a line of receivers using UTD and VEFIE [21].	22
2.9	Geometry of a PEC cube illuminated by a dipole source.	23
2.10	Comparison of electric field along a line of receivers using UTD and Method of Moment.	23
3.1	Shooting and bouncing ray (SBR) technique.	25
3.2	Use of image method to compute accurate ray trajectories.	27
3.3	Representation of a building in Cartesian coordinate system in 3-D space.	28
3.4	3-D model of a tree used in ray-tracing to account for the vegetation loss[32]	29
3.5	Two ray ground reflection model.	30
3.6	Comparison of two ray path loss with free space path loss.	31
3.7	Change in effective ground height due to pedestrian and vehicular traffic.	32
3.8	Lit region of a wall reflection can be found using image theory.	32
3.9	The region exterior to the walls that make up the edge forms the lit region of a diffracting edge.	33
3.10	Faces are projected onto a projection plane from transmitter perspective after back face culling [48].	34
3.11	A sweep line with polygon subtraction algorithm is applied to obtain the visible surfaces in 2-D [48].	35
3.12	An outdoor scenario for which BSP tree is computed [50].	36

3.13	Step by step BSP tree computation for example in Figure 3.12. a) Division of scene in two planes with respect to root node 9. b) BSP tree computation for all nodes on right side of root node 9. c) Complete BSP tree [50].	37
3.14	Computation of visible faces in horizontal plane using polar sweep algorithm [56].	38
3.15	An example of a typical image tree.	39
3.16	Top view of a test environment for ray-object intersection test.	41
3.17	Ray-object intersection test to show how a ray is validated for example in Figure 3.16. a) Ray-object intersection test for ray segment between receiver and second order reflection image. b) Ray-object intersection test for ray segment between second order reflection image and first order diffraction image. c) Ray-object intersection test for ray segment between first order diffraction image and transmitter.	42
3.18	Validation of a ray in 3-D space for example in Figure 3.16.	43
3.19	A typical power delay profile of a multipath channel [42].	46
4.1	Path loss (dB) versus transmitter receiver (T-R) separation in km for different cities in Germany [58].	49
4.2	Scatter plot of path loss exponent and base station height for three terrain categories. Solid curves are least-squares regression fit to $a - bh_b + c/h_b$ [67].	53
4.3	Geometry for COST-231 Walfisch Ikegami Model.	55
4.4	Geometry for Vogler model with irregular buildings height and spacing [75].	57
4.5	Geometry for Flat Edge Model.	59
4.6	Computation of diffraction loss in different knife-edge models.	62
4.7	Comparison of knife-edge models against Vogler model [86].	63
4.8	Uniform rectangular space division. Values of D_x and D_y determine the next cell the ray enters [92].	65
4.9	Adaptive multi-level space division [100].	67
4.10	Accurate illuminate zones of wall reflections [101].	68
4.11	An example of how environment is divided into 2-D anxels with respect to source for LOS rays [22].	69
4.12	A 3-D anxel is represented by a solid angle [22].	70
4.13	Buildings database simplification for Helsinki city [106].	72
4.14	a) Sectorized approach for a group of receiver points. b) The unfolding of the ray path to give range of angles [108].	74
4.15	A ray launched in vertical plane can undergo different phenomena [114].	76
4.16	Tiles and segments on a building for extensive pre-processing [116]. .	76

4.17	Complex discontinuities in a typical indoor environment in a) are studied with FDTD and results are combined with ray tracing to give accurate results in b) [121].	78
4.18	Visibility of receiver route to reflection ray entity [127].	79
4.19	Time resolution of the ray optical model and path interpolation [128].	79
4.20	Parallel computing model for 3-D ray tracing simulations [130]. . . .	80
4.21	Importing buildings database in Wireless Insite [139].	82
5.1	Flow Chart of Ray-tracing Algorithm for Mobile Receiver	88
5.2	Lit and shadow polygons	90
5.3	Ray-object intersection test for ray validation [158].	93
5.4	Validation test of a 2-D point inside a convex polygon	95
5.5	Map of Munich along with three routes Metro-200, Metro-201 and Metro-202.	99
5.6	Path loss data for the routes is plotted against logarithmic distance. . .	100
5.7	Path loss comparison for Metro-200	102
5.8	Path loss comparison for Metro-201	102
5.9	Path loss comparison for Metro-202	103
5.10	Comparison of over rooftop and lateral field contribution for metro-200.	104
5.11	Comparison of over rooftop and lateral field contribution for metro-201.	105
5.12	Comparison of over rooftop and lateral field contribution for metro-202.	105
5.13	Analysis of second order diffraction mechanism around corners in metro-202.	107
5.14	Analysis of first order diffraction mechanism around corners in metro-202.	108
5.15	Analysis of D-R and R-D propagation mechanism for receivers in Figure 5.14a along metro-202.	109
5.16	Comparison of over rooftop only with measured data.	111
5.17	Comparison of all but over rooftop with measured data.	112
5.18	Comparison of all but ground reflections with measured data.	113
5.19	Comparison of diffraction only with measured data.	114
5.20	Comparison of R-D and D-R only with measured data.	115
5.21	Mapping of lit polygon of images for image-tree reduction [160]. . . .	115
5.22	Comparison of computational performance for different grid dimensions [160]	118
5.23	Histogram of number of lit polygons mapped per grid-square in Munich example [160].	120
5.24	Mapping of lit polygon of images for a mobile route	121
5.25	Selection of route length to avoid missing the valid rays	123
5.26	Selected route simulated for different thresholds	124
5.27	Path loss comparison for different route deviation thresholds	125

5.28	An example of a mobile route passing through lit and shadow polygons associated with a wall reflection image [161].	127
6.1	Flow Chart of Ray-tracing Algorithm for Mobile Transmitter	135
6.2	Determination of visibility angles for a completely visible face.	136
6.3	Determination of visibility angles for a partially visible face.	138
6.4	Intra-visibility angles computation for an edge visible to a face.	139
6.5	Determination of higher order images using intra-visibility matrix. . .	141
6.6	Consideration of constantly varying lit polygon associated with a wall reflection visible to a mobile transmitter.	144
6.7	An example environment with a transmitter moving from X to Y. Two buildings block the visibility for face F_{11} and edges E_{11} and E_{12} so that they are only visible between the distance d_1 and d_2 from X.	146
6.8	Face F_{11} is visible to the mobile transmitter between distance d_1 and d_2 . The maximum visibility region of first order visible face F_{11} is bounded by α_1 and β_2 lines as shown.	148
6.9	CASE-I: Computation of initial distance d_i at which a face becomes visible to an illuminated face. The initial visibility angles (a_1, b_1) of faces F_{m1} and F_{n1} are within the maximum visibility region of face F_{11}	150
6.10	CASE-I: Computation of final distance d_f for which a face remains visible to an illuminated face.	151
6.11	CASE-II: Final visibility angles of face F_{m1} are within the maximum visibility region of illuminated face F_{11} . F_{m1} becomes visible to F_{11} corresponding to transmitter location at d_1	152
6.12	CASE III: Face F_{m1} remains visible to illuminated face F_{11} for the entire length of multiple transmitters between d_1 and d_2	154
6.13	Face F_{11} is visible to the mobile transmitter between distance d_1 and d_2 . The maximum visibility region of first order visible face F_{11} is bounded by α_2 and β_1 lines as shown.	155
6.14	CASE-I: Computation of initial distance d_i at which a face becomes visible to an illuminated face when the transmitter is moving in opposite direction.	157
6.15	CASE-I: Computation of final distance d_f for which a face remains visible to an illuminated face for transmitter moving in opposite direction.	158
6.16	Computation of higher order visible faces for example in Figure 6.7.	159
6.17	Higher order visibility computation for example in Figure 6.7 for three transmitter locations A, B and C using the visibility table.	161
6.18	Map of Munich city with a line of 76 transmitter points along a street. Arrow shows the reference direction used for distance computations.	162
6.19	Comparison of first order diffraction mechanism using the reciprocity principle.	165

List of Tables

4.1	Reported path loss exponent (n) values for different environments [42]	50
4.2	Values of Erceg Model Parameters [67]	54
5.1	Measured data collected along three routes in Munich city. $f_c = 947\text{MHz}$, $h_{tx} = 13\text{m}$, $h_{rx} = 1.5\text{m}$	100
5.2	Standard deviation of error (σ) and Mean error (η) along three metro routes in Munich city.	101
5.3	Comparison of CPU time for metro routes.	103
5.4	Comparison of mean and standard deviation of error with measured data for different combination of rays	110
5.5	Lit polygons mapping database for example in Figure 5.21 [160]	116
5.6	Memory and lit polygons mapping time required for different grid resolutions [160]	118
5.7	Comparison of CPU time for metro routes using lit polygons mapping.	119
5.8	Standard deviation of error (σ) and time reduction for different route deviation thresholds.	126
5.9	Comparison of CPU time for metro routes using lit polygons mapping for linear mobile route.	126
5.10	Comparison of CPU time for metro routes using lit and shadow polygons mapping for linear mobile route.	128
5.11	Comparison of CPU time for metro routes in Munich city using the acceleration techniques developed in this work.	130
6.1	Visibility table entries for building B_1 in Figure 6.7.	147
6.2	Modified Visibility table entries for building B_1 in Figure 6.7.	160
6.3	Run time for visibility table and image-tree computation for 76 transmitter locations that considers only wall reflections in Munich test environment.	163
6.4	Run time for visibility table and image-tree computation for 76 transmitter locations that considers both wall reflection and edge diffraction in Munich test environment.	163

6.5 Comparison of memory reduction and run time increment for simulating the transmitter route in Munich test environment using two sub-routes and three sub-routes respectively. 167

Abstract

Recent times have seen a significant increase in radio networks capacity demands resulting in small cells deployment. The application of standard radio channel models is not straightforward in such environments. The radio wave propagation becomes site-specific as it is greatly affected by the objects present in the environment. A ray-tracing model computes the dominant paths through which radio energy propagates considering the geometry of the environment. The aim of this work is to develop efficient ray-tracing acceleration techniques for radio wave propagation in urban environments.

A radio wave that interacts with a wall or an edge of a building undergoes reflection or diffraction respectively. The horizontal area where the reflected or diffracted rays can possibly propagate represents the lit region of an illuminated wall or edge. The buildings present in the lit region block the rays to form shadow regions. A valid ray exists at a given receiver location only if it is located inside the lit region and outside of all the shadow regions of an illuminated wall or edge. The lit and shadow polygons are represented by four sides so that a geometrical test requires four computations to validate if a receiver is located inside or outside of a polygon. A recursive algorithm has been developed to validate the rays at all receiver locations.

A mobile receiver enters and leaves the lit regions and the associated shadow regions of illuminated walls and edges as it moves along a linear route. The entry and exit points of the receiver through the lit polygons and the associated shadow polygons are pre-computed to produce a database of relative location of polygons intersection along the route. A novel method has been developed that makes use of this database to accelerate the ray computations. The geometrical test to validate a ray-segment is replaced by a simple check that compares the receiver location with the polygons intersections along the route.

The database of visible walls and edges, known as visibility list, is always required for ray tracing computations. The visibility checks must therefore be performed independently each time the transmitter location is changed. This increases the pre-processing time for the ray tracing model and limits its application for mobile transmitter scenarios. A database that pre-computes the list of visible walls and edges to each wall and edge in the environment, or so-called the intra-visibility matrix is proposed. A novel algorithm is developed that determines the visibility list for a mobile transmitter moving along a linear trajectory using the intra-visibility matrix. This work presents ray tracing acceleration techniques for both a mobile receiver and transmitter. The algorithm for

mobile receiver has been validated by comparing the path loss against measured data available from COST 231 project. The ray tracing acceleration algorithm for mobile transmitter can reduce the pre-processing time by up to 90% and accurately predicts the ray paths as validated against the COST 231 measured data using the reciprocity principle.

Chapter 1

Introduction

The foundation of radio communications was laid in 1860 when James Clark Maxwell put forward his theory of electromagnetism. According to this theory a radio wave can be propagated by varying its electrical field. This theory was practically implemented by Heinrich Hertz in 1887 when he was able to transmit and receive radio waves using the antenna in his laboratory [1]. J J Thompson first suggested propagation of electromagnetic waves through hollow tubes in 1893 [2]. This idea served as the basis of radar and satellite communications in the following years. Guglielmo Marconi made the first practical realization of radio communications as he was able to provide continuous communication with ships in 1897. He invented the radio transmitter and receiver and commercialized radio communications. The development of solid state radio frequency hardware in the 1970s gave birth to a new wireless era. Since then the graph of wireless technologies has risen very sharply and high quality radio communications has been made possible.

The first generation of radio communications was an analog cellular system based on Frequency Division Multiple Access (FDMA). The first mobile system, Advanced Mobile Phone System (AMPS), was introduced in United States in 1983. Digital communication systems were introduced later in 1990s that provided both voice and some basic data services. These systems were called the second generation (2G) of radio services and included GSM and IS-95 based primarily on Code Division Multiple Access (CDMA). The third generation (3G) systems provided improved spectral efficiency and higher network capacity for voice, video and broadband wireless data services. 3G networks in United States were based on CDMA2000 while the European equivalent system UMTS was based on Wideband CDMA (WCDMA) air interface [3]. The fourth generation (4G) of radio communications introduced in 2010 provides enhanced roaming and broadband multimedia services with very high data rates on a common Internet Protocol (IP) based platform [4]. The development of fifth generation (5G) systems is being investigated that will provide 100 to 1000 times higher data rates than the 4G systems. These high data rates will be achieved by using extremely dense networks for spectrum reuse, millimeter wave spectrum for increased bandwidth and

advances in multiple-input multiple-output (MIMO) systems for increased spectral efficiency [5].

1.1 Motivation for Radio Channel Modeling

Modeling of the radio channel is a key step for the design and implementation of a wireless communications system. A typical radio propagation environment can be indoor or outdoor. The indoor environment covers a few meters and can include a small building or a small area such as a shopping mall or a football stadium etc. while an outdoor environment can be an urban, suburban or rural area covering few kilometres. A radio signal loses its power (*large scale fading*) as it propagates through the space. As the radio signal propagates in an environment, it interacts with the objects (buildings, walls, hills or ground) in that environment. This interaction leads to the reflection, transmission, diffraction and scattering of the radio signal depending on the shape, size, material and the relative location of the object in the environment. The signals arriving at the receiver can add constructively or destructively depending on how long it takes it to arrive at the receiver. This phenomenon of slight change in the location of the receiver that leads to large signal variations is called *small scale* or *multipath fading*.

Before a radio system can be designed, one must consider how far the radio signals will propagate in the environment (radio coverage prediction) and how the receiver will handle local signal variations due to multipath fading. Radio coverage prediction determines the number of base stations, power output and characteristics of the transmitting antennae required for the link. While the small scale fading defines the receiver characteristics and its ability to cope with multipath signals. These parameters can be estimated using the field measurements which is expensive and time consuming. An alternative is to use the radio channel models to predict the radio channel parameters.

1.2 Contribution and Overview

This work presents several published work on ray tracing algorithms for urban propagation prediction. A background of electromagnetic theory associated with high frequency fields is described. The laws of reflection, refraction and geometrical and uniform theory of diffraction are studied. The basic techniques for ray tracing are presented followed by a brief study of radio channel models and some ray tracing acceleration techniques found in the literature. The buildings are simply represented by vertical surfaces and edges. A ray tracing model computes the radio energy in specular directions. The scattering from urban furniture and rough surfaces can be significant and should be included in ray tracing models.

The contribution of this thesis can be listed as follows.

- Development of an efficient ray-object intersection test to accelerate the ray computations based on simple 2-D polygons representation of scatterers.
- Reduction in active image tree for a receiver to speed up the ray computations based on mapping of lit and shadow polygons.
- Development of fast ray validation test for a mobile receiver based on pre-processed database of lit and shadow polygons mapping.
- Development of an intra-visibility matrix database to compute the image tree for a transmitter.
- Development of a fast ray tracing algorithm for a mobile transmitter based on pre-processed intra-visibility database.

The overall structure of this thesis is as follows.

Chapter 2 provides electromagnetic background of high frequency fields associated with the use of rays. The constitutive parameters, material types and medium classification is described. The asymptotic solution of high frequency problem is presented to characterise the rays. The laws of reflection, transmission, geometrical and uniform theory of diffraction are described.

Chapter 3 provides an overview of general techniques in ray tracing. The basics of visibility algorithms, image-tree creation and the ray-object intersection test for ray validation are presented. The parameters that characterise a radio channel are also discussed.

Chapter 4 provides a through study of radio channel models including empirical, theoretical and site-specific. A literature review of all the efficient ray tracing acceleration techniques is presented. Future trends and limitations of ray tracing models are also discussed.

Chapter 5 provides an efficient representation of lit and shadow regions associated with the images as polygons. An efficient ray-object intersection test is developed to accelerate the ray validation. The significance of different propagation mechanisms in a typical urban environment is studied. The model is extended to efficiently compute the valid rays for a mobile receiver in urban environments.

Chapter 6 presents a database of walls' and edges' intra-visibility along with angular information for the given urban environment. The model identifies the walls and edges that are visible to the mobile transmitter for the required order of ray interaction using the intra-visibility matrix. The time required for visibility pre-processing is reduced as the ray tracing model uses the intra-visibility matrix to readily identify the visible faces and edges for the mobile transmitter.

Chapter 7 provides general conclusions and possible future developments.

Chapter 2

Electromagnetic Theory

The solution of Maxwell's equations describes radio wave propagation in a given medium. However, high frequency electromagnetic problems can be approximately solved using a more suitable approach based on high frequency solution of geometrical optics. A *high frequency problem* is defined as one for which the properties of medium and scatterer size do not change over a wavelength interval. The mathematical techniques that are developed to analyse high frequency problem are known as *asymptotic methods* [6].

The *classical geometrical optics* was developed to study light phenomena using ray optics. The ancient Greek mathematicians Euclid and Ptolemy presented basic theories of reflection and refraction of light respectively. The correct law of refraction was later derived experimentally by Willebrord Snell in 1621. The French mathematician Fermat presented his famous principle in 1654 stating that a ray independent of whether it is subjected to reflection or diffraction, travels from one point to another in the shortest time.

The phenomenon of diffraction could not be explained by classical geometrical optics. It was later discovered that light waves are governed by Maxwell's equations. The work of Luneberg[7] and Kline [8] established the more accurate relation between Maxwell equations and the geometrical concepts. This extended the classical geometrical optics to the more accurate and so-called *modern geometrical optics*. Joseph B. Keller [9] presented his well known geometrical theory of diffraction (GTD) that incorporates diffraction phenomena using a geometrical approach. However, GTD fails abruptly at shadow boundaries where it gives infinite fields. The uniform theory of diffraction (UTD) was developed by Kouyoumjian *et al.* [10] and gives a continuous solution across the shadow boundaries as well.

This chapter introduces the background of electromagnetic theory associated with the use of rays. The constitutive parameters that characterises the propagation medium are briefly explained. The types of material as well as the medium classification is described. The solution of Maxwell equations using high-frequency techniques is presented. The properties of high-frequency fields associated with the use of rays are

listed. The laws of reflection, transmission (refraction), geometrical and uniform theory of diffraction are also discussed to give a complete theoretical background.

2.1 Constitutive Parameters

The interaction of a radio wave with an object depends on the size, shape and electrical characteristics of the object's material. The following *constitutive relations* give three *constitutive parameters* that define the electrical characteristics of the material.

$$\mathbf{D} = \epsilon \mathbf{E} \quad (2.1)$$

$$\mathbf{B} = \mu \mathbf{H} \quad (2.2)$$

$$\mathbf{J}_c = \sigma \mathbf{E} \quad (2.3)$$

The permittivity ϵ of a material is the measure of electric flux density \mathbf{D} produced as a result of electric field intensity \mathbf{E} applied on the material as given by equation 2.1. The relative permittivity of a material is also called the *dielectric constant* and gives the electric charge that a material can store relative to free-space.

$$\epsilon_r = \frac{\epsilon}{\epsilon_0} \quad (2.4)$$

where, $\epsilon_0 = 8.854 \times 10^{-12}$ (Farads/meter) is free-space permittivity.

The permeability μ of a material is the measure of magnetic flux density \mathbf{B} produced as a result of magnetic field intensity \mathbf{H} applied on the material as given by equation 2.2. The relative permeability of a material is the ratio of its permeability to the permeability of free-space.

$$\mu_r = \frac{\mu}{\mu_0} \quad (2.5)$$

where, $\mu_0 = 4\pi \times 10^{-7}$ (Henries/meter) is free-space permeability.

The conductivity σ of a material is the measure of conduction current density \mathbf{J}_c as a result of electric field intensity \mathbf{E} applied on the material as given by equation 2.3. It characterises the conductive properties of a material due to free-electrons present in its valence shell. The conductivity of free-space is zero.

2.2 Types of Materials

Depending on the constitutive parameters materials can be classified broadly into four types.

A *dielectric* or *insulator* is a material in which there are no free-electrons available in the atomic structure. However applying an external electric field intensity can shift

the charge balance within the atomic structure to give an electric displacement current. The shift of charge balance within the atomic structure creates electric dipoles and this effect is referred to as *electronic polarization*. The polarization effect is predominant in dielectric materials and is reflected in the value of dielectric constant ϵ .

A *magnetic* material is classified as one that produces a higher magnetic flux density when subjected to an external magnetic field. The magnetic flux produces magnetic dipoles within the material just like electric dipoles in dielectrics to give a magnetisation current. The value of permeability μ defines the magnetic properties of a material. Materials with value of relative permittivity μ_r in the order of 10^2 - 10^5 such as iron, nickel and cobalt etc. are called ferromagnetic materials.

A *conductor* material has an abundance of free-electrons available in the atomic structure. When an external electric field is applied free-electrons move towards the surface of the material to create an electric conduction current. The value of conductivity σ range between 10^2 S/m to 10^7 S/m for conductors.

An intrinsic *semiconductor* material has conductivity σ value between the insulator and conductor in the range of 10^{-3} S/m to 10^0 S/m. A relatively small energy equal to the band gap between the valence and conduction bands is required to free the electrons from the valence band into the conduction band. These free-electrons creates a net positive charge in the valence shell designated as *holes*. Germanium and silicon are the two most important semiconductors in electrical engineering as they are widely used for manufacturing of electronic devices.

2.3 Classification Of Media

A medium can be classified into different types depending on how its constitutive parameters change within the material.

A material whose constitutive parameters do not change with the applied field strength is known as a *linear* medium. Most materials exhibit linear properties until a certain limit of the applied field strength is reached. Beyond that the medium becomes non-linear

A material whose constitutive parameters do not change with position is called a *homogeneous* medium. Almost all materials exhibit inhomogeneous properties in practice. However the difference is generally so small that a material can be considered as perfectly homogeneous.

A material whose constitutive parameters change with frequency is called a *dispersive* medium. All materials exhibit some sort of dispersive characteristics. However, the permittivity of dielectric materials and permeability of ferromagnetic materials have relatively noticeable dispersive properties.

A material whose constitutive parameters do not change with the direction of applied field is called an *isotropic* material. Crystals exhibit anisotropic characteristics as their dielectric constant changes with the direction of applied field.

2.4 High Frequency Fields associated with Rays

The time harmonic fields in a homogeneous lossless medium are given by Maxwell's equations as follows.

$$\nabla \times \mathbf{E}(\mathbf{r}, \omega) + j\omega\mu\mathbf{H}(\mathbf{r}, \omega) = 0 \quad (2.6)$$

$$\nabla \times \mathbf{H}(\mathbf{r}, \omega) - j\omega\varepsilon\mathbf{E}(\mathbf{r}, \omega) = 0 \quad (2.7)$$

$$\nabla \cdot \mathbf{E}(\mathbf{r}, \omega) = 0 \quad (2.8)$$

$$\nabla \cdot \mathbf{H}(\mathbf{r}, \omega) = 0 \quad (2.9)$$

Eliminating \mathbf{H} from 2.6 and replacing in 2.7 gives the vector Helmholtz equation as follows,

$$\nabla^2\mathbf{E}(\mathbf{r}, \omega) + k^2\mathbf{E}(\mathbf{r}, \omega) = 0 \quad (2.10)$$

where $k^2 = \omega^2\mu\varepsilon$ and $\nabla^2\mathbf{E} = \nabla\nabla \cdot \mathbf{E} - \nabla \times \nabla \times \mathbf{E}$. A similar expression can be derived for \mathbf{H} .

The anticipated high-frequency asymptotic solution of electromagnetic fields, proposed by Luneberg-Kline can be given as follows [6],

$$\mathbf{E}(\mathbf{r}, \omega) \sim e^{-jk\psi(\mathbf{r})} \sum_{n=0}^{\infty} \frac{\mathbf{E}_n(\mathbf{r})}{(j\omega)^n} \quad (2.11)$$

$$\mathbf{H}(\mathbf{r}, \omega) \sim e^{-jk\psi(\mathbf{r})} \sum_{n=0}^{\infty} \frac{\mathbf{H}_n(\mathbf{r})}{(j\omega)^n} \quad (2.12)$$

where $\psi(\mathbf{r})$ is the so-called *eikonal* or *phase function* given as,

$$|\nabla\psi|^2 = n^2 \quad (2.13)$$

where n is the refractive index of the propagation medium and is equal to 1 for free-space.

The *zeroth-order transport equation* that governs the flow of the energy in the medium is given by,

$$2(\nabla\psi \cdot \nabla)\mathbf{E}_0 + (\nabla^2\psi)\mathbf{E}_0 = 0 \quad (2.14)$$

trajectory is given by,

$$\mathbf{E}(s) = |\mathbf{E}_0(0)| e^{-jk\psi(0)} \sqrt{\frac{\rho_1 \rho_2}{(\rho_1 + s)(\rho_2 + s)}} e^{-jks} \quad (2.15)$$

ρ_1 and ρ_2 represent the principal radii of curvature of the wave front on the *astigmatic ray tube* as shown in Figure 2.1.

7. The total GO field at a given point is the sum of all ray fields passing through that point. This allows us to compute the total field at a given receiver location as the sum of all direct, reflected, transmitted and diffracted ray fields as will be discussed later.
8. If the surfaces of constant phase and amplitude are planar everywhere, the GO fields for such a plane wave ray tube are simplified to,

$$\mathbf{E}(s) = \mathbf{E}(0) e^{-jks} \quad (2.16)$$

as $\rho_1 \rightarrow \infty$ and $\rho_2 \rightarrow \infty$ for a plane wave.

9. If the surfaces with constant phase and amplitude are concentric cylinders, the GO field expression for such a cylindrical wave ray tube is given by,

$$\mathbf{E}(s) = \mathbf{E}(0) \sqrt{\frac{\rho}{(\rho + s)}} e^{-jks} \quad (2.17)$$

as $\rho_1 \rightarrow \infty$ and $\rho_2 = \rho$ for a cylindrical wave.

10. If the surfaces with constant phase and amplitude are concentric spheres, the GO field for such a spherical wave ray tube is given by,

$$\mathbf{E}(s) = \mathbf{E}(0) \frac{\rho}{(\rho + s)} e^{-jks} \quad (2.18)$$

as $\rho_1 = \rho_2 = \rho$ for a spherical wave.

2.6 Interaction of High-Frequency Field with Surfaces

Having analysed how the GO field propagates in a given medium, it is also of interest to find out what happens when it interacts with a surface. The problem of ray interaction with surfaces can be divided into two types. The first is when a ray interacts with a continuous smooth surface and produces a reflection. The smooth surface refers to a scatterer whose dimensions are relatively larger in terms of the wavelength at the frequency of operation so that the high-frequency asymptotic methods are applicable. The second type of ray interaction is when a discontinuity in the scatterer surface is

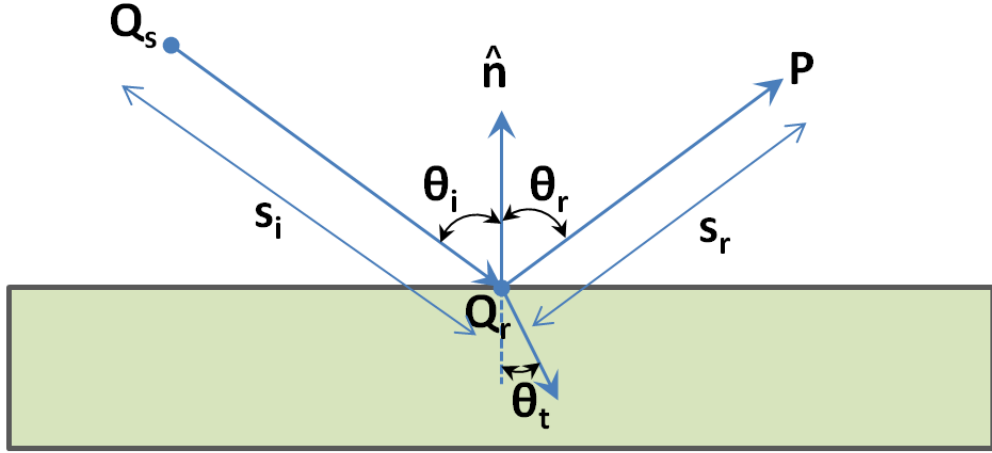


Figure 2.2 Incident and reflected ray at a point on a surface.

encountered. i.e., the ray interacts with the edge of a surface and diffraction occurs. The following gives an overview of reflection and diffraction and how the associated fields can be computed using the GO techniques.

2.6.1 Reflection

Consider a ray propagating in free-space from some source which impinges on a smooth surface at point Q_r as shown in Figure 2.2. The incident ray is described by vector \hat{s}_i with initial GO field $\mathbf{E}_i(Q_s)$ at a reference point Q_s . The incident field at the reflection point Q_r that lies at distance s_i from the incident ray reference point Q_s can be given by using 2.15.

$$\mathbf{E}_i(Q_r) = \mathbf{E}_i(Q_s) \sqrt{\frac{\rho_1 \rho_2}{(\rho_1 + s_i)(\rho_2 + s_i)}} e^{-jks_i} \quad (2.19)$$

The above expression for the incident field can be replaced with the corresponding GO field as given by equations 2.16, 2.17 and 2.18 depending on whether the field at Q_s is a plane, cylindrical or spherical wave. The reflected field after reflection can be given by,

$$\mathbf{E}_r(Q_r) = \mathbf{R} \cdot \mathbf{E}_i(Q_r) \quad (2.20)$$

\mathbf{R} is the reflection coefficient and is dyadic in general as both $\mathbf{E}_i(Q_r)$ and $\mathbf{E}_r(Q_r)$ are vectors. If $\hat{\mathbf{n}}$ is the unit normal to the surface, then the unit vectors $\hat{\mathbf{s}}_i$ and $\hat{\mathbf{n}}$ define the plane of incidence. The incident electric field \mathbf{E}_i can be resolved into two components parallel and perpendicular to the plane of incidence as shown in Figure 2.3. Likewise,

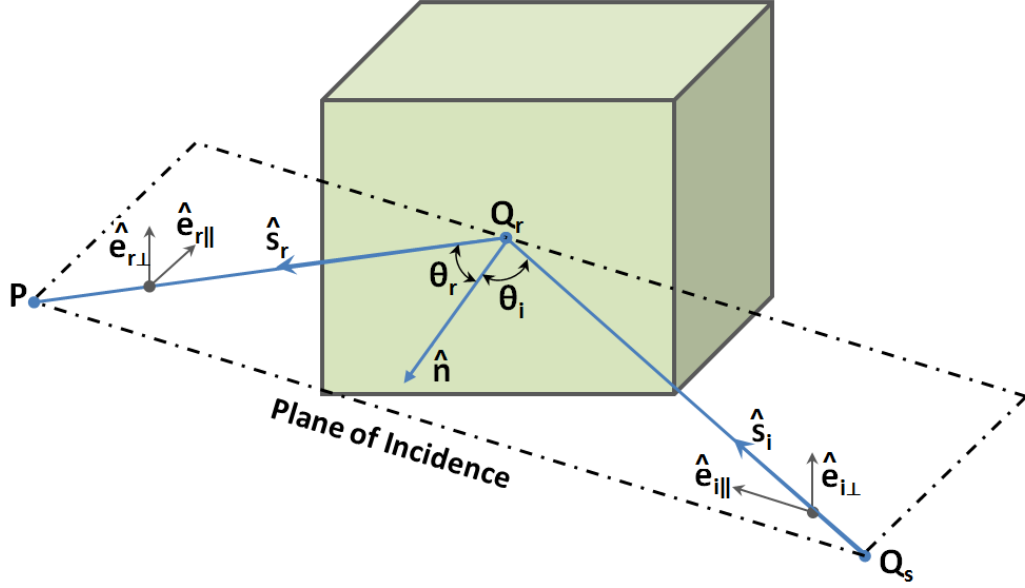


Figure 2.3 The planes of incidence and reflection in ray-fixed coordinate system.

the reflected electric field $\mathbf{E}_r(Q_r)$ can also be resolved into a parallel and perpendicular component. The following relation is true for the component vectors [12].

$$\hat{\mathbf{e}}_{i\perp} \times \hat{\mathbf{s}}_i = \hat{\mathbf{e}}_{i\parallel} \quad (2.21)$$

$$\hat{\mathbf{e}}_{r\perp} \times \hat{\mathbf{s}}_r = \hat{\mathbf{e}}_{r\parallel} \quad (2.22)$$

$$\hat{\mathbf{e}}_{i\parallel} = \hat{\mathbf{s}}_i \times (\hat{\mathbf{n}} \times \hat{\mathbf{s}}_i) \quad (2.23)$$

$$\hat{\mathbf{e}}_{r\parallel} = \hat{\mathbf{s}}_r \times (\hat{\mathbf{n}} \times \hat{\mathbf{s}}_r) \quad (2.24)$$

Applying the Luneberg-Kline asymptotic expression for GO field using 2.11 and satisfying the boundary conditions, the following can be derived,

$$\theta_i = \theta_r \quad (\text{Snell's law of Reflection}) \quad (2.25)$$

$$k_1 \sin \theta_i = k_2 \sin \theta_t \quad (\text{Snell's law of Refraction}) \quad (2.26)$$

These are the well-known *Snell's law of reflection* and *refraction* that relates the angles of incidence, refraction and reflection at the boundary. The incident and reflected rays are in same plane so that the vectors $\hat{\mathbf{s}}_i$, $\hat{\mathbf{n}}$ and $\hat{\mathbf{s}}_r$ are coplanar as shown in Figure 2.3. Mathematically,

$$\hat{\mathbf{n}} \cdot \hat{\mathbf{s}}_i = -\hat{\mathbf{n}} \cdot \hat{\mathbf{s}}_r \quad (2.27)$$

$$\hat{\mathbf{n}} \times \hat{\mathbf{s}}_i = \hat{\mathbf{n}} \times \hat{\mathbf{s}}_r \quad (2.28)$$

The reflection coefficient \mathbf{R} can also be decomposed into two components parallel and perpendicular to the incidence plane and given by [13],

$$R_{\perp} = \frac{\eta_2 \cos \theta_i - \eta_1 \cos \theta_t}{\eta_2 \cos \theta_i + \eta_1 \cos \theta_t} \quad (2.29)$$

$$R_{\parallel} = \frac{\eta_2 \cos \theta_t - \eta_1 \cos \theta_i}{\eta_2 \cos \theta_t + \eta_1 \cos \theta_i} \quad (2.30)$$

where η_1 and η_2 represents the intrinsic wave impedance of free-space and the medium from which the reflection occurs respectively and is given by,

$$\eta = \sqrt{\frac{j\omega\mu}{\sigma + j\omega\epsilon}} \simeq \sqrt{\frac{\mu}{\epsilon}} \text{ (for lossless medium)} \quad (2.31)$$

Using matrix notation,

$$\mathbf{E}_r(Q_r) = \begin{bmatrix} E_{r\parallel}(Q_r) \\ E_{r\perp}(Q_r) \end{bmatrix} \quad (2.32)$$

$$\mathbf{E}_i(Q_r) = \begin{bmatrix} E_{i\parallel}(Q_r) \\ E_{i\perp}(Q_r) \end{bmatrix} \quad (2.33)$$

$$\mathbf{R} = \begin{bmatrix} R_{\parallel} & 0 \\ 0 & R_{\perp} \end{bmatrix} \quad (2.34)$$

Equation 2.20 can be re-written as follows,

$$E_{r\parallel} = R_{\parallel} E_{i\parallel} \quad (2.35)$$

$$E_{r\perp} = R_{\perp} E_{i\perp} \quad (2.36)$$

The GO reflected field that arrives at the point P located at distance s_r is given by,

$$\mathbf{E}_r(P) = \mathbf{E}_r(Q_r) \frac{s_i}{s_i + s_r} e^{-jks_r} \quad (2.37)$$

The equations 2.20 - 2.37 are used to compute the specular reflection from the walls in the ray tracing model developed in this work in chapters 5 and 6.

2.6.2 Wedge Diffraction

The interaction of a ray propagating in a homogeneous medium with a sharp discontinuity in surface structure such as an edge diffracts the radio energy in all directions. Diffraction accounts for the propagation of signals in so-called *shadow regions* where direct line of sight is not possible. The classical GO methods fail to account for the diffracted fields in shadow regions. J.B. Keller corrected the GO field by adding the diffracted rays into the solution. He formulated the *Geometrical Theory of Diffraction (GTD)* based on the generalised Fermat's principle to find the point of diffraction and the direction of diffracted rays. The law states that [9]

A diffracted ray and the corresponding incident ray make equal angles with the edge at the point of diffraction, provided they are in the same medium. They lie on opposite sides of the plane normal to the edge at the point of diffraction.

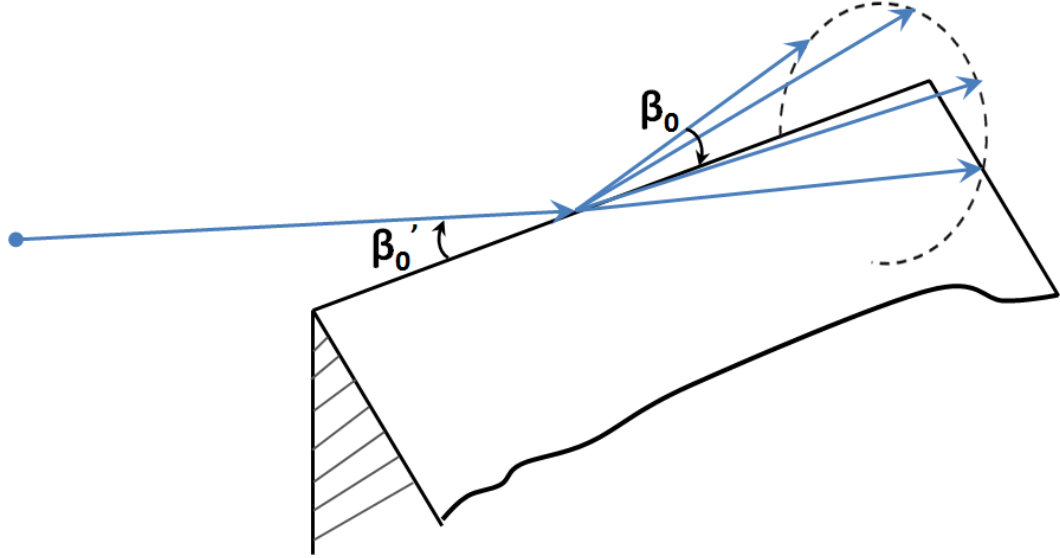


Figure 2.4 Cone of diffracted rays [11].

A ray incident on an edge at angle β_0' produces a cone of diffracted rays with half-angle β_0 as shown in Figure 2.4. The law of diffraction states that these angles are equal such that $\beta_0' = \beta_0$.

Consider a two dimensional (2-D) semi-infinite wedge of interior angle α illuminated by a line source at Q_s as shown in Figure 2.5. Three different regions are highlighted. The GO field exists in regions I and II only and consists of incident field (\mathbf{E}_i) and reflected field (\mathbf{E}_r). The diffracted field (\mathbf{E}_d) exists in all regions. The total field in all three regions is given by [11],

$$\mathbf{E}_{total} = \begin{cases} \mathbf{E}_i + \mathbf{E}_r + \mathbf{E}_d & 0 \leq \phi < \pi - \phi' \quad (\text{Region I}) \\ \mathbf{E}_i + \mathbf{E}_d & \pi - \phi' < \phi < \pi - \phi \quad (\text{Region II}) \\ \mathbf{E}_d & \pi - \phi < \phi \leq 2\pi - \alpha \quad (\text{Region III}) \end{cases}$$

The GO fields \mathbf{E}_i and \mathbf{E}_r are given by equations 2.15 and 2.37 as discussed earlier. The diffracted field \mathbf{E}_d can be represented in the general form below:

$$\mathbf{E}_d(P) = \mathbf{E}_i(Q_d) \cdot D \sqrt{\frac{s'}{s(s+s')}} e^{-jks} \quad (2.38)$$

The diffracted field is a combination of incident diffracted field (\mathbf{E}_{di}) and reflected diffracted field (\mathbf{E}_{dr}) so that,

$$E_d = E_{di} + R_{edge} \cdot E_{dr} \quad (2.39)$$

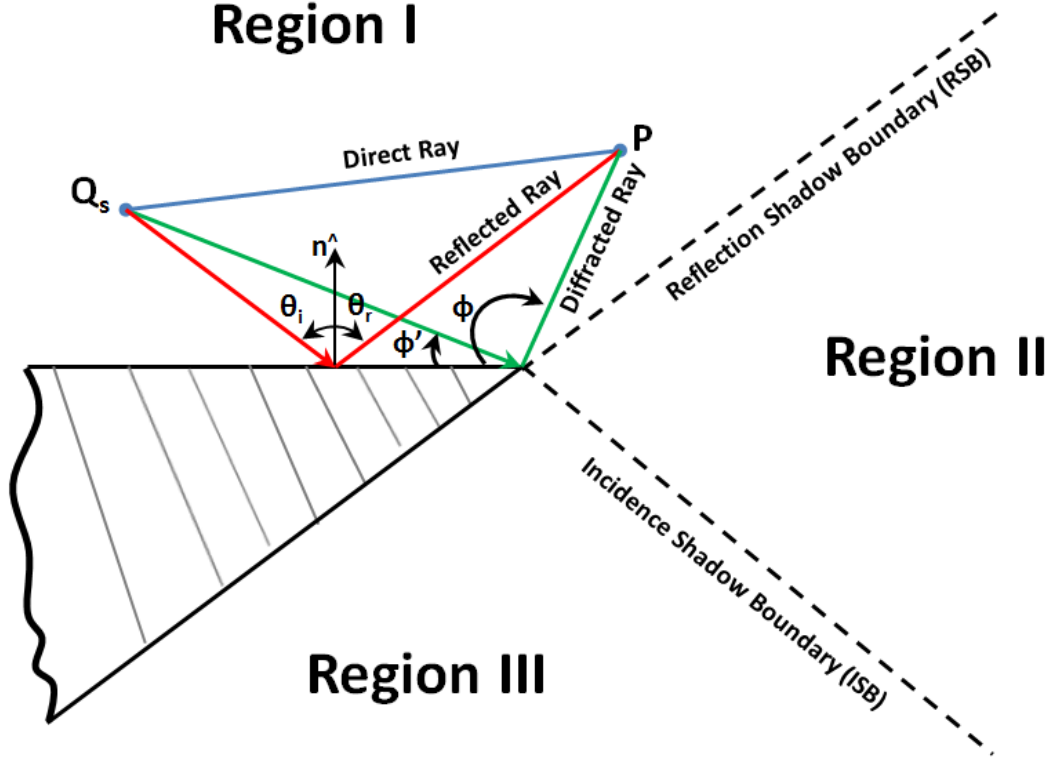


Figure 2.5 Geometry for scattering from a wedge [11].

Keller's diffraction function gives the total diffracted field as below [9].

$$E_d = K \left[\frac{1}{\cos\left(\frac{\pi}{n}\right) - \cos\left(\frac{\phi - \phi'}{n}\right)} + R_{edge} \frac{1}{\cos\left(\frac{\pi}{n}\right) - \cos\left(\frac{\phi + \phi'}{n}\right)} \right] \frac{e^{-jks}}{\sqrt{s}} \quad (2.40)$$

where $K = \frac{e^{-j\pi/4}}{\sqrt{2\pi\beta}} \frac{1}{n} \sin\left(\frac{\pi}{n}\right)$ and R_{edge} is the reflection coefficient at the edge of the wedge surface. The value of R_{edge} is +1 for hard polarization and -1 for soft polarization for a perfectly conducting wedge.

There are still shortcomings in GTD as it fails to give continuous fields at the incidence and reflection shadow boundaries (ISB and RSB). The *Uniform Theory of Diffraction* (UTD) [10] gives accurate field in all regions. To find the diffracted field for oblique incidence, an edge fixed coordinate system can be introduced such that β_0 and ϕ components of the incident and diffracted fields are parallel and perpendicular to the plane of incidence and diffraction, respectively. Figure 2.6 represents the planes and components of the incident and diffracted fields.

The diffracted field in matrix form can be written as,

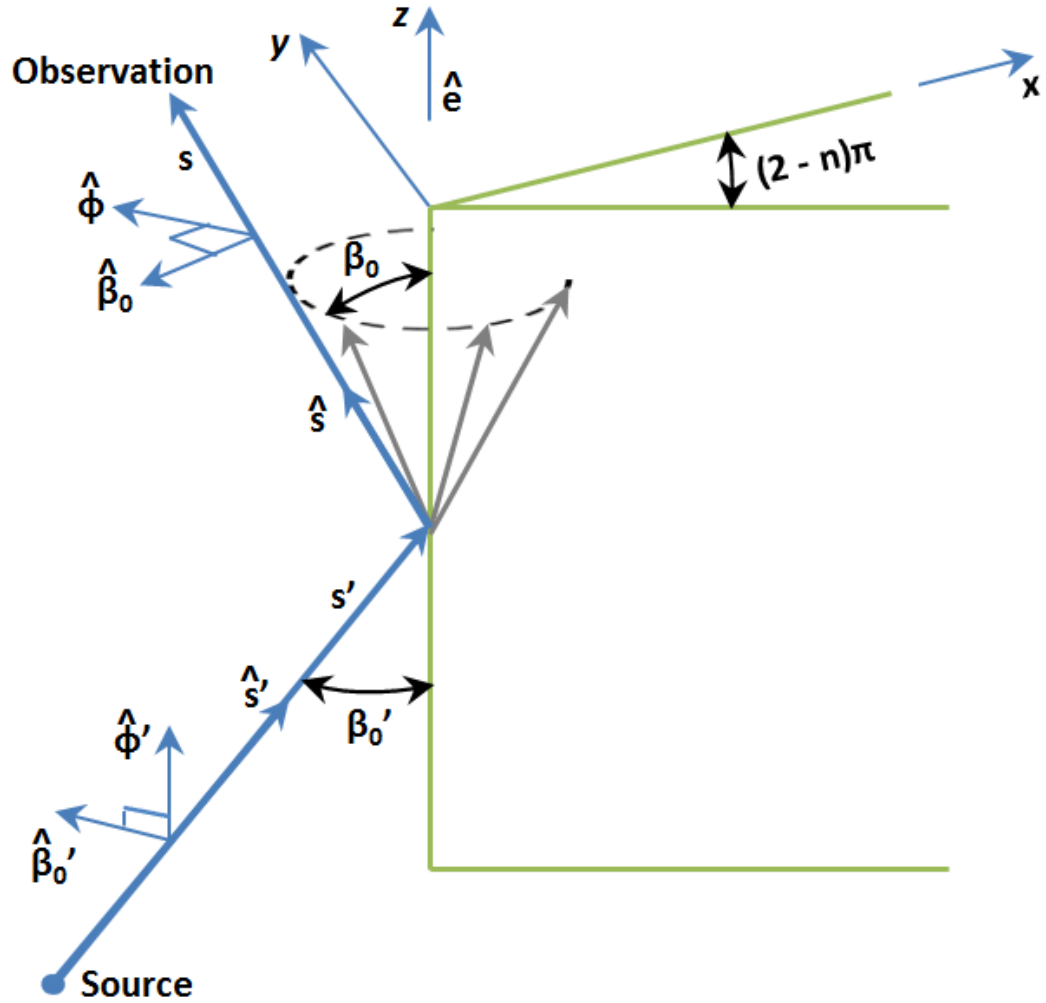


Figure 2.6 Edge fixed coordinate system for oblique incidence wedge diffraction [13].

$$\begin{bmatrix} E_{\beta_0}^d(s) \\ E_{\phi}^d(s) \end{bmatrix} = \begin{bmatrix} -D_s & 0 \\ 0 & -D_h \end{bmatrix} \begin{bmatrix} E_{\beta_0'}^i(Q_D) \\ E_{\phi'}^i(Q_D) \end{bmatrix} A(s, s') e^{-jks} \quad (2.41)$$

where,

$E_{\beta_0'}^i(Q_D) = \mathbf{E}_i \cdot \hat{\beta}_0'$ = component of incident field parallel to the plane of incidence

$E_{\phi'}^i(Q_D) = \mathbf{E}_i \cdot \hat{\phi}'$ = component of incident field perpendicular to the plane of incidence

D_s and D_h are scalar diffraction coefficients, given as

$$D_s(L; \phi - \phi'; n; \beta_0') = D_i(L, \phi - \phi', n, \beta_0') + R_{\perp edge} D_r(L, \phi - \phi', n, \beta_0') \quad (2.42)$$

$$D_h(L; \phi - \phi'; n; \beta_0') = D_i(L, \phi - \phi', n, \beta_0') + R_{\parallel edge} D_r(L, \phi - \phi', n, \beta_0') \quad (2.43)$$

where $R_{\perp edge}$ and $R_{\parallel edge}$ are the perpendicular and parallel components of reflection coefficient at edge and are calculated using 2.29 and 2.30 respectively. The incident and reflected diffraction coefficients D_i and D_r can be given as follows,

$$D_i(L, \phi - \phi', n, \beta'_0) = -\frac{e^{-j\frac{\pi}{4}}}{2n\sqrt{2\pi\beta} \sin\beta'_0} \left\{ \begin{array}{l} \cot \left[\frac{\pi + (\phi - \phi')}{2n} \right] F \left[\beta L g^+(\phi - \phi') \right] \\ + \cot \left[\frac{\pi - (\phi - \phi')}{2n} \right] F \left[\beta L g^-(\phi - \phi') \right] \end{array} \right\} \quad (2.44)$$

$$D_r(L, \phi + \phi', n, \beta'_0) = -\frac{e^{-j\frac{\pi}{4}}}{2n\sqrt{2\pi\beta} \sin\beta'_0} \left\{ \begin{array}{l} \cot \left[\frac{\pi + (\phi + \phi')}{2n} \right] F \left[\beta L g^+(\phi + \phi') \right] \\ + \cot \left[\frac{\pi - (\phi + \phi')}{2n} \right] F \left[\beta L g^-(\phi + \phi') \right] \end{array} \right\} \quad (2.45)$$

The $F[X]$ in the above relations is the *Fresnel transition function* introduced in the solution to enforce the continuity of the total fields across the shadow boundaries. The transition function is given by,

$$F(X) = 2j\sqrt{X}e^{jX} \int_{\sqrt{X}}^{\infty} e^{-ju^2} du \quad (2.46)$$

The value of the Fresnel transition function is calculated by using the following approximations,

$$F(X) \approx \left[\sqrt{\pi X} - 2Xe^{j\frac{\pi}{4}} - \frac{2}{3}X^2e^{-j\frac{\pi}{4}} \right] e^{j(\frac{\pi}{4}+X)} \quad (X < 0.3)$$

$$F(X) \approx \left[1 + j\frac{1}{2X} - \frac{3}{4}\frac{1}{X^2} - j\frac{15}{8}\frac{1}{X^3} + \frac{75}{16}\frac{1}{X^4} \right] \quad (X > 5.5)$$

For values of $0.3 \leq X \leq 5.5$, the transition function is approximated using an interpolation scheme.

For $X < 0$, the value is the complex conjugate of the transition function for the corresponding positive value of X . i.e.,

$$F(X) = F^*(|X|)$$

The distance parameter L for different wave incidence is given by,

$$L = \begin{cases} s \sin^2 \beta'_0 & \text{plane wave incidence} \\ \frac{ss' \sin \beta_0 \sin \beta'_0}{s \sin \beta_0 + s' \sin \beta'_0} & \text{cylindrical wave incidence} \\ \frac{ss' \sin^2 \beta'_0}{s + s'} & \text{spherical wave incidence} \end{cases} \quad (2.47)$$

The spatial attenuation factor $A(s', s)$ is given as,

$$A(s', s) = \begin{cases} \frac{1}{\sqrt{s}} & \text{plane wave incidence} \\ \frac{1}{\sqrt{s \sin \beta_0}} & \text{cylindrical wave incidence} \\ \sqrt{\frac{s'}{s(s + s')}} & \text{spherical wave incidence} \end{cases} \quad (2.48)$$

The equations 2.41 - 2.48 are used to compute the total diffracted field from the vertical edges of buildings in the ray tracing model developed in this work in chapters 5 and 6.

2.7 Scattering

The propagation mechanisms discussed earlier describe the interaction of radio wave with smooth planar surface (specular reflection) and perfectly or imperfectly conducting wedges (diffraction). If the dimensions of a surface are comparable to the wavelength of the radio wave, it can no longer be considered to be smooth. The interaction of a radio wave with a non smooth surface does not give a specular reflection. In fact the irregularities in the surface structure cause the radio signal to scatter in random directions.

At higher frequencies (>1 GHz), diffuse or rough surface scattering due to the irregularities in reflecting structures can produce a significant contribution to the received power. Therefore the rough surface scattering is modeled in radio channel prediction tools at higher frequencies. Several models [14–17] have been reported in literature that include the diffuse scattering component into radio propagation tools for accurate prediction. These models are discussed later in section 4.4.6.

The scattering from urban furniture including trees, lamp-posts and traffic signals, road signs etc. is also very significant in urban propagation. The objects situated in a 100m radius of the transmitter contributes a significant scattering [18]. The scattering from these objects can account for the received signal in NLOS conditions and areas with low buildings density. It was shown by Rizk *et. al* [19] that scattering from

lamp-posts can be as significant as the specular reflection and diffraction in NLOS scenarios in urban mobile radio.

Guan *et. al* [20] proposed an analytical approach to model the radar cross section (RCS) of traffic signs. The model can easily be implemented in a ray tracing tool for radio channel prediction in vehicle-to-X (V2X) communications. The model uses geometrical theory of diffraction (GTD) approach with simple analytical formulas that gives the monostatic radar cross section for different shapes of traffic signs. The model has been verified with full wave simulations and measurements. It was shown that inclusion of the proposed model improves the accuracy of ray traing tools for V2X channel simulation.

2.8 Application of UTD to Predict Fields in Electrically Small Problems

In the following, UTD has been applied to compute the total fields from a 2-D wedge and a 3-D cube illuminated by a line source and an electric dipole respectively. The results are compared with full-wave methods to verify the implementation of UTD to accurately compute total fields before it can be applied for path loss predictions in large urban environments in the following chapters.

2.8.1 2-D Fields from a Wedge Illuminated by a Line Source

Consider a line source illuminating a square with $\epsilon_r = 5$ and $\sigma = 0.5$ as shown in Figure 2.7. This square is a special case of wedge with internal angle equal to $\pi/2$. In other words,

$$(2 - n)\pi = \frac{\pi}{2}$$

or,

$$n = 1.5$$

The fields are calculated on a line of receivers. Three areas can be distinguished in Figure 2.7.

The lower region on the receiver line consists of points where only a diffracted field (emanating from the north east corner of the scatterer) exists. Above that is a region where there are LOS incident rays as well as the diffracted region, while at the top of the line is a region where there are direct, reflected and diffracted fields. The fields are calculated using the UTD formulations as discussed above assuming a line source. The UTD ray trace fields are compared against the fields calculated using a 2D full-wave solver based on Volumetric Electric Field Integral Equation (VEFIE) formulation [21]. There is an excellent agreement between the two methods as shown in Figure 2.8.

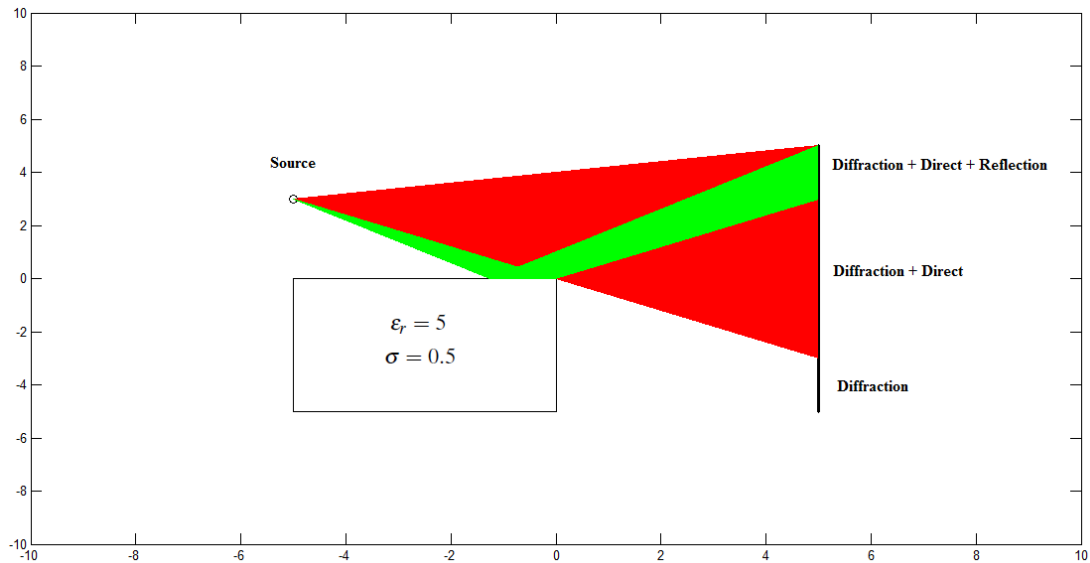


Figure 2.7 Geometry of a wedge illuminated by a line source [21].

2.8.2 3-D Fields from a Cube Illuminated by a Dipole

Consider a finite Perfect Electrical Conductor (PEC) cube illuminated by a dipole as shown in Figure 2.9.

The fields are calculated for a line of receiver points. The points on the receiver line can also be divided into three different regions that have only the diffracted fields, the diffracted and direct fields, and the diffracted, direct and reflected fields. The UTD formulation as discussed in previous sections is used to calculate only the most dominant diffracted fields contributed by the vertical edge at the origin. The divergence at $y = -5$ is contributed by diffraction from the corner at $(-3, -3)$. The UTD fields are compared against the fields calculated using the Method of Moment (MoM) solution of the surface Electric Field Integral Equation (EFIE). Figure 2.10 shows a very good agreement between the plots.

2.9 Conclusion

A background of electromagnetic theory associated with the use of rays is presented. The constitutive parameters that characterise the propagation medium, material types and the medium classification is described. The asymptotic methods for approximate solution of high frequency problem are presented to characterise the high frequency fields associated with rays. The laws of reflection, transmission, geometrical and uniform theory of diffraction are described. The expressions for specular reflection from a smooth surface and the Fresnel reflection coefficient are listed. The projection of incident and reflected fields in the respective planes is also described. These formulae are used to compute the specular reflection from building walls in our ray tracing

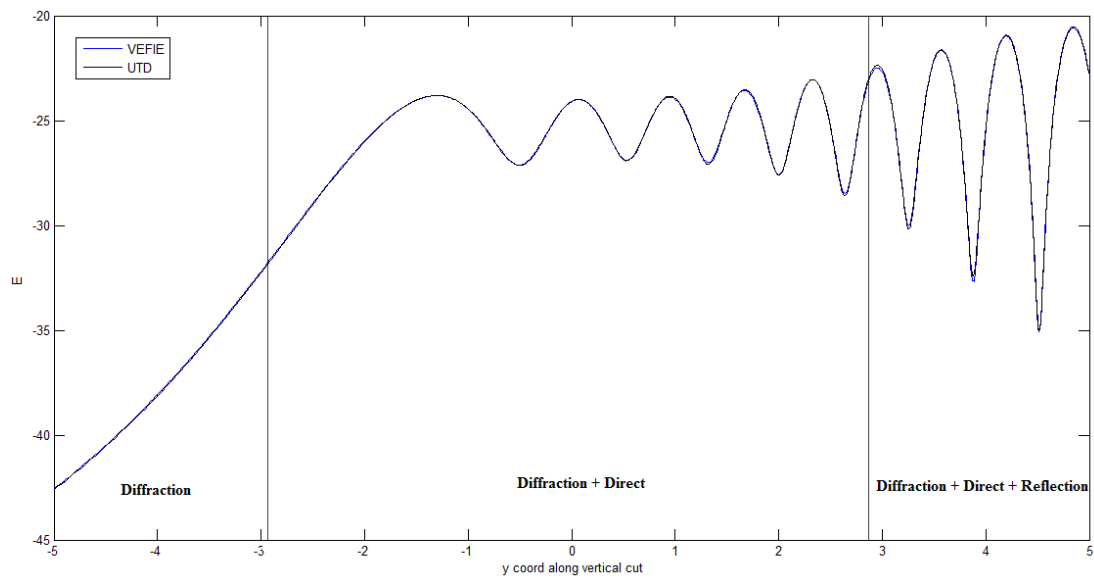


Figure 2.8 Comparison of electric field (dB) along a line of receivers using UTD and VEFIE [21].

computations in chapter 5 and 6. Similarly the expressions for wedge diffraction and diffraction coefficient are listed. The edge based coordinate system to decompose the incident and diffracted fields for oblique incident is introduced. This approach is used to compute the diffracted field from vertical edges of buildings in our ray tracing computations in chapter 5 and 6.

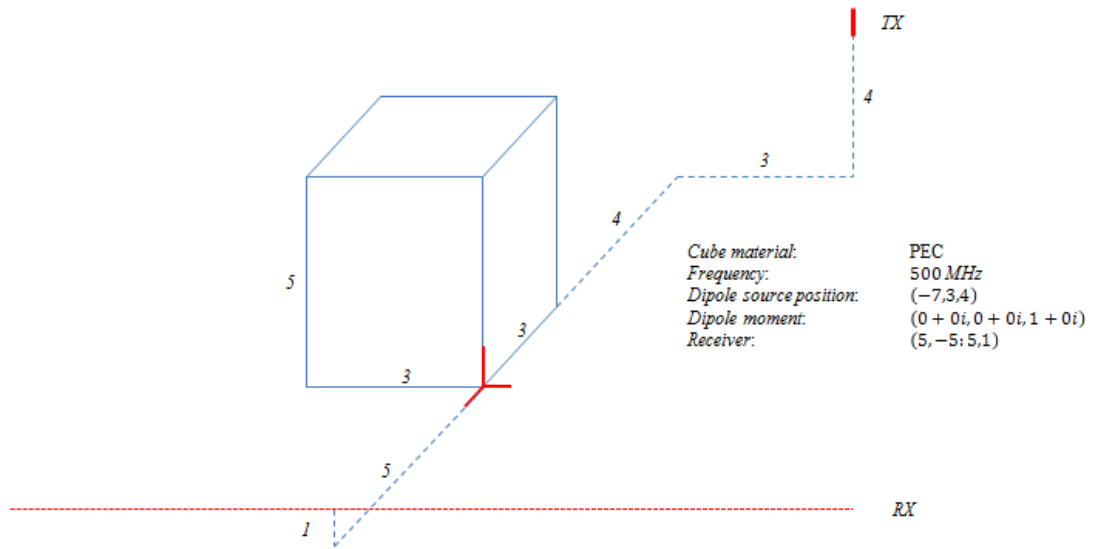


Figure 2.9 Geometry of a PEC cube illuminated by a dipole source.

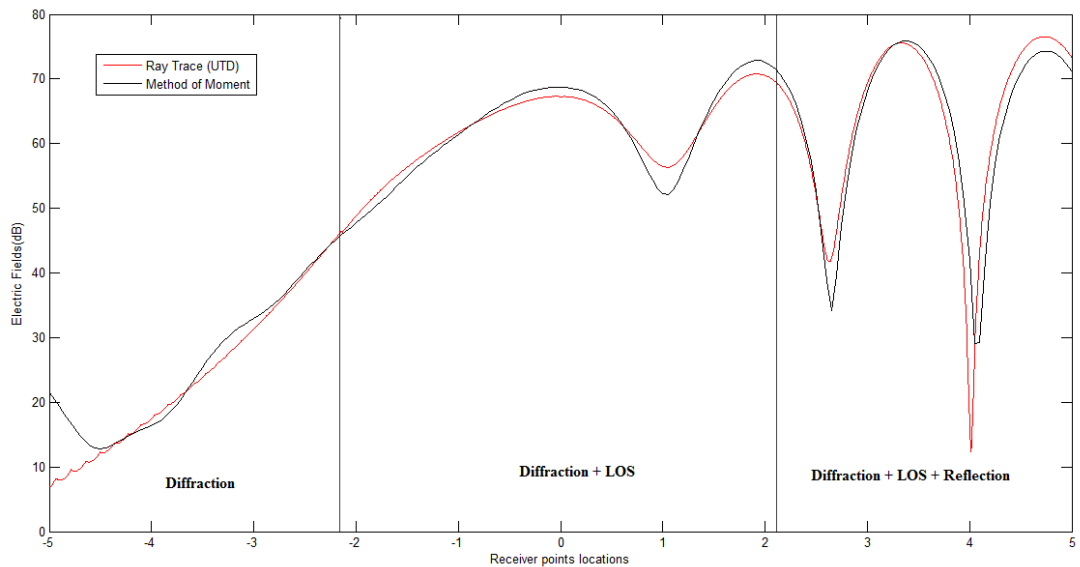


Figure 2.10 Comparison of electric field along a line of receivers using UTD and Method of Moment.

Chapter 3

General Methods in Ray Tracing

Ray tracing models are high-frequency methods that approximate a radio wave propagating in a homogeneous medium as a ray. A ray interacts with objects in the propagation environment and undergoes reflection, transmission and diffraction depending on the scatterer size and point of interaction. Once the valid rays are found at a receiver location, the associated fields can be calculated using Geometrical Optics (GO) and the Uniform Theory of Diffraction (UTD) as discussed in the previous chapter. The validity of ray tracing models depends largely on the modeling of electrical properties of the objects in the propagation environment, inclusion of all the relevant scatterers and the application of correct GO and UTD techniques to evaluate the fields. The speed of these models is limited by the numbers of objects in the environment, coverage area and the order of ray interaction considered.

This chapter describes the implementation of ray tracing. The effect of objects in the propagation environment including buildings, vegetation and pedestrians and vehicular traffic on radio wave propagation is explained. Visibility algorithms that are commonly used to identify the visible surfaces in ray tracing models are described. The creation of image tree and ray-object intersection test to validate rays is explained. Finally the parameters that characterise a radio channel are briefly described.

3.1 Ray Tracing Techniques

There are three techniques to find the ray trajectories in ray tracing models, namely shooting and bouncing ray, image method and hybrid method.

3.1.1 Shooting and Bouncing Ray (SBR)

Shooting and bouncing ray is commonly known as *ray launching* method and consists of the following steps.

- Rays of a fixed width separated by certain fixed angles in azimuth and inclination plane are launched from the transmitter in all directions. These solid angle rays are also known as ray tubes.
- Each ray is checked until it arrives within a tolerance of the receiver location or goes out of the environment. If a ray interacts with an object, it undergoes reflection or diffraction.
- A sphere is placed at the receiver and all the valid rays arriving at the sphere are used to compute the total field at the receiver location.

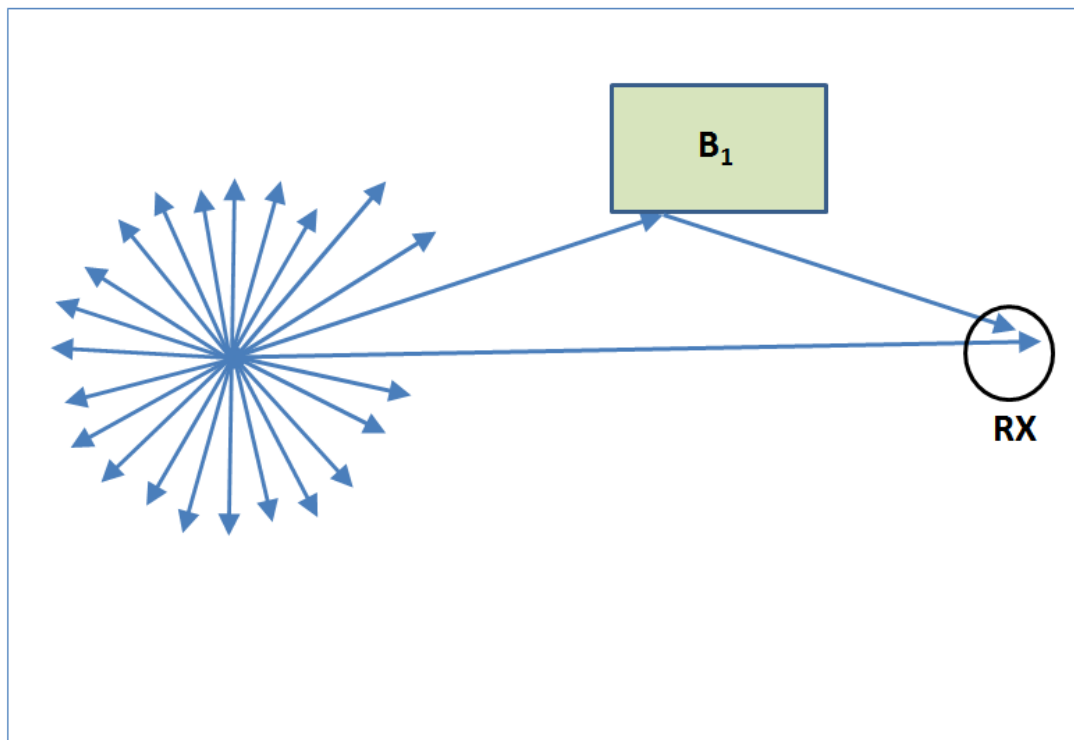


Figure 3.1 Shooting and bouncing ray (SBR) technique.

Figure 3.1 shows an example of SBR technique for 2-D ray tracing. Rays are launched from transmitter in the horizontal plane in all directions. A ray hits a wall of

building B_1 and undergoes reflection as shown. The reflected ray intersects the circle at receiver location RX . A valid reflection as well as a direct ray is received at the receiver. The associated fields can be computed using the geometrical optics techniques discussed in the previous chapter.

The following practical aspects must be addressed before using a SBR method. The angular width between two rays launched from the transmitter must be carefully selected. Another important issue is the ray-object intersection test to validate ray segments between reflection or diffraction point and the transmitter or receiver. A naive SBR algorithm checks all the buildings in the environment to validate a ray segment that can take up to 90% of total CPU time [22]. The radius of the reception sphere determines the rays arriving at a receiver point and should be selected equal to $\frac{\alpha d}{\sqrt{3}}$, where α represents the angle between two adjacent rays and d is the ray length.

3.1.2 Image Method

The image method computes the accurate ray trajectory using image theory. Images of transmitter with respect to visible faces are calculated that are used to determine the reflection points for valid ray paths. An image point is computed so that the distance from the source to relevant face is always equal to the distance between that face and image point. An example of image method for a second order reflected ray is shown in Figure 3.2. The second reflection point R_2 is found by drawing a line from the second order image TX'' to the receiver RX as shown. The first order reflection point R_1 is obtained by drawing the line from first order image TX' to R_2 . The ray is then constructed by piecewise segments from TX to R_1 to R_2 .

The image method suffers from inefficiency with large numbers of building walls and higher order of ray interaction.

3.1.3 Hybrid Method

This method combines the efficiency of SBR and the accuracy of the images method. The visible surfaces that can produce valid rays are found using the SBR approach, while the image method is used to determine the interaction points and finds the actual ray paths. This hybrid approach is more frequently used and is commonly known as *ray tracing*. The process consists of the following steps.

- Rays separated by certain angles in azimuth and inclination plane are launched from the transmitter in all directions.
- If a ray intersects a wall, a reflection point is found using image theory. If a ray intersects an edge, a diffraction point is found using Fermat's principle of least time.

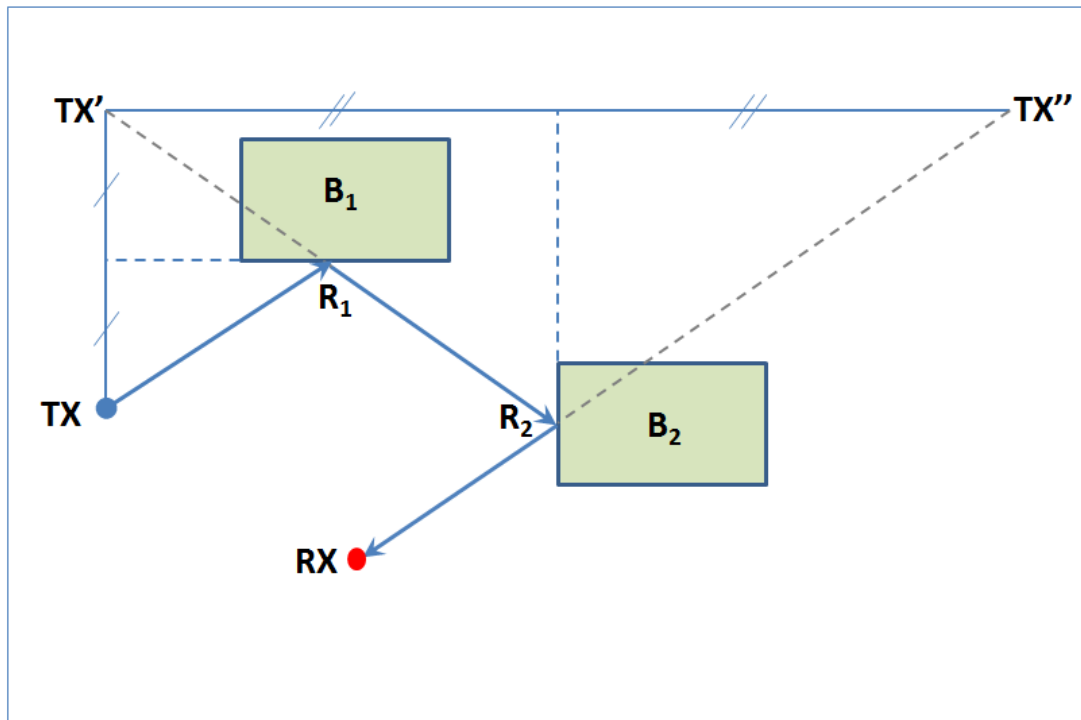


Figure 3.2 Use of image method to compute accurate ray trajectories.

- The sum of all rays arriving at the receiver location are used to compute the total field.

3.2 Modeling of Objects in the Propagation Environment

There are buildings, trees, vehicles and pedestrians in a typical urban propagation environment. The interaction of radio energy with these objects determine the received signal at a given receiver location. Therefore a ray tracing model must include these objects in the propagation environment to compute all the reflected, diffracted and transmitted rays. Please note that the effect of urban furniture as discussed in sections 3.2.2 and 3.2.3 are not included in the ray tracing model developed in this work in chapters 5 and 6.

The modeling of different objects in the environment in a typical ray tracing model for urban propagation is discussed in the following.

3.2.1 Buildings

Buildings are modelled as 3-D cylinders in the environment with given permittivity ϵ , permeability μ_0 and conductivity σ values. Each building is made up of flat vertical and horizontal faces that are represented by convex polygons. A building has only two

horizontal faces to represent the floor and roof of the building. The outer walls of the buildings are represented by vertical faces. All the vertical faces have associated surface normals that are used to find the reflected fields. Buildings are represented in a three dimensional coordinate system with x and y representing the location on horizontal plane while the z coordinate represents the height h of the building.

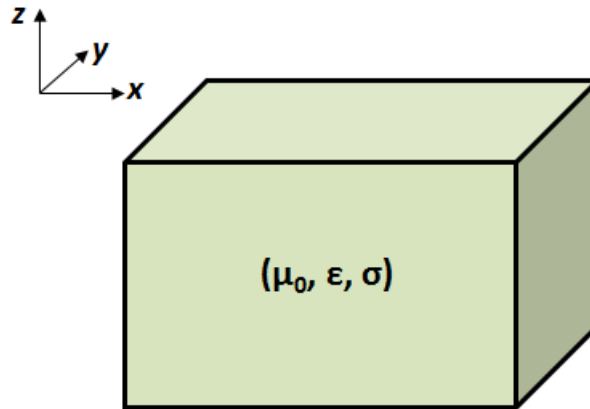


Figure 3.3 Representation of a building in Cartesian coordinate system in 3-D space.

The reflection coefficient depends on the constitutive parameters of the building walls. Many studies have been carried out to investigate the effects of material characteristics on reflected and diffracted fields from the buildings in urban environments. Rizk *et al.* [23] suggested a few preliminary comparisons be performed between the simulated and measured results for different values of wall parameters and then to select the values that give closest match between the measured and simulated fields. Athanasiadou *et al.* [24, 25] showed that wall conductivity in the order of $10^{-3} S/m$ and relative permittivity value around 5 gives good agreement with measured results at UHF frequencies in a typical urban environment.

A typical urban ray tracing model considers the buildings as blocks of concrete for simplification. The transmitted fields inside the buildings are not usually computed. De Jong *et al.* [26] proposed a model that gives the attenuation through the buildings using an attenuation factor (α_b) that depends on the internal building structure. The average value of attenuation factor was found to be approximately 2.1 dB/m.

There has been a great deal of interest in outdoor-to-indoor propagation for better coverage prediction inside the buildings. With the increase in the use of energy efficient materials in modern buildings, the propagation loss inside buildings has increased. Rodriguez *et al.* [27] investigated that propagation loss in modern energy efficient buildings range between 24.86 dB to 31.98 dB as compared to only 5.16 dB in old buildings over the frequency range 0.18-18 GHz. Similar results have been reported in [28–30]. Future millimeter-wave systems must consider the attenuation loss in building walls that increases linearly with frequency for accurate outdoor-to-indoor channel modeling [31].

3.2.2 Vegetation

The vegetation present in a typical urban environment causes the radio waves to be absorbed, scatter and depolarise [32]. The absorption of radio waves in leaf structure transforms the radio energy into heat energy. The scattering effect accounts for the spread of radio energy in random directions. The depolarisation effect refers to the change in polarisation of the radio wave as it travels within a foliage structure.

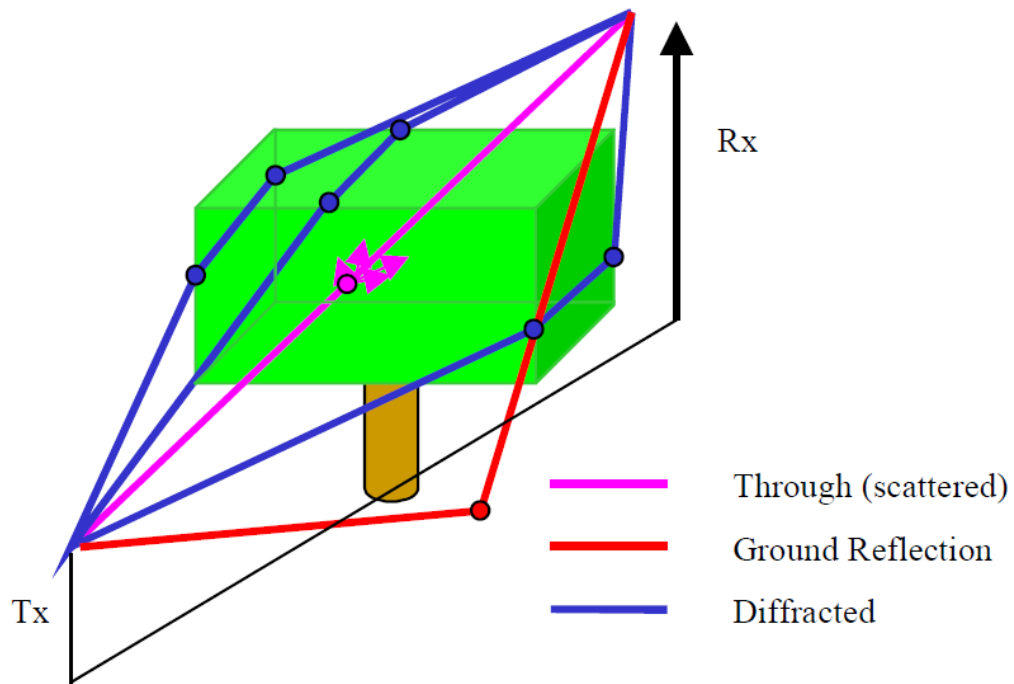


Figure 3.4 3-D model of a tree used in ray-tracing to account for the vegetation loss[32]

Caldeirinha *et al.* [33] used an FDTD model to study the absorption inside a leaf due to moisture and the scattering energy. He also proposed that a full tree model can be developed using the proposed leaf structure to investigate the absorption and scattering from the vegetation in a given environment. Weisberger [34] presented an empirical formula for attenuation loss L dB/m through a series of trees over the frequency 0.23 – 95 GHz as follows,

$$L = 0.45 f^{0.284} \quad (3.1)$$

Several ray tracing models [35–40] that incorporates radio wave propagation through vegetation have been reported in literature. The field scattered from the trees must also be accounted along with attenuation to accurately predict the received power in urban micro-cellular environments [37]. Trees can be modelled as point scatterers and the expressions for scattered field are proposed in [36, 39, 40]. The parameters that define the scattered field are extracted using measurements. An efficient ray based model to predict radio coverage in vegetated residential environments for Non Line of

Sight (NLOS) receiver in street level is proposed in [38]. The buildings are modelled as absorbing screens. The total field is accurately predicted as the model includes multi-screens diffraction, rooftop-to-street diffraction and additional attenuation loss through vegetation. The cylindrical geometry of trees can scatter the radio waves over a large area to provide multipath propagation in future millimeter wave systems [41].

3.2.3 Pedestrians and Vehicular Traffic

The effect of pedestrians and vehicular traffic is not considered for radio coverage prediction in a typical urban environment. However the presence of pedestrians and vehicular traffic may affect the direct line of sight (LOS) channels in urban street canyons. An urban street canyon is characterised by high-rise buildings on both sides of the street so that radio waves propagate in horizontal plane containing the transmitter and receiver.

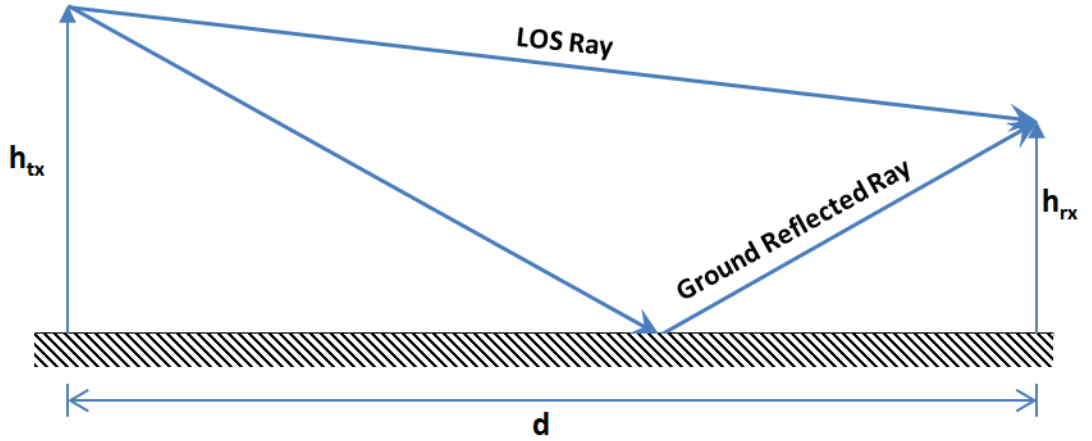


Figure 3.5 Two ray ground reflection model.

A two ray model that takes the direct LOS and ground reflected ray can be used for path loss prediction as shown in Figure 3.5.

The received power at a distance d from the transmitter can be given as follows [42],

$$P_r = P_t G_t G_r \frac{h_t^2 h_r^2}{d^4} \quad (3.2)$$

where G_t and G_r is transmitter and receiver antenna gains and h_t and h_r are transmitter and receiver antenna heights respectively.

so that path loss for two-ray model including the antenna gains can be expressed as,

$$PL(dB) = 40 \log d - (10 \log G_t + 10 \log G_r + 20 \log h_t + 20 \log h_r) \quad (3.3)$$

It can be seen that the received power falls off with distance raised to the fourth power or 40 dB/decade at large distances ($d \gg \sqrt{h_t h_r}$) as compared to 20 dB/decade

in free-space. A *breakpoint distance* (d_{bp}) is defined as the horizontal distance between transmitter and receiver after which the path loss characteristics of two-ray model deviates from the traditional free-space path loss as shown in Figure 3.6. The breakpoint distance is also known as the *first Fresnel zone distance*.

$$d_{bp} = \frac{4h_t h_r}{\lambda} \quad (3.4)$$

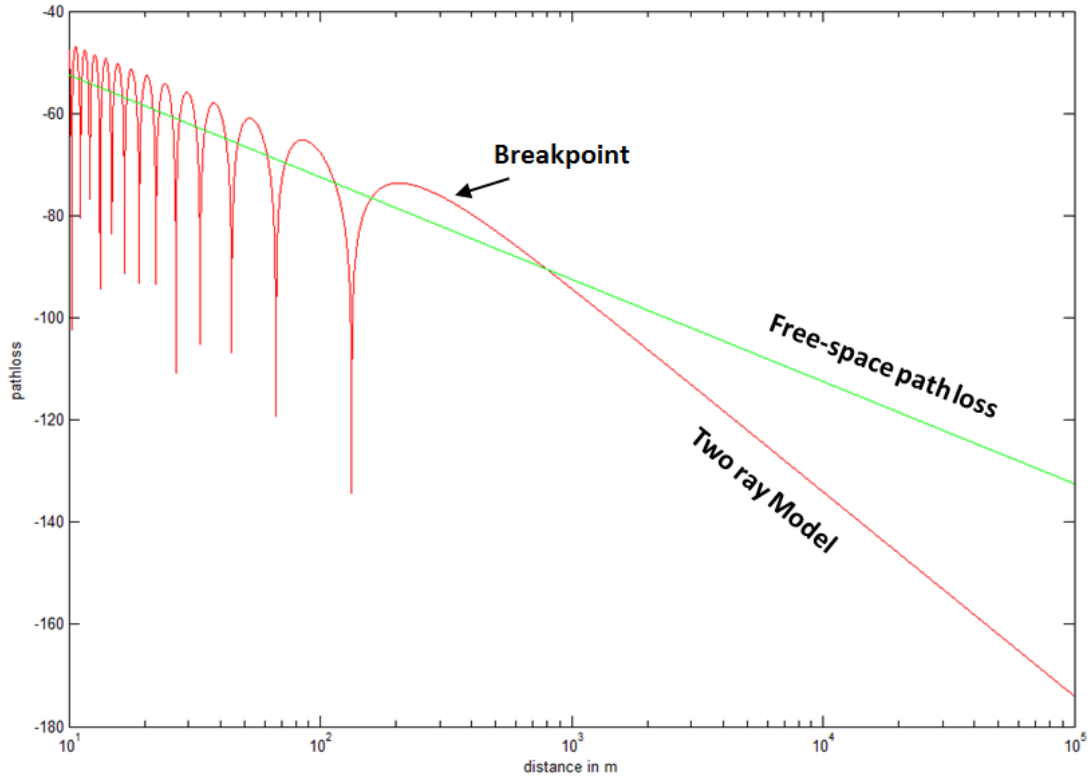


Figure 3.6 Comparison of two ray path loss with free space path loss.

The effective breakpoint distance is shorter than the theoretical value due to a change in the effective heights of the transmitter and receiver if a blockage is present in front of the reflection point as shown in Figure 3.7. The effective breakpoint distance in this case is given as [43],

$$d'_{bp} = \frac{4(h_t - h_0)(h_r - h_0)}{\lambda} \quad (3.5)$$

Measurements were performed on an urban street in Tokyo, Japan by Masui *et al.* [44, 45] at different times of the day. The average day time traffic on the street was up to 290 vehicles and 500 pedestrians passing per 30 minutes. The average traffic reduced down to 80 vehicles and 3 pedestrians passing per 30 minutes at midnight. The effective ground height at day time was found to be 0.6 m and that reduced at midnight. Further work by Masui *et al.* [46] and Hernandez-valdez *et al.* [47] investigated the lower and upper bound on LOS path loss due to different traffic conditions in urban micro-cellular environments.

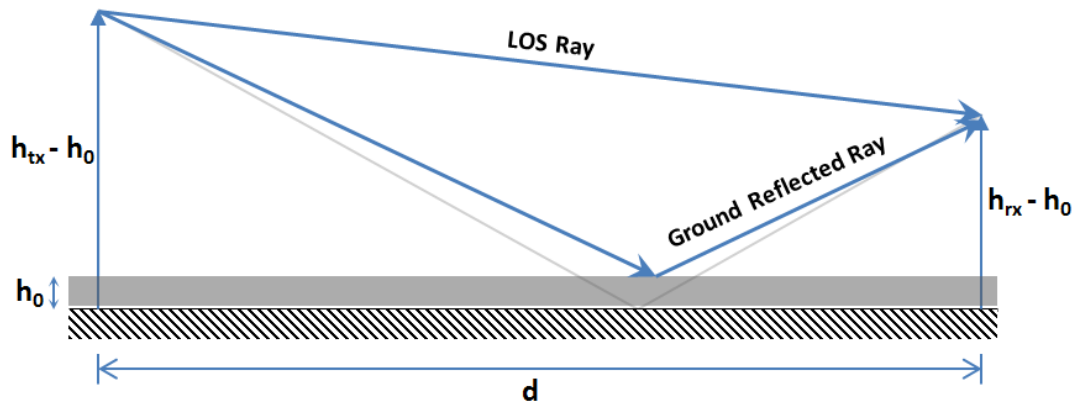


Figure 3.7 Change in effective ground height due to pedestrian and vehicular traffic.

3.3 Visibility Algorithms

The walls and edges that can be seen by the transmitter produce the first order reflection and diffraction rays respectively. A wall visible to a transmitter can produce reflected rays in a restricted region termed as the *lit region* that can be found using image theory as shown in Figure 3.8. The walls and edges that are visible within the lit region of a first order wall reflection may produce second order rays. The region exterior to the walls that make up an edge defines the lit region for a vertical edge as shown in Figure 3.9. A transmitter can see a number of walls and edges in a given environment that in turn can see further walls and edges. A visibility algorithm determines the walls and edges that are visible to a given transmitter location for given order of ray interaction to create a *visibility list*. It is during the ray tracing stage that each possible ray path between the transmitter and receiver is subjected to a *ray-object intersection test* to validate each ray. The visibility algorithm is a pre-processing step and is the most CPU intensive part of the ray tracing model before the valid rays between the transmitter and receiver can be identified.

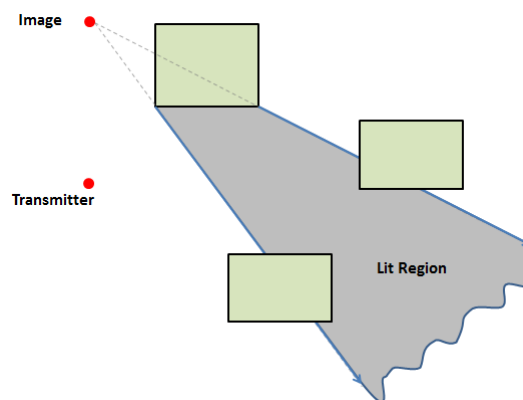


Figure 3.8 Lit region of a wall reflection can be found using image theory.

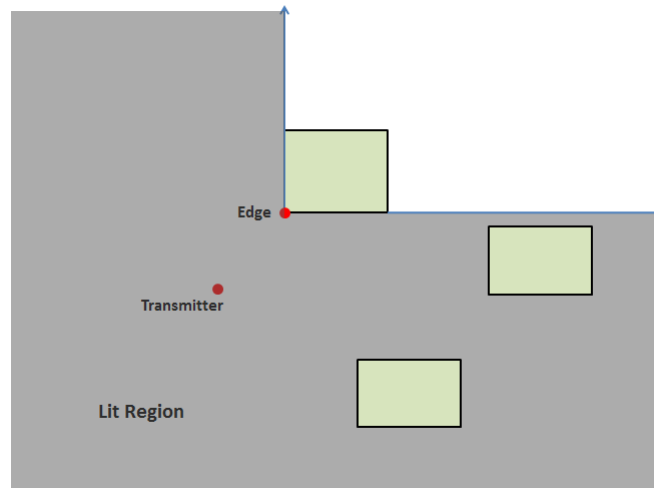


Figure 3.9 The region exterior to the walls that make up the edge forms the lit region of a diffracting edge.

There are many efficient visibility algorithms proposed in the literature [48–54]. Some of the most common visibility algorithms including dimensional reduction technique, binary space partitioning and polar sweep algorithm for ray tracing will be discussed in the following.

3.3.1 Dimensional Reduction Technique

This technique proposed by Maurer *et al.* [48] has been applied to identify visible surfaces for ray tracing. The algorithm is based on successive dimensional reduction of 3-D vector data of buildings in the given environment. This algorithm identifies the visible surfaces for the required order of ray interaction.

The algorithm consists of the following steps. Refer to Figures 3.10 and 3.11 for the discussion that follows.

1. The surfaces that are visible to the transmitter or the receivers are the only ones that make valid rays. The first step excludes all the faces of each building that do not face the transmitter or the receivers. This is called *back face culling*.
2. In the next step, 3-D vector data of the remaining faces is projected onto a 2-D plane with an omni-directional transmitter perspective. The faces that are close to the transmitter produce larger projected shadows on the projection plane as shown in Figure 3.10.
3. The next step involves the identification of visible surfaces in 2-D. A polygon subtraction with sweep-line algorithm is applied on all the projected faces to identify the visible surfaces as shown in Figure 3.11.
4. Since 3-D vector data of each face is available, inverse projection is applied to get the visible surfaces in 3-D space.

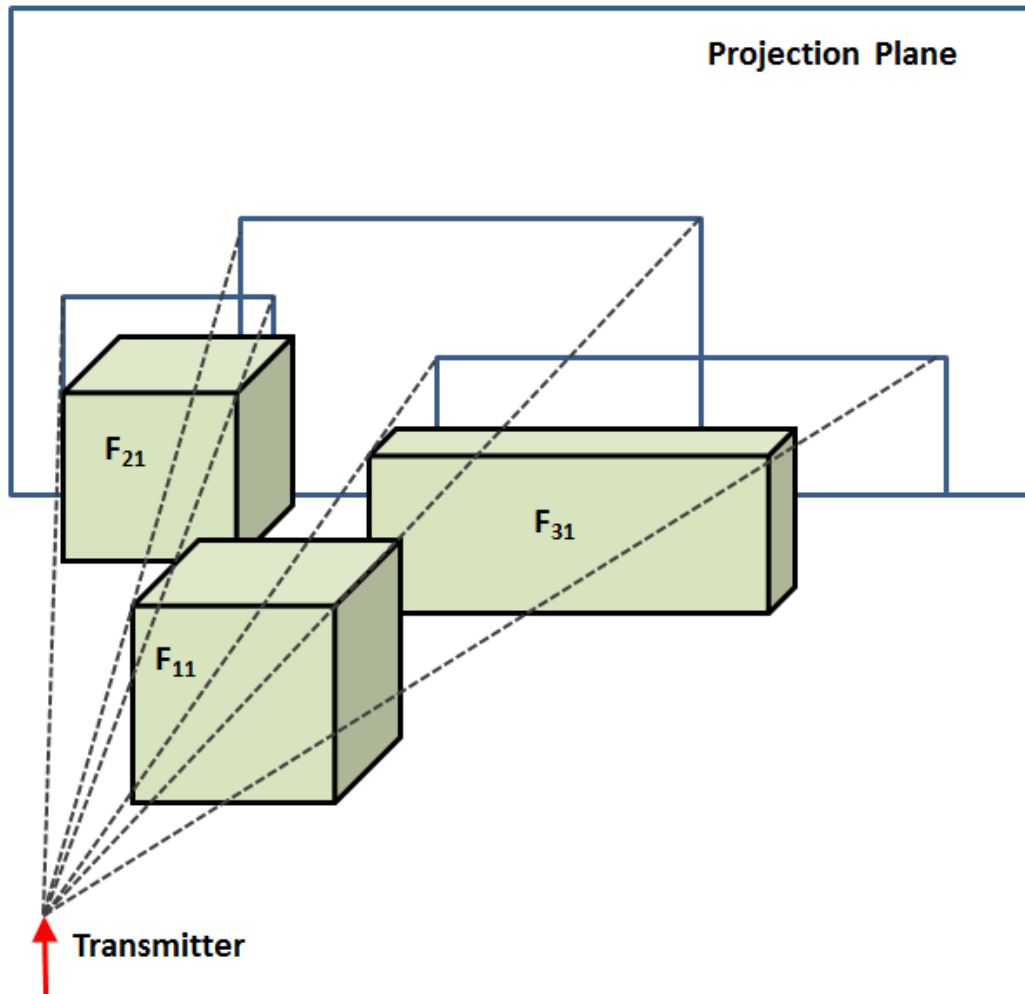


Figure 3.10 Faces are projected onto a projection plane from transmitter perspective after back face culling [48].

5. For higher order reflection images, the algorithm is modified to only project the buildings that lie in the parent image's lit region in front of the wall. Buildings that lie outside the lit region are not included for visibility analysis.

3.3.2 Binary Space Partitioning (BSP) Algorithm

The binary space partitioning (BSP) algorithm proposed by Torres *et al.* [49, 50] has been successfully applied for both outdoor and indoor radio channel prediction. The BSP algorithm is adopted from 3-D computer graphics in which a scene is subdivided into a front and rear view from an observer perspective. A binary structure called a *BSP tree* is created that divides the environment into two spaces. One side of the tree structure contains all the faces that are visible to both transmitter and receiver. The other side contains all the remaining faces that will not make valid rays and should not be tested for visibility.

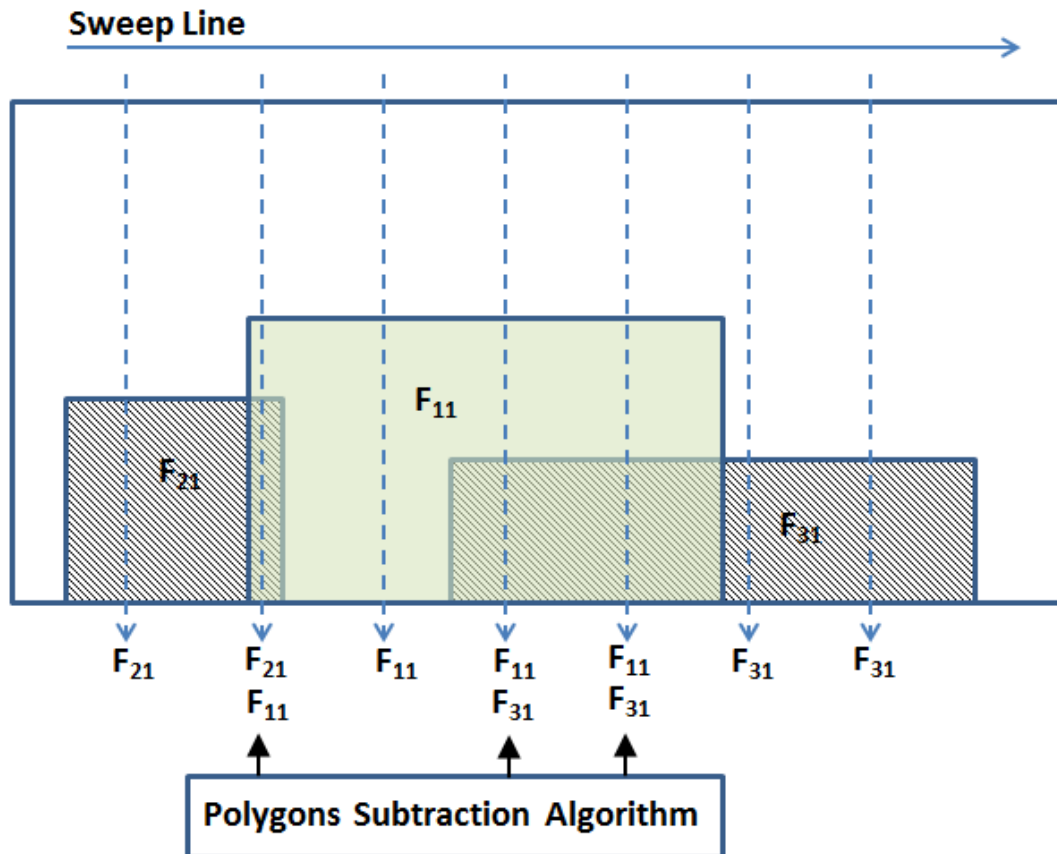


Figure 3.11 A sweep line with polygon subtraction algorithm is applied to obtain the visible surfaces in 2-D [48].

Consider an outdoor scenario as shown in Figure 3.12. The creation of a BSP tree for this example is shown step by step in Figure 3.13. Face 9 is chosen as the root node and all the visible and invisible nodes are arranged on the left and right side of the root node respectively as shown in Figure 3.13a.

The following algorithm is applied to complete the BSP tree.

1. A suitable face depending on the location of transmitter and receiver is chosen as the root node of the BSP tree. A line is drawn to divide the environment in two spaces and a direction vector is identified in front of the face.
2. All the faces that are in front of the direction vector are listed on the left side of the root. The faces that lie entirely behind the direction vector are listed on right side of the root.
3. The following procedure is recursively applied for each face on both sides of the root node until BSP tree is completed. Figure 3.13b shows each step.
 - (a) Select a face from a list and make it a node.
 - (b) Identify all the remaining faces from the list which lie in front of the face. They make a list on left side of the node.

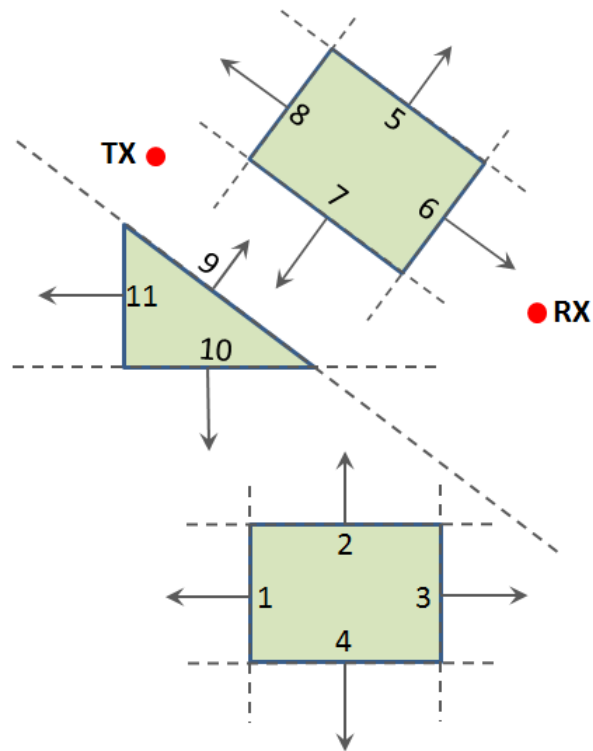


Figure 3.12 An outdoor scenario for which BSP tree is computed [50].

- (c) The faces that lie behind the face will make a list on right side of the node.
- (d) Repeat for next face.

Another similar technique proposed by Bittner *et al.* [51, 52] uses line space partitioning (LSP) to compute visibility for point to area in large urban environments. Ng *et al.* [53, 54] proposed a hybrid BSP tree structure within a quad-tree to eliminate floating point errors in implementing face-to-face visibility in large urban areas. The algorithm also uses *occlusion-culling* that eliminates the back-facing surfaces as in back face culling as well as the blocked faces in shadow regions.

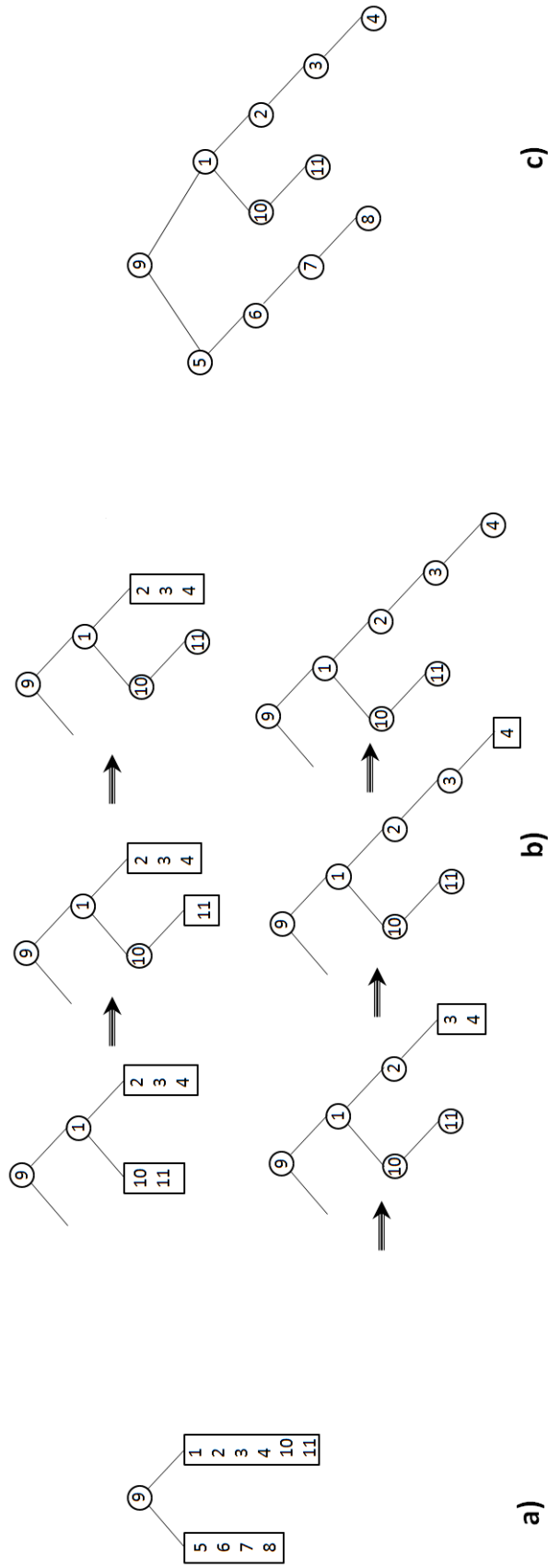


Figure 3.13 Step by step BSP tree computation for example in Figure 3.12. a) Division of scene in two planes with respect to root node 9. b) BSP tree computation for all nodes on right side of root node 9. c) Complete BSP tree [50].

3.3.3 Polar Sweep Algorithm

The polar sweep algorithm was proposed by Agelet *et al.* [55, 56] for visibility determination in both indoor and outdoor environments. The given environment is recursively divided into quadrant of decreasing size until the number of buildings or faces in a quadrant is less than a minimum number. This technique is called a *quad-tree* approach and is adopted from image processing.

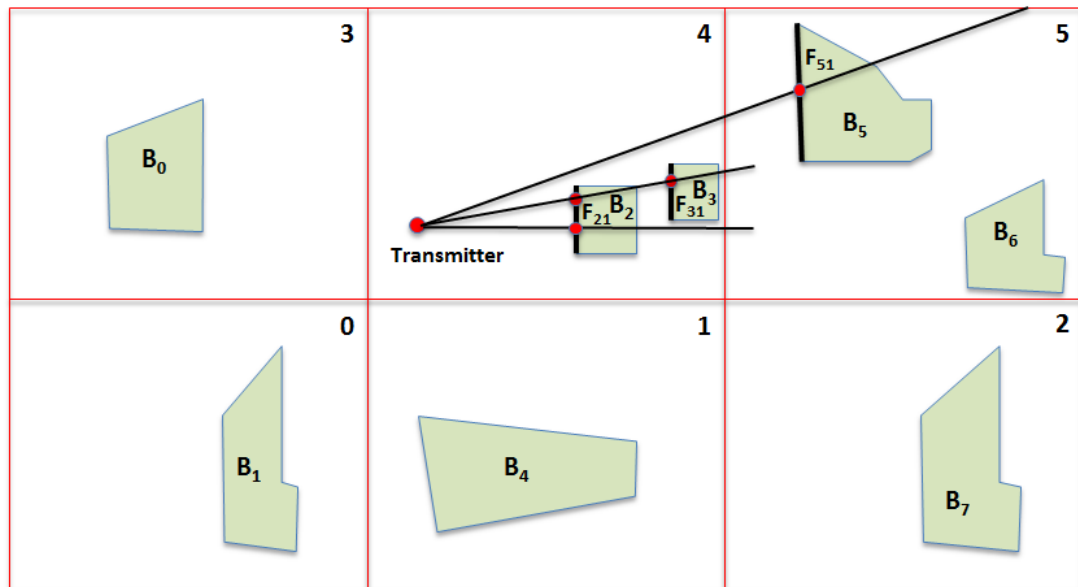


Figure 3.14 Computation of visible faces in horizontal plane using polar sweep algorithm [56].

The algorithm consists of the following steps. Refer to Figure 3.14 for the discussion that follows.

1. Rays are launched from the transmitter TX in a clockwise direction at a fixed interval in the 2-D plane for horizontal visibility or combined with azimuth elevation scan for 3-D case.
2. Since the visible faces are more likely to be located near transmitter TX , the faces in the quadrant where TX is located are first tested for intersection with the launched ray.
3. A valid intersection is found only if
 - (a) The point of intersection lies on the vertical face.
 - (b) The vertical face is facing towards the transmitter.
4. If a ray intersects more than one face, the distance of each intersection from the TX is calculated. The closest face with least distance is chosen as visible face.

5. If no valid intersection is found in the TX quadrant, buildings in the next quadrant that the ray enters are tested for visibility.
6. To find higher order reflection, a similar approach is used. However, rays are launched from the image point and confined to the lit region as stated earlier. Only the faces which lie in front of the respective wall are tested for visibility.
7. In case of diffraction, rays are launched in all direction just like transmitter except the region formed by two walls that make the edge.

3.4 Image-Tree

Having identified all the faces and edges that may produce the reflection and diffraction rays for the required order of interaction, the visibility information must be efficiently stored for ray tracing. The visibility analysis performed to find all the visible faces and edges for the required order of ray interaction is commonly represented by a tree structure called the *image-tree*. The transmitter is always the root node of an image tree. The walls and edges that are visible to the transmitter may produce first order rays and form the first layer of the image-tree. The walls and edges that are visible to the first order images may produce second order rays and form the second layer of image-tree and so on. A typical image tree is shown in Figure 3.15.

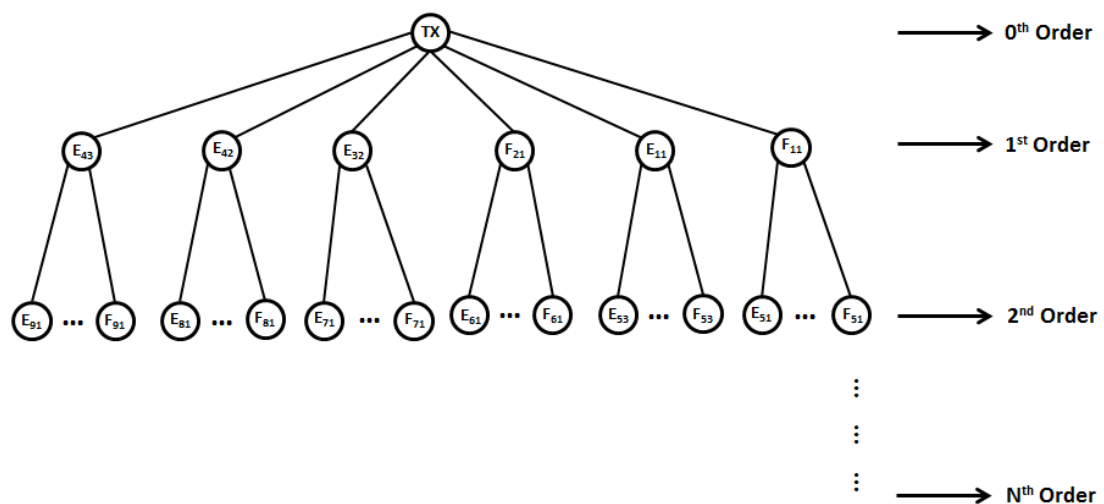


Figure 3.15 An example of a typical image tree.

Each node of an image tree is associated with a certain face or edge of a certain building in the environment. Other attributes associated with an image include order, type (reflection or diffraction) and location in 3-D space. The location for a reflection image is found using image theory while the location of a diffraction image is the diffracting edge itself. Image indexing is also required so that an image can be traced back to its parent image. For a smaller environment with fewer images, a numerical tool

such as *MATLAB*[®] can be used to store images and numerically compute the ray paths. However, object oriented programming languages such as C++ are more frequently used to compute ray tracing algorithms for both outdoor and indoor environments. A C++ *class* is used as a basic data structure to handle all the data associated with an image node in the image tree. The accuracy of computations is good as the C++ program uses 64 bit *double* to store the data associated with buildings vertices, image points and intersection points at the walls etc.

The *image class* for a typical ray tracing algorithm can be given as follows. An *array* of image class can be defined in a C++ program to allocate the memory for a large number of images required in a ray tracing algorithm.

```
class image{
    int building_index;
    int face_index;
    int type;          // Reflection or Diffraction
    int order;
    int index;
    int parent_image_index;
    Point3d location; // image location in 3-D space
}
```

3.5 Ray-Object Intersection Test

Having identified the potential scatterers (faces and edges) that may produce rays for the specified order of interaction, the visibility list is stored as an image tree as discussed. Each node in the image tree may produce a valid ray between transmitter and receiver.

An *Nth* order ray consists of three types of ray segments. The first segment is between the receiver and the *Nth* order image, the second type of segments join the *Nth* order image to the 1st order image and the last segment joins 1st order image to transmitter. A valid ray is formed between a transmitter and receiver only if the individual ray segments do not intersect with any building in the environment.

A *ray-object intersection test* is performed to ensure that all the ray segments do not intersect with any building in the environment. The ray-object intersection test will be explained with an example for a test environment shown in Figure 3.16. Edge E_{11} of building B_1 is visible to the transmitter and makes a first order image. Face F_{21} of building B_2 is visible to this edge to make a second order image. We are interested to find if a valid second order ray $TX - E_{11} - F_{21} - RX$ (diffraction followed by reflection) exists between the transmitter and receiver. Refer to Figure 3.17 for the discussion that follows.

1. A line is drawn from the receiver to the second order reflection image point. The intersection of this line with the face F_{21} gives the reflection point as shown

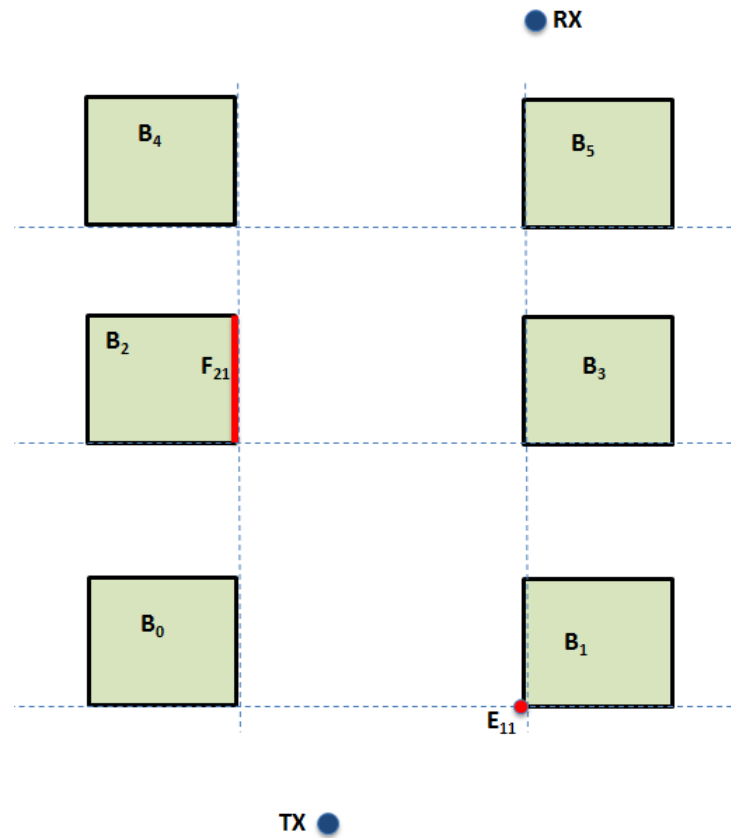


Figure 3.16 Top view of a test environment for ray-object intersection test.

in Figure 3.17a. The line between this reflection point and RX is the first ray segment between the receiver and second order reflection. If the ray is to be valid then this ray segment must not intersect with any building. In a *brute-force* ray tracing approach, a geometrical test is performed to check the intersection of this line with all the buildings in the environment.

2. After establishing a valid ray segment between the receiver and N th order image, each ray segment between the N th order image to 1st order image is validated one by one using a recursive algorithm. In this example, a line is drawn from reflection point to 1st order diffraction image at edge E_{11} as shown in Figure 3.17b. A geometrical test is performed again to validate that the ray segment does not intersect with any building in the environment.
3. Finally, a line is drawn between first order image E_{11} and transmitter TX to form the last ray segment as shown in Figure 3.17c. Again a geometrical test is performed to validate the ray segment.

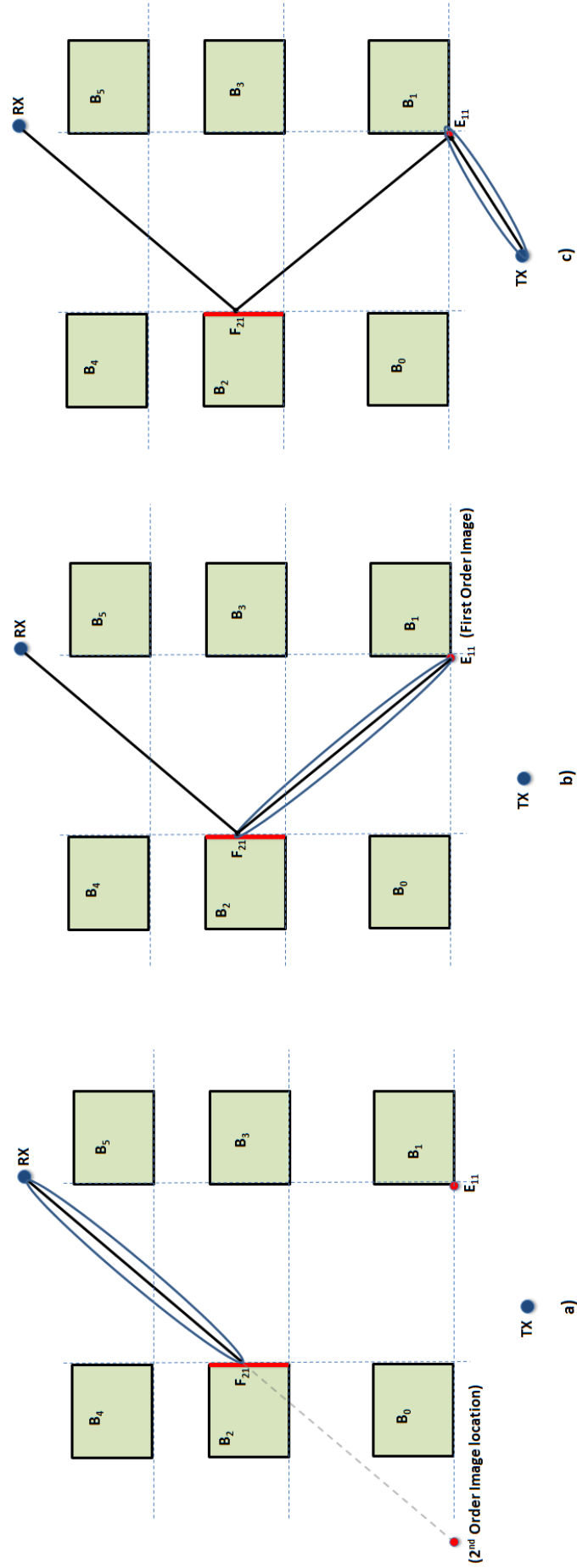


Figure 3.17 Ray-object intersection test to show how a ray is validated for example in Figure 3.16. a) Ray-object intersection test for ray segment between receiver and second order reflection image. b) Ray-object intersection test for ray segment between second order reflection image and first order diffraction image. c) Ray-object intersection test for ray segment between first order diffraction image and transmitter.

The ray-object intersection test is performed to validate the ray in the horizontal plane. However, the transmitter and receiver have different heights in a typical urban propagation environment. According to the Fermat's principle of least time, all the ray segments between transmitter and receiver must lie in a plane. If h_{TX} and h_{RX} represent the heights of transmitter and receiver respectively, and d_1, d_2 and d_3 represent the horizontal distances of the individual ray segments for the example discussed above. Then, the height of intersection points h_1 and h_2 at buildings B_1 and B_2 can be found as follows.

$$h_1 = h_{TX} - \frac{d_1}{d_1 + d_2 + d_3} (h_{TX} - h_{RX})$$

$$h_2 = h_{TX} - \frac{d_1 + d_2}{d_1 + d_2 + d_3} (h_{TX} - h_{RX})$$

The heights h_1 and h_2 must be positive values and less than the actual building heights for a valid 3-D ray. i.e.

$$0 < h_1 < H_1$$

$$0 < h_2 < H_2$$

Figure 3.18 shows the validation of the second order ray in 3-D space. Only the buildings B_1 and B_2 are shown. This procedure is repeated for all the images in the image tree and the valid rays are stored in a database for post-processing.

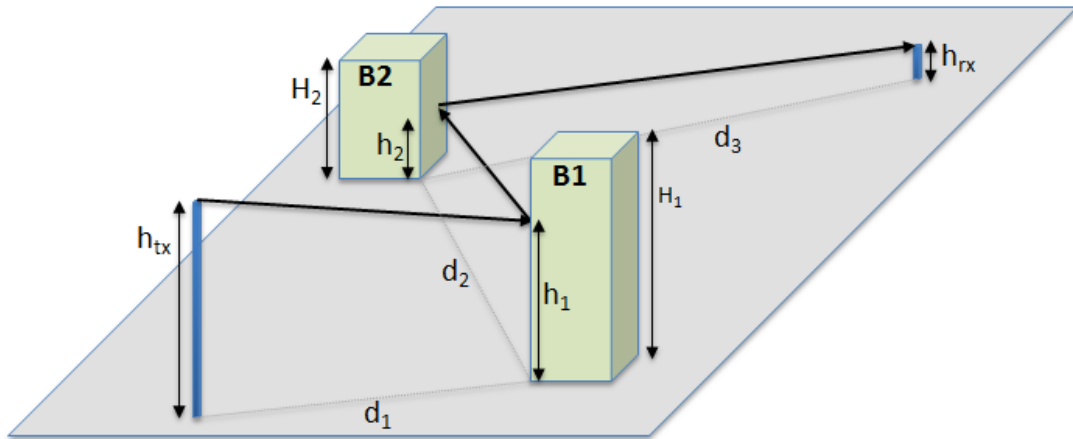


Figure 3.18 Validation of a ray in 3-D space for example in Figure 3.16.

3.6 Characterization of the Radio Channel

A typical outdoor radio propagation environment consists of many scatterers including buildings, vehicles, pedestrians and trees. The radio signals interact with these scatterers and arrive at the receiver. The signal received at the receiver may consist of a direct LOS signal superimposed by the delayed signals after reflection, diffraction or scattering from random directions. This interaction of radio waves with the scatterers in the propagation environment creates a radio channel. The scatterers and the transmitter or receiver can be stationary or mobile. The radio channel will change as the scatterers, transmitter or receiver move in the environment. Different parameters are used in the literature to define the characteristics of a radio channel.

Some of the important channel parameters are discussed as follows.

3.6.1 Path Loss

Path loss is the ratio of the power transmitted by the transmitter to the power received at the receiver. This parameter signifies the power loss that occurs in the channel. Path loss is a fundamental parameter that describes the channel as most, if not all of the channel models give the path loss relation for that particular scenario. This parameter is used to determine the power output and radiation pattern of transmitter antenna.

Mathematically,

$$PL(dB) = 10\log_{10}\left(\frac{P_{transmitted}}{P_{received}}\right) = P_{transmitted}(dB) - P_{received}(dB) \quad (3.6)$$

The Friis equation, assuming unity antenna gains and d as the TX - RX separation, gives the free-space path loss as

$$PL(dB) = 10\log_{10}\left(\frac{P_{transmitted}}{P_{received}}\right) = -10\log_{10}\left[\frac{\lambda^2}{(4\pi)^2 d^2}\right] \quad (3.7)$$

The total received power in a multipath channel is the sum of powers of all rays arriving at the receiver. Please note that ray tracing model developed in this work does not discard the rays based on a power threshold. Instead, all the rays are computed and the contribution is added to the received power.

$$P_{received} = \sum_i P_i \quad (3.8)$$

where P_i is the power of i th ray and can be given as,

$$P_i(W) = \frac{\lambda^2}{480\pi^2} |E|^2 \quad (3.9)$$

$$P_i(mW) = \frac{\lambda^2}{480\pi^2} \frac{|E|^2}{1 mW} \quad (3.10)$$

$$P_i(dB) = 10 \log_{10} \left[\frac{\lambda^2}{480\pi^2} |E|^2 \right] \quad (3.11)$$

$$P_i(dBm) = 10 \log_{10} \left[\frac{\frac{\lambda^2}{480\pi^2} |E|^2}{1 mW} \right] \quad (3.12)$$

3.6.2 Channel Impulse Response (CIR)

The radio channel between a stationary transmitter and receiver with stationary scatterers can be modeled as a linear time invariant (LTI) system. However if the transmitter, receiver and / or scatterers are moving in the environment, the channel can be modeled as a time varying linear filter. The received signal will be the convolution of the input signal with the channel impulse response and can be expressed as [42]:

$$y(t) = \int_{-\infty}^{\infty} x(\tau) h(t, \tau) .d\tau = x(\tau) \otimes h(t, \tau) \quad (3.13)$$

The received signal in a multipath environment is a combination of attenuated and time delayed multipath signals. The channel impulse response can be expressed as:

$$h(t, \tau) = \sum_{i=0}^{N-1} a_i(t, \tau) \exp(j\theta_i) \delta(\tau - \tau_i(t)) \quad (3.14)$$

where, $a_i(t, \tau)$, $\tau_i(t)$ and θ_i are the amplitude, excess delay and phase shift of the i th multipath component respectively.

3.6.3 Time Dispersion Parameters

A *power delay profile* (PDP) represents the relative power of multipath components of the received signal as the function of time. It represents the relative power received from each delayed multipath component. A typical PDP is shown in Figure 3.19. Two important parameters namely *mean excess delay* and *rms delay spread* that quantify the multipath richness of a radio channel are derived from the power delay profile [42].

Mean Excess Delay

The mean excess delay ($\bar{\tau}$) is the first moment of the power delay profile and is defined as:

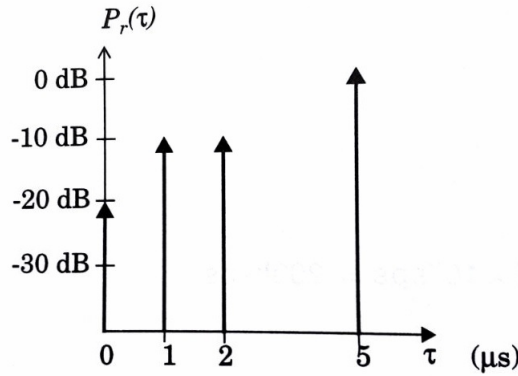


Figure 3.19 A typical power delay profile of a multipath channel [42].

$$\bar{\tau} = \frac{\sum P(\tau_k) \tau_k}{\sum P(\tau_k)} \quad (3.15)$$

RMS Delay Spread

The rms delay spread (σ_τ) is square root of the second central moment of the power delay profile and is defined as

$$\sigma_\tau = \sqrt{\bar{\tau}^2 - (\bar{\tau})^2} \quad (3.16)$$

where,

$$\bar{\tau}^2 = \frac{\sum P(\tau_k) \tau_k^2}{\sum P(\tau_k)}$$

Coherence Bandwidth

Coherence bandwidth (B_c) is defined as the range of frequencies over which the channel will not affect the spectral components of the transmitted signal and can be considered as flat. The coherence bandwidth is related to rms delay spread by [42]

$$B_c = \frac{1}{5\sigma_\tau} \quad (3.17)$$

3.6.4 Frequency Dispersion Parameters

The radio channel characterized by multipath propagation inherits a time dispersion limit which is represented by parameters such as rms delay spread and coherence bandwidth. However, these parameters do not represent the time varying nature of the channel due to relative motion between transmitter and receiver. If the relative speed of motion between transmitter and receiver is v , then the *maximum doppler shift* in frequency is given by,

$$f_m = v/\lambda$$

Coherence time (T_c) is used to characterize the frequency dispersiveness of the channel in time domain and is inversely proportional to the doppler spread as [42]

$$T_c = \sqrt{\frac{9}{16\pi f_m^2}} = \frac{0.423}{f_m} \quad (3.18)$$

3.7 Conclusion

This chapter introduces the methods and techniques in ray tracing. The effect of different objects including buildings, vegetation, pedestrians and vehicular traffic on outdoor radio wave propagation is explained. The selection of appropriate constitutive parameters to model the building walls in a ray tracing model is critical. Scattering from vegetation and urban furniture is significant in outdoor propagation and must be included in ray tracing. Several visibility algorithms that compute the visible surfaces in ray tracing models are reviewed. The concept of image tree and ray-object intersection test is explained with examples. These techniques form the basis of ray tracing model developed in this work as explained in chapters 5 and 6. The parameters that characterise a radio channel are briefly described in the last.

Chapter 4

Literature Review

There are mainly two types of radio channel models depending on the type of channel parameters they provide.

1. Small scale models
2. Large scale models

Small scale models are used to predict the small scale parameters of the channel such as delay spread, coherence bandwidth, doppler spread and coherence time that are used to design the receiver characteristics. These models provide the bit error rate (BER) of a communication system that measures the quality of service (QoS). *Large scale models* are used to determine the large scale fading or path loss to predict the power output and radiation characteristics of transmitter. These models can be further divided into three types [57].

1. *Empirical Models*: Path loss equations are derived from field measurements. These models can be applied to environments similar to the one where measurements are performed.
2. *Theoretical Models*: These models consider the geometry of the environment for ideal conditions such as uniform building heights and street width etc. for path loss prediction and can be applied in similar environments.
3. *Site specific Models*: These models are more accurate as they take into account the complete structure of a specific site to predict the path loss in a given scenario. With the use of smaller cell size for high capacity requirements, more site specific models are required.

This chapter reviews the literature on radio channel models. Large scale models including empirical, theoretical and site specific models are introduced. An overview of efficient ray tracing algorithms reported in the literature is given. Limitations of ray tracing models and future trends are described at the end.

4.1 Empirical Models

It is well known from measured data that in general power received by a mobile decreases logarithmically with distance. If path loss at a reference distance d_0 is already known, a general expression for path loss at a given distance d will be as follows.

$$PL(d) = PL(d_0) + 10n \log(d/d_0) \quad d > d_0 \quad (4.1)$$

where n is a suitable path loss exponent (also represented by γ) whose value for different environments is given in Table 4.1 [42].

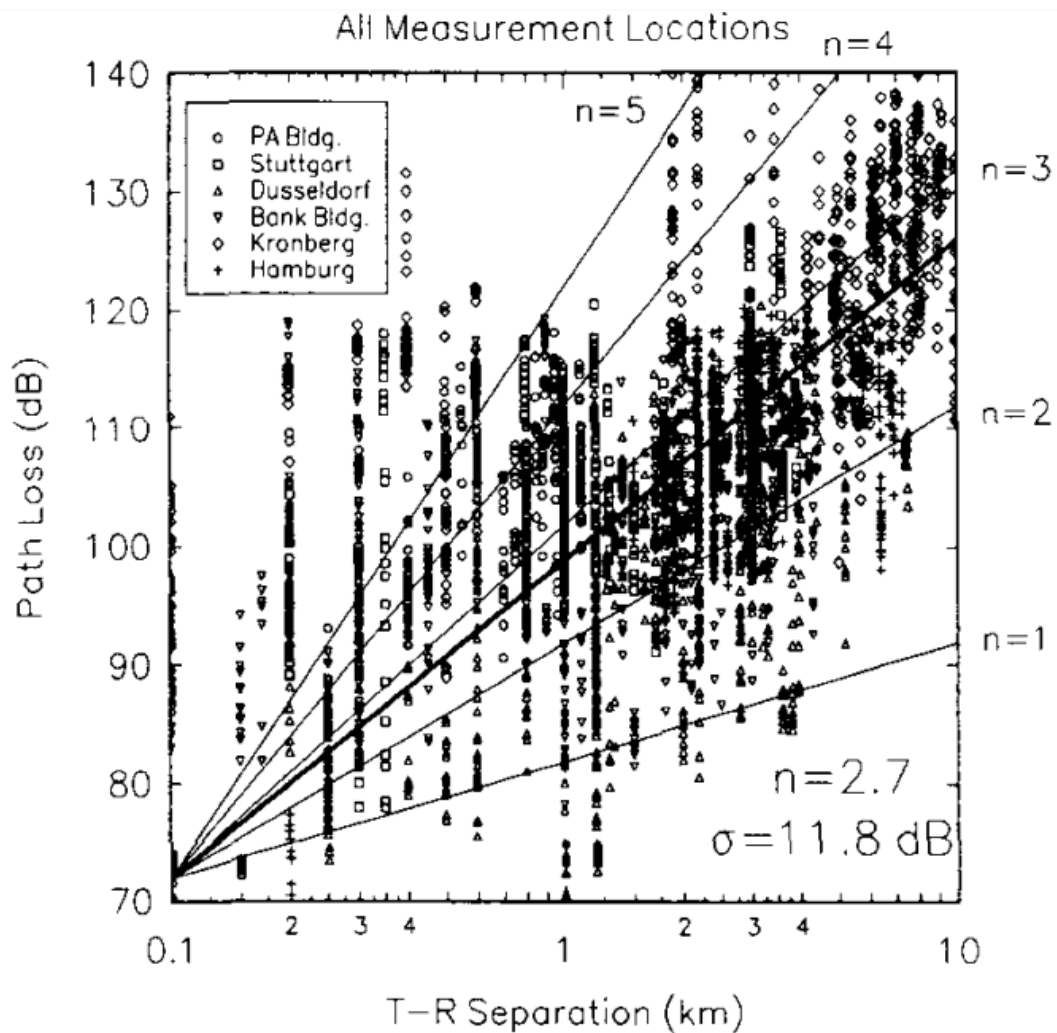


Figure 4.1 Path loss (dB) versus transmitter receiver (T-R) separation in km for different cities in Germany [58].

Two different receiver locations at the same distance from a transmitter however may have different received power due to clutter between the transmitter and receiver. Measurements have shown that the received power at a certain distance d is random and log-normally distributed across a mean value [59]. Equation 4.1 can be rewritten as follows,

Table 4.1 Reported path loss exponent (n) values for different environments [42]

Environment	Path loss exponent (n)
Free space	2
Urban	2.7 - 3.5
Shadowed urban	3 - 5
Indoor LOS	1.6 - 1.8
Indoor NLOS	4 - 6
Factories shadowed	2 - 3

$$PL(d) = PL(d_0) + 10n \log(d/d_0) + X_\sigma \quad d > d_0 \quad (4.2)$$

where X_σ is a random log-normal variable with standard deviation σ (dB). Empirical models are derived from extensive field measurements and take the form of the general expression as given in 4.2. The following empirical models including Okumura, Hata, Lee and Erceg have been very popular and are frequently used for radio network planning.

4.1.1 Okumura Model

Okumura et al. [60] presented this model based on field strength curves derived after extensive measurements for open, quasi-open, rural, urban and sub-urban areas in Japan. These curves give the field strength in terms of frequency (f_c), base station antenna height (h_b), mobile antenna height (h_m) and distance between base station and mobile (d) at 1KW Effective Radiation Power (ERP) per dipole. The model gives path loss for 1 to 100 Km diameter macro-cells for a 30 to 1000 m high base station at 150-920 MHz.

The general expression for path loss is given by,

$$PL(dB) = PL_{free-space} + Am,u(f_c, d) - G(h_b) - G(h_m) - Gc \quad (4.3)$$

where,

$PL_{free-space}$ = free-space path loss.

$Am,u(f_c, d)$ = median attenuation relative to free-space in urban area.

$G(h_b), G(h_m)$ = height gain factors of base station and mobile antennas respectively.

Gc = correction factor due to environment.

$PL_{free-space}, G(h_b)$ and $G(h_m)$ are calculated using simple formulas. Values of $Am,u(f_c, d)$ and Gc is derived from curves for specified values of f_c, h_b, h_m and d for the given environment.

4.1.2 Hata Model

Hata proposed simple expressions [61] for path loss prediction using the curves in the Okumura model. This model provides path loss for urban, sub-urban and open areas. The empirical formula for path loss in urban areas is given as follows.

$$PL_{urban}(dB) = 69.55 + 26.16 \log f_c - 13.82 \log h_b - a(h_m) + (44.9 - 6.55 \log h_b) \log d \quad (4.4)$$

where,

$a(h_m)$ is the correction factor for mobile antenna height and is given by

$a(h_m) = (1.1 \log f_c - 0.7)h_m - (1.56 \log f_c - 0.8)$ for small and medium cities.

For large cities,

$$a(h_m) = \begin{cases} 8.29(\log 1.54h_m)^2 - 1.1 & f_c \leq 200 \text{ MHz.} \\ 3.2(\log 11.75h_m)^2 - 4.97 & f_c \geq 400 \text{ MHz.} \end{cases}$$

Path loss for sub-urban areas is given by,

$$PL_{sub-urban}(dB) = PL_{urban} - 2(\log(f_c/28))^2 - 5.4 \quad (4.5)$$

Path loss for open areas is given by,

$$PL_{open}(dB) = PL_{urban} - 4.78(\log(f_c))^2 - 40.94 \quad (4.6)$$

where,

- $150 \text{ MHz} \leq f_c \leq 1500 \text{ MHz}$
- $30 \text{ m} \leq h_b \leq 200 \text{ m}$
- $1 \text{ m} \leq h_m \leq 10 \text{ m}$
- $1 \text{ km} \leq d \leq 20 \text{ km}$

International Telecommunication Union (ITU) recommendations [62, 63] corrected the effective base station height parameter of the Hata model and extended its range d up to 100 Km. The COST-231 Hata model extended the maximum frequency from 1500 MHz to 2000 MHz. Medeisis *et al.* [64] observed that path loss measurements in rural areas of Lithuania do not match well with the Hata model. Offset and slope of the basic path loss expression were tuned using statistical analysis of measurements with least squares method to match the results with measurements. Later work by Akhoonzadeh-Asl *et al.* [65] identified four parameters of Hata model that can be optimised by using the following general expression for field strength recommended by ITU-R P.370 [62].

$$E_{HATA} = A + B \times \log h_b + (C + D \times \log h_b) \times (\log d)^b \quad (4.7)$$

The Levenberg-Marquardt Algorithm (LMA) was proposed to optimise the parameters values so that the sum of difference between simulated and measured data is minimum.

4.1.3 Lee Model

Lee [66] proposed this model in 1982 and it became very popular in the United States for network planning at 900 MHz. The model first computes *area-to-area* path loss for a general flat terrain. This is used as a basis to compute *point-to-point* path loss by including free-space loss in case of LOS or knife-edge diffraction loss for obstructions between transmitter and receiver. An adjustment factor (α_0) is also applied to account for antenna heights, transmitter power and antenna gains.

The general expression for received power by a mobile at distance d is given as follows.

$$P_r(d) = P_r(d_0) - 10\gamma \log(d/d_0) - L + \alpha_0 \quad d > d_0 \quad (4.8)$$

where L accounts for the free-space or obstruction loss between transmitter and receiver. The parameters of the model can be obtained for a particular environment using simple measurements.

4.1.4 Erceg Model

Erceg *et al.* [67] performed measurements in 95 macro-cells across the United States for sub-urban areas at 1.9 GHz. The data was collected for three different terrain categories as follows.

- **Category A:** Hilly terrain with moderate to heavy tree density.
- **Category B:** Hilly terrain with light tree density OR Flat terrain with moderate to heavy tree density.
- **Category C:** Flat terrain with light tree density.

The basic expression for the Erceg model is the same as is given in equation 4.2. i.e.

$$PL(d) = A + 10\gamma \log(d/d_0) + X_\sigma \quad (4.9)$$

where X_σ is a log-normal variable with standard deviation σ (dB). However, regression analysis of the collected data showed that the path loss exponent γ is also a

Gaussian random variable that varies between macro-cells across each terrain category and depends on the base station height (h_b) as follows.

$$\gamma = (a - bh_b + c/h_b) + x\sigma_\gamma \quad 10m \leq h_b \leq 80m \quad (4.10)$$

where σ_γ is standard deviation of path loss exponent γ and x is a zero-mean Gaussian variable with unit standard deviation.

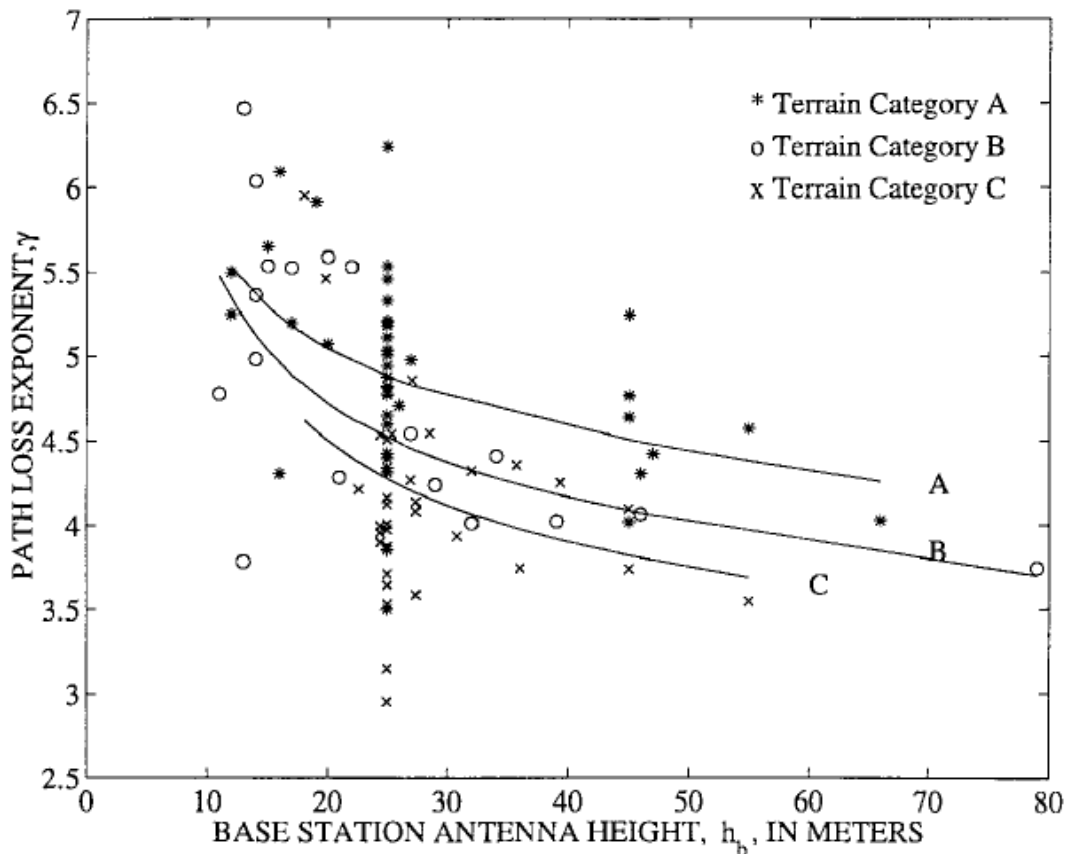


Figure 4.2 Scatter plot of path loss exponent and base station height for three terrain categories. Solid curves are least-squares regression fit to $a - bh_b + c/h_b$ [67].

The standard deviation of path loss σ in 4.9 is also a Gaussian variable and can be given as,

$$\sigma = \mu_\sigma + z\sigma_\sigma \quad (4.11)$$

where μ_σ is mean and σ_σ is standard deviation of σ . z is a zero-mean Gaussian variable with unit standard deviation.

The value of parameters a , b , c and σ_γ in 4.10 and μ_σ and σ_σ in 4.11 for three terrain categories was found as given in Table 4.2.

Table 4.2 Values of Erceg Model Parameters [67]

Parameter	Terrain Category		
	A	B	C
a	4.6	4.0	3.6
b	0.0075	0.0065	0.0050
c	12.6	17.1	20.0
σ_γ	0.57	0.75	0.59
μ_σ	10.6	9.6	8.2
σ_σ	2.3	3.0	1.6

4.2 Vertical Plane Models

Several over rooftop models have been reported in literature. These models compute a dominant ray in the vertical plane between the transmitter and receiver. However these models can also be categorised under *theoretical models* as the following assumptions are made.

- Transmitter is located above rooftop.
- Receiver is located on street level well below average building height.
- Buildings have uniform heights and are located along streets that have uniform width.
- The incident angle is small so that the buildings can be represented by perfectly absorbing half screens.

4.2.1 COST-231 Walfisch Ikegami Model

This model is developed based on the work by Bertoni *et al.* [68] and Ikegami *et al.* [69]. The model computes path loss for a mobile at street level in an urban environment at UHF bands. The model is developed for uniform height buildings that are uniformly spaced.

The model has three components as follows.

- Free-space path loss (L_0) that depends on $TX - RX$ separation.
- Multiple over-rooftop diffraction loss that occurs due to buildings present between transmitter and receiver. Buildings are represented by half-screens so that multi-screen diffraction loss (L_{msd}) is computed using Kirchhoff-Huygens integral.

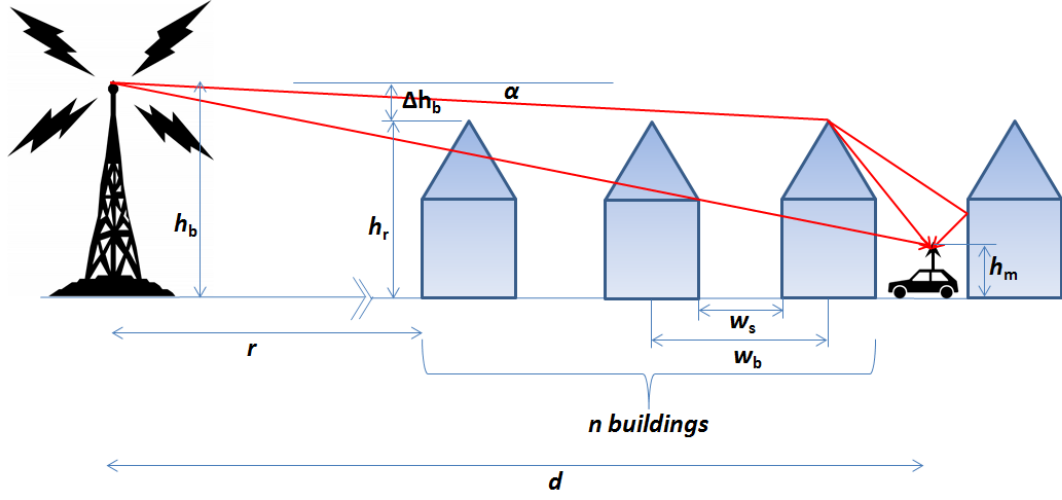


Figure 4.3 Geometry for COST-231 Walfisch Ikegami Model.

- Rooftop-to-street diffraction loss (L_{rts}) that also includes the street canyon effects in which the receiver is located.

Mathematically,

$$PL = \begin{cases} L_0 + L_{msd} + L_{rts} & L_{msd} + L_{rts} > 0 \\ L_0 & L_{msd} + L_{rts} \leq 0 \end{cases} \quad (4.12)$$

where,

$$L_0 = 32.4 + 20 \log(d_{km}) + 20 \log(f_{MHz})$$

$$L_{rts} = -16.9 - 10 \log w_s + 10 \log f_{MHz} + 20 \log \Delta h_{mobile} + L_{ori}$$

here w_s is street-width in meters and Δh_m is difference between height of roof and height of mobile. i.e.

$$\Delta h_m = h_r - h_m$$

L_{ori} is the orientation loss and is given by,

$$L_{ori} = \begin{cases} -10 + 0.354\phi & 0^\circ \leq \phi < 35^\circ \\ 2.5 + 0.075(\phi - 35) & 35^\circ \leq \phi < 55^\circ \\ 4.0 - 0.114(\phi - 55) & 55^\circ \leq \phi \leq 90^\circ \end{cases}$$

where ϕ is angle of incidence relative to street direction.

Multi-screen diffraction loss (L_{msd}) is given by,

$$L_{msd} = L_{bsh} + k_a + k_d \log d + k_f \log f - 9 \log w_b$$

where w_b is the uniform distance between centre of buildings in two streets as shown in Figure 4.3. Δh_b is difference between height of roof and height of base station. i.e.

$$\Delta h_b = h_b - h_r$$

Base station height loss L_{bsh} and k_a are given as,

$$L_{bsh} = \begin{cases} -18 \log(1 + \Delta h_b) & h_b > h_r \\ 0 & h_b \leq h_r \end{cases}$$

$$k_a = \begin{cases} 54 & h_{base} > h_r \\ 54 - 0.8\Delta h_b & d \geq 0.5km \text{ and } h_b \leq h_r \\ 54 - 1.6\Delta h_b d & d < 0.5km \text{ and } h_b \leq h_r \end{cases}$$

The dependence of multi-screen diffraction loss on distance and frequency is given by factors k_d and k_f respectively as follows.

$$k_d = \begin{cases} 18 & h_b > h_r \\ 18 - 15 \frac{\Delta h_b}{h_r} & h_b \leq h_r \end{cases}$$

and

$$k_f = -4 + 0.7 \left(\frac{f}{925} - 1 \right)$$

for medium sized cities and sub-urban areas with moderate tree densities.

$$k_f = -4 + 1.5 \left(\frac{f}{925} - 1 \right)$$

for metropolitan areas.

The range of different parameters for the Walfisch-Ikegami model is given as follows.

- $800MHz \leq f \leq 2000MHz$
- $4m \leq h_b \leq 50m$
- $1m \leq h_m \leq 3m$
- $0.02Km \leq d \leq 5Km$

For urban areas the following values for other parameters can be used if not known,

- $w_b = 20 \sim 50m$
- $w_s = 0.5w_b$
- $\phi = 90^\circ$
- $h_r = 3 \times (\text{floors})$

This model has been very popular for radio network planning. Har et al. [70] identified an error in the rooftop-to-street diffraction loss and presented the correct formulation. Garcia et al. [71] investigated the accuracy of model for hilly terrain and found that the correction in the Walfisch-Ikegami model proposed by [70] does not provide better results than the original model. The model has also been investigated for ad hoc network planning in urban environments by Gruber et al [72]. Schwengler *et al.* [73] validated the model applicability at the 5.8 GHz band. A history of development of the Walfisch-Ikegami model and the corrections and extensions suggested over time are reviewed in detail in [74].

4.2.2 Vogler Model

Vogler [75] derived an analytical expression for an attenuation function in the case of multiple edge diffraction for variable building heights and spacing. The attenuation function consists of multiple integrals that can be represented by a series.

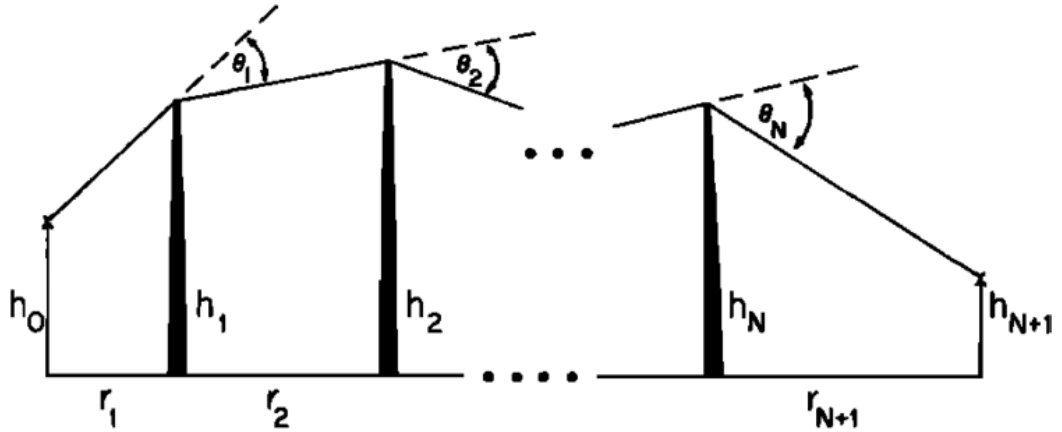


Figure 4.4 Geometry for Vogler model with irregular buildings height and spacing [75].

For n buildings of variable heights and r_i distance between two adjacent knife-edges as shown in Figure 4.4, the attenuation function is given as follows [75],

$$A = C_n \pi^{-n/2} I_n \exp(\sigma_n) \quad (4.13)$$

where, I_n represents the repeated integral of error function and consists of n integrals as,

$$I_n = \int_0^\infty du_1 \cdots \int_0^\infty du_n \left\{ e^A [\cos B - j \sin B] \right\} \quad (4.14)$$

where,

$$A = \sum_{m=1}^{n-1} \left[2\alpha_m u_m u_{m+1} - u_m^2 - \sqrt{2} u_m b_m \right] - u_n^2 - \sqrt{2} u_n b_n \quad (4.15)$$

and,

$$B = \sum_{m=1}^n \left[\sqrt{2}u_m b_m + b_m^2 \right] \quad (4.16)$$

α_m represents the coupling between the adjacent edges

$$\alpha_m = \left[\frac{r_m r_{m+2}}{(r_m + r_{m+1})(r_{m+1} + r_{m+2})} \right]^{1/2} \quad m = 1, \dots, n-1 \quad (4.17)$$

and b_m is the normalised Fresnel diffraction parameter. The value of b_m indicates how likely an edge will obstruct the signal and is given by,

$$b_m = \beta_m / \sqrt{j} \quad (4.18)$$

where,

$$\beta_m = \theta_m \left[\frac{jkr_m r_{m+1}}{2(r_m + r_{m+1})} \right]^{1/2} \quad m = 1, \dots, n \quad (4.19)$$

θ is the angle between two adjacent knife-edges as shown and k is the wave number $k = 2\pi/\lambda$.

The remaining terms in equation 4.14 are given as,

$$C_n = \begin{cases} 1 & n = 1 \\ \left[\frac{r_2 r_3 \cdots r_n (r_1 + r_2 + \cdots r_n + r_{n+1})}{(r_1 + r_2)(r_2 + r_3) \cdots (r_n + r_{n+1})} \right]^{1/2} & n \geq 2 \end{cases} \quad (4.20)$$

and,

$$\sigma_n = \beta_1^2 + \cdots + \beta_n^2 \quad (4.21)$$

The Vogler model can accurately estimate the over rooftop attenuation for non-uniform spacing and heights. Since the model requires solving n integrals where n is equal to number of edges, the computation time becomes too large for a large number of edges. A computer program can be used to compute the attenuation function. Generally the model is used to compute the attenuation for up to 10 edges.

4.2.3 Flat Edge Model

Saunders *et al.* [76] proposed a complete solution to the Walfisch-Ikegami model [68] in the so called *flat edge model*. The model can accurately predict the attenuation for a small to large number of uniformly spaced and equal heights buildings. The model also extends the Walfisch-Ikegami model for transmitter located below the building height. Consider the geometry of Walfisch-Ikegami model again in Figure 4.5,

The field at the final edge relative to free-space can be given as [76]

$$A_n(t) = S_n(t) \exp(jt^2) \quad (4.22)$$

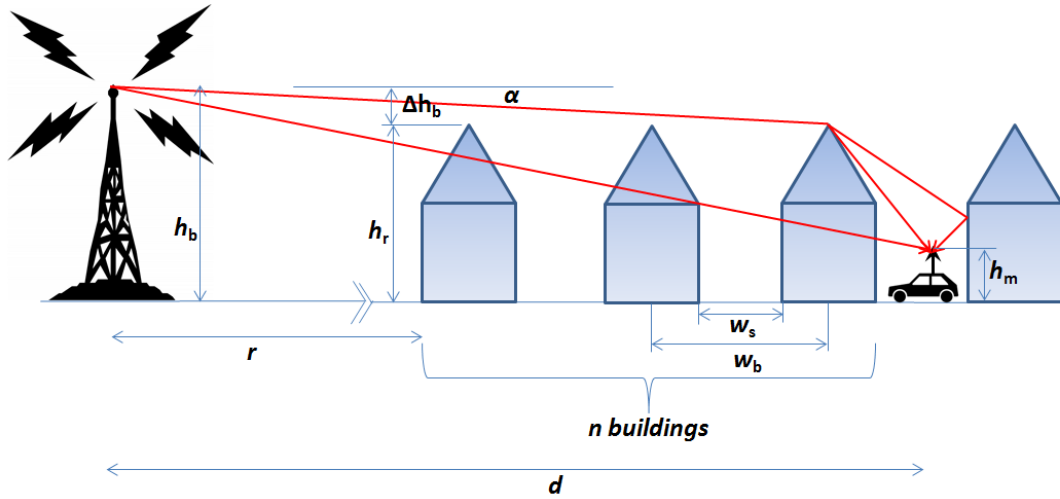


Figure 4.5 Geometry for Flat Edge Model.

where,

$$t = \alpha \sqrt{\frac{kw_s}{2}} = \alpha \sqrt{\frac{\pi w_s}{\lambda}} \quad (4.23)$$

Assuming $r \gg nw_s$ gives the initial value $S_0 \equiv 1$ and,

$$S_n(t) = \frac{1}{n} \sum_{m=0}^{n-1} S_m(t) F_s(jt\sqrt{n-m}) \quad n \geq 1 \quad (4.24)$$

where F_s is the Fresnel integral function as discussed in chapter 2 and is given by equation 2.46.

4.2.4 Saunders and Bonar Hybrid Model

Saunders and Bonar combined the Vogler method with flat edge model to give a hybrid model [77] that can be used for loss prediction over a large number of buildings with irregular heights and spacings.

The model combines the two methods as follows [77].

- Edges with negligible obstruction are neglected from the vertical profile of buildings. The selection criteria is based on a threshold value of b_m as defined in section 4.2.2. All the edges below this threshold value are not included.
- The Flat edge model is used to compute the field strength E_1 at the edge of the final building in the profile.
- Next, a smaller number of edges, say 5 out of 20, are selected that have the highest value of b_m . i.e. only the edges that have the most dominant obstruction are selected.

- The Vogler method using a Monte-Carlo approach is applied to compute the field strength E_2 for these edges.
- The flat edge model is also used to compute the field strength E_3 for these edges as well.
- The total field E_d for the complete profile is computed using the normalised field as follows.

$$E_d = E_1 E_2 / E_3 \quad (4.25)$$

The model is fully automated as it can compute the over rooftop fields irrespective of the buildings heights and spacings.

4.2.5 Knife-Edge Diffraction Models

Several models that approximate the obstructions, buildings and hills as knife-edges have been in use between 1950 to 1980. These models include Bullington [78], Epstein-Peterson [79], Deygout [80] and Giovanelli [81].

A brief introduction is presented in the following that describes the major difference between these models.

Bullington Model

This is the simplest model that computes an equivalent single knife-edge at the intersection of closest knife-edges with respect to both the transmitter and receiver as shown in Figure 4.6a. All the remaining knife-edges are neglected that adds inaccuracies in diffraction loss.

Epstein-Peterson Model

This model includes the diffraction loss introduced by each of the knife-edge present between transmitter and receiver. The diffraction loss is computed hop-by-hop formed by each knife-edge that obstructs the line of sight. The basic principle of Epstein-Peterson model is shown in Figure 4.6b.

The model computes loss for the following three hops.

- $TX - H_1 - H_2$ with obstruction height h_1
- $H_1 - H_2 - H_3$ with obstruction height h_2
- $H_2 - H_3 - RX$ with obstruction height h_3

It can be shown that the obstruction effective height for j th hop is [82]

$$h_j = H_j - H_{j-1} - \left(\frac{d_j(H_{j+1} - H_{j-1})}{d_j + d_{j+1}} \right) \quad (4.26)$$

The knife-edge diffraction parameter for the j th obstruction can be given as,

$$v_j = h_j \sqrt{\frac{2(d_j + d_{j+1})}{\lambda(d_j)(d_{j+1})}} \quad (4.27)$$

The diffraction loss for the j th knife-edge is [83]

$$A_j(dB) = 6.9 + 20 \log \left(\left(\sqrt{(v_j - 0.1)^2 + 1} \right) + v_j - 0.1 \right) \quad (4.28)$$

Total diffraction loss for m knife-edges can be given as,

$$A = \sum_{j=1}^m \left(6.9 + 20 \log \left(\left(\sqrt{(v_j - 0.1)^2 + 1} \right) + v_j - 0.1 \right) \right) \quad (4.29)$$

Deygout Model

This model applies a more accurate technique to compute the knife-edge diffraction than the Epstein-Peterson model. An edge with the highest value of diffraction parameter is selected as the *principal edge* as shown in Figure 4.6c. The diffraction parameter for obstructing edges between the transmitter and principal edge is computed with respect to the principle edge. Similar approach is applied to compute the diffraction parameter between the principal edge and receiver. The total loss is the sum of all the individual diffraction loss computed using individual diffraction parameters as in previous section for Epstein-Peterson model.

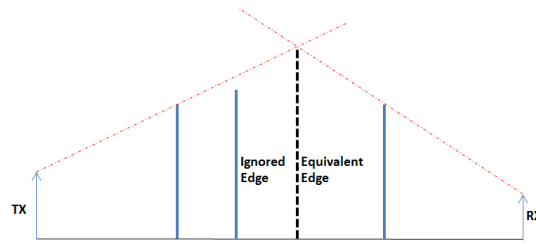
Giovanelli Model [81] suggests further correction in Deygout model by proposing a GTD solution for attenuation factor computation. This model behaves more similarly to the rigorous Vogler model than the Deygout model. Although two models have the same performance in the case of grazing incidence.

Performance Comparison of Knife-edge Models

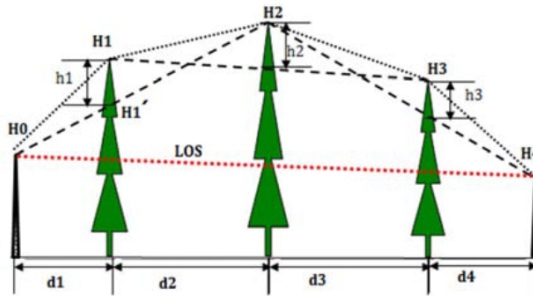
Several studies [84–87] have been carried out to compare the performance of different knife-edge models.

The following results can be inferred from these studies.

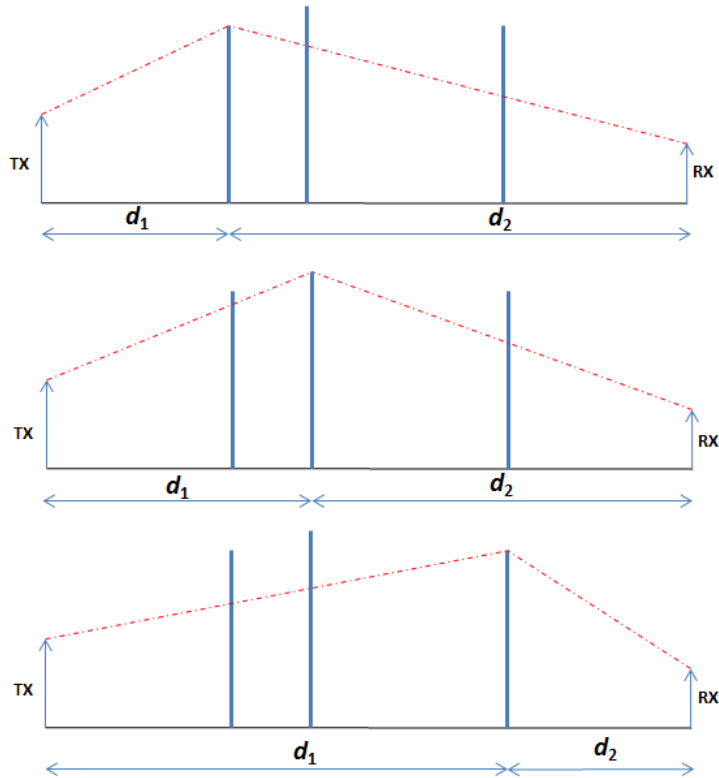
- Knife-edge models can produce results with considerable accuracy while reducing the computation time as compared to Vogler method.
- Bullington model gives the least accurate results and cannot be applied for cases with a large number of knife-edges.
- Epstein-Peterson, Deygout and Giovanelli models tend to over-estimate the diffraction loss for large number of knife-edges. However, the Giovanelli model gives the best result comparatively.



(a) Computation of equivalent knife-edge in Bullington model.



(b) Diffraction loss using Epstein-Peterson method [82].



(c) Computation of principle edge in Deygout model.

Figure 4.6 Computation of diffraction loss in different knife-edge models.

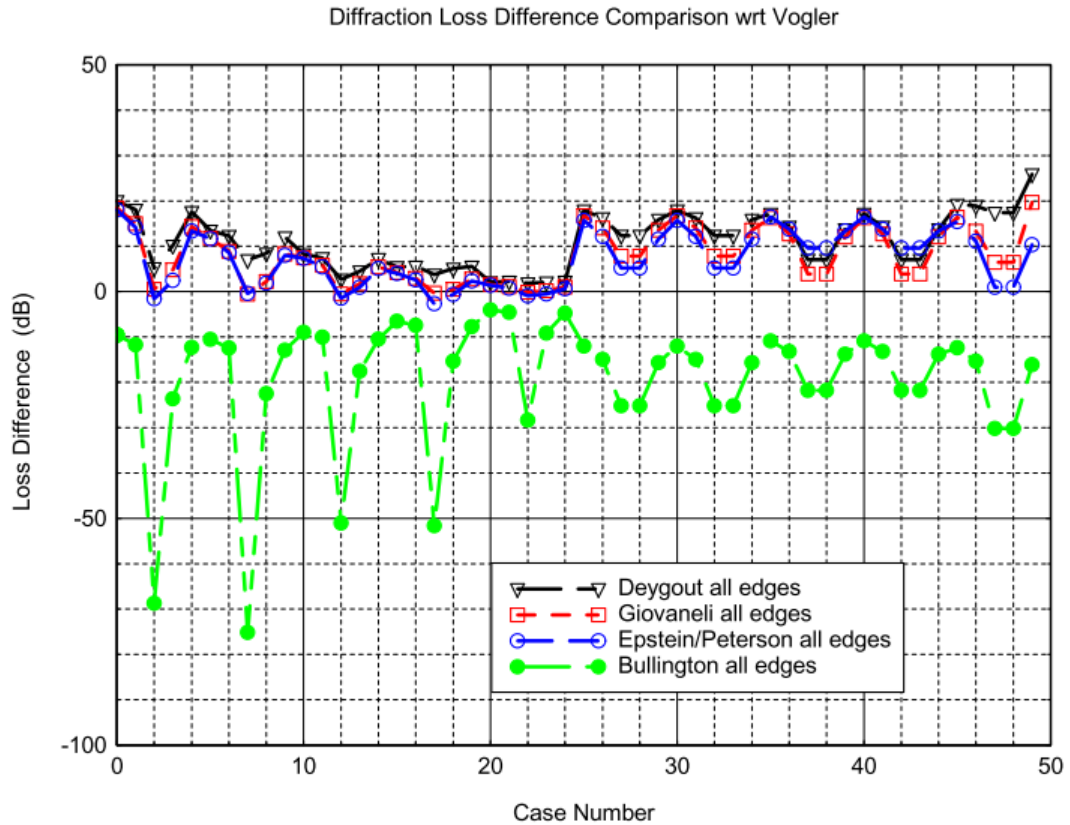


Figure 4.7 Comparison of knife-edge models against Vogler model [86].

- Bullington model is the fastest method followed by Epstein-Peterson, Deygout and Giovaneli.
- If the ray path from one edge to the other is in the transition region and close to incidence shadow boundary, none of the above methods can predict the diffraction loss accurately.

4.3 Ray Tracing Models

Cell size has decreased with the increase in capacity requirements of radio networks. This has resulted in deployment of base station antennas below the average building height for a better frequency re-use factor. Since the base station antenna is below the rooftop level, vertical propagation is negligible. The radio wave interacts with buildings, vehicles, trees etc. and undergoes reflection, diffraction or scattering before arriving at the receiver. A multipath channel exists between the transmitter and receiver in a typical urban micro-cellular environment. The empirical and theoretical models discussed above cannot accurately predict the radio channel in such case as the scatterers present in the environment determine the radio propagation. Ray tracing models consider all the scatterers to compute the dominant paths through which the radio energy propagates as discussed in previous chapters.

Computer programs are used for ray tracing that take buildings database, frequency and transmitter and receiver antennas characteristics as inputs to compute the channel parameters. Ray tracing models become computationally intensive if there are large number of objects in the environment or a higher order of ray interaction is considered. Immense computational resources including higher CPU time and larger computing memory are required to model such scenarios. The ray tracing models are approximate methods and have inherently limited accuracy, the research community is interested to develop fast ray tracing algorithms for seamless radio channel modeling.

4.4 Efficient Ray Tracing Techniques

Many efficient ray tracing models have been proposed in literature [57, 88–90]. Fast ray tracing is achieved using two techniques [57].

- Reduce the number of objects on which the ray-object intersection test has to be performed.
- Accelerate the ray-object intersection test.

Efficient ray tracing models use one or both of the techniques to accelerate the ray tracing. The following gives an overview of common techniques used for efficient ray tracing models.

4.4.1 Space Division Methods

The basic principle of space division methods is to divide the environment into smaller regions and assign the objects to regions in which they reside. Each time a ray-segment between receiver and wall or edge, transmitter and wall or edge, or transmitter and receiver must be validated, only the objects present in the regions intersected by ray-segment need a ray-object intersection test. Time acceleration is achieved as only a smaller number of objects has to be tested than a brute-force approach in which all the objects in the environment must be tested. Space division is performed as a *pre-processing* step before the rays are launched from transmitter. These methods are therefore independent of transmitter location.

There are two types of space division methods depending on how the environment is divided into smaller regions and how the objects are assigned or mapped to these regions.

Uniform Space Division

In uniform space division, the environment is divided into a grid of uniform size rectangular cells. Iskander *et al.* [91, 92] proposed an efficient 2-D ray tracing model

based on the *uniform rectangular grid* approach. The model makes use of the Cleary and Wyvil algorithm [93] for ray's traversing in a uniform rectangular space division scenario. A cell is surrounded by 8 cells around it and the next cell in which the ray enters must be found. Instead of checking the ray intersection with all the 8 cells, model uses the direction and slope of the ray to determine the next cell the ray enters.

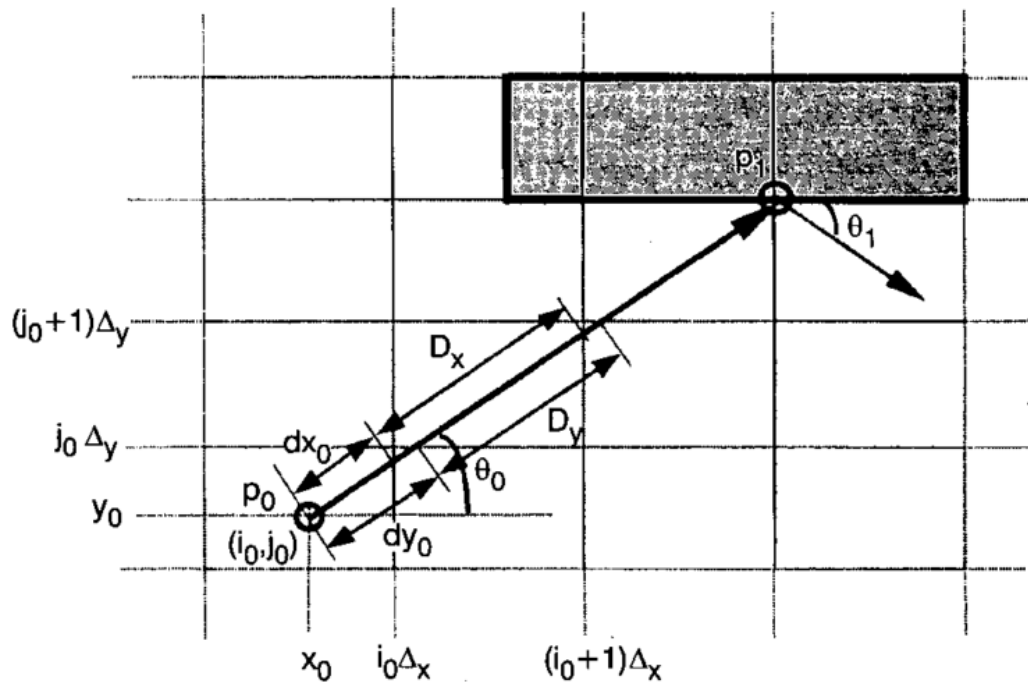


Figure 4.8 Uniform rectangular space division. Values of D_x and D_y determine the next cell the ray enters [92].

The following steps are performed to traverse a ray.

- Environment is divided into a uniform rectangular grid.
- Appropriate cell size is selected. The algorithm gives the best performance when the building outer walls coincide with the grid lines for outdoor ray tracing.
- Internal walls and rooms are coincided with grid lines for indoor ray tracing.
- Each cell is labelled with an index. If cell is on a building or wall, the index is that of the building or wall. If there is no building or wall inside a cell, it is assigned 0 index.
- A ray is launched from the transmitter. Direction vector and slope parameters dx_0, D_x, dy_0, D_y are determined.
- if $D_x > D_y$, then the ray enters into next horizontal cell. If $D_x < D_y$, then the ray enters into next vertical cell. If $D_x = D_y$ then the ray enters into next diagonal cell depending on the direction of the ray.

- If the cell index of the current cell is equal to the next cell index, the ray is still travelling in the same medium. However if the index changes, ray undergoes reflection or diffraction.
- A ray is traversed until a termination criterion is met.

Another space division approach divides the environment into a mesh of triangles for 2-D and tetrahedrons for 3-D ray tracing. Iskander *et al.* presented several *triangular grid methods* for both 2-D and 3-D ray tracing for indoor, outdoor and outdoor-to-indoor scenarios in [94–97].

The following steps are performed to traverse a ray.

- Environment is divided into an unstructured triangular grid.
- There are two types of sides (edges) of a triangle. One is true wall coincident with the edge and the other is a dummy edge when no wall coincides with the edge.
- A ray is launched from the transmitter. Direction vector and triangle edge determines the direction of traversal.
- A ray from an edge can only hit remaining two edges of the triangle.
- If the ray hits a dummy edge, it continues in the same direction. However if the ray hits a real wall it undergoes reflection or diffraction.
- A simple dot product between the direction vector and the vector that defines the edge is used to get the direction in which ray travels.
- A ray is traversed until a termination criteria is met.

Both the rectangular and triangular grid methods are very efficient and can reduce the run time by a large extent. However rectangular grid approach requires that walls must be aligned with the grid lines so is best suited for smaller environments as in indoor applications. Triangular grid being the unstructured approach on the other hand works well with large areas and suits outdoor applications. Iskander *et al.* presented a hybrid method that can achieve further acceleration and can be easily used for large complex environments in [98].

Bounding Volume Hierarchy (BVH)

Uniform space partitioning assumes that objects are uniformly located in a given environment. However it is possible that one or more cells contain a larger number of objects than the rest of the cells. In this case, the ray-object intersection test for a particular set of ray-segments passing through crowded cells can be unnecessarily time

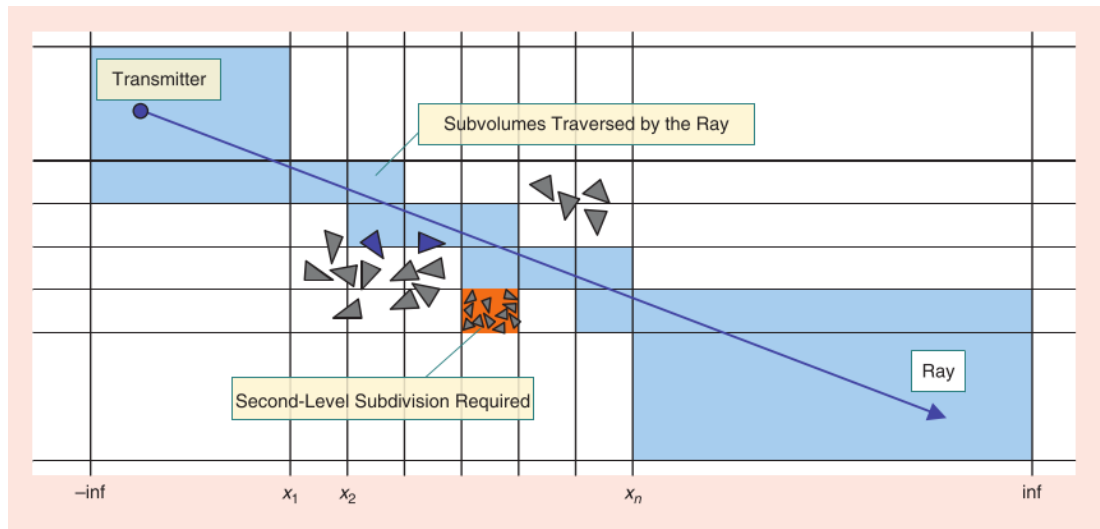


Figure 4.9 Adaptive multi-level space division [100].

consuming. The *Bounding volume hierarchy* approach divides the environment into bounding volumes with different sizes so that the number of objects in all of the cells is almost uniform.

An example of a scene where BVH can be applied is shown in Figure 4.9. As we can see the orange cell contains a large number of objects and must be further divided into smaller regions.

A *k-d (k-dimensional) tree* approach [99] is widely used to create a bounding volume hierarchy for ray tracing. In a simple ($k = 2$) 2-D tree example the environment is divided into two equal planes by a horizontal line. The scene is further divided into two halves by a vertical line. This process is repeated until a termination criterion is met.

Binary space partitioning (BSP) [49, 50], quadtree [55, 56] and octree are other examples of BVH and have already been thoroughly presented in Chapter 3 sections 3.3.2 and 3.3.3 under visibility algorithms. Weinmann [100] presented an adaptive and automated multi-level space division tool that can quickly divide the scene into smaller cells until the objects density per cell is almost uniform. The results shows an acceleration of up to 90% as compared to uniform space division methods.

4.4.2 Transmitter Dependant Methods

Space division methods are pre-processing techniques applied on an environment without the knowledge of transmitter location. In the following, an overview of ray tracing acceleration methods is given that are performed based on the transmitter location. Although the methods can be very efficient, the pre-processing techniques must be repeated each time the transmitter location is changed.

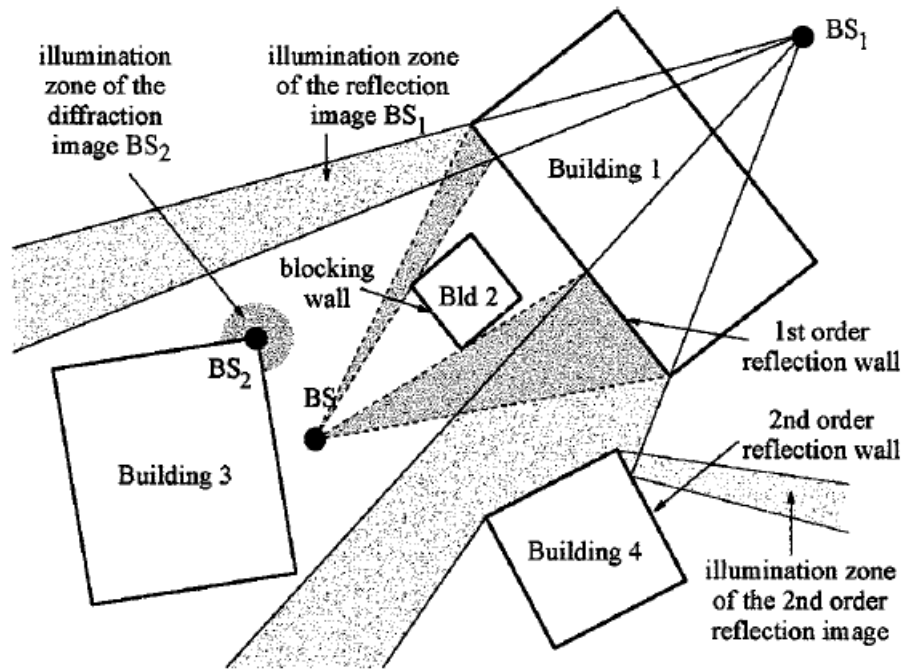


Figure 4.10 Accurate illuminate zones of wall reflections [101].

Accurate Illumination Zone Method

This idea was first proposed by Rizk *et al.* [23] for urban microcellular propagation and later used by Athanasiadou *et al.* [101]. The basic principle of this method is to define the exact *illumination region* where the rays associated with an image, transmitter, wall or edge, can possibly propagate *considering all the blocking elements present in the environment*. Instead of performing the time consuming ray-object intersection test, this method only requires a simple check whether or not the receiver is inside this illumination zone. A valid ray will exist only if the receiver is found inside the illumination region.

An example of how illumination zones of images are created is shown in Figure 4.10 taken from [101].

Some of the features and limitations of this technique are listed below.

- The advantage of this method is that a ray does not have to be traced back from receiver to transmitter segment-by-segment as in a typical ray-object intersection test. The illumination region of an image gives the exact region where a ray will exist and the receiver is only tested to check if it is located inside this region.
- Since reflection from a wall confines the illumination beam to a smaller area, the illumination zone gets narrower for higher order reflection images. Thus the complexity of implementing this method decreases for higher order reflections.
- However applying this technique for edge diffraction can produce very complex shaped illumination zones.

- The geometrical test to determine if a receiver is located inside an illumination zone is proportional to the number of sides of the illumination polygon that defines the illumination region of an image. Thus using this method for complex environments may not be suitable as the geometrical test may become slower.

Angular Z-Buffer Method

The Angular Z-Buffer (AZB) method is adopted from the light buffer technique [102] widely used in computer graphics applications. Catedra *et al.* [22, 103, 104] proposed this technique for fast ray-tracing in radio propagation prediction. The algorithm divides the environment into angular sectors called *anxels* as shown in Figure 4.11.

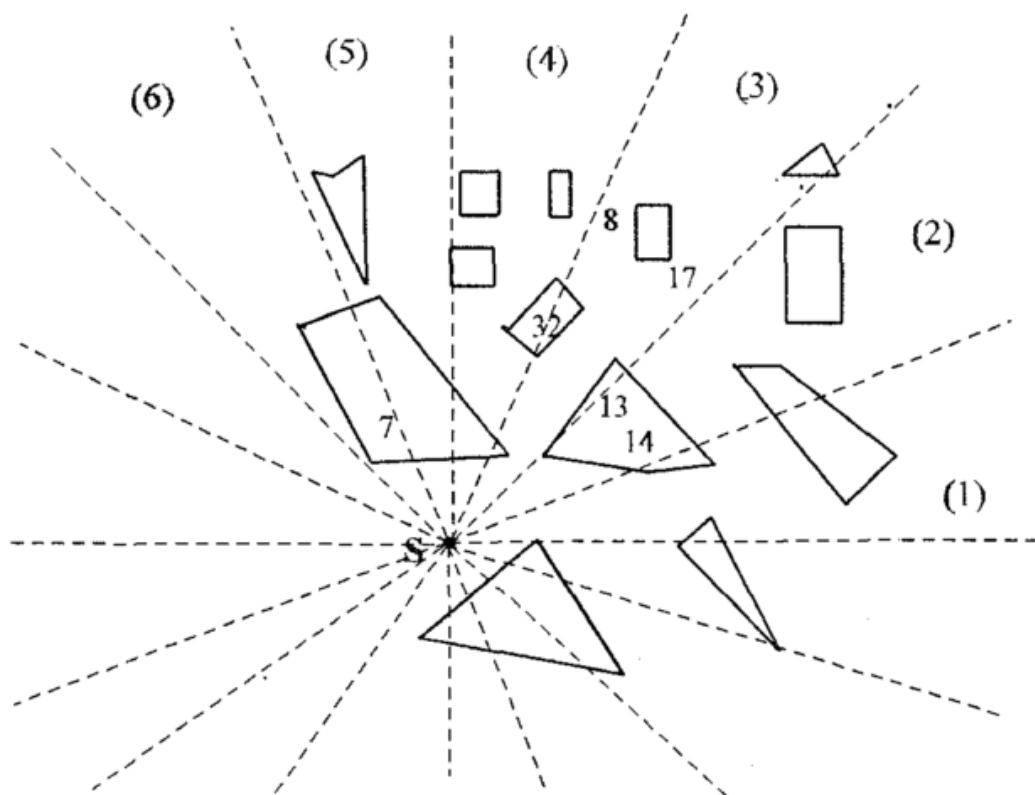


Figure 4.11 An example of how environment is divided into 2-D anxels with respect to source for LOS rays [22].

The following explains how the algorithm works to efficiently determine different types of rays.

- The distance of each wall from the source point is computed and maintained in an ascending list.
- For a LOS ray, the environment is divided into fixed width anxels with respect to a common vertex at transmitter.

- Walls are assigned the anxel index in which they reside so that only the walls associated with the anxel in which receiver is located are considered.
- The distance of the closest wall in the list is compared with the receiver distance. If receiver is closer than the first wall in the list, receiver is not shadowed and a valid LOS ray exists.
- However if the distance of closest wall is less than the receiver's distance, a shadow test is performed to see whether the receiver is shadowed by the wall. If the receiver is not shadowed, the algorithm checks the next wall in the list. This is repeated until a wall shadows the receiver or none of the walls shadow the receiver in which case the ray is deemed valid.
- In the case of reflections, only the region in front of the reflecting wall is considered. The lit region in front of the wall only is divided into anxels. Similarly, a restricted region defined by the Keller cone is considered for diffraction.
- The idea can be used for complete 3-D ray tracing by using a solid angle as anxel as shown in Figure 4.12.

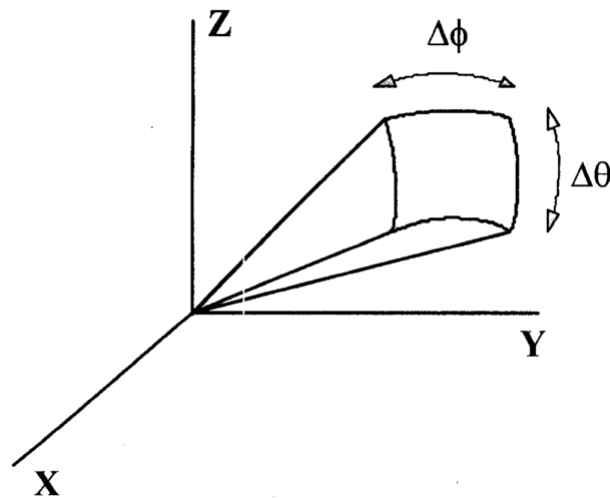


Figure 4.12 A 3-D anxel is represented by a solid angle [22].

Catedra *et al.* presented a software tool *FASPRO* with a user-friendly graphical user interface (GUI) based on the AZB algorithm. The tool inputs the building database from commonly available topographical data files for outdoor and a CAD file for indoor scenarios. The tool computes the radio coverage map and small scale channel parameters including Probability Distribution Function (PDF) and Cumulative Probability Distribution (CPD) of power and Level Crossing Rate (LCR) etc. It was shown that the model can reduce the run time by up to 90% for typical indoor applications as compared to an un-accelerated ray tracing model. The average standard deviation of error (STD)

between the simulated and measured data was about 8 dB [103]. A mathematical error in calculating the maximum angular width of an anxel in the AZB algorithm was identified by Saeidi *et al.* [105]. It was shown that the modified formulation can achieve further accuracy.

Power Threshold Method

Degli-Esposti *et al.* [106] proposed a number of efficient acceleration techniques for fast ray tracing in large urban environments. The proposed model reduces the number of objects on which ray tracing must be performed in a number of ways. Fast ray tracing is achieved as follows.

- The large urban buildings database is usually not very accurate and the building shapes can be complex. The complex and unnecessary edges of buildings can be simplified to trim the database size. This reduces the time and memory requirements of a ray tracing model.
- The buildings database is very large and not all the buildings are involved in the rays propagation. The proposed model only includes the "*active set*" of buildings that can produce valid rays [107]. All the other buildings are discarded to further reduce the database size. An example of active map in central Helsinki is shown in red in Figure [106].
- The model also proposed a "Tree-Pruning" technique to discard all the images and the associated child images for which the received power falls below a threshold. This technique allows us to discard all the rays whose power contribution is relatively small.

It was shown that the proposed acceleration techniques can achieve up to 90% time reduction in large urban environments with negligible deterioration in accuracy. The time reduction is even better for demanding applications in large environments that require higher order of ray interaction.

4.4.3 Receiver Dependant Methods

The acceleration techniques discussed so far reduce the ray tracing computations for a single receiver. In other words, the rays need to be computed independently for each receiver location. The following algorithms accelerate the ray tracing by considering a group of receiver points that lie along a line or grid. These algorithms are also termed as "*point-to-area*" ray tracing.

O'Brien *et al.* [108] proposed a sectorized approach that gives the maximum illumination zone of a wall reflection or vertical edge diffraction. A line of receivers is located in this maximum illumination zone. As it can be seen from Figure 4.14 that

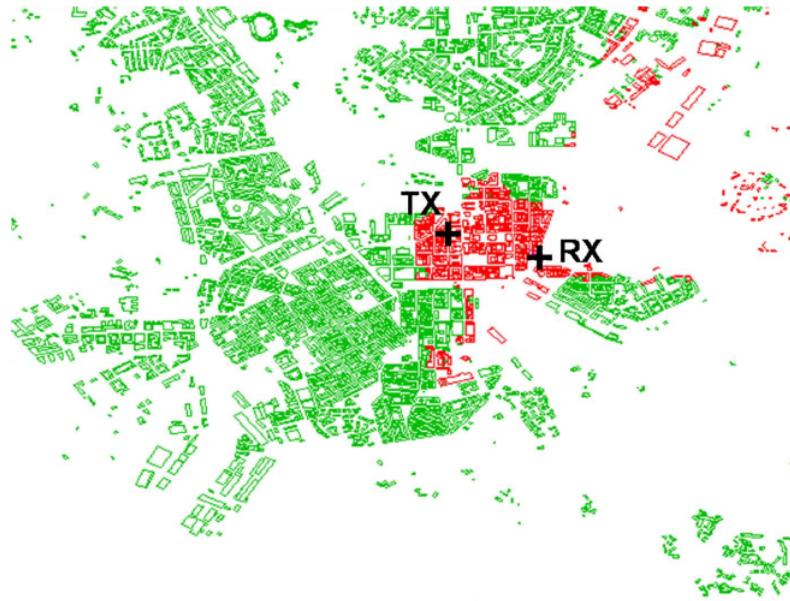


Figure 4.13 Buildings database simplification for Helsinki city [106].

sector of third order reflection image gives a range of points O_1 to O_2 that can receive a valid reflection ray. The algorithm suggests that verification of only the farthest receiver point along the zone is required thus accelerating the ray computations. A sectorized ray is also unfolded in the vertical plane to give a range of angles over which the valid ray can be received along the line of receiver points. Other similar methods for point-to-area ray tracing include *cell-scanning* by Yun *et al.* [109] and *tube-tracing* by Saeidi *et al.* [110]. These models compute the intersection of a ray tube with the receiving plane efficiently to compute the rays that arrive at a receiver grid.

A fully 3-D Intelligent Ray Launching Algorithm (IRLA) was proposed by Lai *et al.* [111, 112] for large number of pixels that supports both outdoor and indoor applications. This model is based on discretization (rasterization) of environment into a large number of cubes, each of which contains a set of information. The algorithm starts by collecting all the line of sight cubes where the secondary rays are required to launch from. Rays are launched from each line of sight cube and traced for reflections and horizontal diffractions. The algorithm also finds the ground border cubes and launches rays from transmitter to get the vertical diffraction. The algorithm can be very time efficient for simplified environment database and also supports multi-threading. A 2.5D version of the algorithm [113] was also proposed to reduce the memory requirements and achieve the higher speed at the expense of slight loss of accuracy as the terrain effects are not included.

4.4.4 2-D/2.5-D Simplification Methods

A full 3-D ray tracing model that launches rays in both inclination (θ) and azimuth (ϕ) plane is rarely used. Most of the ray tracing models apply a 2-D approach to

identify the rays. In a simple 2-D model the visibility is performed by launching rays in horizontal plane only. This is a valid approach when both the transmitter and receiver are located at the same height. This simplification is also used for indoor and microcellular applications where transmitter is well below the average building height. A hybrid 2-D to 3-D or so-called 2.5-D model considers the transmitter and receiver antenna and building heights to compute a ray in 3-D space as explained in section 5.3. An over-rooftop ray in the vertical plane is also included for a 2.5-D ray tracing model.

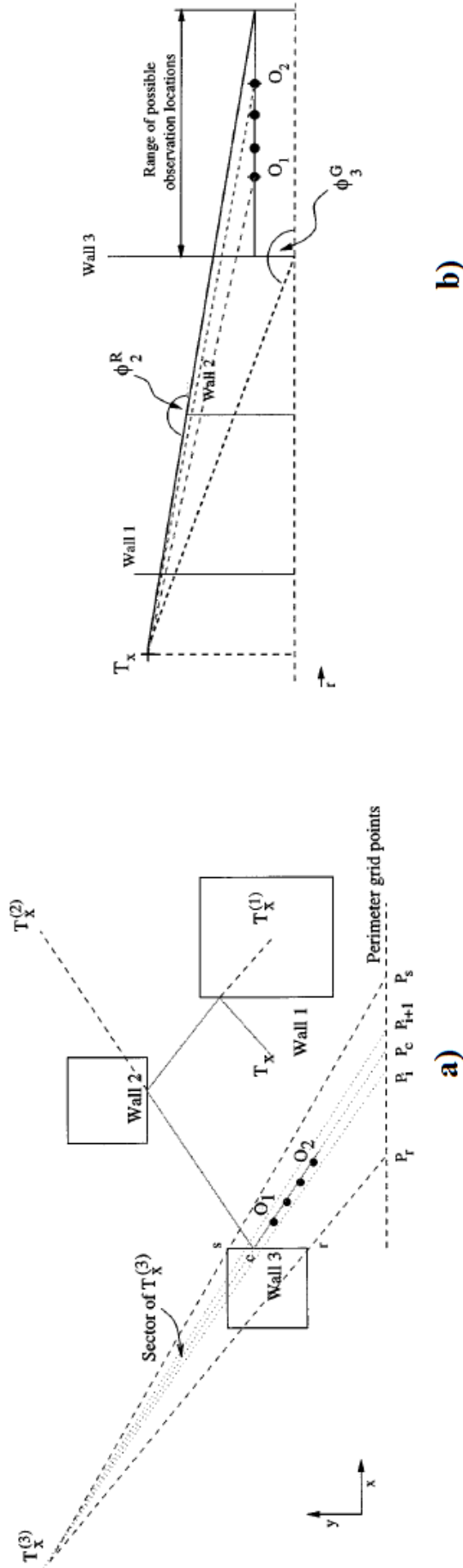


Figure 4.14 a) Sectorized approach for a group of receiver points. b) The unfolding of the ray path to give range of angles [108].

A vertical plane launch (VPL) technique was proposed by Liang *et al.* [114]. This method approximates full 3-D propagation by including wall reflections, vertical edge diffraction and over rooftop (horizontal edge) diffraction. A ray launched from the transmitter interacts with a wall and produces a reflection as well as horizontal edge diffraction. This over rooftop diffracted ray can propagate further to undergo similar mechanisms until it reaches the receiver. Figure 4.15 shows how a single ray launched from transmitter can undergo reflection, over rooftop diffraction, vertical edge diffraction and a combination of all these mechanisms.

Measurements were performed to validate the model at 900 MHz and 1900 MHz in urban environment for both a street level and rooftop level transmitter. An average standard deviation of error in measured and simulated path loss was 6.85 dB and 9.50 dB for street level and rooftop level transmitter respectively. It can be seen that the accuracy of the model is better for rooftop level transmitter as expected.

A similar model was proposed by Rossi *et al.* [115] that combines ray launching and ray tracing in two 2-D planes to give 2.5-D propagation modeling. The model can predict path loss for large urban areas with standard deviation of error below 5 dB. The model can also extract small scaling fading parameters with very good accuracy.

4.4.5 Exhaustive Pre-Processing Methods

Hoppe *et al.* [116–119] proposed an exhaustive pre-processing based ray tracing model. The basic principle of this method exploits the fact that visibility of walls and edges with each other remains the same in a given environment. The method therefore pre-computes all the possible ray-segments between walls and edges for all the receiver points. COST-231 Walfisch Ikegami model [68] is used to compute the over rooftop diffraction ray in vertical plane.

Walls are subdivided into tiles and edges are divided into segments as shown in Figure 4.16. The visibility of each tile with all the other tiles is computed during the pre-processing. The centre of each tile is considered for visibility. Further pre-processing involves creating a grid of receiver points in the propagation environment and computing the rays at each receiver point from all tiles. Projection of the angles of the rays are also computed. A similar procedure is used to determine the visibility of segment to segment and segment to tiles. Once the database has been computed, the model can compute the valid rays for any transmitter location very rapidly. Results from [116–119] showed that the pre-processing database for large urban environments can take up to 10 hours. This database is later used to compute the coverage map of full city in seconds for a given transmitter location. The average standard deviation of error in simulated path loss for Munich city was less than 7 dB.

Toscano *et al.* [120] also proposed a similar exhaustive database pre-processing for large urban environments. The model used a quadtree approach to accelerate the visibility computations between tiles and segments.

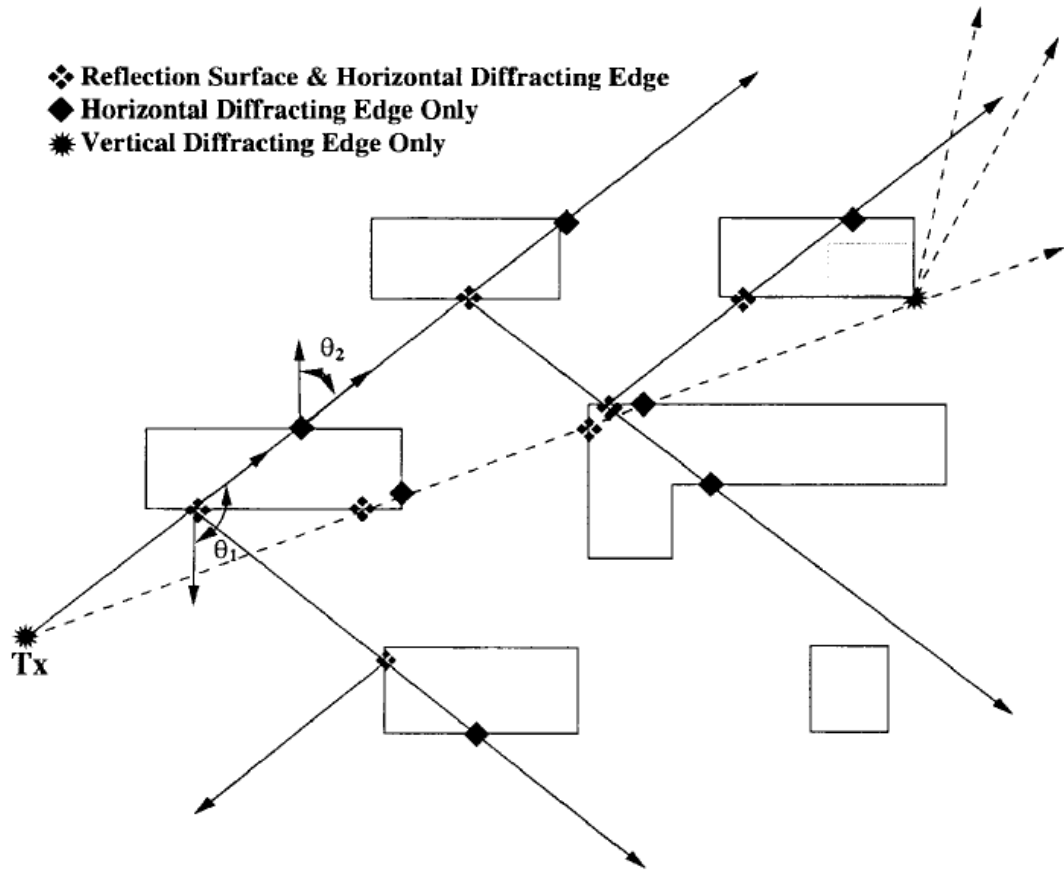


Figure 4.15 A ray launched in vertical plane can undergo different phenomena [114].

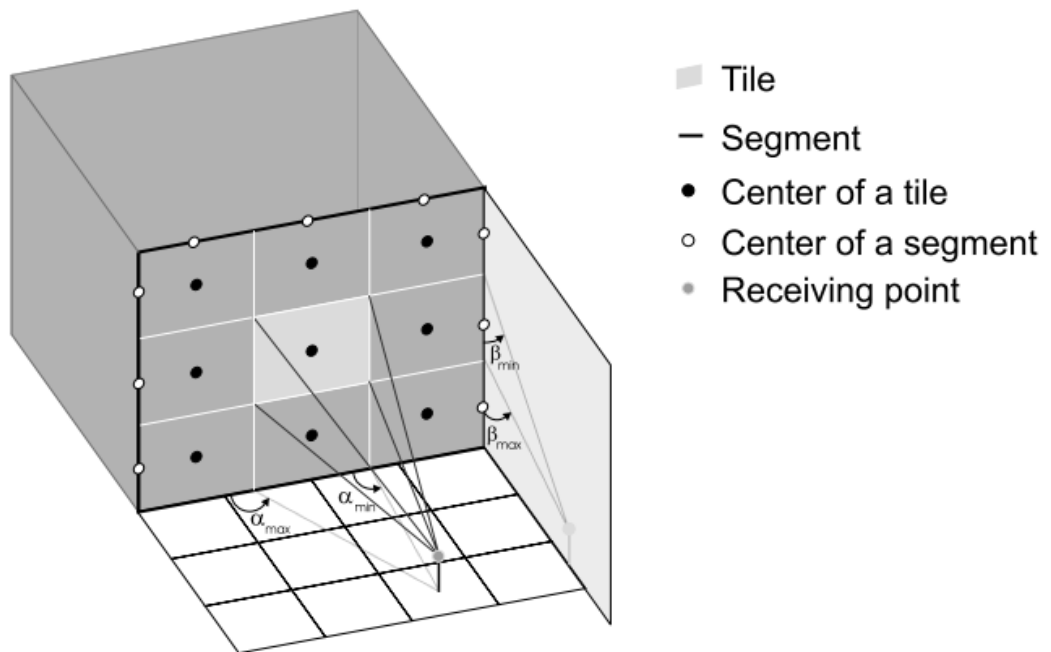


Figure 4.16 Tiles and segments on a building for extensive pre-processing [116].

4.4.6 Hybrid Methods

A ray tracing model only accounts for specular reflection and diffraction from buildings. Other propagation mechanisms such as transmission through buildings, vegetation and diffuse or rough surface scattering are usually not included in a ray tracing model. Computing higher order rays for receiver locations far away from the transmitter adds computational burden to make the ray tracing very slow. Therefore several hybrid models have been proposed that include other propagation mechanisms for accurate solution or use simple empirical models for fast results.

Diffuse scattering from objects is important for higher frequencies above 1 GHz. Several models combine diffuse scattering component with ray tracing to accurately predict the radio channel at higher frequencies. Ng *et al.* [14] proposed a radiance based rough surface scattering model to account for the diffuse scattering combined with GO model for outdoor scenarios. Reynaud *et al.* [15] proposed a similar approach for indoor channels. Tian *et al.* [16, 17] proposed a semi-deterministic approach to model the dense scattering component based on framework of graph theory coupled with an off-line ray tracing model. Scattering objects are discretized and digital maps are used to set the graph. The model gives best results at millimeter wave and TeraHertz frequencies for both indoor and outdoor channels.

Excluding the scattering from smaller objects in the environment may add inaccuracies in simulated channels. Several models use full-wave techniques to predict the scattering from smaller objects and combine it with a ray tracing model. Wang *et al.* [121] applied FDTD to study the small regions with complex discontinuities in structures and ray tracing in wide areas for indoor and outdoor-to-indoor scenarios at 2.4 GHz. Figure 4.17a shows an indoor environment taken from [121]. Scattering from lossy door and window are simulated using FDTD and combined with ray tracing. Figure 4.17b shows that without using FDTD, ray tracing provide very inaccurate results. FDTD provides a great accuracy and is only applied on small structures for fast solution. A similar work by Schiavone *et al.* [122] studied ultra-wideband (UWB) indoor channels that combines a black box approach to study scattering from smaller objects with ray tracing.

Typical ray tracing models assume homogeneous wall material for radio channel prediction. In practice walls are made up of inhomogeneous material so ray tracing cannot accurately predict transmission through walls for indoor channels. Wang *et al.* [123] proposed FDTD to compute tangential fields at wall borders using FDTD that in turn is used to send higher order rays for indoor and outdoor-to-indoor channels without loss of accuracy. Another approach proposed by Thiel *et al.* [124] studied radio wave propagation in inhomogeneous periodic wall structures using FDTD and combined the results with a ray tracing model for accurate prediction.

Kanatas *et al.* [125] made use of the observation that the $1/R^2$ dependence of path loss in direct LOS channel for urban environment is not correct. Ray tracing

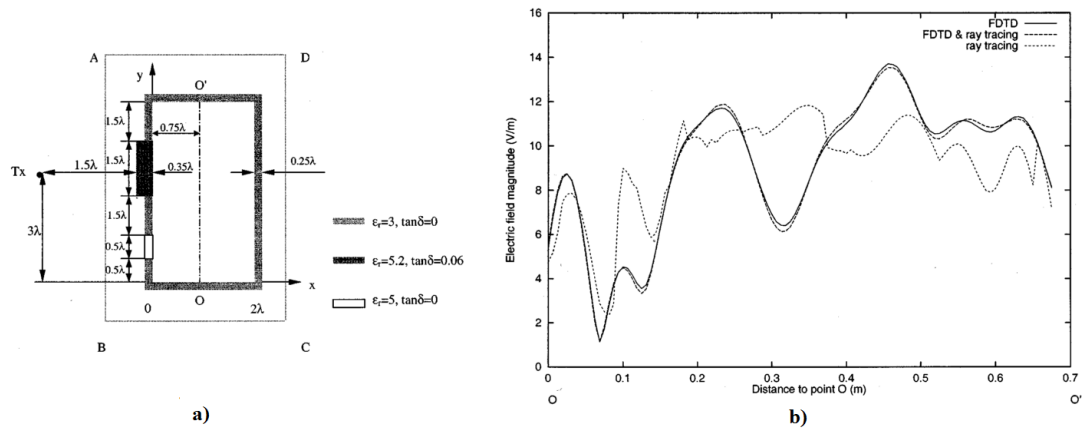


Figure 4.17 Complex discontinuities in a typical indoor environment in a) are studied with FDTD and results are combined with ray tracing to give accurate results in b) [121].

combined with a path loss correction factor was applied to match the predicted result with measurements. A run time efficient hybrid model for path loss prediction in dense urban small macro-cells with base station above rooftop is reported by Kurner *et al.* [126]. The model combines a vertical plane model (VPM) and a multipath model (MPM) that also accounts for vegetation loss. The vertical plane model accounts for the street canyon in LOS and the over-rooftop ray for NLOS scenarios. The Walfisch-Ikegami model is used in the case of uniform buildings heights and street width and the modified Deygout model is used for non-uniform building heights and street width. The multipath model includes scattering effects from closely located buildings only for receiver points within a certain distance from the base station. An empirical approach to compute outdoor-to-indoor path loss for ground floor is also presented. Coverage prediction for higher order floors using height gain formulas is included in the model. The model has been verified to give an average standard deviation of error of 7-9 dB with mean value of error less than 3 dB.

4.4.7 Interpolation Methods

Performing a ray tracing for higher resolution channel data may require a large memory and time. Several interpolation schemes have been proposed that can interpolate channel data between two points for which ray tracing data is available.

Mataga *et al.* [127] proposed the concept of a *ray entity* to store a large number of rays efficiently. A ray entity is defined as a set of rays that undergo the same series of propagation phenomena. For example, a first order reflection ray for all points between $Rx1$ and $Rx2$ along the receiver route represent a single ray entity as shown in Figure 4.18. Computing and saving all the rays for intermediate points requires a large memory. This model suggests that all the rays can equivalently be stored as a single ray entity. A ray tracing model gives the received power only on certain points along the route.

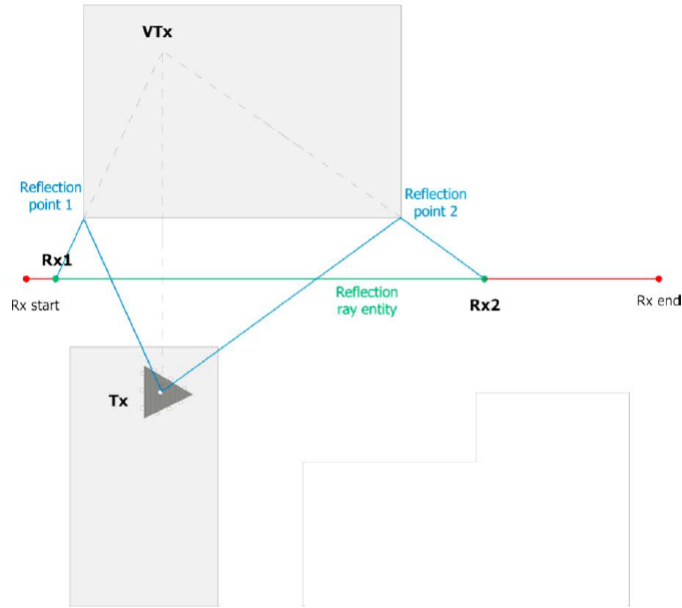


Figure 4.18 Visibility of receiver route to reflection ray entity [127].

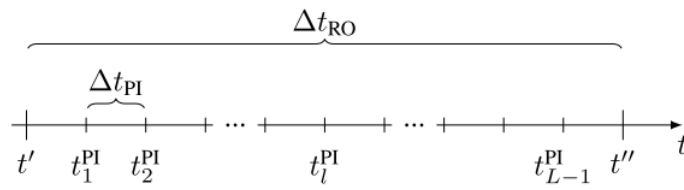


Figure 4.19 Time resolution of the ray optical model and path interpolation [128].

The model proposed a fourth and fifth degree polynomial curve fitting to interpolate the received power at intermediate points. The results show that very high resolution channel data can be obtained by post-processing the available low resolution ray tracing data. Also the ray entity representation can save the memory 11 to 12 times.

Ray tracing for inter-vehicular communications (V2V) must be performed at very high resolution to accurately estimate the fast fading characteristics of time-varying channel. Nuckelt *et al.* [128] proposed an efficient method that reduces the utilization rate of ray tracing. Ray tracing is performed at low resolution and the coefficient $a_k(t)$ of each multipath component (MPC) is computed to give the channel impulse response,

$$h(t, \tau) = \sum_{k=1}^{N_p(t)} a_k(t) \cdot e^{-j(2\pi f\tau_k(t) + \phi_k(t))} \cdot \delta(\tau - \tau_k(t))$$

where k th MPC is defined by $a_k(t)$ amplitude with $\tau_k(t)$ delay and $\phi_k(t)$ additional phase shift.

Motion vectors are defined to obtain interpolation trajectory of transmitter, receiver and all the scatterers assuming a linear acceleration of mobiles. The proposed model performs ray tracing at two intervals t' and t'' and interpolates the MPC coefficients

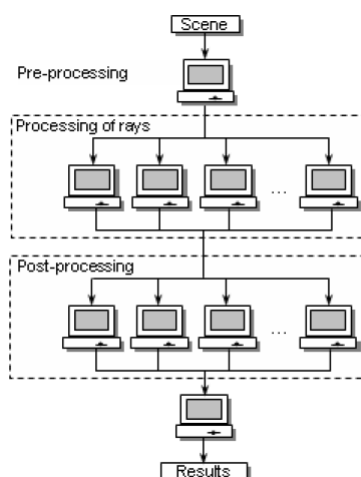


Figure 4.20 Parallel computing model for 3-D ray tracing simulations [130].

for the intermediate points as shown in Figure 4.19. Three types of MPCs have to be distinguished as follows.

- An MPC that lasts between t' and t'' is linearly interpolated for intermediate points.
- An MPC that is present at t' but is missing at t'' . multipath coefficient a_k is assumed 30 dB below the previous interval for each intermediate point.
- An MPC that is missing at t' but is present at t'' . multipath coefficient a_k is assumed 30 dB below the subsequent interval for each intermediate point.

The value of 30 dB is derived from measurements.

The model has been verified for simulation of V2V channel between two high speed vehicles in a typical urban scenario. Results show that the ray tracing simulation time can be reduced from weeks to hours with a slight degradation in accuracy using the proposed technique.

4.4.8 Parallel Computing and GPUs

A ray tracing model can be very time consuming for a complex environment if a higher order of ray interaction is computed. There has been a great interest in recent times to use parallel computation techniques and powerful graphical processing units (GPUs) to efficiently perform the ray tracing for radio wave propagation prediction. Cavalcante *et al.* [129–131] proposed several efficient techniques to parallelize 3-D ray tracing that make use of a cluster of workstations as shown in Figure 4.20. The proposed parallel computing techniques provide a simple and time efficient 3-D ray tracing model that can include diffuse scattering for further accuracy.

Graphical processing units (GPUs) are equipped with very large memory and hundreds of cores that can function in parallel. NVIDIA has introduced the well known Compute Unified Device Architecture (CUDA) that enables massive parallel processes on a GPU. NVIDIA has also made available its open source framework NVIDIA OptiX™ for developers to build exceedingly fast ray tracing applications on NVIDIA GPUs. Rick *et al.* [132] used NVIDIA 8800 GTX device that uses Single Instruction Multiple Data (SIMD) architecture. GPU acceleration along with efficient shadow algorithms are used to readily predict the radio coverage in a large urban environment. The model can compute the radio channel for more than 20 receiver points per second with an average standard deviation of error of less than 7 dB. Tan *et al.* [133] proposed a full 3-D beam tracing algorithm based on a fast k - d tree on GPU for indoor environments.

A recent trend in radio wave propagation prediction is to use commercial 3-D video game engines. These devices are equipped with a rendering engine to efficiently model the 3-D propagation scenario, a physics engine that can detect collision to compute the rays and an efficient memory management system. Several papers have been published by Navarro *et al.* [134–138] that use game engines for very fast and accurate ray tracing in both outdoor and indoor complex environments.

4.4.9 Commercial Tools

Ray tracing models provide time efficient solutions with considerable accuracy. Therefore they are widely used in industry and academia. Telecom operators use commercially available tools for radio network planning. Fast and accurate commercial tools come with attractive visual interfaces to view and analyse the radio propagation, coverage maps and other channel parameters. There has been a rise in the number of companies that offer commercial software for radio network planning. The following gives a brief introduction to some of the most common commercial tools used in both industry and academia.

Wireless Insite

Wireless Insite was developed by Remcom, a leading company providing electromagnetic simulation software to industry and academia for the past 20 years. Wireless Insite is a very powerful electromagnetic simulation tool that accurately predicts the effect of buildings, vehicles, trees etc. and terrain on radio wave propagation [139]. It provides ray tracing coupled with empirical models based solution for urban, indoor and rough terrains over a frequency range from 50 MHz to 100 GHz. This tool can provide network planning for 4G, LTE, LTE-A, 5G MIMO, Massive MIMO and indoor Wi-Fi networks. Virtual buildings, full city maps and terrain can be constructed using a GUI based editor or imported from popular file extensions such as DXF, *shapefile* etc. Both

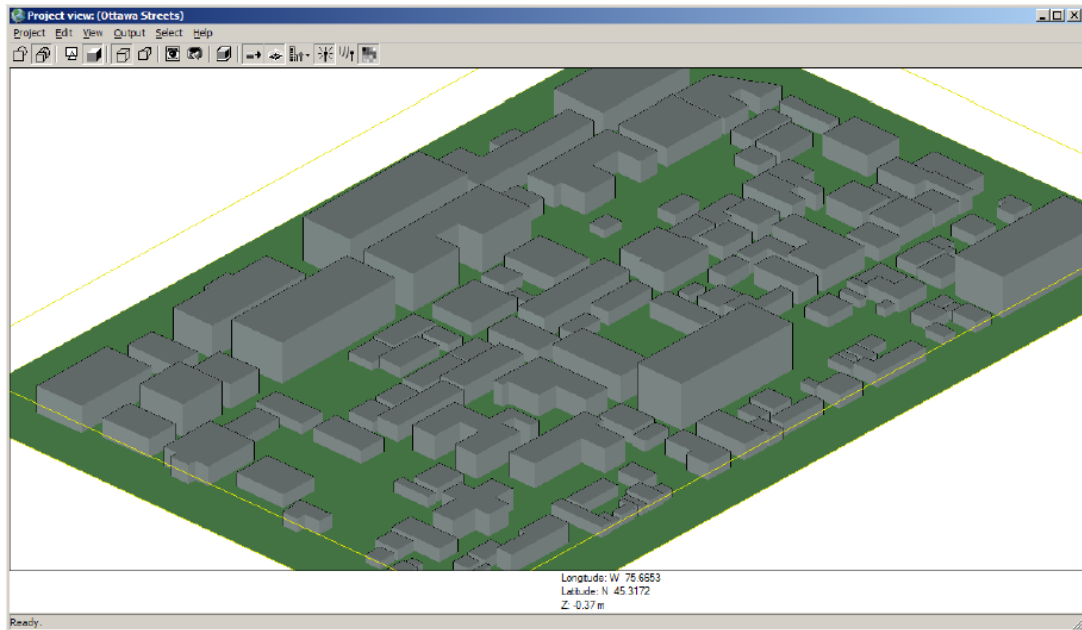


Figure 4.21 Importing buildings database in Wireless Insite [139].

urban and indoor furniture can be imported from built-in libraries with configurable electrical characteristics. The model also supports digital maps and aerial imagery. It can provide GPU application as well as multi-threaded CPU acceleration. Transmitter and receiver antennas radiation pattern can be specified. The receiver can be a single point or a mobile route in a given environment. The model supports many channel models including ray tracing, free-space, urban canyon, vertical plane, COST Hata, Walfisch-Ikegami and COST modified building penetration model for outdoor-to-indoor propagation.

WinProp

WinProp was originally designed by AWE Communications limited that was later acquired by Altair HyperWorks in 2016. HyperWorks provides comprehensive simulation platforms for industry to optimize the product design. One of the most popular electromagnetic solver used in industry and academia, FEKO is designed by Altair HyperWorks. WinProp has been added to FEKO as a radio propagation prediction tool [140]. This tool is based on full 3-D ray tracing that make use of exhaustive pre-processing techniques proposed by Hoppe *et al.* [116–119] as discussed in section 4.4.5.

WinProp engine includes empirical, semi-empirical, ray tracing and a unique Dominant Path Model (DPM) [141]. This tool supports a wide range of propagation scenarios including indoor, urban, rural, vehicular, tunnels and underground as well as satellite communications. The model also supports different database inputs and produces all channel data output for network planning of standard air interfaces.

WaveSight

WaveSight radio prediction tool is a product of Wavecall Inc. The tool is already fully integrated in industrial network planning tools and can be used as stand-alone as well [142]. This tool applies ray tracing using Uniform Theory of Diffraction (UTD) to accurately compute radio coverage and channel parameters in complex urban and rural areas. The model is widely used for radio network planning in TDMA, GSM, GPRS, CDMA, UMTS and WiMAX networks for micro and macro-cells.

4.4.10 Other Methods

Most of the traditional techniques for ray tracing have been discussed earlier. However, some other methods have also been reported in literature. One such approach was proposed by Chen *et al.* [143]. The technique applies *progressive and approximate techniques* to predict the radio coverage and gives the user control to trade-off between accuracy and run times. The algorithm computes a smaller number of ray paths and gives the results to the user for feedback. The user decides to add more rays if the results are not accurate enough. The process is repeated until a considerable accuracy is achieved.

Another non-traditional approach was proposed by Moreno *et al.* [144] that make use of well known Binary Particle Swarm Optimization (BPSO) algorithm for indoor WLAN network design. The model computes received power for a set of access points (APs) to be deployed using ray tracing. A fitness function is defined that optimizes the radio coverage while minimising the number of APs to save the computation cost. Azpilicueta *et al.* [145] combined 3-D ray launching with Neural Networks to reduce the simulation time by up to 80% for indoor networks.

4.5 Limitations of Ray Tracing Models

The following factors must always be considered before a ray tracing model is applied for radio propagation prediction.

1. Ray tracing is a high frequency asymptotic solution of Maxwell's equations. Therefore ray tracing is expected to produce accurate results at higher frequencies. Prediction error increases greatly at lower frequencies. Nonetheless, ray tracing is considerably accurate at UHF frequencies for network planning.
2. Computing a higher order of rays gives better results at the expense of higher run time. There is always a trade-off between the accuracy and speed of a ray tracing model.
3. Inaccuracies in buildings database increases prediction errors [24, 25, 106]. Database simplification can reduce inaccuracies [107].

4. Reflection and diffraction are always considered in a typical outdoor ray tracing model. Radio waves can easily penetrate into buildings at lower frequencies of the order of 100s of MHz [146]. Transmission through buildings can still be significant at UHF frequencies when no other propagation phenomena is available at certain receiver locations in urban scenarios [147, 26].
5. At higher frequencies of the order of 10s of GHz, scattering from building walls due to surface roughness becomes significant and must be included in the ray tracing model for accurate prediction [148].
6. In micro-cellular environments where transmitter is well below average building height, lateral propagation is more important [149].
7. In macro-cellular environments where the transmitter is located above the average building height, vertical over rooftop propagation is significant [149]. Lateral propagation is still important in a radius of 300-500m from base station [126].
8. A suitable over rooftop model must be included in ray tracing for a macro-cell. Although the knife-edge models are quite accurate, heuristic UTD over rooftop models have been proposed that include slope diffraction for very accurate results [150–152].

4.6 Future Trends in Ray Tracing

Recent years have seen a tremendous increase in the use of ray tracing for radio networks planning and this trend seems set to continue in future. Being a high-frequency phenomenon makes ray tracing tool a better candidate for future millimeter wave channel modeling. The accuracy of the buildings database and terrain properties is critical for prediction accuracy. The availability of geo-spatial data from services such as Google Maps has made it possible to get very accurate high resolution buildings and terrain data. There is a great deal of interest to develop ray tracing tools with the capability to import the environment data from Google Maps and Google Earth [153–156]. With the development of high speed graphical processing units and game engines, future ray tracing models will provide real time radio channel modeling capability. Technologies such as big data and machine learning will be embedded into ray tracing tools for intelligent and accurate channel predictions [89]. Ray tracing models will be an essential part of future wireless communication systems [157].

Conclusion

A study of over one hundred references related to radio channel and coverage models including empirical, theoretical and site-specific (coverage prediction models) is pre-

sented in this chapter. A survey of all (known so far by the author) the efficient ray tracing acceleration techniques is carried out to establish the limitations and trends in future ray tracing models. There is always a trade-off between the speed and accuracy of ray tracing models. The following three issues define the limitation of a ray tracing model. Firstly, the modeling of radio propagation environment. The availability of accurate buildings database and urban furniture is critical to the accuracy of a ray tracing model. Secondly, the modeling of radio propagation mechanisms. A typical ray tracing model computes specular wall reflections and vertical edge diffraction. The over rooftop diffraction and scattering from urban furniture is significant in outdoor environments. The inclusion of all (or most significant) propagation mechanisms improves the accuracy of ray tracing models. Thirdly, the underpinning speed up technique to accelerate the ray tracing computations. Most, if not all, of the ray tracing acceleration techniques are based on some pre-processing. If a speed up technique is based on some over-simplification or an interpolation of pre-determined computations, the accuracy of channel prediction will be compromised. Despite all the limitations, the ray tracing models are appropriate candidate for future millimeter wave channel modeling. It is expected that the ray tracing tools will be an essential part of future radio systems.

Chapter 5

Ray Tracing Acceleration for a Mobile Receiver

A ray tracing model predicts the radio channel between the transmitter and receiver. A typical outdoor propagation model requires that the radio channel must be predicted between a fixed transmitter and a mobile receiver for point-to-multipoint scenarios. Most of the ray tracing acceleration techniques speed up the ray computations for point-to-point case. However speed up techniques have been reported in literature [108–110] for point-to-multipoint scenarios as discussed in section 4.4.3. This chapter is focused on ray tracing acceleration for a mobile receiver. An efficient pre-processing technique that make use of so-called *lit* and *shadow polygons* is introduced. The lit and shadow regions define the horizontal area illuminated or shadowed by a source respectively. A fast ray-object intersection test is developed to compute the valid rays at a given receiver location. This model is used to compute path loss in an urban environment and the results are compared against measured data. The mapping of lit and shadow polygons to the environment is proposed to further accelerate the ray tracing computations. This model forms the basis of a novel ray tracing algorithm that computes valid rays for a mobile receiver efficiently. The efficient algorithms presented in this chapter have been published in [158–161]. A flow chart of the ray tracing algorithm developed in this chapter is shown in Figure 5.1. The different sections of the model will be explained later in the remainder of this chapter.

5.1 Introduction

A visibility algorithm is applied to create a list of walls and vertical edges that are visible to the transmitter. These visible walls and the vertical edges may produce the first order rays and form the first order images. The walls and vertical edges visible to the first order images may produce the second order rays and form the second order images and so on. A recursive algorithm computes the image-tree for the required order of ray interaction. Each node on the image-tree represents a wall or an edge visible to its parent image. The term "node" or "visible node" will therefore be used to represent a wall or an edge visible to an image in the following discussions. The ray tracing algorithm performs a ray-object intersection test on the segments connecting entries on the image-tree to check whether it makes a valid ray between the transmitter and the receiver. This ray-object intersection test for a first order reflection ray is performed by first connecting the receiver to a first order reflection image through each first order visible wall on the image-tree. If no building is intersected by this ray a ray-segment is formed by connecting the receiver and the reflection point. This intersection test is also performed for the ray-segment between the reflection point and the transmitter. A valid reflection ray in the 2-D plane is obtained if this ray-segment is also not obstructed by any building in the environment.

A naive ray tracing algorithm validates a ray-segment by performing a ray-object intersection test between, the line connecting the receiver or transmitter to the image point through the visible wall or vertical edge, with all the buildings in the environment. Agelet *et al.* [56] proposed a bounding box technique with quad-tree approach in which the coverage area is divided into quadrants and buildings are mapped to the quadrant in which they reside. This method first determines the quadrants or grid-squares intercepted by the ray-segment under test. The ray-object intersection test is accelerated as only a small number of buildings, within the grid-squares intercepted by the ray-segment, need to be tested. [23, 101] proposed the concept of an *accurate illumination zone* or the *lit region* of an image. This method takes into account all the faces and edges visible to a face or edge illuminated by an image and forms the exact region where a valid ray will exist. The image-tree does not grow exponentially as the illumination region shrinks for higher order reflection rays. This technique significantly reduces the size of the image-tree and the ray-object intersection test is replaced by a simple check as explained in the previous chapter section 4.4.2. However determination of accurate illumination zones may not be straightforward for complex urban environments.

A simple and efficient pre-processing technique based on lit and shadow polygons is presented in the next section.

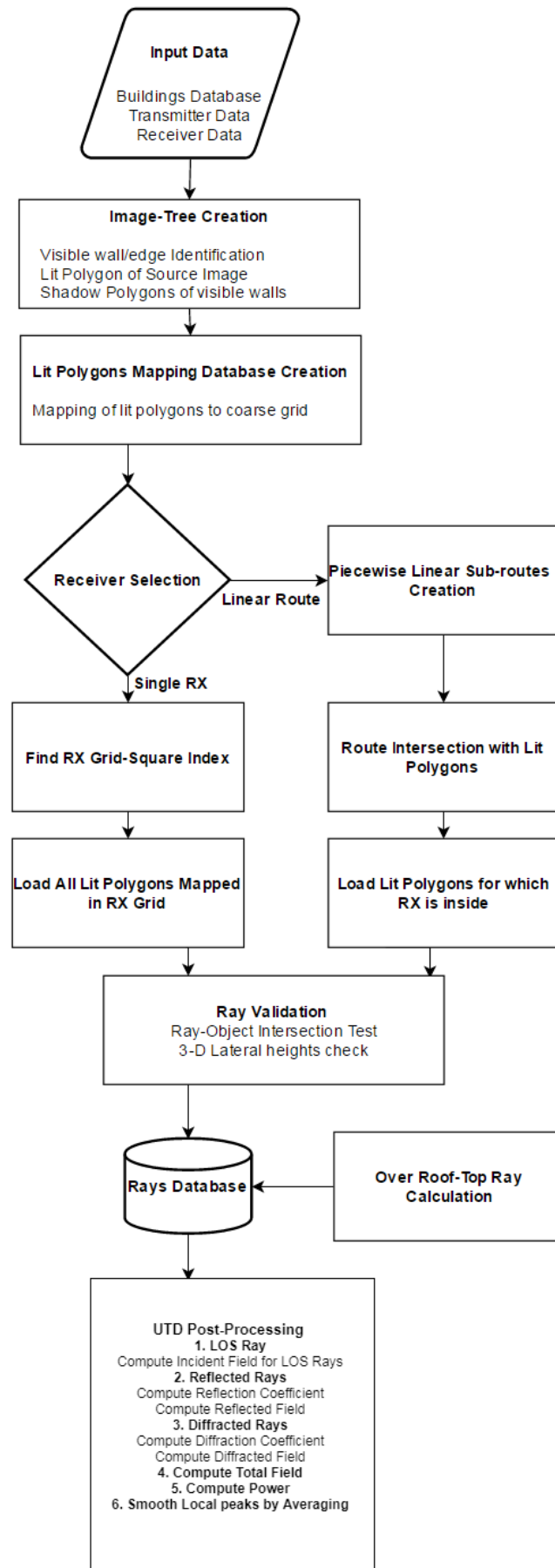


Figure 5.1 Flow Chart of Ray-tracing Algorithm for Mobile Receiver

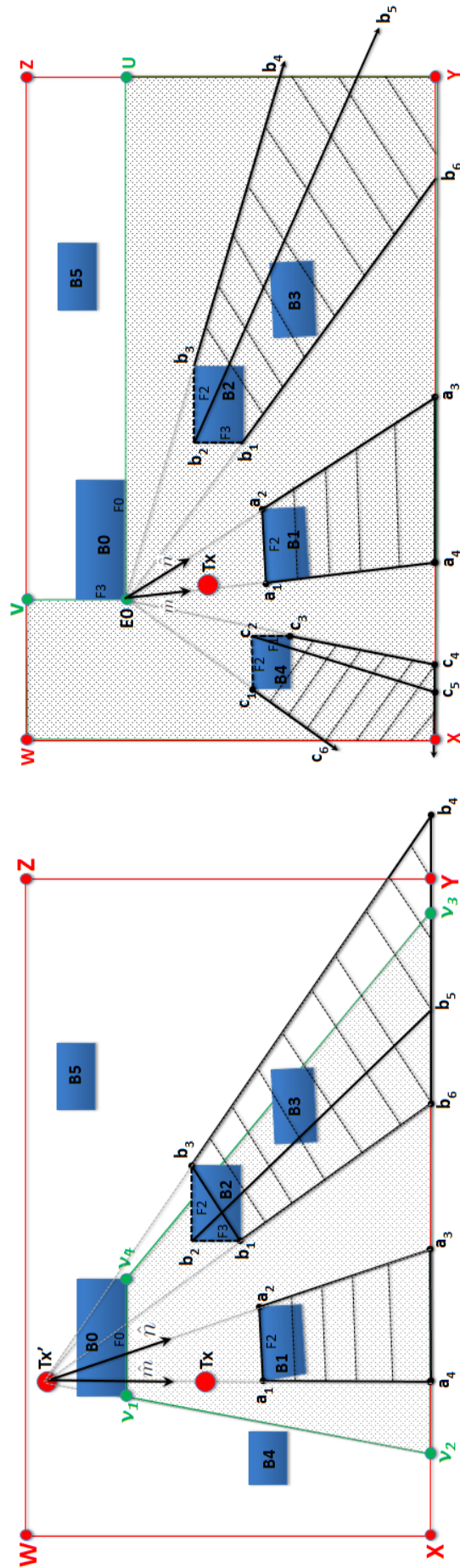
5.2 Lit and Shadow Polygons

A ray from the transmitter reflects or diffracts after interaction with a first order visible wall and edge respectively. The reflected and diffracted rays propagate into a restricted region that can be determined by the *image point*. The image point for wall reflection is given by image theory, while the reference point for vertical edge diffraction is the diffracting edge itself.

A maximum region can be identified in the propagation environment where the rays can propagate after interaction with a wall or edge. A *lit polygon* of an image is defined as the maximum horizontal area within which it is possible for the reflected or diffracted rays associated with an image to propagate *if there were no other buildings in the environment*. However in practice there are buildings that block the reflected and diffracted rays to form shadow regions. The shadow areas formed by buildings in the lit polygon of an image are represented by the *shadow polygons*.

The formation of lit polygon for a reflection image and the corresponding shadow polygons can be explained with the help of Figure 5.2a. A top view of a simple environment with six buildings is shown. W, X, Y and Z are coverage boundary vertices. Face $F0$ of building $B0$ is visible to transmitter TX . We are interested to find the lit polygon and its corresponding shadow polygons for the reflection image associated with $F0$. An image point TX' is identified using image theory as shown. The unit vectors from the image point towards both the edges of $F0$ can be drawn. These unit vectors can be extended up to (or beyond) the boundary lines of environment so that the region enclosed by the vertices v_1, v_2, v_3 and v_4 represents the *lit region* for the first order wall reflection. The polygon formed by these vertices is the lit polygon for the reflection image. One face of building $B1$ is visible to the first order wall reflection image and $B1$ lies completely within the lit region. The building $B2$ has one face completely and another face partially visible so that $B2$ lies partially within the lit region.

These visible buildings within the lit region will block the first order reflection rays from face $F0$ to form shadow regions. The hatched polygons extending beyond the buildings $B1$ and $B2$ represents the shadow regions for the first order reflection rays. The unit vectors from the image point TX' towards both the vertices a_1 and a_2 of visible face $F2$ of $B1$ are shown as \hat{m} and \hat{n} in figure 5.2a. The shadow polygon is formed by extending these unit vectors from visible face vertices, a_1 and a_2 , to the coverage boundary at points, a_4 and a_3 , respectively. The shadow region for $B2$ that has more than one faces within lit region can be accurately described by the polygon formed by vertices b_1, b_2, b_3, b_4 and b_6 as shown. This shadow region can be represented by two shadow polygons for both visible faces $F2$ and $F3$ and is computed in a similar way as that for $B1$ by defining unit vectors from TX' to edge vertices. A part of shadow polygon for the partially visible face of $B2$ lies outside the lit polygon. This does not affect the ray-segment validation test as will be discussed later. Building $B3$ is not



(a) Lit and shadow polygons for a wall reflection

(b) Lit and shadow polygons for an edge diffraction

Figure 5.2 Lit and shadow polygons

visible to the reflection image as it lies completely within the shadow region formed by $B2$.

The lit polygon and the associated shadow regions for a diffraction image can be explained with the help of Figure 5.2b. Diffraction from a vertical edge spreads the signal in all directions exterior to the building so that the visibility region of diffraction from the edge E_0 consists of all the coverage area except the region defined by two faces that form the diffracting edge. In other words, the lit polygon for the diffraction image is formed by the vertices E_0, V, W, X, Y and U as shown. The orientation of the vertical faces that form the diffracting edge can produce irregular shapes for the lit polygon. For simplification the lit polygon for diffraction image is defined by the complimentary polygon with only four vertices E_0, V, Z and U . The visible buildings within the lit region form the shadow regions for the diffraction image. Shadow polygons are computed in a similar way as that for a reflection image. However the unit vectors are drawn from the diffracting edge point.

A recursive algorithm is developed to compute all the lit and shadow polygons for the required order of ray interaction. The transmitter, considered as the zeroth order image, has an associated lit polygon defined by the coverage boundary vertices. A horizontal polar sweep algorithm [56] computes the first order visible faces and vertical edges. The first order visible faces define the shadow polygons for zeroth order image the transmitter. Then lit polygons are defined for all the first order visible faces and edges. A visibility algorithm is performed in the restricted region of each first order image to find the second order visible faces and edges. The visible faces within the lit polygon of first order images define the shadow polygons for the first order images and so on.

Algorithm 1 Image tree and lit/shadow polygons database creation

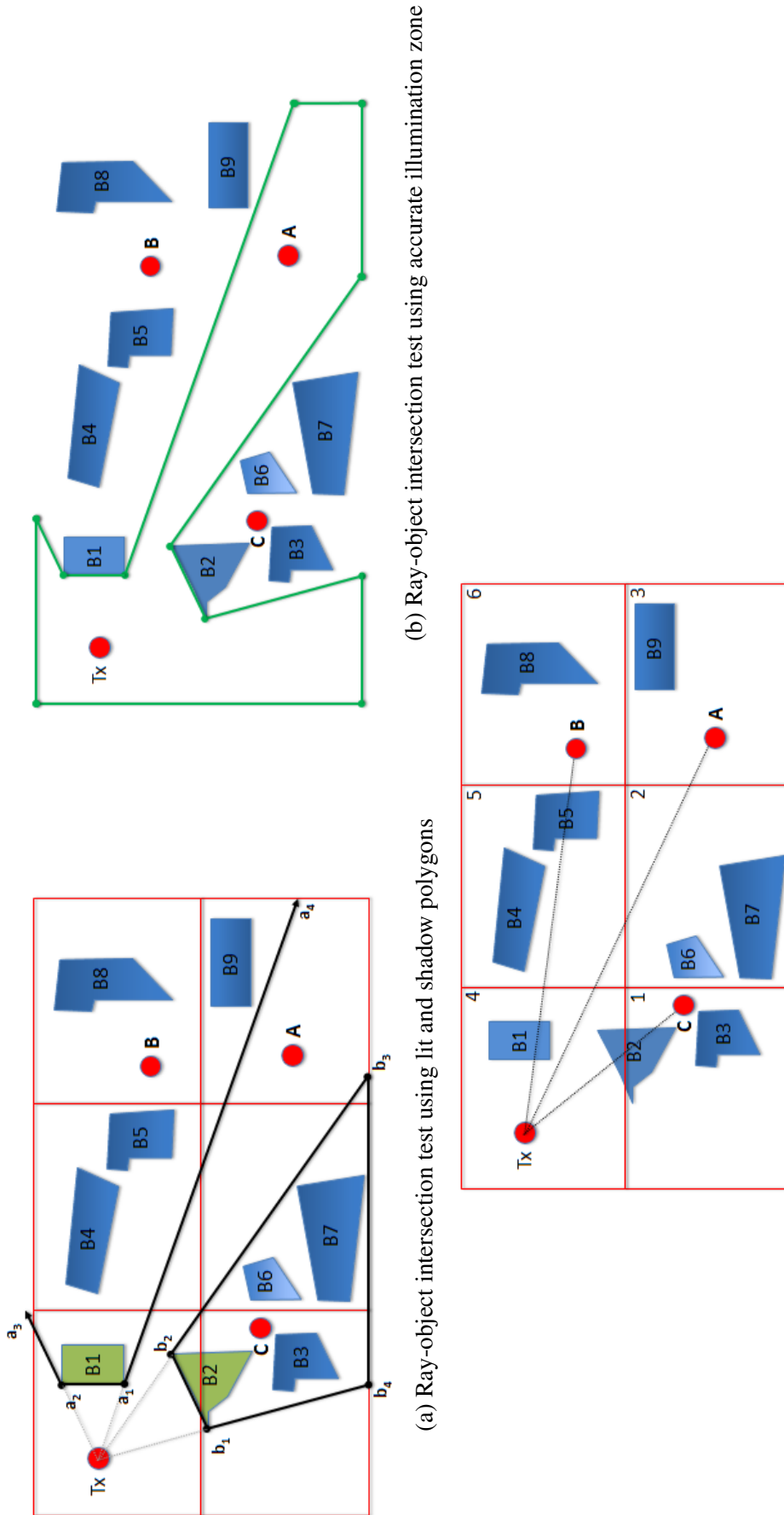
```
Input Data: TX location, building data;  
Output Data: Image tree and Lit/shadow polygons database;  
image-level = 0;  
number-of-images = 1;  
image-list = [TX];  
for number-of-images in image-list do  
    identify lit polygons;  
    identify visible faces and edges in lit polygons;  
    identify shadow polygons;  
    image-level++;  
    populate image-list;
```

5.3 Fast Ray-Object Intersection Test

An efficient ray tracing algorithm requires a fast ray-object intersection test to accelerate the ray-segments validation. The concept of lit and shadow polygons introduced in the previous section is used to achieve this objective. Recall that a lit polygon of an image represents the maximum coverage area within which the rays associated with that image can propagate. The shadow polygons represent the shadow regions formed due to obstructions within a lit polygon. It can be deduced that subtracting all the shadow polygons from a lit polygon will give the exact region where a valid ray-segment can exist. Although it may seem similar to the accurate illumination zone method [23, 101] the approach presented here is simple and can be faster in certain scenarios as discussed in the following. Moreover the use of lit and shadow polygon allows us to determine the valid ray segments efficiently for a mobile receiver as discussed later in the chapter.

The fast ray-object intersection test is explained with the help of Figure 5.3a. A LOS ray can be considered as a zeroth order ray as it is a direct ray between the receiver and the zeroth order image transmitter (TX). There are nine buildings in the environment and we are interested to find if a valid LOS ray is received at three receiver points A , B and C . One face of both the buildings $B1$ and $B2$ are visible to the transmitter TX . These visible buildings form shadow polygons as shown. The exact location of vertices a_3 and a_4 for the shadow polygon of building $B1$ is chosen such that these points lie far away from the coverage boundary. The line connecting a_3 and a_4 must not intersect any area within the environment to make sure that all the buildings in the shadow region lie inside the shadow polygon.

A receiver point will receive a valid LOS ray if it does not lie in the shadow regions formed by buildings that are visible to the transmitter. In other words, it must lie outside both the shadow polygons of buildings $B1$ and $B2$. Thus its ray-segment can be validated by simply checking if the receiver point is not inside any of the shadow polygons. Both the lit and shadow polygons are defined by four vertices so that the internal angles are always less than π radians that makes these polygons *convex*. There are many efficient methods to determine whether a 2-D point lies inside or outside a convex polygon [162]. One such method is explained with the help of Figure 5.4a. First consider a point X that lies inside the convex polygon with vertices a_1, a_2, a_3 and a_4 . $a_1\vec{a}_2$ represents the vector from a_1 pointing towards a_2 , and $a_1\vec{X}$ represents the vector from a_1 pointing towards the 2-D point X . The cross product $a_1\vec{a}_2 \times a_1\vec{X}$ points into the page as shown. The method also computes cross products $a_2\vec{a}_3 \times a_2\vec{X}$, $a_3\vec{a}_4 \times a_3\vec{X}$ and $a_4\vec{a}_1 \times a_4\vec{X}$ for all the vertices of convex polygon in a cyclic way, anti-clockwise in this case. For the point X to lie *inside* the convex polygon all the cross products must point in the same direction, into the page in this case. Now consider the case shown in Figure 5.4b where X is located outside the convex polygon. It can be seen that the cross product $a_2\vec{a}_3 \times a_2\vec{X}$ points out of the page while cross products for the rest of the



(b) Ray-object intersection test using accurate illumination zone

(a) Ray-object intersection test using lit and shadow polygons

(c) Ray-object intersection test using space division

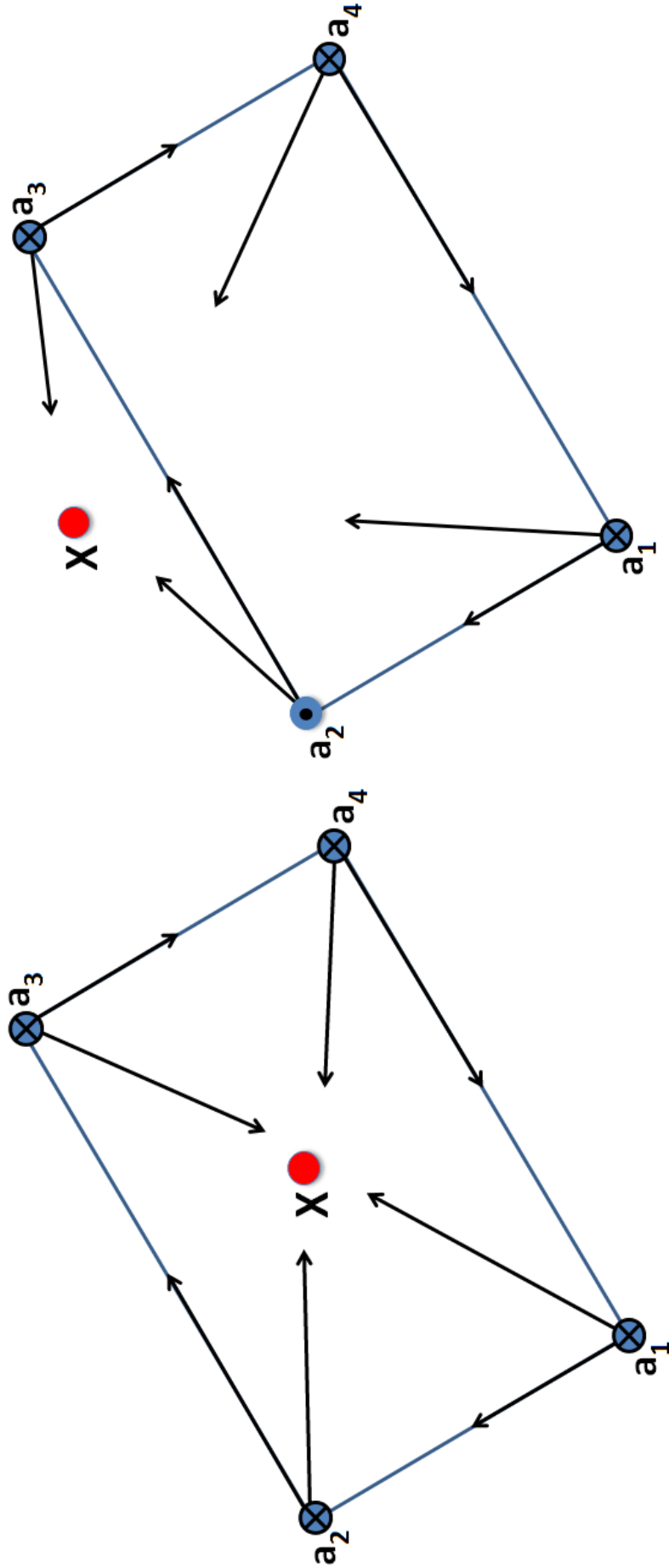
Figure 5.3 Ray-object intersection test for ray validation [158].

vertices point into the page. An algorithm can be developed that keeps checking the direction vector after each cross product and stops immediately if one of the vector points in the opposite direction. Thus a maximum of four cross products are required to validate whether a 2-D point lies inside a shadow polygon.

Going back to the example in Figure 5.3, the algorithm checks all the receiver points A , B and C if they are not located inside either of the shadow polygons of buildings $B1$ and $B2$. It is assumed that the algorithm first checks for the shadow polygon associated with building $B1$ followed by the shadow polygon associated with building $B2$. The receiver point B lies inside the shadow polygon associated with building $B1$ and requires a maximum of four cross product checks before it fails the test. The receiver point C lies inside the shadow polygon formed by the building $B2$ and fails the test before a maximum of eight cross product checks are performed. The receiver point A requires eight cross product checks and does not fail the test as it is located outside both the shadow polygons. Thus a valid LOS ray exists only for the receiver point A .

The accurate illumination zone of the transmitter, for the same problem as above, has also been determined [23, 101]. The illumination zone for this simple case consists of a polygon with 11 sides as shown in the figure 5.3b. The polygon shown here is a *concave polygon* as at least one of the interior angles is higher than π radians. A simple test such as for the convex polygon in figure 5.4 cannot be implemented for a concave polygon. A simple method is to draw a long horizontal line from the point and check the number of sides that intersect with this line. Zero or even number of intersections will indicate that the point is outside the polygon while the odd number of intersections will indicate that the point is inside the concave polygon. There are some other techniques as well. All the methods that determine if a 2-D point is inside a concave polygon require a number of intersection tests equal to the number of sides of the polygon. Thus at least 11 computations will be required for all the points A , B and C to validate LOS ray as compared to 4, 8 and 8 cross product checks using the proposed method. Therefore the technique proposed in this work that makes use of lit and shadow polygons is simple and faster. Although the comparison performed here is for a simple example, the proposed technique will be much simpler and faster for a vertical edge diffraction in a complex urban environment.

The proposed method is also compared with a space division method such as bounding box with quad-tree approach [56] to determine the direct LOS ray for the same example and is shown in Figure 5.3c. The environment is divided into rectangular grid-squares and the buildings are mapped to the grids in which they reside. To determine if a direct LOS ray exist between a receiver point and the transmitter, a line is drawn from the receiver to TX . Only the buildings within the grid-squares intersected by this line are tested for ray-object intersection test. The RX point C intersects grids 1 and 4 only. Intersection test with all the sides of buildings $B1$, $B2$ and $B3$ are required to validate the direct LOS ray between TX and receiver point C . Likewise, buildings



(a) All cross products are pointing in the same direction

(b) One cross product is in the opposite direction

Figure 5.4 Validation test of a 2-D point inside a convex polygon

$B1, B2, B4, B5$ and $B8$ in grid-squares 4, 5 and 6 are tested for the receiver point B . Seven buildings located in grid-squares 2, 3, 4 and 5 are tested for receiver point A . This method is faster than the naive ray tracing algorithm in which all the buildings in the environment are tested to validate a ray. However, this method can be inefficient for large separation between the transmitter and the receiver in dense urban environments.

The example given above describes the ray validation for a simple LOS ray. A higher order ray needs to be tested for each of its constituent ray-segment. The proposed ray-object intersection test for an N th order ray can be described as follows.

1. Receiver RX is tested for a valid ray-segment between the receiver and the N th order image. For an N th order ray-segment to be valid, the algorithm checks that receiver point is inside the lit polygon of the N th order image and outside of all the shadow polygons associated with the N th order image.
2. Since a complementary polygon is used for lit region representation in diffraction images, receiver point must lie outside of the lit polygon as well as outside of all the shadow polygons for a valid diffraction.
3. In case a valid ray-segment is found between RX and N th order image, the reflection or diffraction point becomes an intermediate receiver point. This reflection or diffraction point is tested for a valid ray-segment to its parent $(N - 1)$ th order image.
4. This algorithm is repeated until the ray-segment between 1st order image and transmitter TX is validated as discussed for the example above. If any ray-segment fails the object-intersection test, the algorithm immediately stops and moves on to the next image in the image-tree.
5. The ray-segment validation is performed in the horizontal plane. Antenna and building heights are then checked to produce a valid ray in 3-D space.

The proposed method is a simple and fast approach to validate the rays. Instead of creating one complex illumination zone or checking a large number of buildings, the proposed method creates a lit polygon and a set of associated shadow polygons for each image in the image-tree. Although the accurate illumination zone approach is simple and fast for higher order reflection images, the creation of illumination zones is not straightforward. The illumination zone for transmitter and diffraction images become very complex for dense urban environments. The lit and shadow polygons always have four sides only and are simple to use. This 2-D polygons representation allows to easily determine the location of a receiver in region of interest, lit or shadow zone.

Algorithm 2 Ray-Object Intersection Test for Ray Validation

Input Data: TX location, RX location, building data, lit and shadow polygons database;

Output Data: Valid rays database;

```

for (i = 0; i < number_of_images; i++) do
    index = i;
    image = image_list[index];
    N = Image order for image;
    test_point = RX location;
    ray_is_valid = TRUE;
    for (j = N; (j ≥ 0) ∧ (ray_is_valid); j = j - 1) do
        lit_polygon = lit_polygon_list[index];
        m = number of shadow polygons for image;
        if outside_polygon(lit_polygon, test_point) then
            ray_is_valid = FALSE;
        for (k = 0; (k ≤ m) ∧ (ray_is_valid); k++) do
            shadow_polygon = shadow_polygons_list[index][k];
            if inside_polygon(shadow_polygon, test_point) then
                ray_is_valid = FALSE;
        if ray_is_valid then
            intersection_point = find_ray_intersection(test_point, image);
            make_ray_segment(test_point, intersection_point);
            test_point = intersection_point;
            index = Parent image index of image;
            image = image_list[index];
    if ray_is_valid then
        ray_2d = combine_ray_segments();
        validate_in_3d(ray_2d);
    populate rays database;

```

5.4 Performance of Initial Model

A ray tracing model has been developed that makes use of lit and shadow polygons and performs the ray-object intersection test as described above. The ray tracing model is used to predict the path loss in Munich city and the results are compared with the measured data. The following gives an overview of the measured data.

5.4.1 Measured Data

The measurement data was collected in downtown Munich by German GSM network operator Mannesmann Mofilfunk GmbH for the COST 231 Action. The COST 231 project was implemented under COST (European CO-operation in the field of Scientific and Technical research), a framework for the implementation of applied research projects in Europe. This project proposed the actions required for the development of 3G mobile services at the start of millenium. Several measurement campaigns were performed as part of this project for indoor as well as outdoor micro and macro cells. A detailed report was published in 1999 [163]. Munich city measurements are frequently used by the research community to compare the accuracy of outdoor propagation models.

The test site area is $2400\text{m} \times 3400\text{m}$ and the vector data of 2088 buildings is provided. The chosen site has a fairly flat ground so that the topography is not usually considered, although the data is available. The measurements are performed along three routes METRO-200, METRO-201 and METRO-202. The length of the routes 200, 201 and 202 are approximately 9km, 3.5km and 10km respectively. The map of Munich city along with the three routes is shown in Figure 5.5. The measurements were performed at 947 MHz. Transmitter and receiver antennas heights were 13m and 1.5m respectively. The measurements were averaged at the centre of approximately a 10m sector along the routes and the measured data converted into path loss. The routes are summarized in Table 5.1.

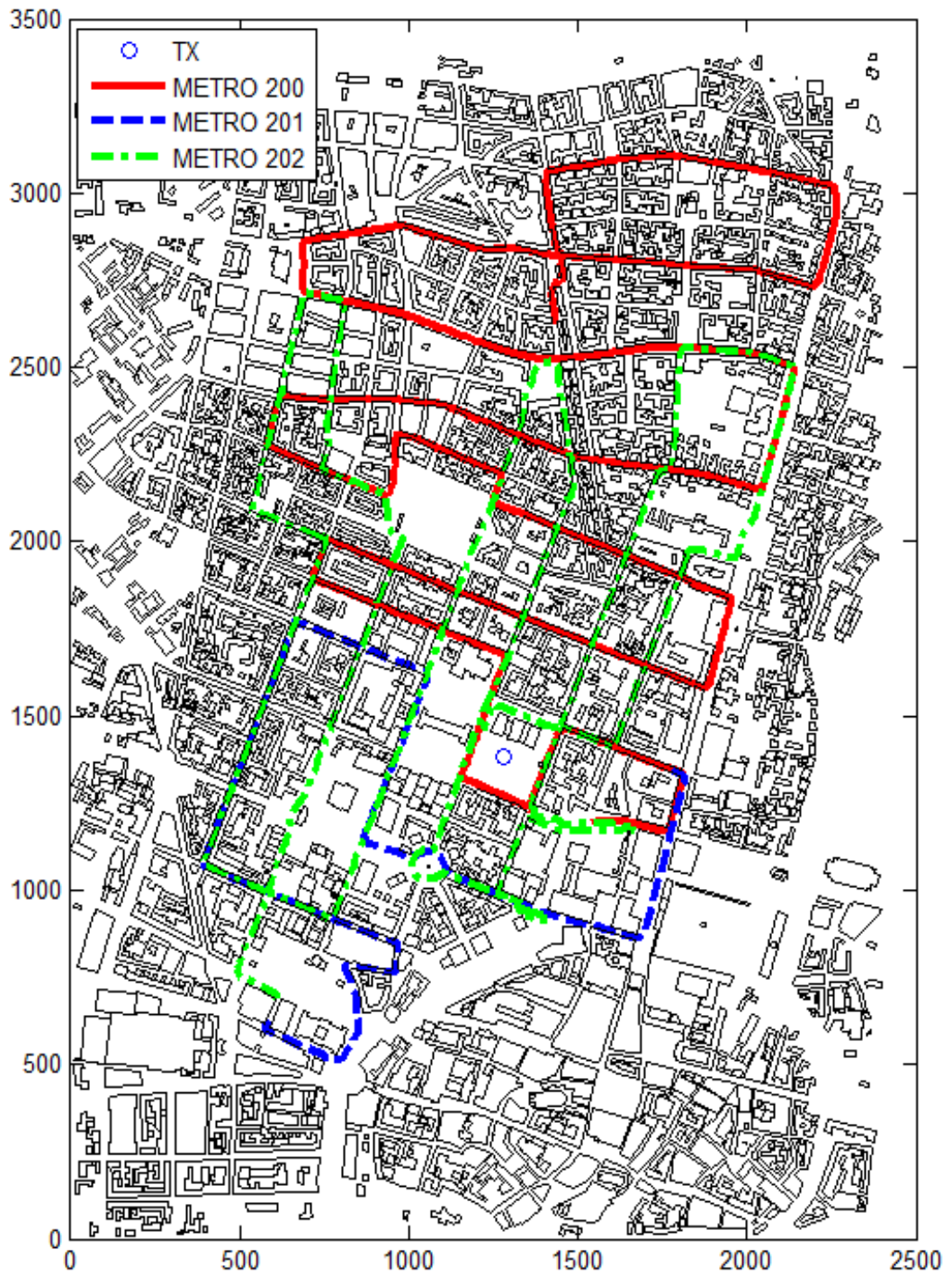


Figure 5.5 Map of Munich along with three routes Metro-200, Metro-201 and Metro-202.

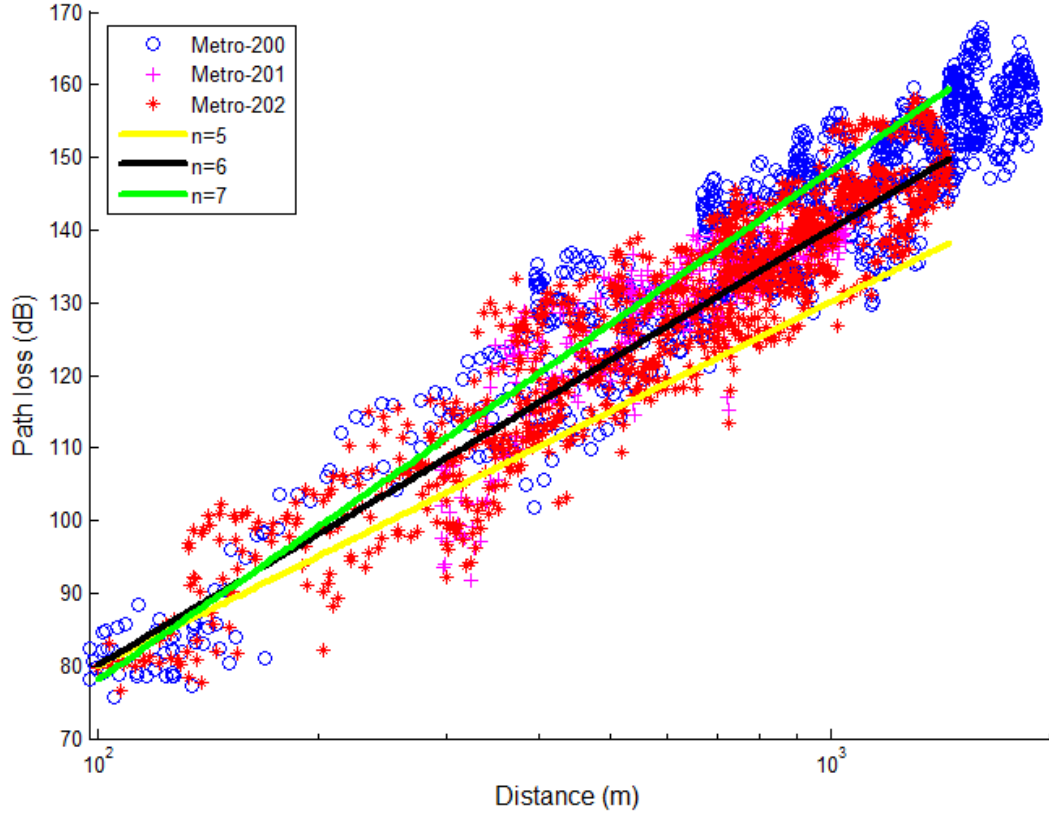


Figure 5.6 Path loss data for the routes is plotted against logarithmic distance.

Table 5.1 Measured data collected along three routes in Munich city. $f_c = 947\text{MHz}$, $h_{tx} = 13\text{m}$, $h_{rx} = 1.5\text{m}$

	Route		
	METRO-200	METRO-201	METRO-202
RX Points	970	355	1,031
Route Length	$\approx 9\text{km}$	$\approx 3.5\text{km}$	$\approx 10\text{km}$
Ground Height	$512 \pm 4\text{m}$	$516 \pm 2\text{m}$	$514 \pm 5\text{m}$

Path loss data for three routes is plotted against the logarithmic distance in Figure 5.6. A curve fitting is also applied with appropriate offset on the measured data. The standard deviation of error of the fitted n -power laws in Figure 5.6 for $n = 5$, $n = 6$ and $n = 7$ for Metro-202 route is 24.84 dB, 26.89 dB, and 29.04 dB respectively. It can be seen that the measured data is scattered over a wide range of path loss coefficients.

5.4.2 Initial Results

A second order image-tree that contains 3730 images was computed. The database of lit polygons and their associated shadow polygons for all the images are also computed

during the pre-processing. The time efficient ray-object intersection test mentioned in the previous section validates the rays in the 2-D plane followed by the lateral height check for each receiver point along the metro routes.

A combination of all the possible second order rays as well as a ground reflection and an over rooftop diffraction ray was computed. The over rooftop ray is computed using the heuristic technique proposed by Tzaras *et al.* [152]. This heuristic approach augments the UTD with slope diffraction to compute the multiple-edge transition zone diffraction. The following rays are computed for each receiver point.

- TX-RX (Direct LOS)
- TX-R-RX (1st order reflection)
- TX-D-RX (1st order diffraction)
- TX-R-R-RX (2nd order reflection)
- TX-D-D-RX (2nd order diffraction)
- TX-R-D-RX (Reflection followed by diffraction)
- TX-D-R-RX (Diffraction followed by reflection)
- TX-G-RX (Ground reflection)
- TX-ORT-RX (Vertical over rooftop diffraction)

A moving average filter with window size of $N = 10$ is applied to remove the local small scale fading effects in the computed fields. Path loss comparison against the measured data for all three routes is shown in Figures 5.7, 5.8 and 5.9. The average standard deviation of error of 8.46 dB with mean error of 2.3 dB is achieved along the metro routes. Table 5.2 lists the standard deviation of error (σ) and mean error (η) for the metro routes.

Table 5.2 Standard deviation of error (σ) and Mean error (η) along three metro routes in Munich city.

	Route		
	METRO-200	METRO-201	METRO-202
Standard deviation of Error (σ)	8.6 dB	7.8 dB	9.0 dB
Mean Error (η)	4.1 dB	1.7 dB	1.1 dB

The computer used in the simulation is a standard desktop with Intel Core i-5 3.3 GHz CPU and 16 GB RAM. Table 5.3 lists the CPU run time for the proposed algorithm that makes use of efficient ray-object intersection test based on lit and shadow polygons

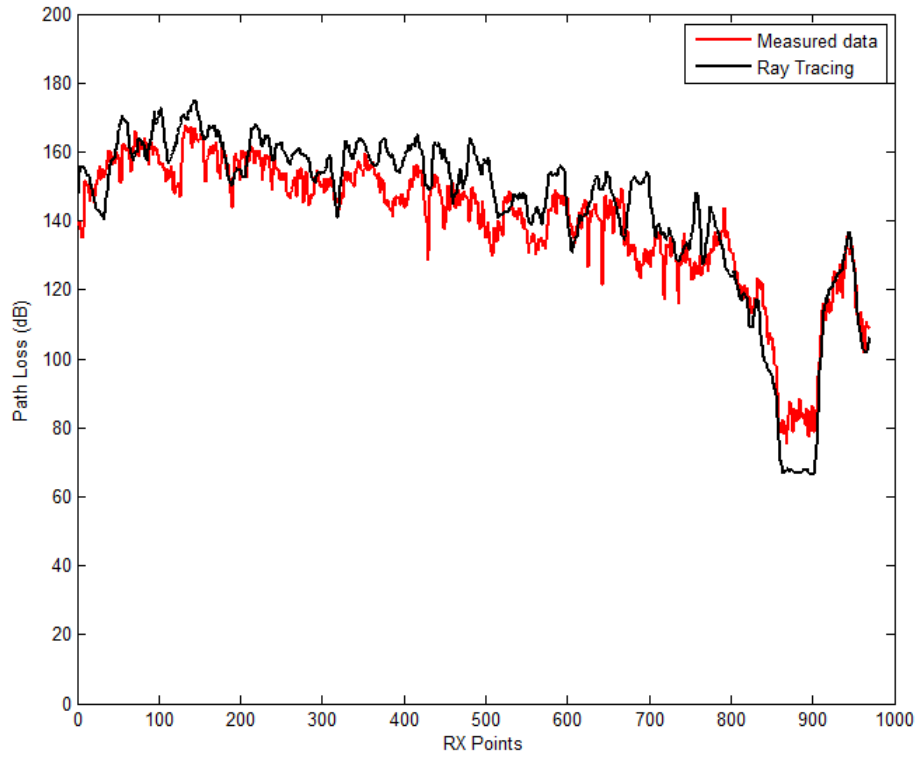


Figure 5.7 Path loss comparison for Metro-200

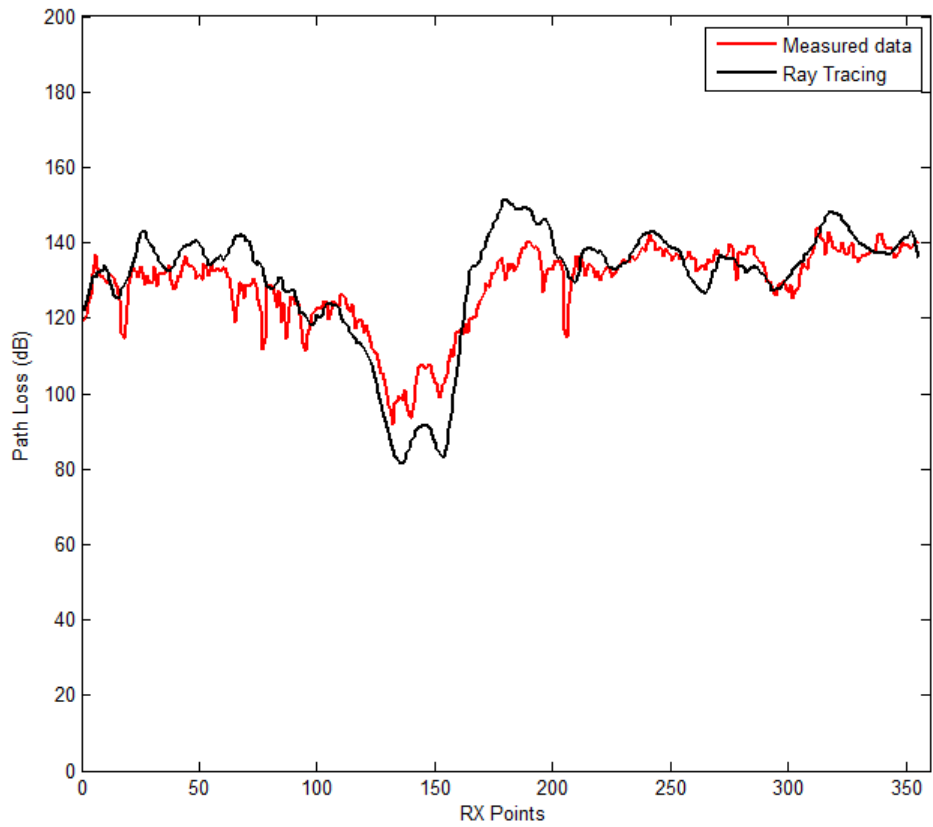


Figure 5.8 Path loss comparison for Metro-201

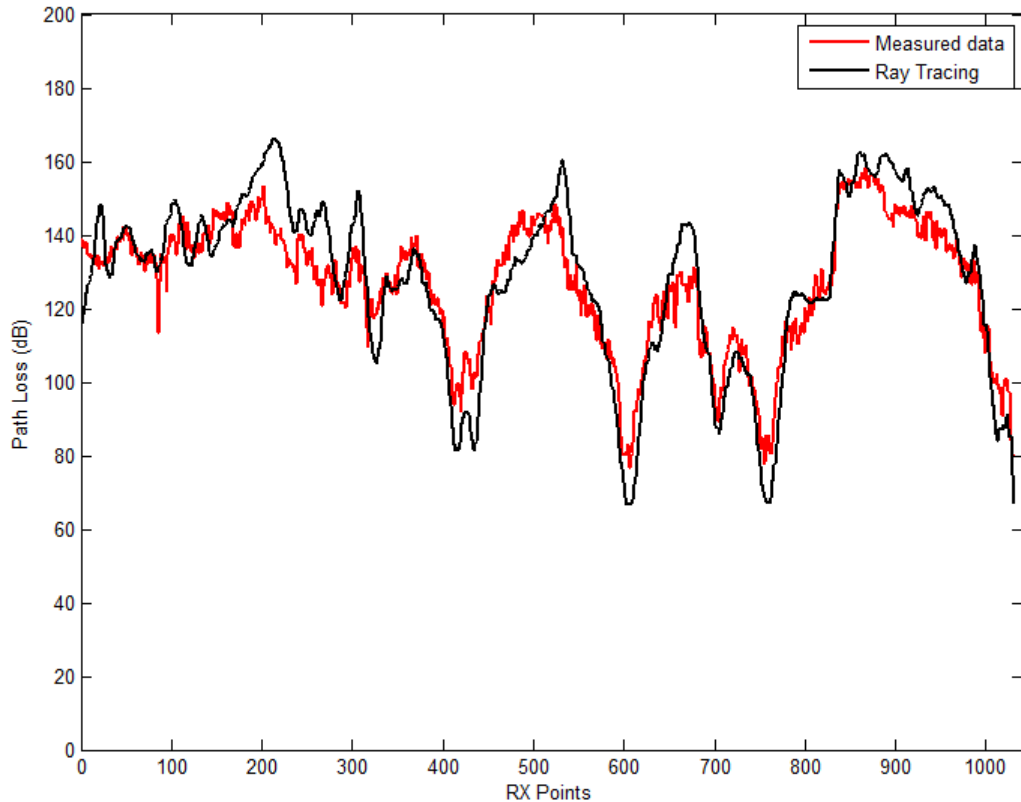


Figure 5.9 Path loss comparison for Metro-202

associated with the use of images. CPU time for un-accelerated ray tracing that only performs the ray-object intersection test on buildings enclosed within the grid-squares intercepted by individual ray-segments are also computed. The proposed ray-object intersection test achieves a reduction of over 90% along all three routes.

Table 5.3 Comparison of CPU time for metro routes.

	Route		
	METRO-200	METRO-201	METRO-202
Un-accelerated ray tracing	≈ 15.5 hrs	≈ 6 hrs	≈ 17 hrs
Proposed method	≈ 1 hr 20 mins	0.5 hr	≈ 1 hr 25 mins
Reduction	91.28%	91.51%	91.55%

5.4.3 Analysis of Propagation Mechanisms

Several types of rays are computed for each receiver point in the Munich example discussed above. In this section the contribution of different propagation mechanisms is investigated to understand radio wave propagation in a typical urban environment. The

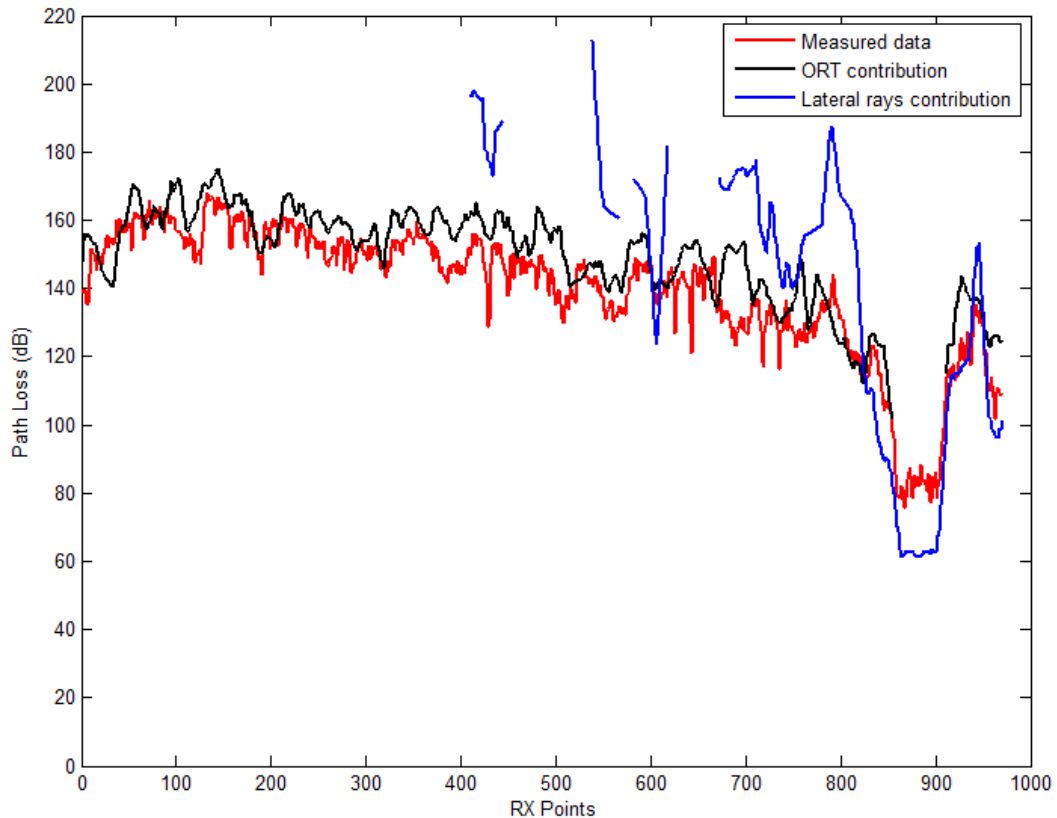


Figure 5.10 Comparison of over rooftop and lateral field contribution for metro-200.

purpose of this study is to develop an insight into the rays contribution in the predicted results.

The height of transmitter antenna in Munich measurements is close to average building height. Therefore the over rooftop (ORT) diffraction is expected to be significant in path loss prediction. A comparison of ORT diffraction contribution against the lateral rays for all three metro routes is shown in Figures 5.10, 5.11 and 5.12. The contribution of ORT diffraction in Metro-200 route constitutes a major part of the prediction result due to two factors. Firstly, the receiver points along the metro-200 are located far away from the transmitter as can be seen in Figure 5.5. e.g. the first 400 receivers are located at a distance of 1.1 km to 1.9 km from the transmitter. This large distance inhibits the ability of lateral rays to reach the receivers. Secondly, the receivers along this route are placed across streets that are perpendicular to the street in direct line of sight of the transmitter. This is valid for the first 840 receivers before the route enters a direct line of sight street. The Metro-201 route although is not very far away from the transmitter but is in deep shadow regions with a short segment in direct line of sight of the transmitter. Therefore ORT diffraction is also significant for this route as shown in the results. The Metro-202 route presents a different case. Most of the receivers are located along streets parallel to the direct line of sight of the transmitter. Therefore both the ORT diffraction and lateral propagation contribute to the prediction results along this route.

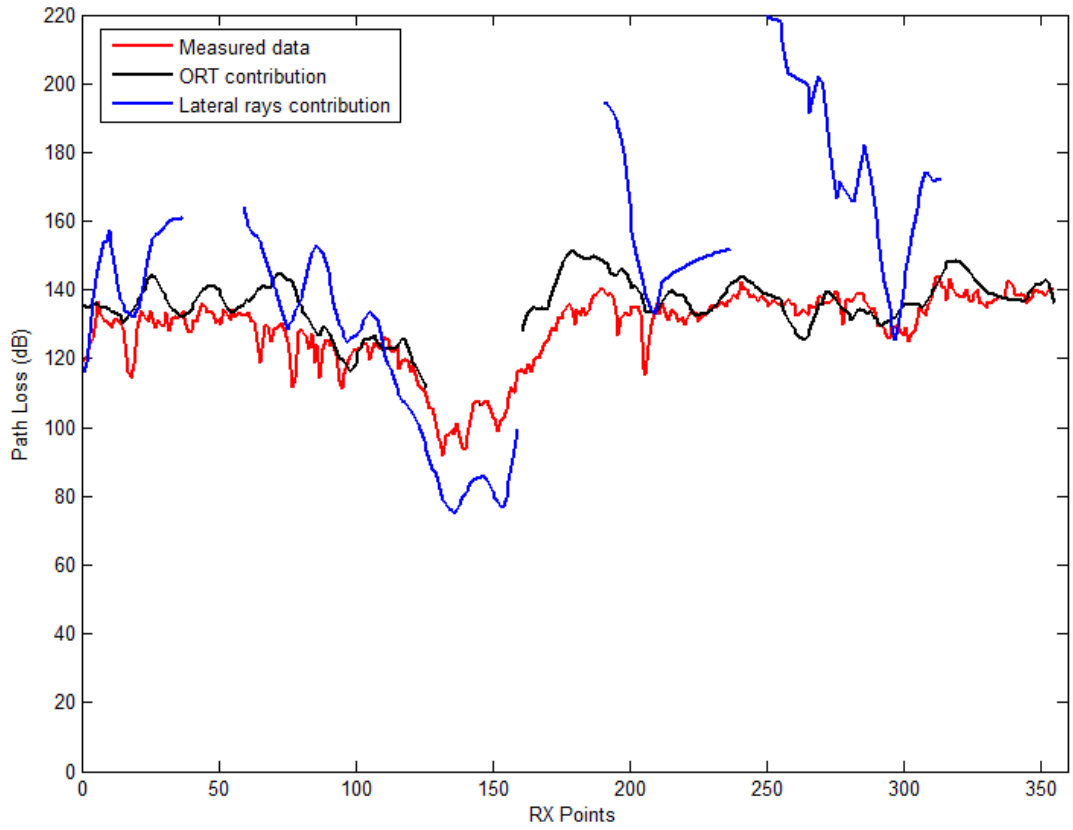


Figure 5.11 Comparison of over rooftop and lateral field contribution for metro-201.

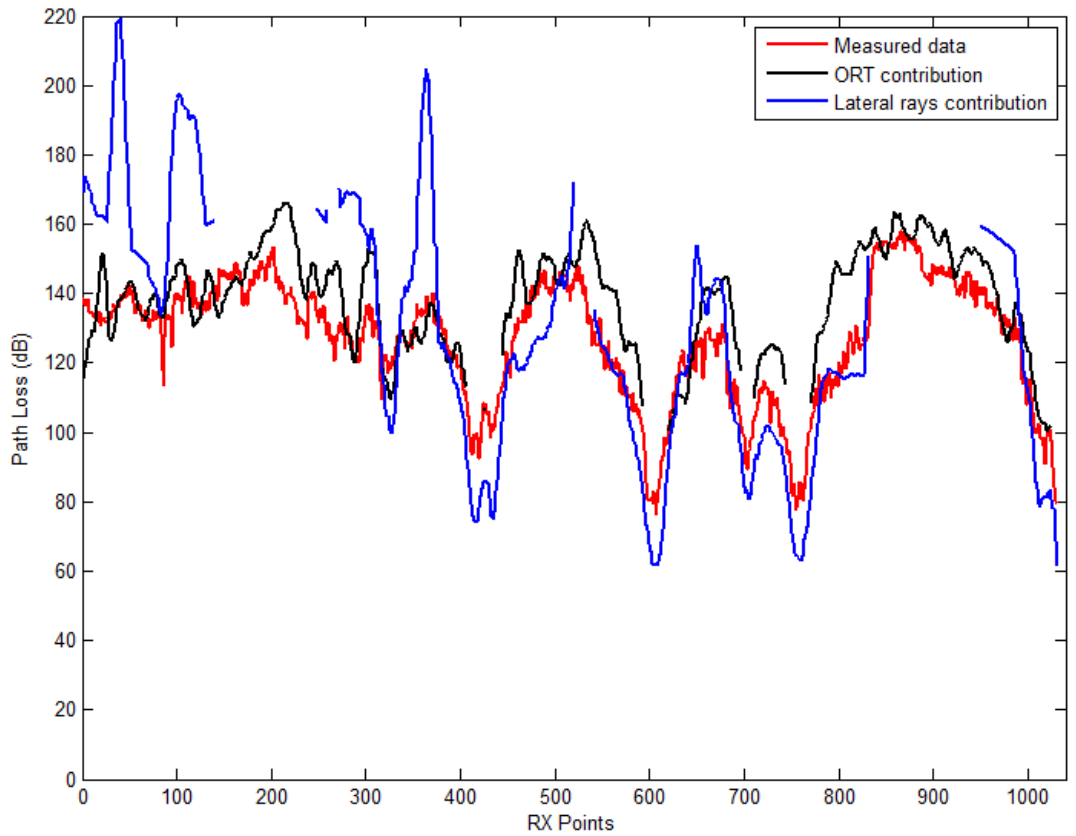


Figure 5.12 Comparison of over rooftop and lateral field contribution for metro-202.

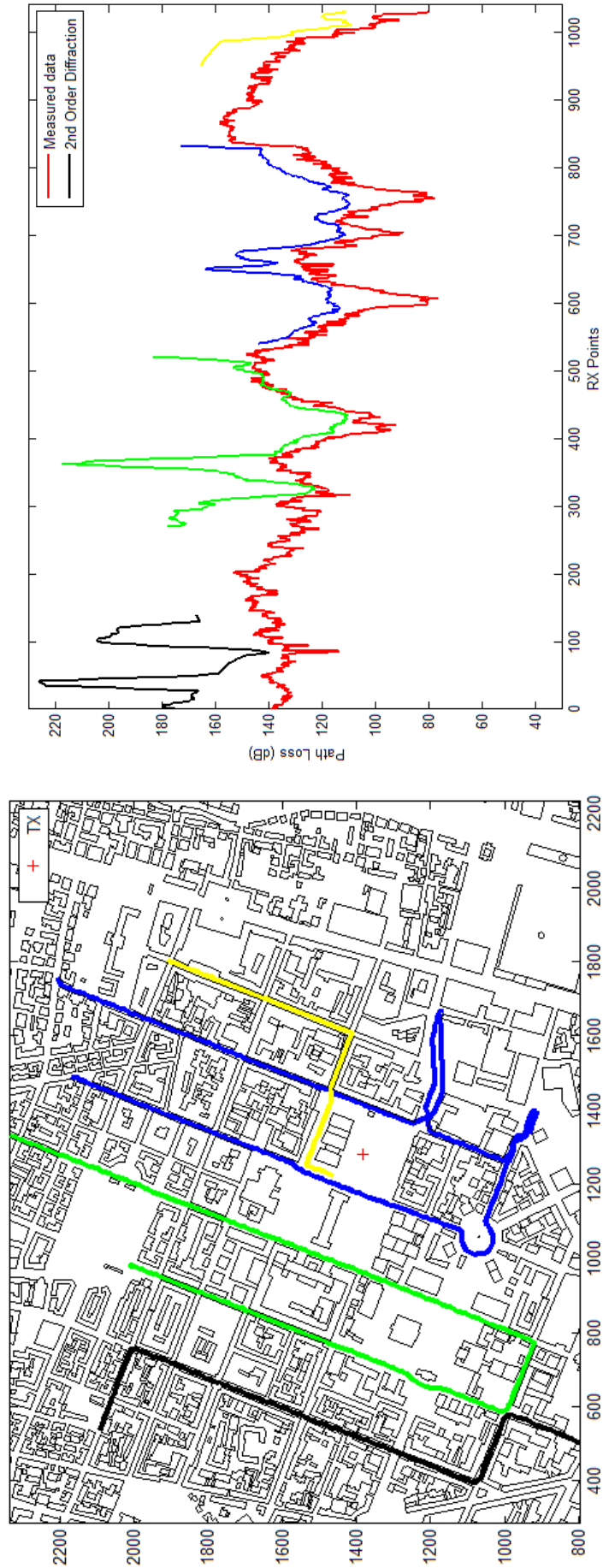
A further investigation of different lateral propagation mechanisms is also performed. The over-estimated path loss along all three routes is mainly contributed by second order diffractions (D-D). The diffracted field strength falls rapidly with distance so that the predicted path loss contributed by double diffractions is relatively higher. Path loss contribution by second order diffractions along four different segments of metro-202 in Figure 5.13a is shown in corresponding colours in Figure 5.13b. It can be seen that double diffractions spreads the radio signal to a wider area. The field contributions by double diffractions is significant near the transmitter as seen in some sections along the route segments shown in green, blue and yellow. However the contribution is not very significant for receivers located far away from the transmitter as shown for the receivers along the segment in black.

Path loss contribution by first order diffraction mechanism along four different segments of metro-202 in Figure 5.14a is also shown in corresponding colours in Figure 5.14b. It can be seen that first order diffraction is very significant along all the route segments shown. Although the first order diffraction mechanism does not propagate as far as the double diffractions, it can still provide a significant contribution along the streets that are parallel to the direct line of sight of the transmitter.

Both first and second order reflection mechanisms exist on a very small number of receivers that are in direct line of sight of the transmitter. However diffraction followed by reflection (D-R) rays are received by a large number of receivers in streets close to the transmitter due to the vertical edges of the buildings that are in direct line of sight of the transmitter. Figure 5.15a shows the significant contribution of D-R mechanism along the streets that are parallel to the direct line of sight of the transmitter. Likewise, the contribution of reflection followed by diffraction (R-D) is also significant along the same streets as shown in Figure 5.15b. A relatively higher contribution as shown by dips in the predicted path loss due to the direct line of sight and ground reflection exists only for a very small number of receivers.

A comparative study of different ray contributions is also performed. The contribution of following rays is computed for comparison with measured data. The comparison is shown in Figures 5.16 - 5.20. The Table 5.4 lists the mean and standard deviation of error of all these combinations of rays with measured data.

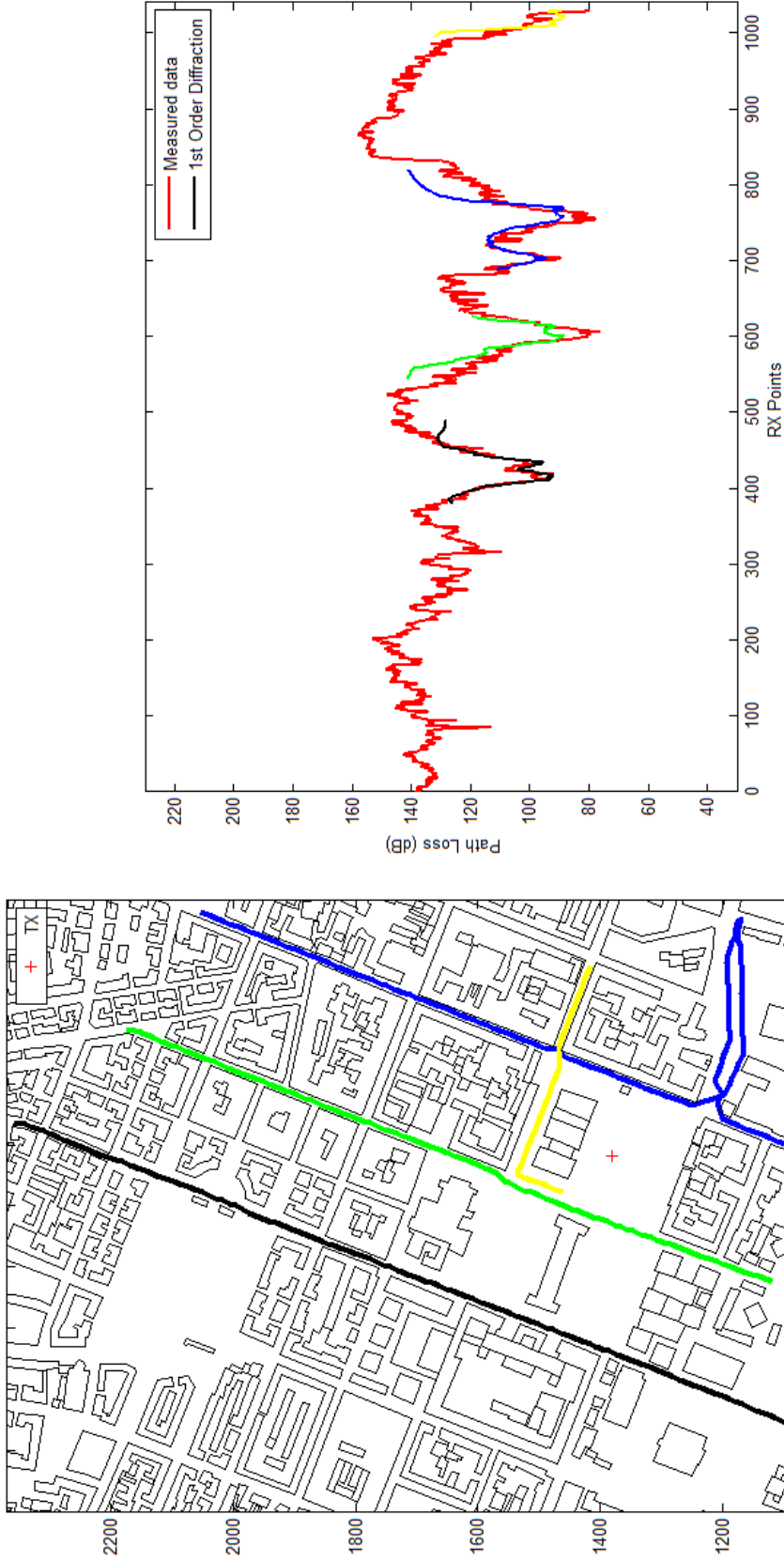
- Over rooftop only (ORT)
- All but over rooftop
- All but ground reflections
- Diffractions only
- Reflection followed by diffraction and diffraction followed by reflection



(b) Path loss contribution by double diffraction mechanism along metro-202.

(a) Receiver locations with valid double diffractions along metro-202.

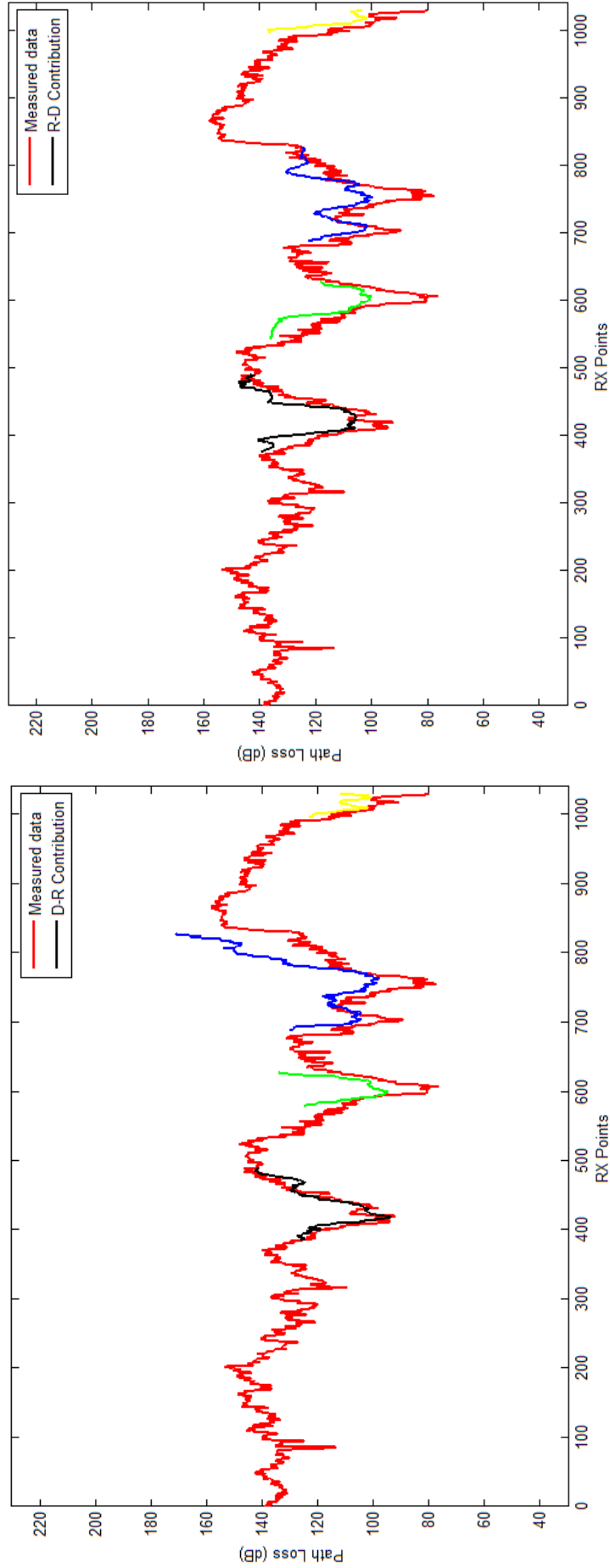
Figure 5.13 Analysis of second order diffraction mechanism around corners in metro-202.



(b) Path loss contribution by single diffraction mechanism along metro-202.

(a) Receiver locations with valid single diffraction rays along metro-202.

Figure 5.14 Analysis of first order diffraction mechanism around corners in metro-202.



(a) Path loss contribution of diffraction followed by reflection mechanism along metro-202. (b) Path loss contribution of reflection followed by diffraction mechanism along metro-202.

Figure 5.15 Analysis of D-R and R-D propagation mechanism for receivers in Figure 5.14a along metro-202.

Table 5.4 Comparison of mean and standard deviation of error with measured data for different combination of rays

	Mean Error	STD. Error
ORT Only	9.60	7.15
All but ORT	18.75	4.63
All but Ground	9.09	1.11
Diffractions Only	19.18	12.93
RD - DR Only	4.52	1.35

Summary

The different propagation mechanisms investigated above for a typical dense urban environment can be summarised as follows.

- Over rooftop diffraction is the most significant propagation mechanism for the locations that are far away from the transmitter or in deep shadow.
- Over rooftop diffraction is also the most significant propagation mechanism along the streets that are perpendicular to the streets in direct line of sight of the transmitter.
- Second order diffraction mechanism may exist for receivers located far away from the transmitter. However the contribution is very small and may be neglected.
- The streets that are parallel to the direct line of sight of the transmitter have significant lateral fields contributed by first order diffraction, second order diffraction, reflection followed by diffraction and diffraction followed by reflection.
- Specular wall reflections, ground reflection and direct line of sight mechanisms provide the strongest field contribution. However these mechanisms may only exist for a very small number of receivers in close proximity to the transmitter.

5.5 Mapping of Lit Polygons

The concept of lit and shadow polygons makes it very simple to compute whether a given receiver point receives a valid reflected or diffracted ray from a given face or edge. However given the large number of buildings in a typical urban environment and considering a higher order of ray interaction, there are potentially many thousands of images and associated polygons to check for each receiver point. For example the second order ray interaction in Munich city requires that each receiver point is tested for 3,730 lit polygons of images and the associated shadow polygons. The receiver points

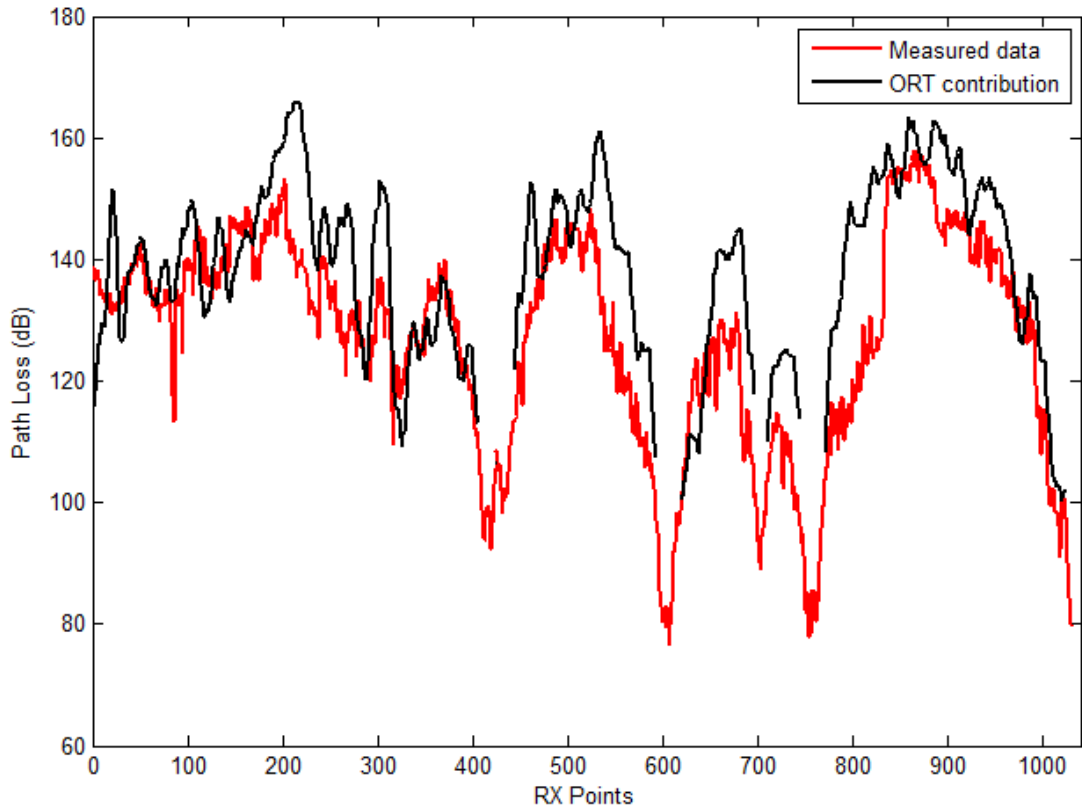


Figure 5.16 Comparison of over rooftop only with measured data.

that are far away from the transmitter do not receive a single valid ray. The receiver points that are located along the streets parallel to the line of sight of transmitter do not receive more than 200 valid rays on average. Although the lit and shadow polygons representation accelerates the ray validation test, a large overhead can be avoided by validating only the images that may produce valid rays for a given receiver point. In this section, we describe a technique to greatly reduce the number of images that need to be considered for a given receiver point by proposing a simple pre-processing step.

Space division methods divide the environment into a grid and the buildings are mapped to the grid-squares in which they reside. This technique accelerates the ray tracing as only the buildings inside the grid-squares intercepted by a ray-segment are subjected to ray-object intersection test. A similar space division technique can be proposed in terms of lit polygons. As we know that a valid ray-segment is formed if the receiver is located inside the lit polygon of an image as well as outside all the shadow polygons associated with that image. The lit polygons associated with all the images can be mapped to the grid. The lit polygons that are mapped to the grid-square in which receiver is located may produce valid rays. Therefore a smaller number of lit polygons are subjected to ray validation test thereby facilitating computational speed up.

The mapping of lit polygon associated with the use of images can be explained with the help of Figure. 5.21. A first order wall reflection (*RI*) and a vertical edge diffraction (*DI*) image with the corresponding lit polygons are shown. In order to map

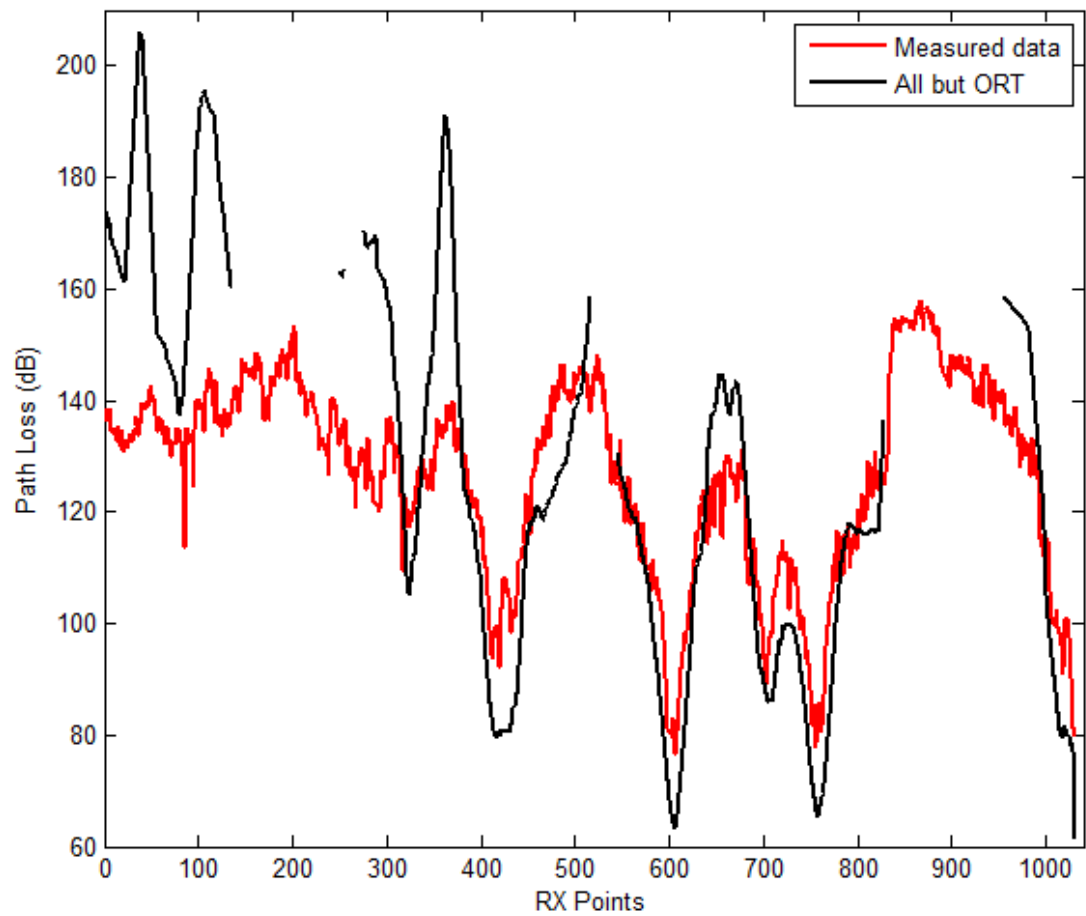


Figure 5.17 Comparison of all but over rooftop with measured data.

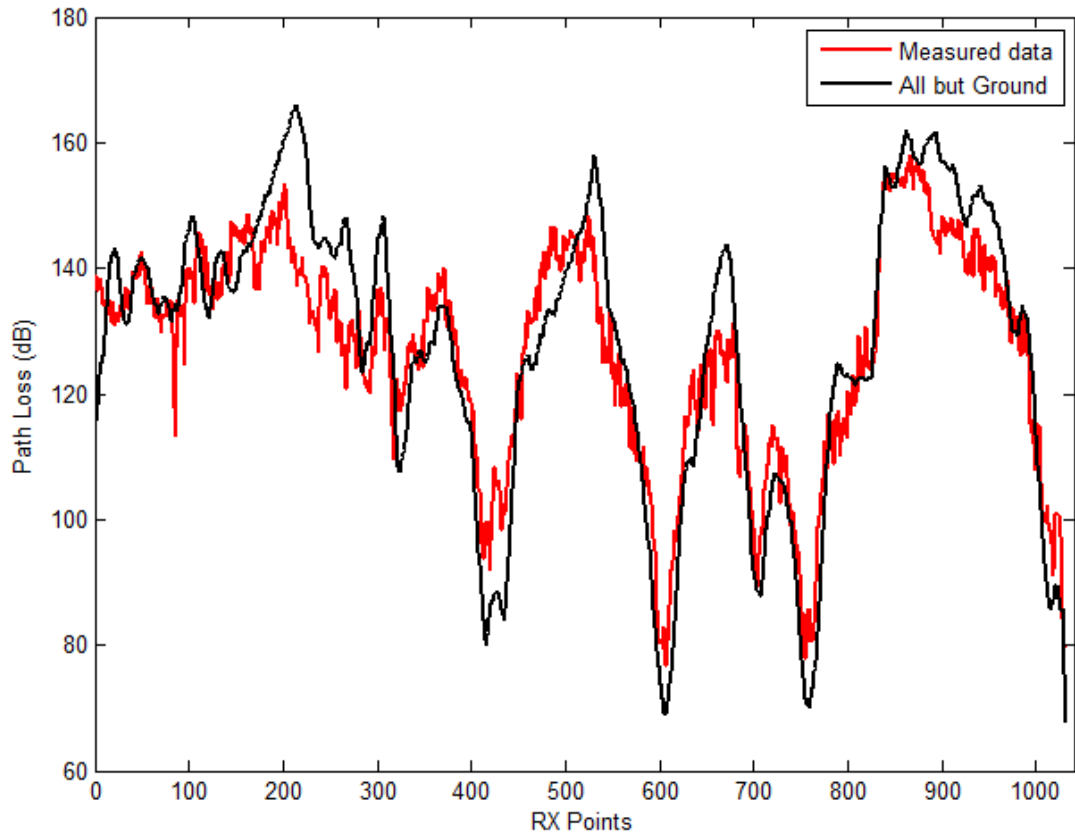


Figure 5.18 Comparison of all but ground reflections with measured data.

the lit polygons to the coarse grid, all the grid-squares that are intersected (partially or completely) by each lit polygon are identified. For example the lit polygon for the reflection image in Figure 5.21 can be mapped to grid-squares 0, 1, 2, 4 and 7 while the lit polygon for the diffraction image is mapped to grid-squares 0, 3, 4, 6, 7 and 8. This mapping produces a list of all the lit polygons that enclose or pass through each grid-square in the environment.

The mapping of lit polygons gives a database of all the images for which the associated rays may exist in a given grid-square. The lit polygon mapping database for the given simple scenario in Figure 5.21 is shown in Table 5.5. This mapping database can be used to greatly reduce the number of images that need to be considered before the reflections and diffractions for a given receiver point can be identified. The algorithm would require that first the grid-square in which receiver is located is identified and then it is simply a matter of only considering reflections and diffractions corresponding to the images with the lit-polygons that pass through that grid-square.

This is illustrated for the above example in Figure 5.21. Consider three random receiver points *A*, *B* and *C*. The receiver point *A* is located in grid-square 6. The lit polygons mapping table indicates that only the diffraction polygon (*DI*) intersects this grid-square. Therefore point *A* must only be subjected to ray-object intersection test for the diffraction image *DI* as it may potentially receive a valid diffraction ray. Similarly,

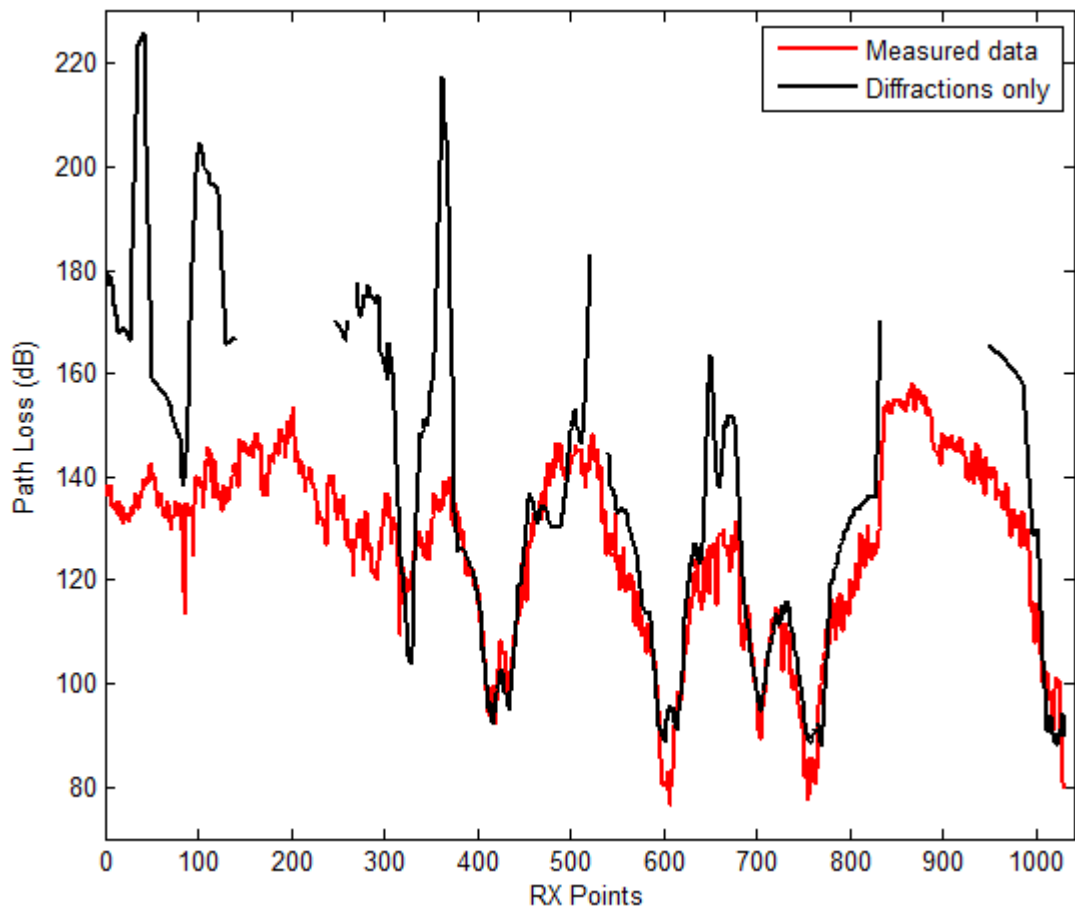


Figure 5.19 Comparison of diffraction only with measured data.

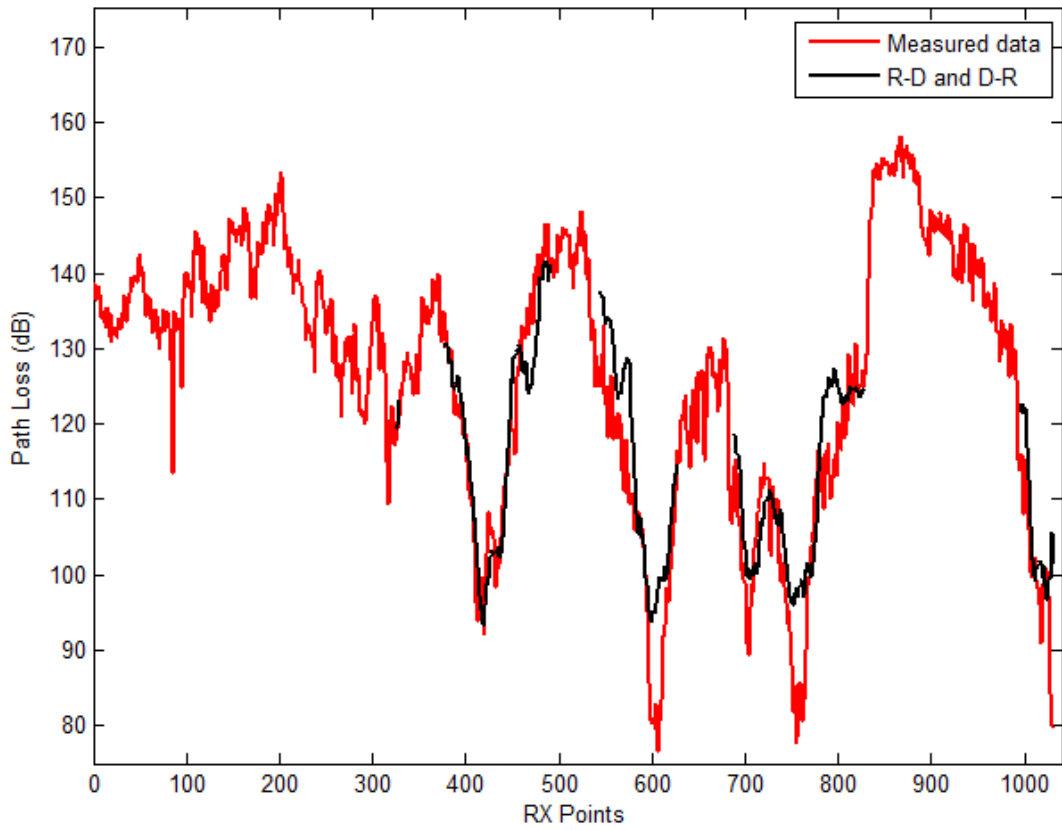


Figure 5.20 Comparison of R-D and D-R only with measured data.

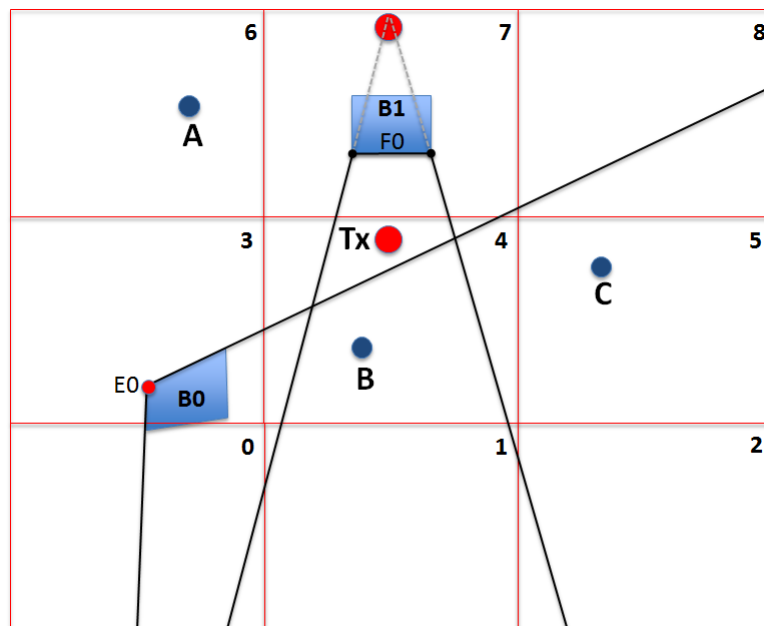


Figure 5.21 Mapping of lit polygon of images for image-tree reduction [160].

Table 5.5 Lit polygons mapping database for example in Figure 5.21 [160]

Grid Square	Polygon - 1	Polygon - 2
0	R1	D1
1	R1	-
2	R1	-
3	D1	-
4	R1	D1
5	-	-
6	D1	-
7	R1	D1
8	D1	-

the lit polygons mapping table for point *B* located in grid-square 4 suggests that the receiver could potentially receive both a reflected and diffracted ray. Therefore receiver point *B* is subjected to a ray-object intersection test for both the images. There is no lit polygon associated with grid-square 5 in the mapping table so that the receiver point *C* need not be tested for either the reflection or diffraction image.

The mapping of lit polygons allows us to distinguish the images that may produce valid rays at a given receiver location before the ray-object intersection test is performed. The images for which the lit polygons are mapped to the receiver grid-square are still subjected to validation test as the receiver must be located inside the lit polygon as well as outside of all the associated shadow polygons for a valid ray. This approach quickly identifies a subset of the image-tree, comprising reflection and diffraction images that potentially could produce reflected or diffracted rays at the particular receiver point. Different subsets will be activated for different receiver points, depending on what grid-square it is in. The ray tracing computations are thus accelerated as each receiver point is tested for a smaller number of images.

5.5.1 Selection of Grid Resolution

The mapping of lit polygons to the coarse grid reduces the active image-tree for a given receiver point as discussed above. The selection of grid-square dimensions is thus critical as it determines the image-tree reduction achieved for a given receiver point. Choosing a larger grid-square size reduces the pre-processing time needed as the number of grid-squares will be less. However a relatively large number of images will have lit polygons mapped per grid-square so that the image-tree reduction for each receiver point is less effective. On the other hand, smaller grid-square size could potentially improve the level of image-tree reduction achieved for each receiver point at the cost of increased pre-processing time. The Munich database is tested for grid resolutions of 50m×50m, 100m×100m, 150m×150m and 200m×200m. Table 5.6 compares the computational requirements for different grid resolutions.

Algorithm 3 Accelerated ray tracing using the lit polygons mapping

```

Input Data: RX location, Lit polygons mapping database;
Output Data: Valid rays in 3-D space;
 $x = \text{find\_grid\_square\_index}(\text{RX location});$ 
 $p = \text{total\_lit\_polygons\_mapped\_in\_grid\_square}(x);$ 
for ( $i = 0; i < p; i++$ ) do
    lit_polygon = lit_polygons_mapped[ $x$ ][ $i$ ];
    index = image index of lit_polygon;
    image = image_list[index];
    N = Image order for image;
    test_point = RX location;
    ray_is_valid = TRUE;
    for ( $j = N; (j \geq 0) \wedge (\text{ray\_is\_valid}); j = j - 1$ ) do
        lit_polygon = lit_polygon_list[index];
         $m = \text{number of shadow polygons for image};$ 
        if outside_polygon(lit_polygon, test_point) then
            ray_is_valid = FALSE;
        for ( $k = 0; (k \leq m) \wedge (\text{ray\_is\_valid}); k++$ ) do
            shadow_polygon = shadow_polygons_list[index][ $k$ ];
            if inside_polygon(shadow_polygon, test_point) then
                ray_is_valid = FALSE;
        if ray_is_valid then
            intersection_point = find_ray_intersection(test_point, image);
            make_ray_segment(test_point, intersection_point);
            test_point = intersection_point;
            index = Parent image index of image;
            image = image_list[index];
    if ray_is_valid then
        ray_2d = combine_ray_segments();
        validate_in_3d(ray_2d);
    populate rays in 3-D space;

```

Table 5.6 Memory and lit polygons mapping time required for different grid resolutions [160]

	Grid Size (50m×50m)	Grid Size (100m×100m)	Grid Size (150m×150m)	Grid Size (200m×200m)
Total grid-squares	3,264	816	368	204
Mapping Database Size (MB)	29.80	7.70	3.85	2.0
Mapping Time (seconds)	8,100	1,774	819	419
Lit Polygons per grid-square (Average)	2,041	2,057	2,164	2,184

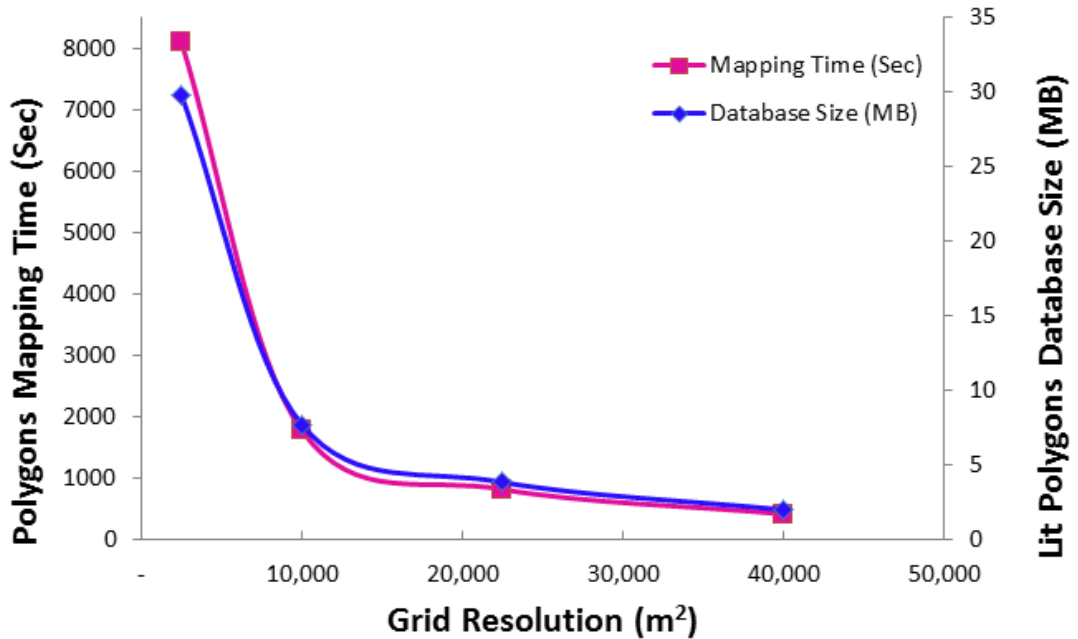


Figure 5.22 Comparison of computational performance for different grid dimensions [160]

The results show that memory and time requirements increase significantly for smaller grid-squares. Figure. 5.22 shows the inverse relation between the memory and time for different grid sizes. The average number of lit polygons mapped per grid-square do not change by a very large number for the grid-square dimensions investigated. This is due to the presence of lit polygons corresponding to diffracting edges. Diffraction spreads out the radio signal in all directions exterior to the diffracting edge so that the corresponding lit polygon encloses a large area. Therefore a reduction in grid-square size eliminates only a smaller number of reflection images while a large number of diffraction images still exist irrespective of the grid dimension.

5.5.2 Results

The reduction in the active image-tree for a given receiver point is investigated to evaluate the effectiveness of the proposed algorithm. The second order image-tree for the Munich database has already been computed and consists of 3,730 lit polygons. A grid-square dimension of 120m×120m is selected and the lit polygons are mapped

Table 5.7 Comparison of CPU time for metro routes using lit polygons mapping.

	Route		
	METRO-200	METRO-201	METRO-202
initial model	≈ 1 hr 20 mins	0.5 hr	≈ 1 hr 25 mins
using lit polygons mapping	40 mins	15 mins	45 mins
Reduction	50.51%	49.15%	47.57%

to this coarse grid. The number of lit polygons mapped per grid-square range from 2,008 to 2,435. A histogram of the number of lit polygons mapped per grid-square is shown in Figure. 5.23. It can be seen that 723 out of 816 grid-squares have 2,000 to 2,100 lit polygons mapped to it. This indicates that almost 90% of the grid-square have an average of 2,050 lit polygons mapped to them. The image-tree percentage reduction can be defined as the ratio of decrease in the average number of images to be tested for a given receiver point to the total images. Thus lit polygons mapping for the Munich database reduces the image-tree for any given receiver point by almost 45% on average. In other words, the image-tree that need to be validated for any given receiver point in the Munich environment is 45% less than the traditional image theory based ray-racing models. This illustrates the acceleration in ray tracing computations that can be achieved using the proposed algorithm.

The proposed algorithm is used to compute path loss for the metro routes in Munich city. CPU time is recorded for all three routes to compute the speed up that can be achieved using the proposed lit polygons mapping pre-processing technique. Table 5.7 lists the run time comparison against the initial model that make use of efficient ray-object intersection test as discussed in the previous section. The mapping of lit polygons reduces the CPU time by almost 50% as expected since the image-tree has been reduced by the same proportion.

5.6 Lit Polygons Mapping for A Linear Mobile Route

Ray tracing for a mobile receiver is performed at fixed locations along the route. Although the mapping of lit polygons accelerates the ray tracing as a smaller number of images are subjected to ray-object intersection test, a mobile receiver still has to be tested for all the mapped images at every receiver location along the route. The ray tracing computations for the receiver along a straight line could be accelerated as the ray-object intersection test is replaced by a simple check to compare the receiver location along the route. The ray-object intersection test first checks for a valid ray-segment between the receiver and the N th order image by confirming if the receiver is located inside the lit polygon of the image. Standard geometrical tests to validate whether a point is

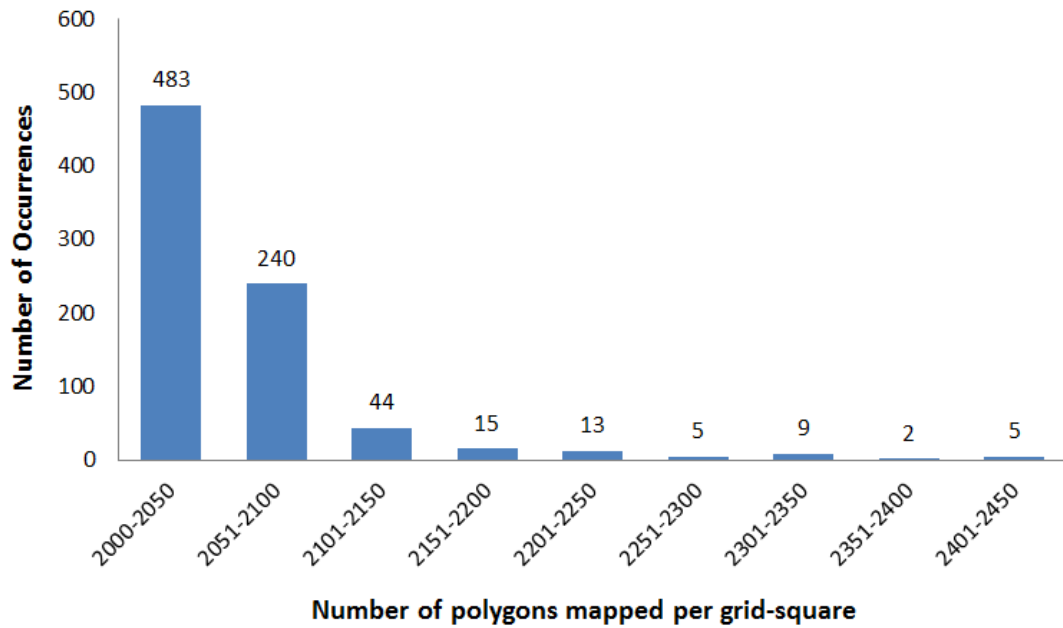


Figure 5.23 Histogram of number of lit polygons mapped per grid-square in Munich example [160].

inside a polygon requires that a number of computations be performed. A lit polygon has four sides so that the algorithm performs at least four computations to determine if the receiver point is inside it as described earlier. We are considering a mobile receiver that enters and leaves the lit polygons associated with images as it moves along a linear route. If the entry and exit points for all the lit polygons traversed by the mobile receiver are pre-computed, the geometrical test can be simplified. Instead of performing the standard geometrical test to validate the $RX - Nth$ order image ray-segment, we only need to compare the receiver location along the route with the entry and exit points of lit polygons.

The idea of lit polygons mapping for a mobile receiver can be explained with the help of Figure 5.24. A mobile receiver moves from point a to point f along the route as shown. The given scenario considers two wall reflection images. The mobile route enters and leaves the lit polygon corresponding to wall reflection from building $B1$ at a distance l_1 and l_3 from the start point a respectively. The entry and exit points for the lit polygon associated with wall reflection from building $B2$ are at a distance of l_2 and l_4 from the start point a respectively. This information suggests that a receiver point may potentially receive a valid reflection ray from building $B1$ only if it lies at a distance between l_1 and l_3 from the start point of the route. Likewise, a valid reflection ray from building $B2$ may exist for a receiver only if it is located at a distance between l_2 and l_4 from the start point.

A lit polygons mapping table as discussed in previous section can also be constructed for this example. This table will suggest that the mobile receiver must be validated for both reflection images along the full length of the route. However, comparing a

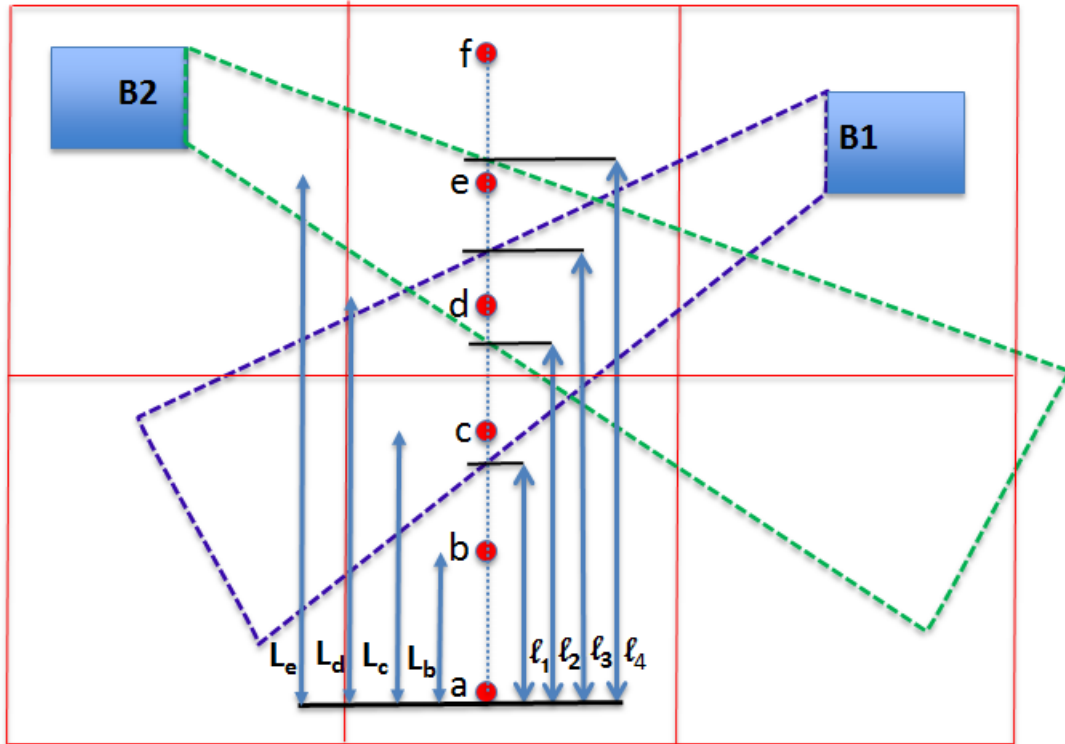


Figure 5.24 Mapping of lit polygon of images for a mobile route

receiver's location with entry and exit points of lit polygons can quickly determine if the valid rays may exist along the route. For example, the receiver point b is located at a distance of L_b from start point a . Instead of performing the geometrical test mentioned in section 5.3 to validate the receiver's location inside a lit polygon, we only need to perform a distance comparison check. This check simply confirms that receiver point is located within l_1 and l_3 ($l_1 < L_b < l_3$) for reflection from building $B1$ and within l_2 and l_4 ($l_2 < L_b < l_4$) for reflection from building $B2$.

To perform ray tracing for any receiver location along the mobile route located at a distance L_N from the start point, a valid reflection ray may exist only if the following is true.

$$l_1 < L_N < l_3$$

$$l_2 < L_N < l_4$$

This indicates that the algorithm does not need to perform the geometrical test with four (cross product) computations to validate the receiver location inside a lit polygon. Instead only two comparisons are required as the entry and exit points of the mobile receiver for both the lit polygons are already known. In practical situations, the intersection of lit polygons of images with the straight line along which the receiver moves is used to list the entry and exit points along the route. The distance of all the entry and exit points from the chosen start point of the mobile route is computed. To

compute the valid rays at a certain point along the route, its distance from the start point is calculated. This distance is compared to the distances of all the lit polygons in the mapping database to trivially find if the receiver is located inside the lit polygon of an image. The ray tracing algorithm is thus accelerated as the geometrical test of determining whether a receiver point is inside a lit polygon is replaced with a simple distance comparison check.

Algorithm 4 Accelerated ray tracing using lit polygons mapping for a mobile receiver

Input Data: TX location, RX_Route[N], Lit polygons mapped along mobile route;

Output Data: Valid rays for each receiver location in 3-D space;

N = total_number_of_receivers_along_mobile_route;

p = total_lit_polygons_mapped_along_mobile_route;

for ($n = 0$; $n < N$; $n++$) **do**

$D = \text{find_distance}(\text{RX_Route}[0], \text{RX_Route}[n]);$

for ($i = 0$; $i < p$; $i++$) **do**

 lit_polygon = lit_polygons_mapped_along_mobile_route[i];

 index = image index of lit_polygon;

 image = image_list[index];

d_1^i = distance at which route *enters* lit polygon i

d_2^i = distance at which route *exits* lit polygon i

 ray_is_valid = **TRUE**;

if ($D < d_1^i$) \vee ($D > d_2^i$) **then**

 ray_is_valid = **FALSE**;

m = number of shadow polygons for image;

for ($j = 0$; $(j < m) \wedge (\text{ray_is_valid})$; $j++$) **do**

 shadow_polygon = shadow_polygons_list[index][j];

if inside_polygon(shadow_polygon, RX_Route[n]) **then**

 ray_is_valid = **FALSE**;

if ray_is_valid **then**

 intersection_point = find_ray_intersection(RX_Route[n], image);

 make_ray_segment(RX_Route[n], intersection_point);

 :

 Repeat Algorithm 2 to validate rest of the ray-segments

 :

if ray_is_valid **then**

 ray_2d = combine_ray_segments();

 validate_in_3d(ray_2d);

 populate rays in 3-D space;

5.6.1 Selection of Route Length

The length of the straight route to characterize the lit polygons mapping along the route must be carefully selected. The receiving equipment in a typical urban measurements campaign is mounted on a vehicle that moves along an approximately straight line

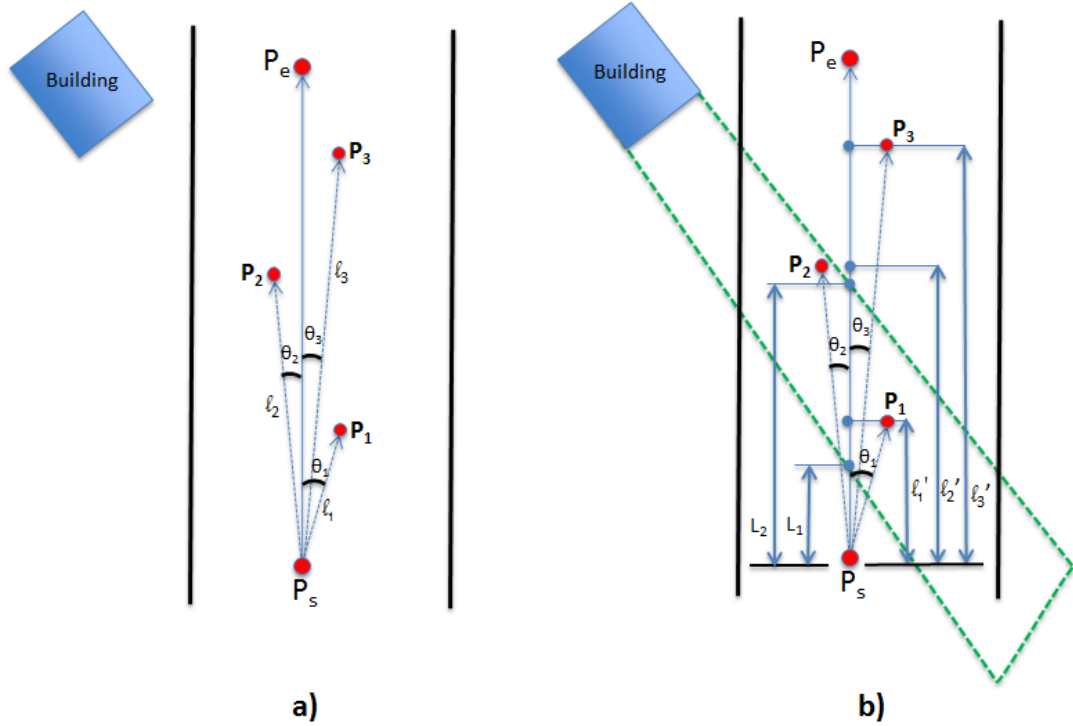


Figure 5.25 Selection of route length to avoid missing the valid rays

(or series of straight lines). It is possible that one or more measurement points may not be in the straight line formed by the start and end point of the route. This change in the receiver position can be due to avoiding the stationary objects such as trees or parked cars along the route. Other scenarios where a line of receiver points cannot be in a straight line include measurements along street turns and roundabouts. It is also possible that the receiver locations are not properly recorded due to GPS errors. In this case, the error in predicted results are expected that depends on the deviation of recorded points from the actual location.

The mapping of lit polygons for a route assumes that all the receiver points are placed along a straight line. It is possible that the relative distance for a receiver point that is slightly outside the straight route suggests that it is not located within the lit polygon of an image even though it lies within its lit polygon or vice versa. This problem can be explained with the help of Figure 5.25. The measurements are taken at five receiver points along a street that are not in the straight line. The points P_s and P_e are chosen as start and end points of the straight line that is used to find the lit polygons intersections. The points P_1 , P_2 and P_3 are located away from the route line.

If \vec{V}_r represents the route vector from P_s to P_e and \vec{V}_i represents the vector from P_s to P_i , where $i = 1, 2, 3$. Then, the angle θ_i between \vec{V}_r and \vec{V}_i can be given as,

$$\cos \theta_i = \frac{\vec{V}_r \cdot \vec{V}_i}{|\vec{V}_r| |\vec{V}_i|} \quad (5.1)$$



Figure 5.26 Selected route simulated for different thresholds

The relative location of each receiver along the route determines the lit polygons that are visible to the receiver. Entry and exit points of all the lit polygons along the straight route are pre-determined. The length of each receiver point along the route that is used to compare if a lit polygon is visible to the receiver is the component of point vector \vec{V}_i along the route vector \vec{V}_r and can be given as follows,

$$\hat{l}_i = l_i \cos \theta_i \quad (5.2)$$

The selected route enters the lit polygon of wall reflection from building $B1$ at distance L_1 and leaves at L_2 as shown in Figure 5.25b. A receiver point may receive a reflection ray if its length across the route is between L_1 and L_2 . The receiver point P_2 is inside the lit polygon of wall reflection as shown. However the length of the receiver P_2 along the route \hat{l}_2 is higher than L_2 which suggest that receiver is not within the lit polygon and will not receive a reflection ray. This shows that the deviation of a receiver point from the selected straight line may give prediction errors if the straight line is not carefully selected. The deviation of receiver points from the route can be defined by a *deviation threshold* that is the average of $\cos \theta_i$ associated with all the receiver points along the route.

For a route with $N+2$ points including the start and end point, the route deviation threshold can be given as follows,

$$DeviationThreshold = \frac{\sum_{i=1}^N \cos \theta_i}{N}$$

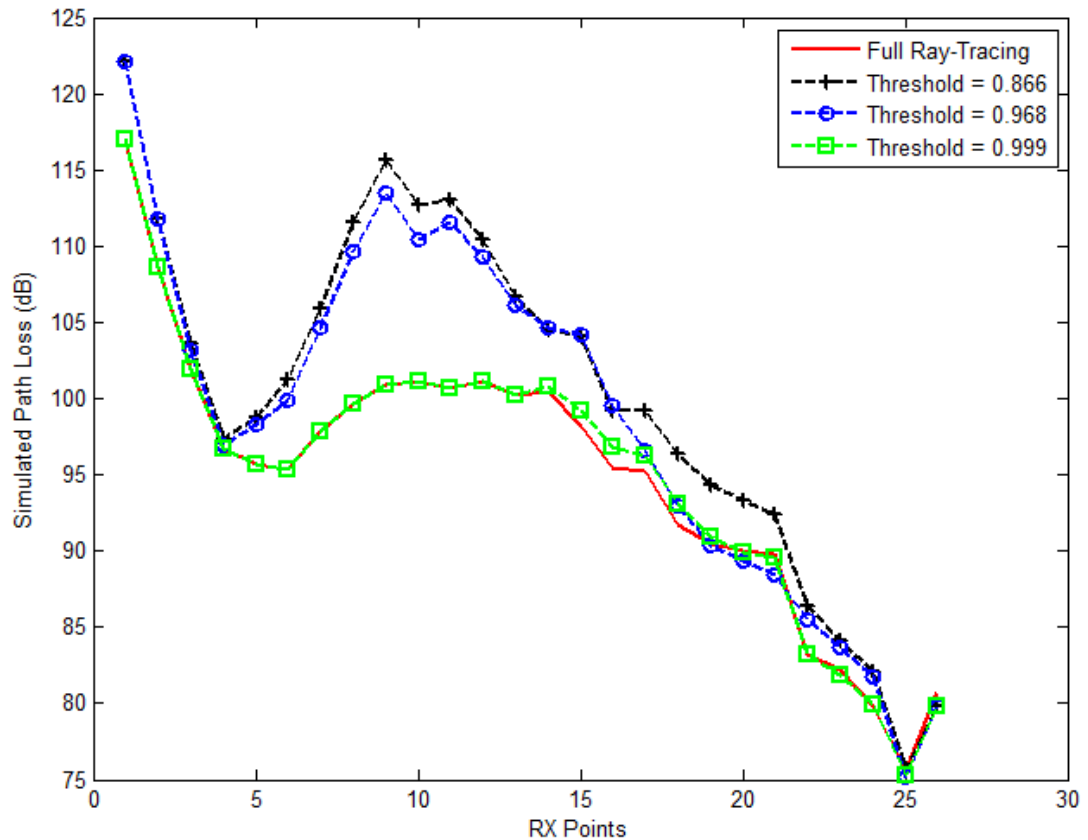


Figure 5.27 Path loss comparison for different route deviation thresholds

A deviation threshold of unity will suggest that all points are along the straight line that joins the start and end points along the route. A mobile route with non collinear receiver points can be divided into smaller sub-routes to reduce the prediction error. To study the effect of non collinearity of receiver locations on the prediction error, a route of 26 measurement points along Metro-202 from the Munich database is selected as shown in Figure 5.26. The proposed accelerated ray tracing is performed for all the receiver points by dividing the route into smaller sub-routes for three different deviation thresholds of 0.866, 0.968 and 0.999. The selected threshold values give the standard deviation of error (σ) of 4.0 dB, 3.9 dB and 0.5 dB respectively as compared to the full ray tracing for individual receivers and is shown in Figure 5.27. Table 5.8 lists the comparison of three different routes. It can be seen that the proposed algorithm has to trade-off between the speed and accuracy of predicted results for a mobile receiver that has non-collinear observation points. The receiver points located away from the simulated route may include or omit valid rays that can add to the prediction error. Dividing a non-linear route into smaller linear routes improves the accuracy at the expense of a relatively smaller time reduction.

Table 5.8 Standard deviation of error (σ) and time reduction for different route deviation thresholds.

	Deviation Threshold	Error (σ)	Time Reduction (%)
Route - 1	0.866	4.0dB	36.90%
Route - 2	0.968	3.9dB	30.90%
Route - 3	0.999	0.5dB	16.67%

5.6.2 Results

The proposed algorithm accelerates the ray validation process by using the pre-computed intersection database for a mobile receiver as it enters and leaves the lit polygons associated with the images along a linear trajectory. The metro routes in Munich city are divided into piecewise linear sub-routes and rays are computed for all the points along the routes using the proposed technique. As we have seen in the previous section that the lit polygons mapping reduces the active image-tree for *individual* receiver points that in turn reduces the CPU time by up to 50% as compared to the full image-tree validation. Table 5.9 compares the CPU times for the proposed algorithm against the lit polygons mapping (LPM) for individual receiver points. It can be seen that a further reduction of at least 40% in CPU time is achieved when the routes are simulated by using the fact that the receiver is moving along a linear route. This acceleration is due to the fact that the geometrical test to validate the ray-segment between the receiver and the N th order image is replaced by a simple distance comparison check.

Table 5.9 Comparison of CPU time for metro routes using lit polygons mapping for linear mobile route.

	Route		
	METRO-200	METRO-201	METRO-202
using individual receivers	40 mins	15 mins	45 mins
using linear route	23 mins	9 mins	26 mins
Reduction	41.66%	40%	42.22%

5.7 Mapping of Shadow Polygons

Although computing the intersection of lit polygons with the mobile receiver route line accelerates the ray validation, the algorithm still has to confirm that each receiver point along the route is outside of all the shadow polygons associated with the images. The ray-object intersection test developed in this work that makes use of lit and shadow

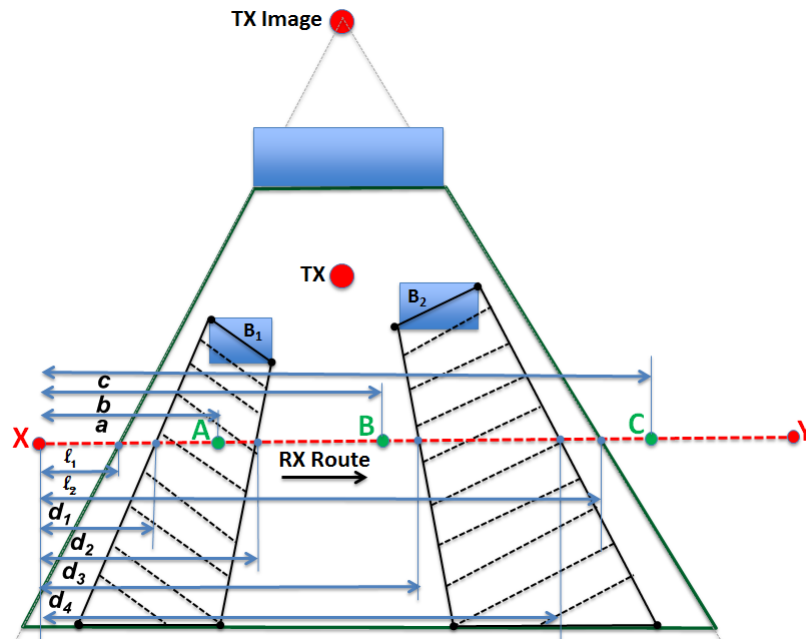


Figure 5.28 An example of a mobile route passing through lit and shadow polygons associated with a wall reflection image [161].

polygons is very efficient as discussed in section 5.3. However it has been shown in the previous section that pre-computed database of route intersection with *lit polygons* further reduces the CPU time by 40%. In this section, the idea has been extended to include the intersection of a mobile route with the lit as well as the associated *shadow polygons*.

The concept of using both the lit and shadow polygons intersection with mobile route for ray tracing acceleration can be explained with the help of Figure 5.28. The mobile receiver moves from point X to point Y along the straight line as shown by the red dashed line. The given scenario considers a first order wall reflection image. The buildings B_1 and B_2 block the reflection rays from the wall and produce shadow regions that are represented by the hatched polygons. The mobile receiver enters and leaves the lit polygon of wall reflection at distance l_1 and l_2 from the start point X respectively. The entry and exit points of the mobile receiver for the shadow polygon formed by building B_1 are at a distance of d_1 and d_2 from the start point X respectively. Likewise, the mobile route enters and leaves the shadow polygon formed by building B_2 at a distance d_3 and d_4 respectively. We are interested to find if a valid reflection ray exists at three receiver points A, B and C along the route. These points are located at distances a, b and c from the start point X respectively. A valid reflection ray will be received by a receiver point only if it is located inside the lit polygon as well as outside of both the shadow polygons. If we only had computed the lit polygon intersection with the route line, we could easily identify that a valid ray may only exist for point A and B as their relative location along the route line is within the lit polygon distances l_1 and l_2 . The point C will not receive a valid reflection as its relative location along the route is

outside the lit polygon. The next test to validate the ray is to confirm if the receiver point is outside of both the shadow polygons formed by buildings B_1 and B_2 . The receiver point A will not receive a valid reflection ray as it is located inside the shadow polygon of B_1 that can be determined by simply comparing its location between the distances d_1 and d_2 ($d_1 \leq a \leq d_2$). The point B will receive a valid reflection ray as it is outside of both shadow polygons formed by B_1 and B_2 with its relative location outside both the distances $[d_1, d_2]$ and $[d_3, d_4]$. The ray tracing algorithm is accelerated as the geometrical test to validate the receiver located inside the lit polygon and outside of all the associated shadow polygons is replaced by a simple distance comparison check.

5.7.1 Results

The proposed model again computes the path loss in Munich city by dividing the metro routes into piecewise linear sub-routes. The database of lit and associated shadow polygons intersection with each sub-route is pre-computed. Table 5.10 lists the run time comparison of proposed model. There is a slight reduction in CPU time as compared to the model that only use lit polygons mapping along a linear route.

Table 5.10 Comparison of CPU time for metro routes using lit and shadow polygons mapping for linear mobile route.

	Route		
	METRO-200	METRO-201	METRO-202
using lit polygons only	1,400 sec	540 sec	1,560 sec
using lit and shadow polygons	1304 sec	490 sec	1,507 mins
Reduction	6.85%	9.25%	3.40%

5.8 Summary of Acceleration Techniques

This chapter has presented four techniques based on lit and shadow polygons associated with images for ray tracing acceleration in urban environments. Firstly, the lit and shadow regions associated with a set of rays are described by polygons. This representation of images in terms of lit and shadow polygons (LSP) allows for a very efficient ray-object intersection test for fast ray tracing. Secondly, lit polygons mapping (LPM) is performed to obtain a subset of images that can produce valid rays for a given receiver based on its location. Thirdly, this lit polygons mapping is combined with linear route (LPM-LR) approach for ray tracing acceleration for a mobile receiver or multiple collinear receiver locations. This approach quickly identifies the images that may produce a valid ray by quickly validating the ray-segment formed between receiver

Algorithm 5 Accelerated ray tracing using lit and shadow polygons mapping for a mobile receiver

Input Data: TX location, RX_Route[N], Lit and shadow polygons mapped along mobile route;

Output Data: Valid rays for each receiver location in 3-D space;

N = total_number_of_receivers_along_mobile_route;

p = total_lit_polygons_mapped_along_mobile_route;

for ($n = 0$; $n < N$; $n++$) **do**

$D = \text{find_distance}(\text{RX_Route}[0], \text{RX_Route}[n]);$

for ($i = 0$; $i < p$; $i++$) **do**

 lit_polygon = lit_polygons_mapped_along_mobile_route[i];

 index = image index of lit_polygon;

 image = image_list[index];

d_1^i = distance at which route *enters* lit polygon i

d_2^i = distance at which route *exits* lit polygon i

 ray_is_valid = **TRUE**;

if ($D < d_1^i$) \vee ($D > d_2^i$) **then**

 ray_is_valid = **FALSE**;

m = number of shadow polygons for image;

d_{m1}^i = distance at which route *enters* m th shadow polygon of lit polygon associated with i th image

d_{m2}^i = distance at which route *exits* m th shadow polygon of lit polygon associated with i th image

for ($j = 0$; ($j < m$) \wedge (ray_is_valid); $j++$) **do**

if ($D > d_{m1}^i$) \wedge ($D < d_{m2}^i$) **then**

 ray_is_valid = **FALSE**;

if ray_is_valid **then**

 intersection_point = find_ray_intersection(RX_Route[n], image);

 make_ray_segment(RX_Route[n], intersection_point);

 :

 Repeat Algorithm 2 to validate rest of the ray-segments

 :

if ray_is_valid **then**

 ray_2d = combine_ray_segments();

 validate_in_3d(ray_2d);

 populate rays in 3-D space;

and N th order image. This approach (LPM-LR) is combined with mapping of shadow polygons intersected along the route (LSPM-LR) to further accelerate the ray computations. Table 5.11 lists the CPU time for these methods against the un-accelerated ray tracing for the metro routes in Munich.

Table 5.11 Comparison of CPU time for metro routes in Munich city using the acceleration techniques developed in this work.

	Route		
	METRO-200	METRO-201	METRO-202
Un-accelerated ray tracing	≈ 15.5 hrs	≈ 6 hrs	≈ 17 hrs
LSP method (sec. 5.3)	≈ 1 hr 20 mins	0.5 hr	≈ 1 hr 25 mins
LPM method (sec. 5.5)	40 mins	15 mins	45 mins
LPM-LR method (sec. 5.6)	23 mins	9 mins	26 mins
LSPM-LR method (sec. 5.7)	≈ 21 mins	8 mins	25 mins

5.9 Conclusion

A novel algorithm to compute the radio channel for a mobile receiver is developed in this chapter. The following stages form the basis of this algorithm.

- The maximum horizontal area where rays can propagate after interaction with a wall or a vertical edge illuminated by a source is represented by lit polygon. The shadow regions formed by buildings within a lit region is represented by lit polygon. An efficient ray-object intersection test determines the valid rays for a given receiver location [158].
- The mapping of lit polygons reduces the active image tree that must be tested for each receiver location that accelerates the ray computations.
- A database of lit polygons intersection with the linear route along which the receiver moves is computed. This database replaces the ray-object intersection test with simple distance comparison to accelerate the ray tracing computations [160].
- A database of shadow polygons intersection with the mobile route is also computed to further speed up the model [161].

The results are compared against the measured data for Munich available from COST 231 project. The analysis of results give an insight into different propagation mechanisms in a typical dense urban environment. It has been established that the

receiver locations near the transmitter have significant contributions from lateral rays. However the propagation is strongly dependant on the geometry of the environment. This suggests the development of more intelligent ray tracing tools for radio propagation prediction.

The model presented in this research includes specular reflections, vertical edge diffraction and over rooftop diffraction only. The average standard deviation of error between the simulated and measured data was about 8dB. This suggests that the accuracy of the model can be further improved by inclusion of scattering from walls and urban furniture. This is proposed for future work. Validation results show that a considerable reduction in CPU time is achieved for propagation prediction in urban environments. The proposed model achieves the fastest average time of 1.5 seconds to validate all the rays for a single receiver.

Chapter 6

Ray Tracing Acceleration for a Mobile Transmitter

There has been a great deal of interest in development of cooperative Intelligent Transportation Systems (ITS) based on vehicle-to-x (V2X) communication in recent times. The base station antenna is placed on moving cars for V2X communications. Therefore the channel in V2X communications is very dynamic. This requires the development of fast and efficient radio channel prediction models for mobile transmitter and receiver. The development of efficient ray tracing model for mobile receiver has been addressed in the previous chapter. The work presented in this chapter is focused on development of efficient ray tracing algorithms for mobile transmitter. The ray tracing models are mostly developed for point-to-multipoint radio channel prediction. Utilizing an efficient ray tracing model for a mobile transmitter scenario requires that pre-processing must be performed for each transmitter location. The visibility between the walls and edges in a given environment, or so-called intra-visibility, is always fixed. The novel algorithm developed in this work uses the pre-computed intra-visibility for efficient computation of visibility list of required order of ray interaction for a mobile transmitter moving along a linear trajectory. The preliminary results obtained from the use of the intra-visibility database to achieve acceleration in visibility computation have been published in [164]. The advanced model that accelerates the pre-processing computation for a mobile transmitter has been submitted for publication in [165].

6.1 Introduction

Image theory based ray-tracing models can accurately compute the ray paths and are widely used for indoor[166, 103], outdoor[23, 56, 25, 106] and vehicular[167, 168] networks. The first step in an image theory based ray tracing model is to apply a recursive visibility algorithm to determine a list of all the walls and edges that are visible for the required order of ray interaction. This visibility list, also known as the image-tree, is then used to compute the valid rays for all the receiver points. Many efficient visibility algorithms have been proposed in literature. Most of these techniques have been adopted from computer graphics to find the visible surfaces for both indoor and outdoor environments [48, 56, 54, 51, 49]. Maurer *et al.* [48] proposed *back face culling* to discard the facets that are not facing towards the transmitter. A sweep-line algorithm with polygon subtraction is applied on the 3-D vector data of the buildings projected in the 2-D plane to determine the visible surfaces. The binary space partitioning (BSP) algorithm [49] creates a binary tree structure of visible nodes based on the half-plane in front of each face. This tree structure quickly identifies the facets between the transmitter and the receiver nodes. Santini *et al.* [169] proposed the BSP algorithm for facet-to-RX and line space partitioning for facet-to-facet visibility. Ng *et al.* [54] combined the BSP algorithm with a quad-tree approach for efficient visibility computations. The model applies *occlusion culling* to discard the facets that lie in the shadow regions of visible facets. An overview of these visibility algorithms has already been presented in section 3.3.

The visibility algorithms are performed for a given location of the transmitter or receiver. The visibility check must be performed each time the transmitter changes its location. This increases the pre-processing time of the ray-tracing model and limits its application for mobile transmitter scenarios such as are found in vehicular networks[170]. An efficient technique proposed by Hoppe *et al.* [116–119] divides the building walls into tiles and edges into segments. An exhaustive pre-processing computes the tiles and segments that are visible to each tile and segment for all the buildings. This visibility data is used to create a large database of all the possible ray-segments for all the receiver points. The model uses this database to quickly compute the rays for a mobile transmitter.

Instead of computing the visibility between tiles and segments, the model developed in this chapter introduces the off-line pre-computation of intra-visibility between walls and edges in the environment [164]. This intra-visibility database contains the angular range over which each wall or edge is visible to all the other walls and edges. The model uses this database, which is constant for a given static environment, to compute a visibility table for multiple transmitter locations along a linear trajectory. This visibility table contains a collective list of visible walls and edges of required order of ray interaction for multiple transmitter locations along a straight line or a mobile transmitter.

A simplified flow chart of the ray-tracing algorithm is shown in Figure 6.1. The different sections of this flow chart will be explained in the later sections of this chapter. Please note that in the remainder of this chapter, the index M will be used for number of transmitter points for which the ray tracing is to be performed, k will be used for the order of ray interaction to be computed and N will be used to indicate the number of receivers for which the valid rays are to be computed.

6.2 Intra-Visibility Matrix

The walls and vertical edges that are visible to the transmitter may produce the first order rays and form the first order images. A wall illuminated by the transmitter can produce higher order rays only if the ray interacts with the walls and edges that lie in the half-plane in front of the wall. This fact forms the basis of back-face culling and binary space partitioning in efficient visibility algorithms. We also know that a reflected ray can only propagate in a confined lit region. The angles the lit region makes with the corresponding edges of the wall depend on the source location and can be determined using image-theory. This suggests that having the knowledge of visible faces and edges along with their angular positions for a given face can lead us to the computation of higher order rays. The buildings present in a given environment are always static and the visibility of vertical faces and edges with each other, or so-called intra-visibility, remains the same. The list of visible faces and edges to each face and edge of all the buildings can be computed on a once-off basis to obtain an intra-visibility matrix. The angular range over which the faces and edges remain visible can also be computed. This section explains the computation of such an intra-visibility database. Accelerated higher order ray computations for a mobile transmitter that make use of this intra-visibility matrix will be explained in section 6.5.

There are some issues that must be addressed before the intra-visibility matrix can be computed. Firstly, how to compute the face-to-face visibility. Secondly, how to determine the angular range over which a face remains visible to another face. A possible solution is to choose a large number of points on both the faces and check if a direct line of sight exists for any pair of points. An efficient approach is presented here. A face can be divided into a large number, say 180, of equally spaced points. A ray is launched from each point on the face at an angle between 0 and 180 degree to completely scan the half-plane in front of the face. The number of rays do not have to be 180 as a smaller number of rays can be enough to fully scan the half-plane in front of the face. A coarse grid is superimposed on the environment and the buildings are mapped to the grid-squares in which they reside. A ray is launched from the face at specified angle and is tested for intersection with grid-squares. All the buildings in the grid-square in which the ray first enters are tested for intersection with this ray. If the ray intersects a building, the visible face is found. Otherwise the ray is tested for

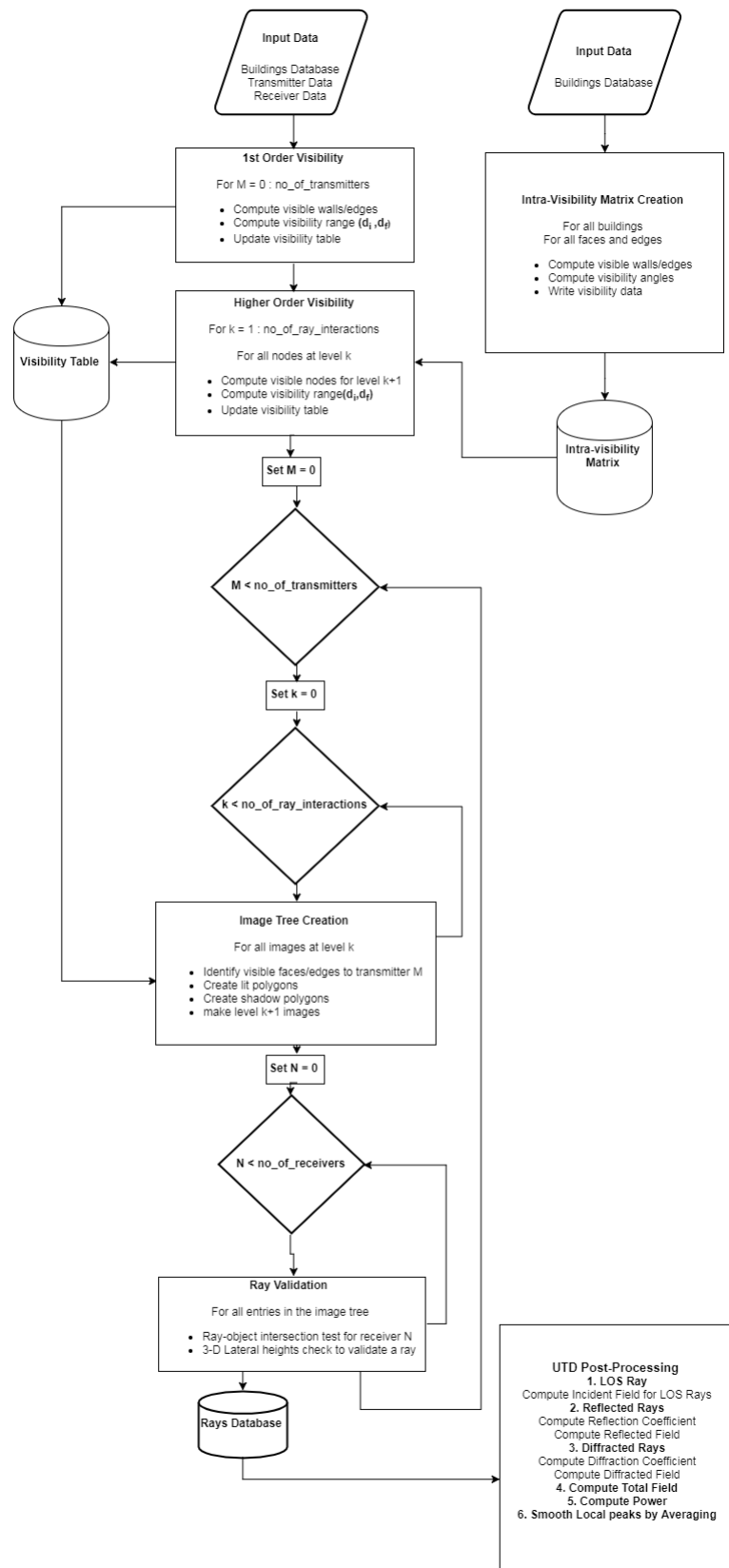


Figure 6.1 Flow Chart of Ray-tracing Algorithm for Mobile Transmitter

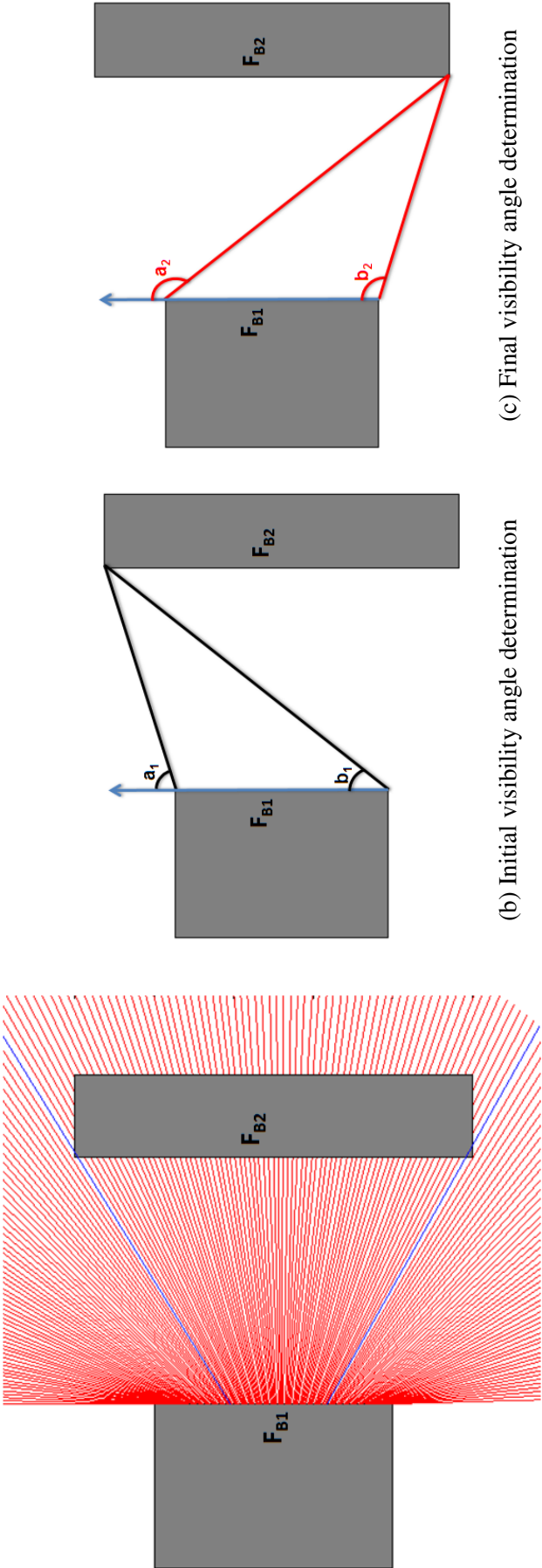


Figure 6.2 Determination of visibility angles for a completely visible face.

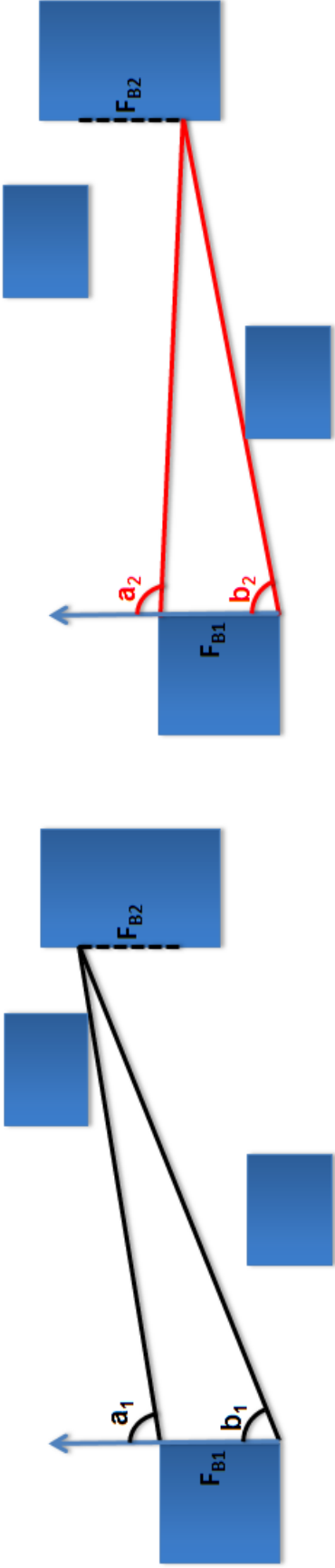
intersection with the buildings in the next grid-square it enters until a valid intersection is found or the ray goes out of the coverage boundary.

Once a valid visible face is found, we must also be able to determine the angular range over which it remains visible. If a face remains visible for more than one consecutive launched rays, the face is visible over a range of angles. Since the rays are being launched from different points at the face, we cannot determine the exact angular range. In fact we need a fixed reference point to determine the angular range. Recalling that the lit region makes certain angles with both the edges of a face that determines the area where higher order rays can possibly propagate. we therefore chose both edges of the given face as fixed reference points for angular range determination.

The idea can be further explained with the help of Figure 6.2. Rays are launched clockwise from the face F_{B1} so that the face F_{B2} is completely visible to it as shown in 6.2a. The face F_{B2} remains visible for a large number of rays between an initial and a final ray shown in blue. The intersection point of the initial and final ray with the face F_{B2} is the initial and final point that is visible to F_{B1} . The angles of both the intersection points with the edges of face F_{B1} are computed. The first set of angles from both edges of face F_{B1} to the initial intersection point are given as a_1 and b_1 as shown in Figure 6.2b. These angles (a_1, b_1) are shown in black and will be referred to as the initial visibility angles in the following discussions. The maximum angle for which the face F_{B2} remains visible is also computed with respect to both edges of face F_{B1} as a_2 and b_2 as shown in Figure 6.2c. These angles (a_2, b_2) are shown in red and will be referred to as final visibility angles in the following discussions. The initial and final visibility angles thus define, for a given face, the angular extent over which it remains visible to another face. Figure 6.3 shows the initial and final visibility angles computation for a partially visible face.

For face-to-edge visibility, we only need to compute one set of angles as an edge is always fixed as shown in Figure 6.4. The visibility angles are computed for reflection images to later compare against the lit polygon angles for higher order rays computations. For edge-to-face and edge-to-edge visibility, we do not need to compute the angular range over which a face or edge is visible to an edge. This is due to the fact that a diffraction ray spreads in all directions external to the walls that make the edge. A face or an edge visible to an edge can always produce a higher order ray irrespective of the source location.

An algorithm is developed to compute the intra-visibility matrix for all the faces and edges of all the buildings in the environment. All the visible faces and edges to a given face along with the visibility angles are computed. On the other hand only the visible faces and edges are computed for a given edge. The database is computed on a once-off basis and saved into a file for later use.



(a) Initial visibility angle determination

(b) Final visibility angle determination

Figure 6.3 Determination of visibility angles for a partially visible face.

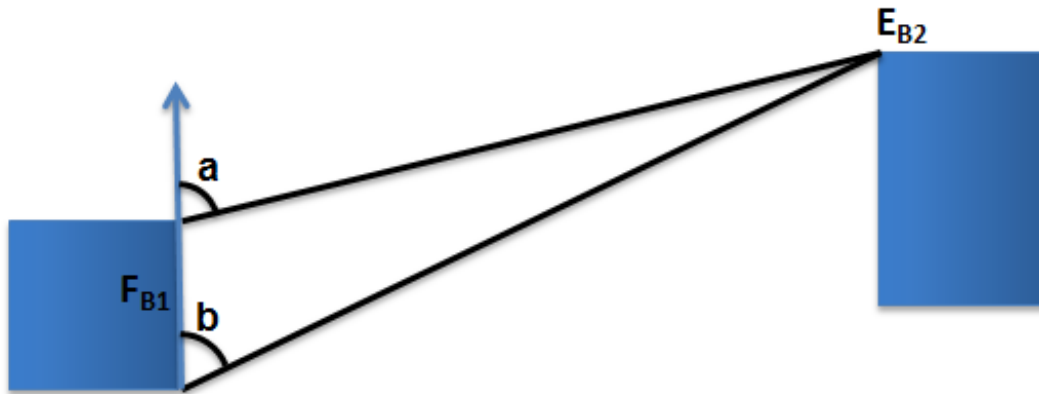


Figure 6.4 Intra-visibility angles computation for an edge visible to a face.

Algorithm 6 Intra-Visibility Matrix Computation

Input Data: building data;
Output Data: Intra-Visibility Matrix;
for $i=0; i < \text{number_of_buildings}; i++$ **do**
 the_building = Buildings_list[i];
 for $j=0; j < \text{number_of_faces}; j++$ **do**
 identify visible faces and edges;
 compute visibility angles;
 write visibility data;
 for $k=0; k < \text{number_of_edges}; k++$ **do**
 identify visible faces and edges;
 write visibility data;

6.3 Initial Model

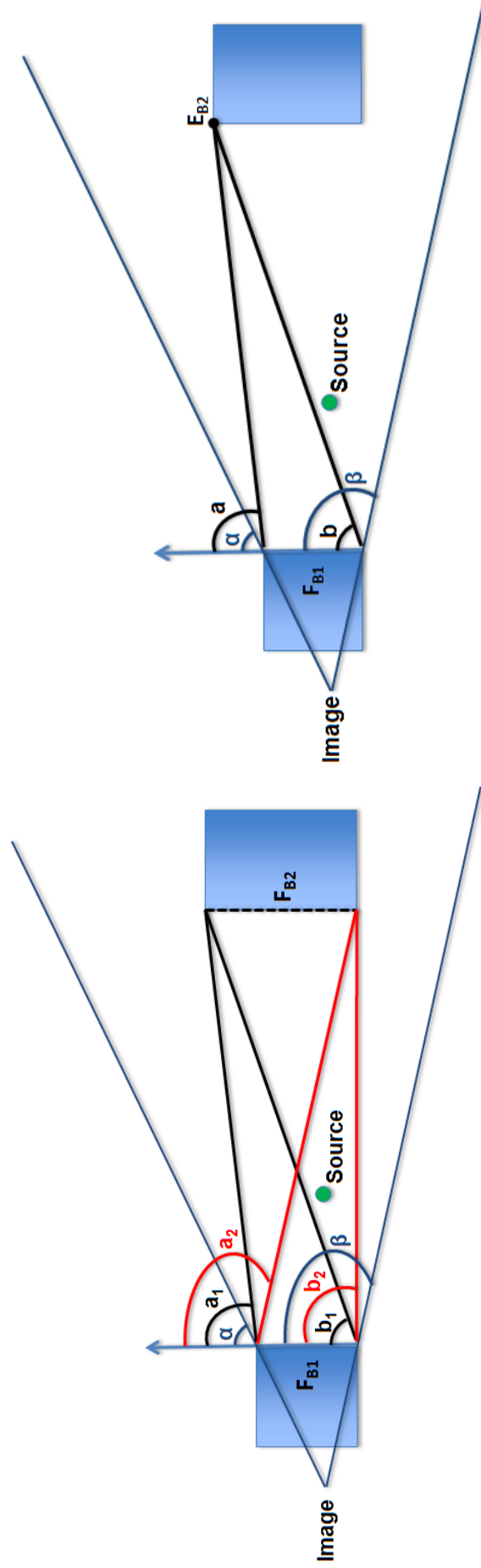
The intra-visibility matrix computation simplifies the recursive visibility algorithm for higher order visibility computations. Once the faces and edges visible to a given transmitter are known, the higher order visible nodes that can produce the higher order rays can be efficiently computed. To see how the intra-visibility matrix can be useful in identifying higher order visible nodes for a given source consider the situation in Figure 6.5a. The face F_{B1} is visible to a source, say transmitter, such that the lit region where the first order reflection rays can possibly propagate having reflected from the face F_{B1} makes the angles α and β with the edges of face F_{B1} as shown. The initial and final visibility angles of face F_{B2} with respect to both the edges of face F_{B1} are (a_1, b_1) and (a_2, b_2) respectively as shown. The face F_{B2} will be visible to face F_{B1} , and consequently will produce a higher order image, only if the face F_{B2} is contained, completely or partially within the lit region. This can only be true if at least one of the following conditions is true.

$$\begin{aligned} (a_1 > \alpha) \wedge (b_1 < \beta) \\ (a_2 > \alpha) \wedge (b_2 < \beta) \end{aligned} \tag{6.1}$$

Likewise for an edge E_{B2} to be visible to the face F_{B1} , the visibility angles (a, b) are compared with the lit polygon angles α and β . The comparison is carried out to make sure the edge is contained within the lit polygon as shown in the Figure. The following condition must be true for edge E_{B2} to be visible to face F_{B1} to produce a higher order image.

$$(a > \alpha) \wedge (b < \beta) \tag{6.2}$$

A ray tracing model has been developed that makes use of the intra-visibility matrix to simplify the higher order visibility computations. As before the list of faces and edges visible to the transmitter are simply computed using a polar sweep algorithm. The faces visible to the transmitter are used to compute the shadow polygons for zeroth order transmitter image. All the faces and edges visible to the transmitter form the first order images and the associated lit polygons are computed. The algorithm computes the visible nodes for both reflection and diffraction images using the intra-visibility matrix. A wall or an edge visible to a source, transmitter or a higher order image, can be represented by a node in the image-tree structure. The term node is therefore used interchangeably for a wall or an edge that is visible to a source in the following discussions. For diffraction images, the algorithm simply fetches all the visible faces and edges from the intra-visibility matrix that form the higher order images. The algorithm also fetches the list of all the nodes visible to the face corresponding to a reflection image. The lit polygon angles α and β for the reflection image are compared



(a) Higher order visible face determination using intra-visibility matrix

(b) Higher order visible edge determination using intra-visibility matrix

Figure 6.5 Determination of higher order images using intra-visibility matrix.

with the visibility angles of all the visible nodes one by one to check for valid higher order images. A recursive algorithm has been developed to compute the image-tree with all the corresponding lit and shadow polygons for required order of ray interaction.

The proposed ray tracing model is used to compute the intra-visibility matrix for Munich database. The database contains 2,088 buildings with 17,445 vertical walls and 17,445 vertical edges. The database is later used to compute the second order image-tree for the same location of the transmitter as used in the measured data discussed in previous chapter. A second order image-tree requires the computation of shadow polygons formed by the faces that are visible to second order images. Therefore the visibility computations are performed for up to third order. The proposed algorithm took 50 minutes to compute the second order image-tree as compared to 2 hours required for the polar sweep method. A reduction of 52% in image-tree computation time is thus observed as compared to the recursive visibility algorithm.

6.4 Ray tracing for a Mobile Transmitter

A time efficient pre-processing technique for image-tree creation is presented in the previous section. The intra-visibility matrix simplifies the recursive visibility algorithm and computes the image-tree for required order of ray interaction efficiently. The proposed algorithm can be extended to compute the image-tree at discrete points along a mobile transmitter route. This approach will be faster than a recursive visibility algorithm as seen in the previous section. However, it may not be the most efficient technique to find the visible faces and edges for a mobile transmitter.

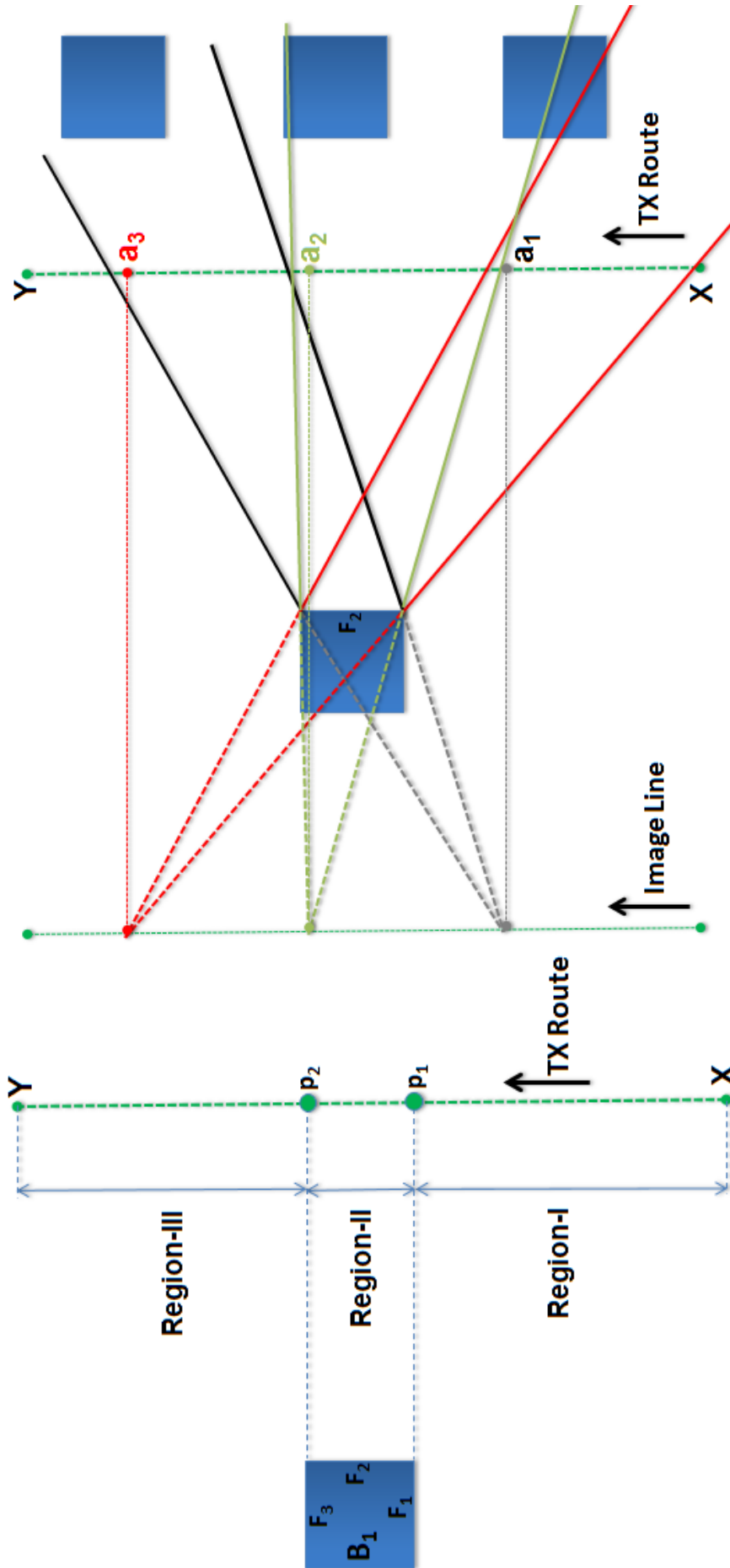
To further understand the ray tracing for a mobile transmitter consider the scenario shown in Figure 6.6. A mobile transmitter moves past a building B_1 as it travels from point X to Y . Three distinct regions can be identified along the transmitter route namely region I from X to p_1 , region II from p_1 to p_2 and region III from p_2 to Y . The faces F_1 and F_3 remain visible to the transmitter in region-I and region-III only respectively. The face F_2 remains visible to the transmitter for the entire length of the transmitter route from X to Y . Having the knowledge of a face that remains visible to the transmitter for a specified length along the route raises the question as to whether this information can be used to help with the production of higher order images. The inherent characteristic of the mobile transmitter is that the lit region associated with the face illuminated by the transmitter keeps changing as the transmitter moves past it. This suggests that the faces and edges that are visible to the illuminated face that produce the higher order images also change with the motion of the transmitter. This is shown for the example that we just discussed in Figure 6.6b. We can see that different buildings and their respective faces become visible to face F_2 of building B_1 at transmitter locations a_1 , a_2 and a_3 along the route. The lit polygons formed by the face F_2 are also shown for three transmitter locations considered along the route.

Algorithm 7 Image-tree computation using the intra-visibility matrix

```

Input Data: TX location, Intra-visibility matrix, Buildings data, order_of_ray_interaction;
Output Data: Image-tree;
image_level = 0;
number_of_images = 1;
image_list = [TX];
identify visible faces and edges to TX;
image_level++;
populate image_list;
for i=1; i < order_of_ray_interaction; i++ do
  for all images at ith image_level do
    the_image = image from the image_list;
    identify building_index associated with the_image;
    the_type = the_image.listtype();      ▷ 1 for reflection; 2 for diffraction.
    identify the_image lit polygon;
    if the_type = 1 then
      identify face_index associated with the_image;
      identify lit polygon angles  $\alpha$  and  $\beta$ ;
      for all nodes visible to face_index from intra-visibility matrix do
        the_node = visible node from intra-visibility matrix;
        identify the_node_type;          ▷ 1 for face; 2 for edge
        if the_node_type = 1 then      ▷ face-to-face visibility
          identify visibility angles  $(a_1, b_1)$  and  $(a_2, b_2)$ ;
          if  $(a_1 > \alpha) \wedge (b_1 < \beta)$  then
            valid visible face found;
            make  $(i + 1)$ th order image and add to image_list;
          else if  $(a_2 > \alpha) \wedge (b_2 < \beta)$  then
            valid visible face found;
            make  $(i + 1)$ th order image and add to image_list;
          else if the_node_type = 2 then      ▷ face-to-edge visibility
            identify visibility angles  $(a, b)$ ;
            if  $(a > \alpha) \wedge (b < \beta)$  then
              valid visible edge found;
              make  $(i + 1)$ th order image and add to image_list;
        else if the_type = 2 then
          identify edge_index associated with the_image;
          for all nodes visible to edge_index from intra-visibility matrix do
            the_node = visible node from intra-visibility matrix;
            identify the_node_type;
            if the_node_type = 1 then      ▷ edge-to-face visibility
              valid visible face found;
              make  $(i + 1)$ th order image and add to image_list;
            else if the_node_type = 2 then      ▷ edge-to-edge visibility
              valid visible edge found;
              make  $(i + 1)$ th order image and add to image_list;
      populate image_list;

```



(b) Lit polygons for the wall reflection at three different transmitter locations

(a) A simple scenario of a mobile transmitter

Figure 6.6 Consideration of constantly varying lit polygon associated with a wall reflection visible to a mobile transmitter.

This suggests that we must also be able to distinguish how the higher order visibility will change for a mobile transmitter. The angular information computed in the intra-visibility matrix can be helpful to establish the higher order visible nodes. A ray tracing model is developed that can efficiently compute the required order of image-tree for a mobile transmitter. The model is explained in the following section.

6.5 Development of Pre-Processed Ray tracing for a Mobile Transmitter

The proposed model computes a *visibility table* that contains the walls and edges visible to a mobile source. The mobile source can be the actual moving transmitter or a virtual (image) source which also moves, due to the motion of the primary transmitter. The visibility table is computed for the desired order of ray interaction using the intra-visibility matrix. The use of the visibility table to compute the image-tree for a given transmitter location along the transmitter route is also presented.

6.5.1 Determination of First Order Visible Walls and Vertical Edges

A particular face may be visible to the mobile transmitter for a certain distance along the transmitter route. The determination of transmitter route length along which a face is visible to the mobile transmitter is thus vital as discussed in the previous section. Visual inspection for a simple environment such as discussed in previous section in Figure 6.6a can give the route length along which a face or an edge remains visible to the mobile transmitter. However determination of this distance for visible faces and edges in a dense urban environment is not straightforward. A face can be obstructed by buildings and may only be visible to the transmitter route for very short duration. A simple approach is to divide the mobile route into discrete points separated by a small distance. The faces and edges visible at each transmitter point along the route is determined. If a face remains visible for more than one consecutive points along the route, the distance for which it remains visible can be computed. The starting point of the algorithm is thus to perform a visibility check for all the transmitter points along the linear route. The location along the transmitter route at which each face and vertical edge becomes visible is determined, as is the location at which they stop being visible. This provides a list of all visible walls and vertical edges as well as the distance along the route for which they remain visible.

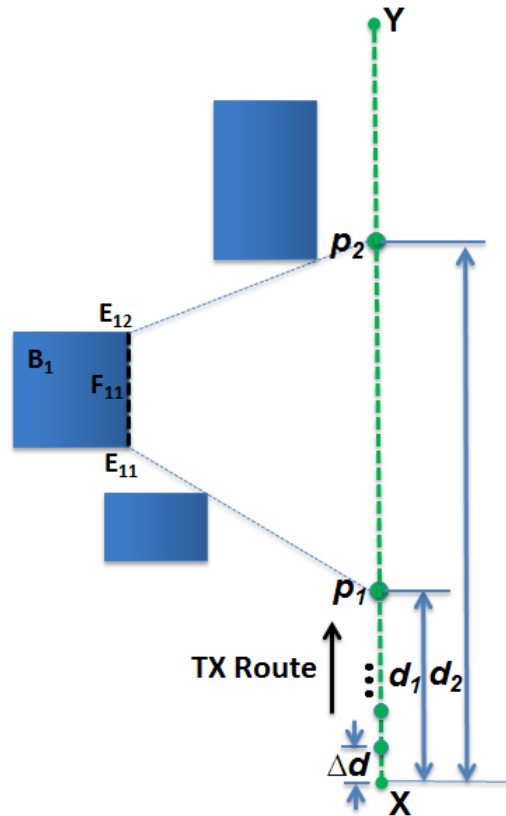


Figure 6.7 An example environment with a transmitter moving from X to Y . Two buildings block the visibility for face F_{11} and edges E_{11} and E_{12} so that they are only visible between the distance d_1 and d_2 from X .

The algorithm can be further explained with the help of Figure 6.7. There are three buildings shown in the environment and the transmitter moves along the route from X to Y as shown. The transmitter route is divided into M points that are Δd distance apart from each other. The algorithm starts by performing a visibility check at location X and proceeds to identify the vertical faces and edges that are visible at all points along the route. The initial distance from start point X at which a particular face or edge becomes visible (d_i) and the maximum distance for which it remains visible (d_f) is also computed. After performing the visibility check for all transmitter points along the route, a visibility table is created that contains all the first order nodes along with the distance over which they are visible. As we can see that there are two buildings that obstruct the visibility of building B_1 so that the face F_{11} and edges E_{11} and E_{12} are visible to the transmitter line only between the points p_1 and p_2 located at distance d_1 and d_2 from the start point X respectively. The respective visibility table entries can be shown in Table 6.1.

We compute the visibility for a sampling of transmitter points along the line. It is apparent that choosing a smaller Δd will give the closest distance at which a face or an edge becomes visible or stop being visible to the transmitter line. The minimum value

Table 6.1 Visibility table entries for building B_1 in Figure 6.7.

Order	Visible Node	Visibility Range		Parent Node
		d_i	d_f	
1	F_{11}	d_1	d_2	TX
1	E_{11}	d_1	d_2	TX
1	E_{12}	d_1	d_2	TX

of Δd should be chosen to give a sampling of transmitter points equal to the number of transmitter locations for which ray-tracing has to be performed along the route.

6.5.2 Determination of Higher Order Visible Nodes for Wall Reflection Images

After computing the visibility table for all transmitter locations, it has been established which faces are visible at which locations along the transmitter route. It has already been discussed that the lit region for the same visible face will vary with transmitter location thereby changing the higher order visible nodes. This section explains how image theory and angular information from the intra-visibility matrix can be used to quickly determine which higher order nodes will be visible as the transmitter moves along its linear route. The exact distance for which each higher order node remains visible is also computed.

Consider again the example shown in Figure 6.7 in which the face F_{11} of building B_1 is visible to the transmitter as long as it is between d_1 and d_2 distance from the start point X . This figure is recreated in Figure 6.8 but the obstructing buildings have been omitted for clarity. For the transmitter at distance d_1 from X , a lit region within which the first order reflection rays propagate can be constructed using image theory. As the transmitter moves from distance d_1 to d_2 , the lit region of the first order reflection image changes for each transmitter location along the route. Figure 6.8 shows the lit regions formed for the start point located at d_1 distance and the finish point located at d_2 distance from X with black and red lines respectively. The respective image points that produce the lit region for each transmitter location are located on a line labelled 1st order image line. The angles α and β of the lit regions with both the edges of the face F_{11} as discussed in the previous section change from α_1, β_1 to α_2, β_2 as the transmitter moves from d_1 to d_2 . The region in front of face F_{11} bounded by α_1 and β_2 is the union of all the lit regions and is thus the *maximum visibility region* in which rays reflected from F_{11} can travel as the transmitter moves between d_1 and d_2 . For any face or edge to be visible to F_{11} and consequently produce a second order image, it must lie (completely or partially) within this maximum visibility region.

As discussed earlier the angular information available from the intra-visibility matrix can be used to easily identify the faces and edges that will lie within this region. However, we must also determine the exact location between d_1 and d_2 for which a face

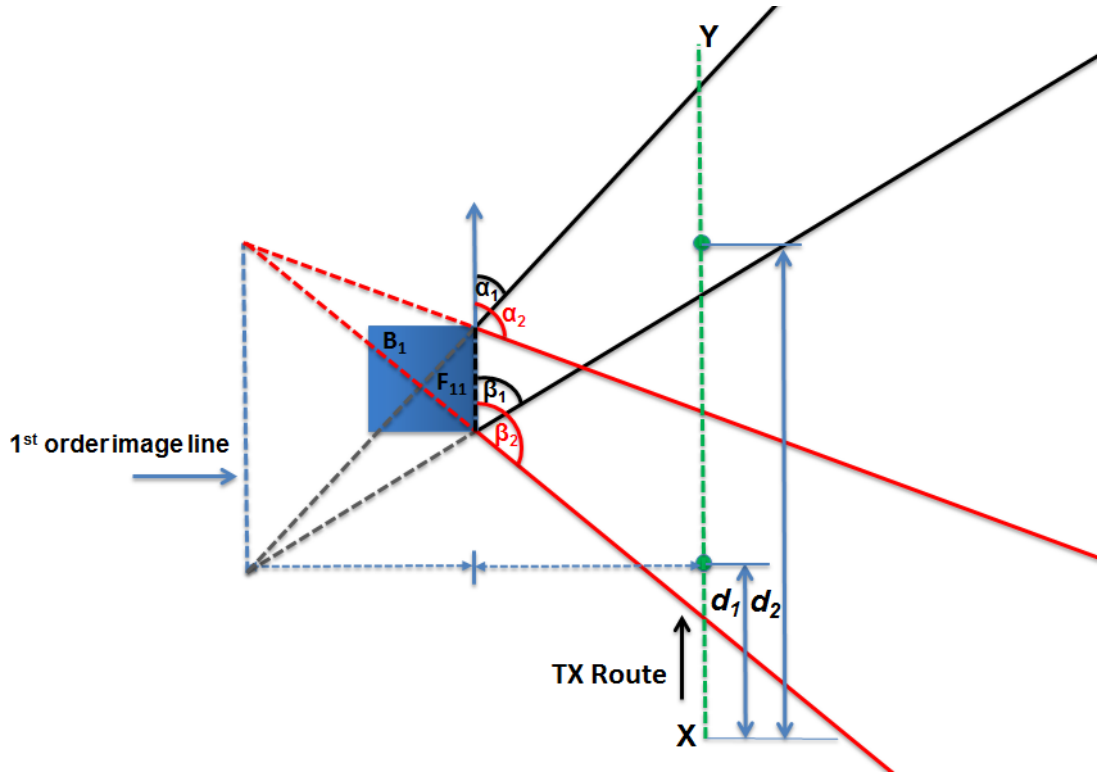


Figure 6.8 Face F_{11} is visible to the mobile transmitter between distance d_1 and d_2 . The maximum visibility region of first order visible face F_{11} is bounded by α_1 and β_2 lines as shown.

or edge remains visible to F_{11} . In other words, we must also find the distance d_i and d_f for each face and edge visible to face F_{11} for the visibility table.

The face F_{11} will be referred to as the illuminated face in the following discussion as it is already visible to the transmitter line. Since the visibility of a face depends on two sets of angles, namely the initial visibility angles (a_1, b_1) and final visibility angles (a_2, b_2) the determination of higher order visible faces depending on their location within the maximum visibility region can be determined for different scenarios as follows.

CASE-I: Initial visibility angles are within the maximum visibility region $((a_1 > \alpha_1) \wedge (b_1 < \beta_2))$

If a face is visible to the illuminated face such that its initial visibility angles (a_1, b_1) are within the maximum visibility region defined by the boundary lines α_1 and β_2 , the distance for which this face remains visible is computed as follows. Referring to Figures 6.9 and 6.10 we see that Face F_{11} is illuminated when the transmitter is between d_1 and d_2 distance from start point X (again we have omitted the obstructing buildings for clarity). We are interested to find the distance for which face F_{m1} and F_{n1} that are located at different locations within the maximum visibility region are visible to F_{11} to make higher order images. First we must find the distance (d_i) at which a face becomes visible. It is possible that a face is visible to the illuminated face as soon as

the illuminated face itself becomes visible to the transmitter. This can be seen in Figure 6.9a where face F_{m1} of building B_m is contained within the lit polygon formed for the transmitter location at d_1 . This can be verified by comparing the initial visibility angle b_1 with the lit polygon angle β_1 . In the figure for clarity we do not show the angle b_1 but instead show the line defined by it (in purple). The condition ($b_1 < \beta_1$) means that the face is visible to the illuminated face to make a higher order image as soon as the illuminated face becomes visible to the transmitter line. Thus the initial distance d_i at which face F_{m1} becomes visible to the illuminated face can be given as,

$$d_i = d_1 \quad ; \text{for } (b_1 < \beta_1)$$

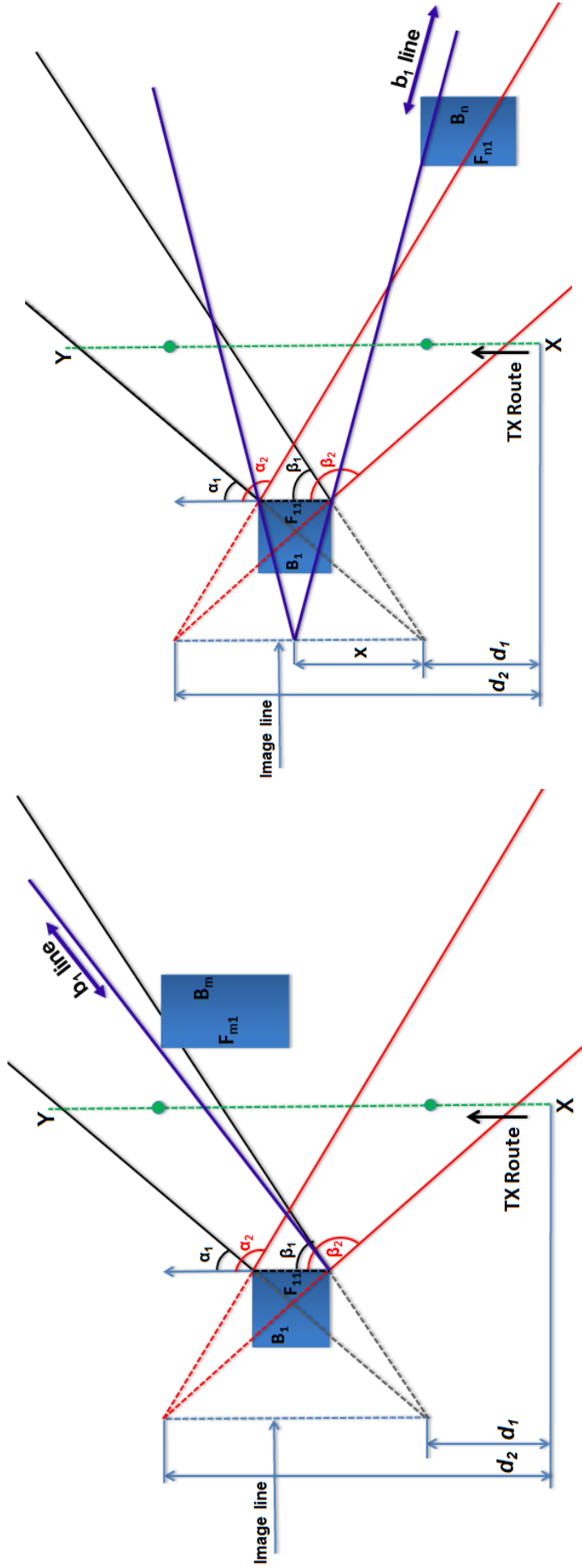
In contrast if a face is not immediately visible to the illuminated face (i.e. $b_1 > \beta_1$) then it is trivial to compute a distance x travelled by the transmitter along the route such that a lit polygon is formed with angle $\beta = b_1$ of the corresponding face. This is shown for face F_{n1} in Figure 6.9b that becomes visible to F_{11} to make a higher order image as the angle β formed by the lit polygon coincides with the b_1 angle of the face F_{n1} . x is located between d_1 and d_2 and can simply be found by the intersection of b_1 line of face F_{n1} with the first order image line as shown. It can be seen from the figure that F_{n1} becomes visible to F_{11} only when the transmitter is located at or above $d_1 + x$. In other words, if a face is contained within the maximum visibility region and is not immediately visible to an illuminated face, we can compute the transmitter location at which it becomes visible by intersection of b_1 line with the image line.

$$d_i = d_1 + x \quad ; \text{for } (b_1 > \beta_1)$$

To find the maximum distance d_f for which a face remains visible, the algorithm checks the angle a_2 corresponding to the final visibility angles. If the final visibility angle a_2 of a face is larger than the maximum visibility polygon angle α_2 then the face remains visible to the illuminated face until the final transmitter location at which the illuminated face itself remains visible to the transmitter line. This is shown for example in Figure 6.10a for face F_{n1} of B_n that remains visible to F_{11} to make a higher order image until the distance d_2 . Again, for clarity we do not show the angle a_2 but instead show the line defined by it (in purple).

$$d_f = d_2 \quad ; \text{for } (a_2 > \alpha_2)$$

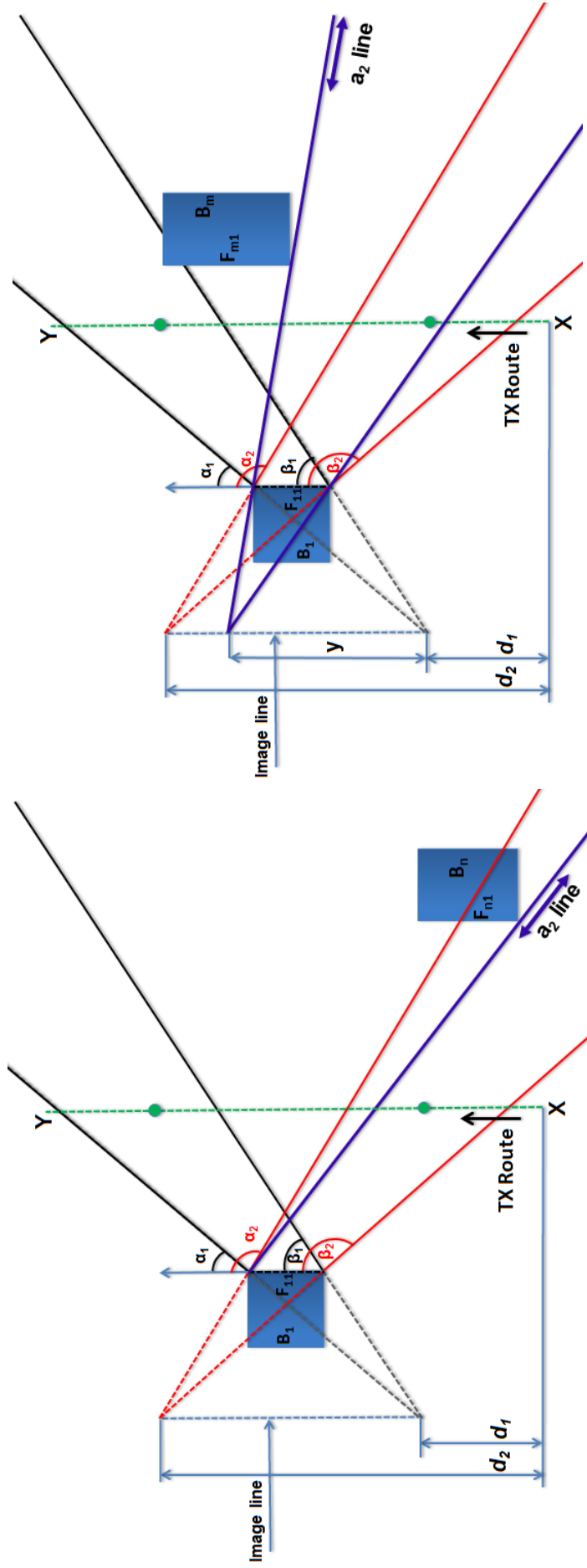
However, if a face does not remain visible to the illuminated face for the entire extent that the illuminated face is visible to the transmitter, then the corresponding maximum distance y for which it remains visible is found by intersection of a_2 line with the image line as shown in Figure 6.10b. The lit polygon can be seen corresponding to the maximum distance $d_1 + y$ for which F_{m1} remains visible to F_{11} to make a higher



(a) Face F_{m1} is visible corresponding to transmitter location at d_1 for $b_1 < \beta_1$

(b) Face F_{n1} becomes visible to transmitter location at $d_1 + x$ for $b_1 > \beta_1$

Figure 6.9 CASE-I: Computation of initial distance d_i at which a face becomes visible to an illuminated face. The initial visibility angles (α_1, b_1) of faces F_{m1} and F_{n1} are within the maximum visibility region of face F_{11} .



(a) Face F_{n1} remains visible corresponding to transmitter final location at d_2 for $a_2 > \alpha_2$
 (b) Face F_{m1} remains visible corresponding to transmitter location at $d_1 + y$ for $a_2 < \alpha_2$

Figure 6.10 CASE-I: Computation of final distance d_f for which a face remains visible to an illuminated face.

image. The face F_{m1} will not be visible to the illuminated face F_{11} for a transmitter located beyond $d_1 + y$ distance.

$$d_f = d_1 + y \quad ; \text{ for } (a_2 < \alpha_2)$$

CASE-II: Final visibility angles are within the maximum visibility region ($(a_2 > \alpha_1) \wedge (b_2 < \beta_2)$)

If the initial visibility angles (a_1, b_1) of a face are not within the maximum visibility region formed by the illuminated face, the algorithm instead checks the final visibility angles (a_2, b_2) . If the final visibility angles of a face are within the maximum visibility region such that $(a_2 > \alpha_1) \wedge (b_2 < \beta_2)$, the face will be visible to the illuminated face to make a higher order image as soon as the illuminated face becomes visible to the transmitter. This can be seen in Figure 6.11 where the face F_{m1} has the final visibility angles (a_2, b_2) confined within the maximum visibility region and becomes visible to illuminated face F_{11} for the transmitter location at distance d_1 . So that,

$$d_i = d_1 \quad ; \text{ for } (a_2 > \alpha_1) \wedge (b_2 < \beta_2)$$

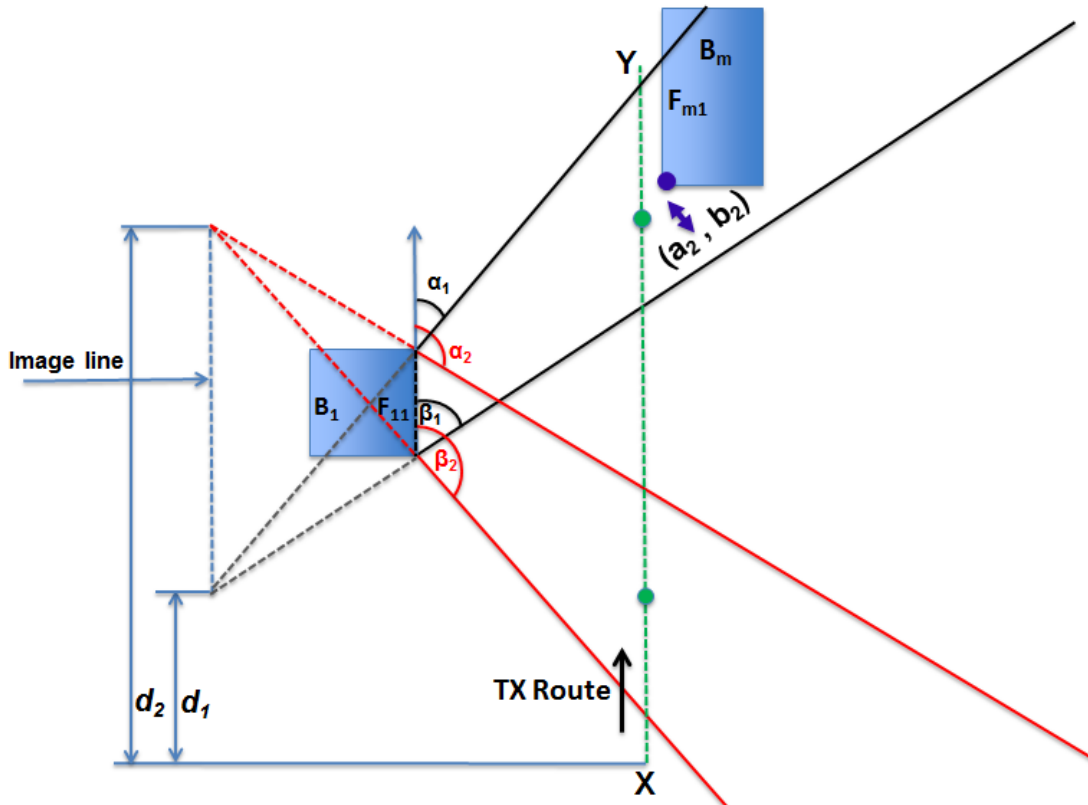


Figure 6.11 CASE-II: Final visibility angles of face F_{m1} are within the maximum visibility region of illuminated face F_{11} . F_{m1} becomes visible to F_{11} corresponding to transmitter location at d_1 .

To find the maximum distance d_f for which it remains visible, the algorithm performs similar checks to those described in the previous section comparing the final visibility angle a_2 of the face with α_2 . It can be shown that

$$d_f = d_2 \quad ; \text{ for } (a_2 > \alpha_2)$$

Otherwise, a distance y can be computed by intersection of the a_2 line with the first order image line to give the maximum distance d_f as,

$$d_f = d_1 + y \quad ; \text{ for } (a_2 < \alpha_2)$$

CASE-III: Face remains fully visible for the entire length of illuminated face(($a_1 < \alpha_1$) \wedge ($b_2 > \beta_2$))

It is also possible that both the initial and final visibility angles of a face are not contained within the maximum lit region although it is fully visible to the illuminated face. An example of such a scenario is shown in Figure 6.12 as the face F_{m1} remains fully visible to F_{11} for the entire length of the transmitter's travel from d_1 to d_2 . The distance for which face F_{m1} remains visible to make a higher order image can be simply given as,

$$d_i = d_1 \quad ; \text{ for } (a_1 < \alpha_1) \wedge (b_2 > \beta_2)$$

$$d_f = d_2 \quad ; \text{ for } (a_1 < \alpha_1) \wedge (b_2 > \beta_2)$$

CASE-IV: Determination of a vertical edge visible within the maximum visibility region

The different scenarios discussed above consider face-to-face visibility for higher order reflections. However, vertical edges are also visible to an illuminated face that may produce reflection followed by diffraction ray-segments. The vertical edges visible to a face are also pre-computed during the intra-visibility matrix computation. Since a vertical edge is visible at a fixed angle, we only have one set of visibility angles (a , b) for the edges. The visibility check for an edge becomes a generalised case and the distances d_i and d_f can be computed using the same approach discussed above for CASE-I so that,

$$a_1 = a_2 = a$$

$$b_1 = b_2 = b$$

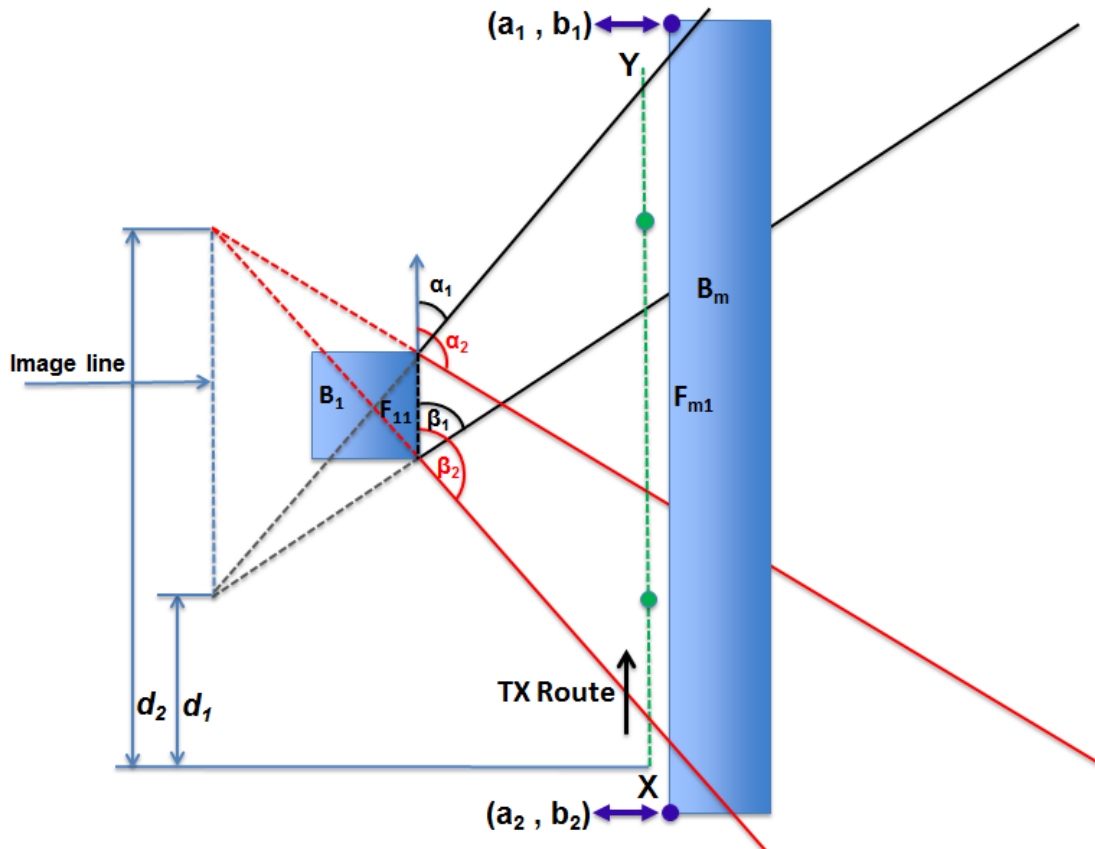


Figure 6.12 CASE III: Face F_{m1} remains visible to illuminated face F_{11} for the entire length of multiple transmitters between d_1 and d_2 .

6.5.3 Direction of the Mobile Transmitter

The visibility distance computations discussed earlier consider that the mobile transmitter is moving towards the illuminated face such that the final lit polygon angles (α_2, β_2) are higher than the initial lit polygon angles (α_1, β_1). In other words, the change in lit polygon angles defined as the difference between the final and initial lit polygon angles ($\Delta\alpha, \Delta\beta$) is positive. Consider the same example in Figure 6.7 with the transmitter moving in opposite direction from Y to X as shown in Figure 6.13. The face F_{11} is visible to the transmitter route between distance d_1 and d_2 from Y as shown. The change in lit polygon angles is negative in this case. i.e. ($\Delta\alpha < 0, \Delta\beta < 0$). As we can see that the maximum visibility polygon is now defined between α_2 and β_1 lines instead of α_1 and β_2 lines in previous example.

To find the distance for which a face remains visible to the illuminated face can therefore be redrawn in Figures 6.14 and 6.15. It must be noted that the illuminated face will first see the second edge with visibility angles (a_2, b_2) since the lit polygon scans anti-clockwise as the transmitter moves from Y to X in this case. To find the distances d_1 and d_2 , the approach is changed as follows.

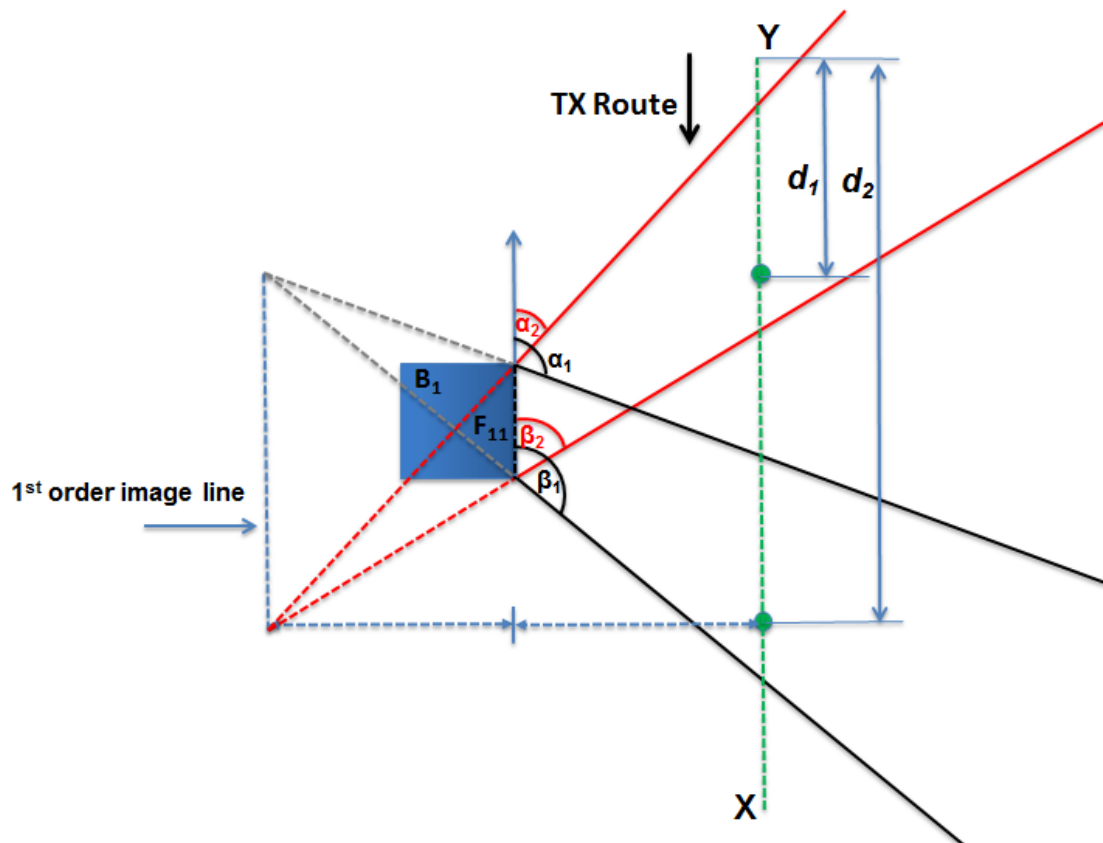


Figure 6.13 Face F_{11} is visible to the mobile transmitter between distance d_1 and d_2 . The maximum visibility region of first order visible face F_{11} is bounded by α_2 and β_1 lines as shown.

A face will be visible to the illuminated face as soon as the illuminated face becomes visible to the transmitter at d_1 if it is contained within the lit polygon formed at d_1 . In this case, this will be true when the final visibility angle (a_2) is higher than the lit polygon angle α_1 formed when the transmitter is at d_1 as shown in Figure 6.14a. The face F_{n1} will produce a higher order image for face F_{11} when the transmitter is at d_1 . If a face is not visible to the illuminated face immediately, again we can find the distance x that the transmitter must move before a face becomes visible to the illuminated face. This is computed for face F_{m1} that becomes visible to the illuminated face at distance $d_1 + x$ when the angle α of the lit polygon formed by it coincides with angle a_2 of the face as shown in Figure 6.14b. The distance x is found by the intersection of a_2 line with the first order image line as shown.

A face will remain visible to the illuminated face until the illuminated face itself remains visible to the transmitter at distance d_2 only if the face is contained within the lit polygon formed at d_2 . This becomes true in this case when the initial visibility angle b_1 is higher than the lit polygon angle β_2 formed when the transmitter is at d_2 . This is shown for face F_{m1} in Figure 6.15a. However if a face does not remain visible to the illuminated face until distance d_2 , we can find the distance y such that it remains visible to the illuminated face up to the distance $d_1 + y$. This is shown in Figure 6.15b for face

F_{n1} that remains visible to the illuminated face at distance $d_1 + y$ when the angle β of the lit polygon formed by it coincides with angle b_1 of the face. The distance y is found by the intersection of b_1 line with the first order image line as shown.

6.5.4 Higher Order Visible Nodes for Vertical Edge Diffraction Images

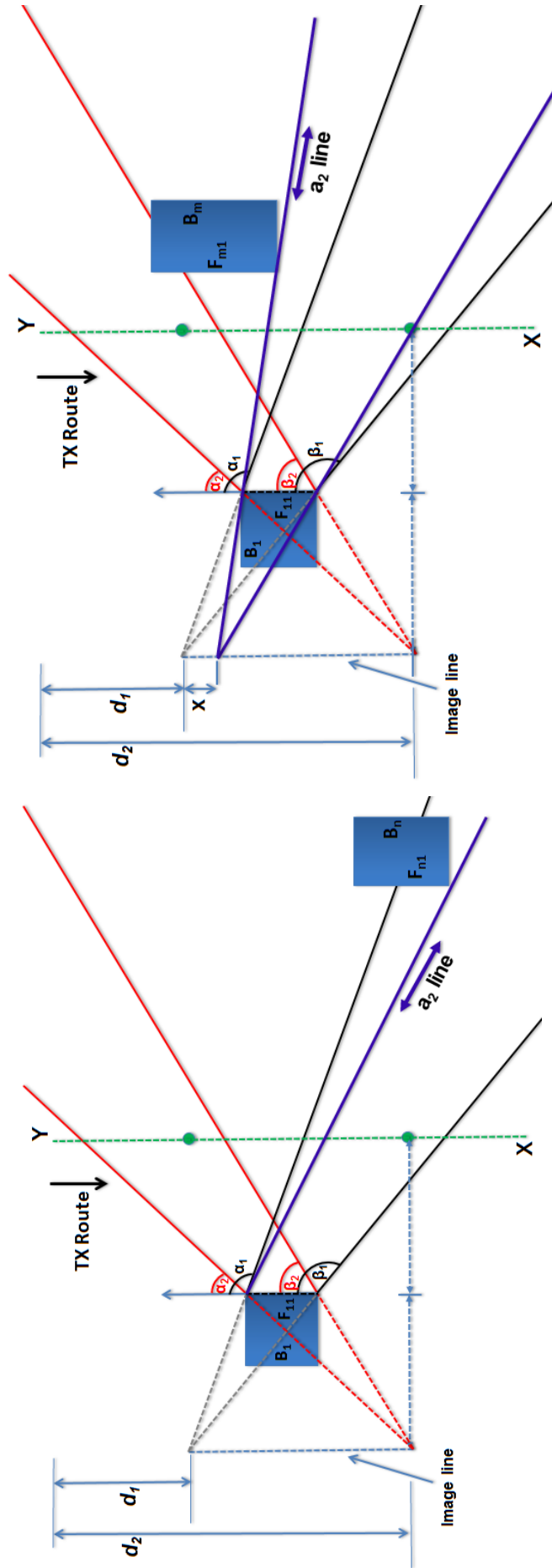
The previous section explains how to determine the vertical faces and edges that are visible to a face illuminated by a transmitter moving along a linear route. The faces and edges that can receive a ray reflected from the illuminated face vary as the transmitter moves. However, the faces and edges that can receive a diffracted ray from an illuminated vertical edge always remain the same and are independent of the transmitter location as it travels. In other words, the faces and edges that are visible to an illuminated edge will form the higher order visible nodes for the entire distance for which the illuminated edge itself is visible to the transmitter. The algorithm simply fetches all the faces and edges visible to an illuminated edge from the intra-visibility matrix and the visibility distance d_i and d_f for each node is the same as for the edge itself.

6.5.5 Image-tree Computation using the Visibility Table

The mobile transmitter produces a continuously changing image-tree as the transmitter location changes. The techniques in the previous section are recursively applied to identify the faces and edges that will produce higher order images along the transmitter route. The distance along the transmitter's trajectory where these higher order nodes appear in (and disappear from) the image tree is also computed. This information is stored in a so-called visibility table.

Figure 6.16 explains the identification of higher order visible faces for the face F_{11} of building B_1 in Figure 6.7 that is visible to the transmitter route between d_1 and d_2 . The obstructing buildings are not shown. Figure 6.16a shows that face F_{21} becomes visible to F_{11} at $d_1 + x_1$ distance where x_1 is specified by the intersection of the b_1 line with first order image line as discussed previously. The face F_{21} remains visible until $d_1 + y_1$ as shown. The distance y_1 is computed by intersection of a_2 line with the first order image line. Similarly, Figure 6.16b illustrates that face F_{31} is visible to F_{21} between $d_{11} + x_2$ and $d_{11} + y_2$, where $d_{11} = d_1 + x_1$. The visibility table given in Table 6.1 can therefore be expanded to include the higher order terms yielding Table 6.2.

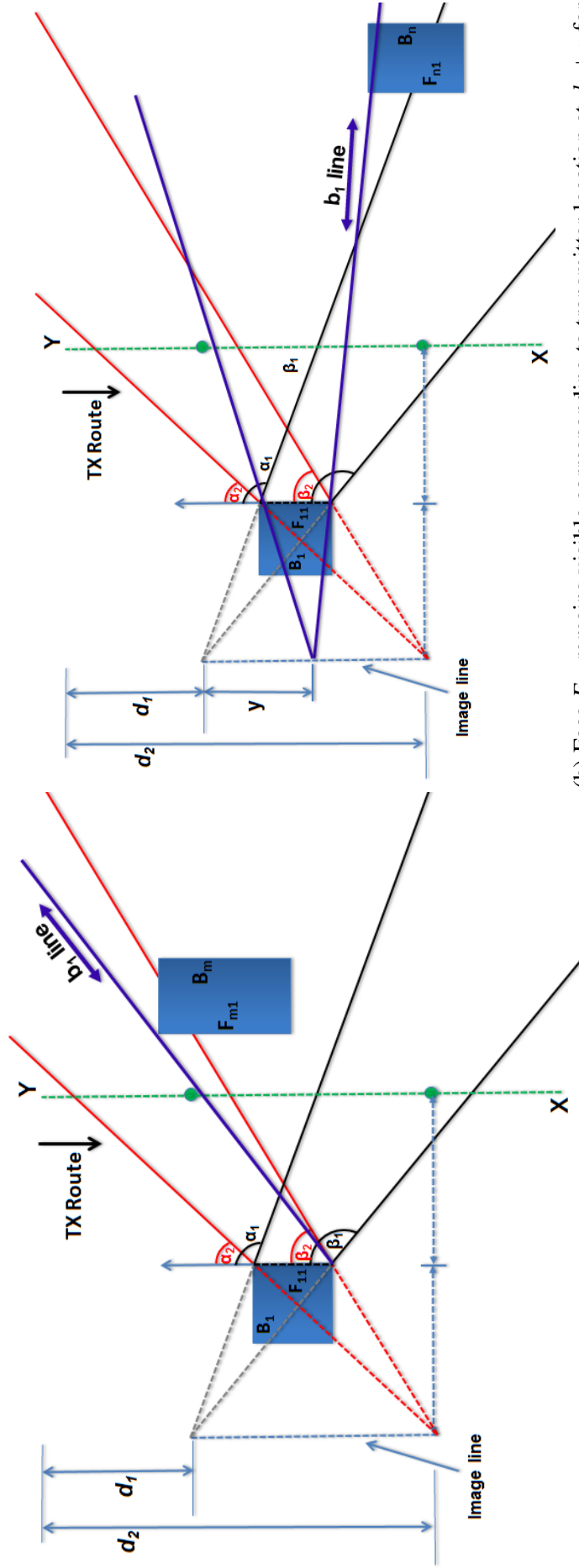
The visibility table can be used to readily determine all the faces and edges that may produce ray segments for *any* transmitter location along its trajectory. Figure 6.17 shows three transmitter locations A , B and C along the mobile route. We are interested to find if the face F_{11} and its higher order visible faces F_{21} and F_{31} are visible to the transmitter at locations A , B and C . Without the visibility table we would need to investigate this



(a) Face F_{n1} is visible corresponding to transmitter location at d_1 for $\alpha_2 > \alpha_1$

(b) Face F_{m1} becomes visible to transmitter location at $d_1 + x$ for $\alpha_2 < \alpha_1$

Figure 6.14 CASE-I: Computation of initial distance d_i at which a face becomes visible to an illuminated face when the transmitter is moving in opposite direction.



(a) Face F_{m1} remains visible corresponding to transmitter final location at d_2 for $b_1 > \beta_2$
 (b) Face F_{n1} remains visible corresponding to transmitter location at $d_1 + y$ for $b_1 < \beta_2$

Figure 6.15 CASE-I: Computation of final distance d_f for which a face remains visible to an illuminated face for transmitter moving in opposite direction.

Table 6.2 Modified Visibility table entries for building B_1 in Figure 6.7.

Order	Visible Node	Visibility Range		Parent Node
		d_i	d_f	
1	F_{11}	d_1	d_2	TX
1	E_{11}	d_1	d_2	TX
1	E_{12}	d_1	d_2	TX
\vdots	\vdots	\vdots	\vdots	\vdots
2	F_{21}	$d_1 + x_1$	$d_1 + y_1$	F_{11}
\vdots	\vdots	\vdots	\vdots	\vdots
3	F_{31}	$d_{11} + x_2$	$d_{11} + y_2$	F_{21}
\vdots	\vdots	\vdots	\vdots	\vdots

independently for the three locations. Instead the visibility table allows us to identify what nodes will be excited simply by identifying how far along the trajectory each transmitter location is. For example, the transmitter A is located at a distance k_1 from the start point X as shown such that $d_1 < k_1 < d_2$. A simple consultation of the visibility table confirms that the face F_{11} will be directly visible to the transmitter at this location as $d_1 < k_1 < d_2$. It can also be noted from the table that the second order face F_{21} becomes visible (via a reflection from F_{11}) to a transmitter only when its location is between $d_1 + x_1$ and $d_1 + y_1$. Thus, the face F_{21} (and so its higher order face F_{31}) will not be visible to the transmitter location A as its relative distance k_1 is less than $d_1 + x_1$. However, the transmitter location B is located above $d_1 + x_1$ and we can conclude that the face F_{11} will be directly visible and the face F_{21} will be indirectly visible (via a reflection from F_{11}) to it. However, the third order face F_{31} will not be visible as the transmitter B is located below the required distance between $d_{11} + x_2$ and $d_{11} + y_2$ as shown. Only the transmitter location C is such that ($d_{11} + x_2 < k_3 < d_{11} + y_2$) meaning that the face F_{11} is directly visible to it and both F_{21} and F_{31} are indirectly visible to it (via a single and double reflection respectively). Thus it is clear that the visibility table allows one to rapidly generate a list of all directly and indirectly visible faces and edges for any transmitter location along the route. Once this list of all visible faces and edges has been determined for a given transmitter location it is a straightforward matter to create an image-tree for the given order of ray interaction. The lit region of an n th order image where an n th order ray can propagate is represented by a lit polygon. The faces and edges visible to the n th order image form the shadow regions for the n th order image as well as the $(n + 1)$ th order images and so on. The algorithm presented here uses lit and shadow polygons to model the image-tree that accelerates the ray-object intersection test for fast ray-tracing as seen in the previous chapter section 5.3.

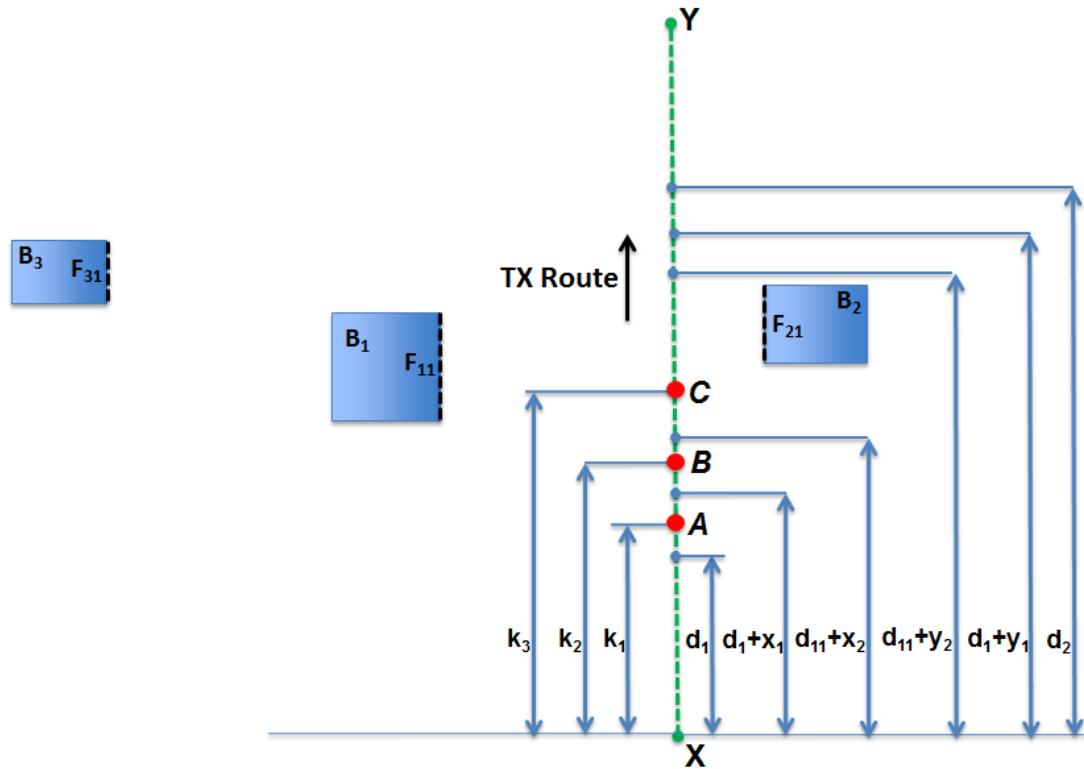


Figure 6.17 Higher order visibility computation for example in Figure 6.7 for three transmitter locations A , B and C using the visibility table.

6.6 Results

The ray-tracing model proposed in this paper is used to compare the pre-process time for a line of 76 transmitter points every 10m along a 750m street in Munich city. The complete buildings database for Munich is not used for the results presented in this section. The test environment is limited to $1000 \times 1000 \text{ m}^2$ centred on the transmitter and contains 182 buildings with 1,457 vertical walls. The mobile transmitter is 5m high and is well below the average building height so that use of the intra-visibility matrix computed using the horizontal polar sweep remains valid. The results presented in this section do not compare the predicted path loss with any measured data as the accuracy of the model has already been assessed in previous chapters. The computer used in the simulation is a standard desktop with an Intel Core i-5 3.3GHz CPU.

Figure 6.18 shows the Munich test area for pre-process time computations.

6.6.1 Run Time Comparison

The results presented in this section describe the pre-processing time reduction that can be achieved using the proposed algorithm that make use of intra-visibility matrix for a mobile transmitter. The initial model presented in section 6.3 uses the intra-visibility matrix to compute the image-tree for a single transmitter location. It has been shown



Figure 6.18 Map of Munich city with a line of 76 transmitter points along a street. Arrow shows the reference direction used for distance computations.

that this technique can achieve a reduction of up to 50% in image-tree computation time for a fixed transmitter location as compared to the polar sweep algorithm. The method is repeated *independently* for all transmitter locations along the mobile route to get the total pre-process time for comparison. The model developed in the previous section facilitates the efficient computation of the visibility list for multiple transmitter locations along a linear route, which reduces the pre-process time significantly as shown in the following results.

If τ_{vt} represents the time required for the visibility table computations and τ_{it} represents the time required to compute the image-tree for a single transmitter location, then the total pre-process time T for M transmitter locations along the route is given by

$$T = \tau_{vt} + \sum_M \tau_{it}$$

In the results presented in this section, the model compares pre-processing time for two cases. Firstly, the model computes the visibility table for a simple scenario involving wall reflections only. Secondly, the model performs higher order visibility verification for both faces and edges to compute the visibility table that gives all types of rays including reflections, diffractions and a combination of both.

Wall Reflections Only

The proposed model computes the face-to-face visibility table for up to 5th order reflections for the given environment. The run time is listed in Table. 6.3. Run time is compared against the initial model in which the intra-visibility matrix is used for individual transmitter locations. It can be seen that the proposed model can reduce the run time for wall reflections by up to 90%.

Table 6.3 Run time for visibility table and image-tree computation for 76 transmitter locations that considers only wall reflections in Munich test environment.

Time	Order = 1	Order = 2	Order = 3	Order = 4	Order = 5
τ_{vt} (seconds)	536	1,327	3,970	12,527	42,450
$\sum_M \tau_{it}$ (seconds)	3	11	33	95	265
Total time (T)	$\approx 9\text{ mins}$	$\approx 22\text{ mins}$	$\approx 1\text{ hr }7\text{ mins}$	$\approx 3.5\text{ hrs}$	$\approx 12\text{ hrs}$
using initial model	$\approx 57\text{ mins}$	$\approx 3\text{ hrs }55\text{ mins}$	$\approx 13\text{ hrs}$	$\approx 31\text{ hrs }40\text{ mins}$	$\approx 73\text{ hrs}$
Reduction	84.34%	90.53%	91.43%	88.92%	83.70%

Wall Reflection and Edge Diffraction

Since the diffracted field decreases rapidly for higher order diffractions, a maximum of second order of diffraction is computed. The visibility table is computed that can be used to validate all the possible combination of up to second order of rays. Table 6.4 lists the run time. It can be seen that the proposed model can reduce the run time by up to 83%.

Table 6.4 Run time for visibility table and image-tree computation for 76 transmitter locations that considers both wall reflection and edge diffraction in Munich test environment.

Time	Order = 1	Order = 2
τ_{vt} (seconds)	898	22,994
$\sum_M \tau_{it}$ (seconds)	10	277
Total time (T)	$\approx 15\text{ mins}$	$\approx 6.5\text{ hrs}$
using initial model	$\approx 1\text{ hr }18\text{ mins}$	$\approx 39.5\text{ hrs}$
Reduction	80.47%	83.64%

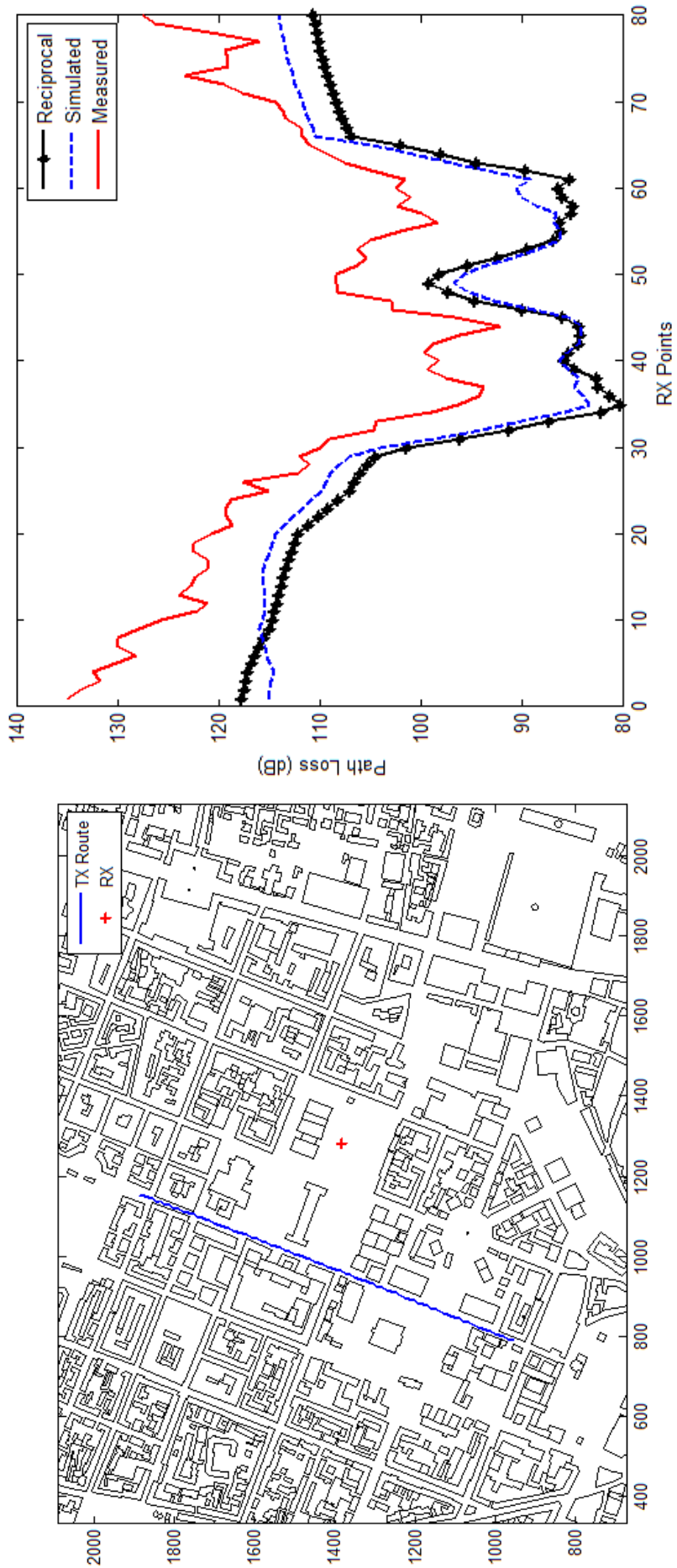
6.6.2 Results Validation

The time acceleration that can be achieved for a mobile transmitter is investigated in the previous section. The algorithm does not make any simplification or interpolation to predict the channel between two or more transmitter positions along the route. Therefore in theory, the proposed algorithm accurately computes the valid rays at all the receiver locations for a given transmitter position. However the comparison of simulated results with measured data is required to validate the proposed model. Unfortunately the measured data for a mobile transmitter scenario is not available. In this section the *reciprocity* principle is applied to compare the path loss with measured data available for Munich as discussed in section 5.1. The proposed algorithm computes the valid rays at the transmitter location in Munich for a line of transmitter points used as receivers in the original measured data. In other words, the role of transmitter and receivers is interchanged. The height of both transmitter and receiver antennas remain the same as it was in the original measured data. i.e. $h_{tx} = 1.5\text{m}$ and $h_{rx} = 13\text{m}$. The intra-visibility matrix was computed for large Munich database that has 2,088 buildings and over 17,000 walls and vertical edges. The creation of intra-visibility matrix for full Munich database took over a week.

The line of transmitter points for which the valid rays to be computed must be properly selected. The contribution of lateral rays must be significant on the selected line of receivers in the original measured data. Referring back to section 5.4.3 in which it was noted that the contribution of different propagation mechanisms was investigated. It was noted that the first order diffraction contributes significantly for four different sections of metro-202 that are close to the transmitter as shown in Figure 5.14. The proposed model can be used to find the valid rays for any of the route sections. However the proposed algorithm accelerates the ray computations for multiple transmitters that are placed along a straight line. Therefore the section of metro-202 shown in black in Figure 5.14a is selected for simulations. The map of Munich and the selected transmitter route and the receiver location is reproduced in Figure 6.19a.

A visibility table is computed for the transmitter routes using the proposed algorithm described in previous section. This table is used to compute the image-tree for all the transmitter locations along the route. The valid rays at the receiver point are also computed for all the transmitter locations. It was found that the rays computed using this approach followed the same paths as computed in section 5.4.3 for multiple receivers. i.e. the valid ray paths between the two points remain the same (other than the direction of wave propagation). This confirms that the proposed model accurately determines the valid ray paths. Path loss contributed by first order diffraction rays for all the transmitter locations is computed and compared against the path loss computed for metro routes in section 5.4.3 and measured data. Path loss comparison is shown in Figure 6.19b.

It can be seen that the path loss contribution of the diffracted field in the reciprocal case is almost the same as computed for metro routes. The standard deviation of error



(a) Map of Munich city with line of transmitters and single receiver.

(b) Path loss comparison with measured data using the reciprocity theorem for single diffraction in Munich example.

Figure 6.19 Comparison of first order diffraction mechanism using the reciprocity principle.

between the field computed using the multiple receivers approach in section 5.4.3 and the reciprocal approach for multiple transmitters is 2 dB. There are two causes of this discrepancy. Firstly it should be noted that the UTD when applied to imperfectly conducting wedges is an approximate solution (in that it does not consider transmission through the wedge). It applies Fresnel reflection coefficients computed with respect to the face of the wedge facing the source. These coefficients depend on the angle of incidence and can thus vary as the source and field points are interchanged. This is especially the case when the face of the wedge that faces the source changes. A second source of error is that precise reciprocity depends on the exact computation contribution of the terms in the UTD formulation. It should be noted that, for computational efficiency, an interpolation scheme is used in the computation of the Fresnel integrals in the diffraction coefficients. This also introduces small errors that affects the reciprocity.

6.6.3 Selection of Transmitter Route Length

The inclusion of vertical edge diffraction greatly increases the size of the visibility table as a large number of faces and edges are potentially visible to a diffracting edge. The results presented for the Munich test environment that compute all the possible combinations of up to second order of diffraction results in a visibility table that occupies 32.40MB of RAM. Although modern computers are equipped with large memory and this particular example may not be a practical issue. However computing the visibility table for large urban environments may impose a sizeable memory requirement. A possible solution for such cases is to divide the transmitter route in shorter sub-routes and compute the visibility table for each route independently. This is due to the fact that a mobile transmitter with a shorter route length may potentially see a limited number of walls and edges thereby reducing the size of visibility table. However it also depends on the environment geometry surrounding the sub-route. The mobile route's segment that passes through a street canyon will potentially see a relatively smaller number of faces and edges than the segment of the same length that travels through an open area.

In this section, the transmitter route in the given test environment is divided into smaller sub-routes and the computational performance is investigated. The transmitter route is divided into two equal routes and the run time and required memory is computed. The same transmitter route is also investigated for run time and memory efficiency for three equal-length sub-routes. The Table. 6.5 lists the performance of the ray-tracing algorithm for each case.

It can be seen from the Table 6.5 that dividing the transmitter route into smaller sub-routes tends to save memory at the expense of higher run time. However, the reduction in memory and increase in the run time does not change linearly with the length of sub-route as it depends on the particular geometry of the environment as discussed earlier.

Table 6.5 Comparison of memory reduction and run time increment for simulating the transmitter route in Munich test environment using two sub-routes and three sub-routes respectively.

	Two Sub-routes		Three Sub-routes		
	sub-route 1	sub-route 2	sub-route 1	sub-route 2	sub-route 3
TX Points	38	38	25	25	26
Run time	$\approx 4\text{ hrs }37\text{ mins}$	$\approx 2\text{ hrs}$	$\approx 3\text{ hrs }27\text{ mins}$	$\approx 2\text{ hrs }23\text{ mins}$	$\approx 1\text{ hr }18\text{ mins}$
Memory	20.88MB	13.07MB	14.16MB	14.15MB	8.80MB
Total Run time	$\approx 6\text{ hrs }37\text{ mins}$		$\approx 7\text{ hrs }8\text{ mins}$		
Maximum Memory	20.88MB		14.16MB		
Run time Increment	2.28%		10.47%		
Memory Reduction	35.5%		56.29%		

6.7 Conclusion

A novel algorithm to compute the radio channel for a mobile transmitter is developed in this chapter. The algorithm can be summarised as follows.

- The intra-visibility between the building's walls and edges remains constant irrespective of the transmitter location. A large database pre-computes the list of visible walls and edges for all the walls and edges in the environment. The angle at which an edge is visible or the angular range over which a wall remains visible is also computed during the database creation.
- This database can be used to fetch all the visible faces and edges to a source for required order of ray interaction.
- Initially, this database was used to compute the valid rays for a single transmitter location and the results were compared with measured data in Munich. [164].
- A novel algorithm is developed to compute a visibility table of required order of ray interaction for a mobile transmitter. This table is used to readily determine the image tree for a mobile transmitter at any location along the linear trajectory. [160].
- Validation results showed that the proposed algorithm can reduce the pre-processing CPU time by up to 90% for a mobile transmitter in outdoor scenario [165].

Chapter 7

Conclusions and Future Work

7.1 Conclusions

A background of electromagnetic theory associated with the use of rays was studied. The high-frequency asymptotic solution of Maxwell's equations gives the dominant paths through which radio energy propagates as rays. These rays follow the laws of reflection and refraction as described by classical geometrical optics. The uniform theory of diffraction gives continuous diffracted fields across shadow boundaries. Ray tracing techniques including visibility algorithms, image-tree computation and ray-object intersection test for ray validation were discussed. The effect of buildings, vegetation, pedestrians and vehicular traffic on radio wave propagation was studied. An overview of radio channel models with a detailed review of the literature on ray tracing acceleration techniques was also presented. The ray tracing models have limits on achievable speed and accuracy that depends on certain factors. The availability of accurate environment details, inclusion of significant propagation mechanisms and scattering from urban furniture, and the over-simplifications for speed up are critical to the performance of a ray tracing model.

The work presented in this research contributes to achieve the time acceleration in ray tracing computations for both a mobile receiver and transmitter. An efficient approach is proposed to represent the lit and shadow regions associated with the scattering objects illuminated by a source as polygons. A ray-object intersection test is developed that accelerates the ray validation for fast ray tracing. The mapping of lit polygons to the quadrants with which they intersect is proposed to accelerate the ray finding process. A novel algorithm based on pre-computed database of lit polygons intersection along the mobile route is developed. This approach accelerates the ray object intersection test for a mobile receiver or multiple collinear receivers. The pre-computation of shadow polygons intersection database further speeds up the ray tracing algorithm. Validation results showed that the algorithm developed in this work can compute all the valid second order rays at a receiver location in about 1.5 seconds on average. Although the

model is very fast, the accuracy of the model can be improved and is left for future work.

The ray tracing acceleration algorithm for a mobile transmitter presented in this work is based on a pre-computed database of intra-visibility of walls and edges. This database computes the walls and edges that are visible to each wall and edge in the given environment. The angular range over which the walls and edges are visible is also computed. The novel algorithm developed in this work efficiently computes a database of all the visible walls and edges, visibility table, of required order of ray interaction for a mobile transmitter along a linear trajectory. This visibility table readily identifies the visible nodes for each transmitter along the route to accelerate the ray tracing. The validation results showed that the pre-process time for a mobile transmitter can be reduced by up to 90% which makes the proposed model a better candidate for vehicular networks.

The novel ray tracing algorithms developed in this work can achieve speed up but there are certain limitations that must be considered. The models use the 2-D polygons to represent the region of interest of illuminated walls and edges. The inaccuracies in buildings database, particularly the introduction of dummy edges in curved walls adds to the deviation in predicted results. The maximum speed up in ray tracing computations for a mobile (receiver or transmitter) is achieved when it moves along a straight line. The ray tracing model has to be tuned for speed and accuracy when the mobile is moving along non linear trajectories such as street corners and roundabouts. The intra-visibility database computations are time consuming and can take days for a typical large urban environment.

7.2 Future Work

Efficient ray tracing models have been developed in this research. The validation results show that significant speed and accuracy can be achieved for both a mobile receiver and transmitter. Future work will further improve the speed and accuracy of the proposed models.

The recent advances in parallel computation and graphical processing units equipped with powerful multi-core processors have found applications in ray tracing for radio wave propagation prediction. The algorithms developed in this research could be implemented on GPU hardware. The well known Compute Unified Device Architecture (CUDA) developed by NVIDIA enables the massive parallel processes on a GPU. The C++ code developed in this research could be translated into CUDA C++ for implementation on a GPU to further speed up the ray tracing algorithms.

The over-rooftop diffraction is significant in urban propagation when the transmitter height is close to the average building height. The ray tracing model presented in this work computes the over-rooftop diffraction using the heuristic technique proposed by

Tzaras *et al.* [152]. This method presents a fast ray based solution to compute the diffracted fields in transition zones for multiple edge diffraction problem. A comparative study could be performed to investigate the accuracy of different over-rooftop prediction models including COST-231 Walfisch Ikegami, Vogler, Flat edge and Deygout as well as the slope diffraction models including Andersen [150] and Rizk *et al.* [151].

Plane surfaces at higher frequencies above 1 GHz cannot be considered perfectly smooth as the surface roughness becomes comparable to the wavelength of the radio wave. Therefore the rough surface or diffused scattering from the objects becomes significant for higher frequencies above 1 GHz. Several models [14–17] combine diffuse scattering component with ray tracing to accurately predict the radio channel at higher frequencies for both indoor and outdoor channels. The ray tracing model presented in this research does not include rough surface scattering as the validation results are compared with measured data at 947 MHz. Future work could include rough surface scattering in the proposed model in order to accurately predict the radio channel for future mm-wave systems.

A ray tracing model computes the contribution of all the valid rays arriving at the receiver. The validation results presented in this work only compute the path loss for comparison with measured data. Several channel characteristics including channel capacity, power delay profile (PDP), delay spread, angle of arrival etc. can be derived by post-processing the raw data available from a ray tracing model. A GUI demonstrator could be developed to visualize the varying channel parameters as the transmitter and receiver move in the given environment. The work could be extended to extract the environment details including buildings database and vegetation from Google or open street maps for real time channel modeling. The demonstrator tool could also include 3-D visualization of rays arriving at a mobile receiver. Similar work has been reported in literature [153–156].

Multiple-Input Multiple-Output (MIMO) systems that use antenna arrays at both transmitter and receiver are being investigated for future 5G high data rate systems. The algorithms presented in this research determine the radio channel for both mobile transmitter and receiver. A mobile transmitter and receiver is realised by multiple transmitters and receivers along the trajectory. The model could therefore be modified with the capability to simulate the radio channel for MIMO systems.

The work presented in this research could also be extended for indoor ray tracing. An indoor model allows a certain number of transmissions through the walls as the transmitted fields are significant for indoor channels. Therefore the concept of shadow polygons has to be modified to allow for the transmission of rays through the obstructions.

Bibliography

- [1] D. L. Sengupta and T. K. Sarka, "Maxwell, Hertz, the Maxwellians, and the Early History of Electromagnetic Waves," *IEEE Antennas and Propagation Magazine*, vol. 45, no. 2, pp. 13–19, 2003.
- [2] I. McNeil, Ed., *An Encyclopaedia of the History of Technology*. Routledge, 1996.
- [3] T. Ojanpera, "Perspectives on 3G System Development," *Personal, Indoor and Mobile Radio Communications, The 9th International Symposium on*, 1998.
- [4] T. Mshvidobadze, "Evolution mobile wireless communication and LTE networks," *Application of Information and Communication Technologies (AICT), 2012 6th International Conference*, pp. 1–7, 2012.
- [5] J. J. G. Andrews, S. Buzzi, W. Choi, S. V. S. Hanly, A. Lozano, A. A. C. K. Soong, and J. J. C. Zhang, "What will 5G be?" *IEEE Journal on Selected Areas in Communications*, vol. 32, no. 6, pp. 1065–1082, 2014.
- [6] R. G. Kouyoumjian, "Asymptotic High-Frequency Methods," *Proceedings of the IEEE*, vol. 53, no. 8, pp. 864–876, 1965.
- [7] R. Luneberg, *Mathematical Theory of Optics*. Brown University Press, 1944.
- [8] M. Kline, "An asymptotic solution of Maxwell's equations," *Communications on Pure and Applied Mathematics*, vol. 4, no. 2-3, pp. 225–262, 1951.
- [9] J. B. Keller, "Geometrical Theory of Diffraction," *Journal of the Optical Society of America*, vol. 52, no. 2, pp. 116–130, 1962.
- [10] R. G. Kouyoumjian and P. H. Pathak, "A uniform Geometrical Theory of Diffraction for an edge in a perfectly conducting surface," *Proceedings of the IEEE*, vol. 62, no. 11, pp. 1448–1461, 1974.
- [11] D. A. McNamara, C. W. I. Pistorius, and J. A. G. Malherbe, *Introduction to the Uniform Geometrical Theory of Diffraction*. Artech House, 1990.
- [12] H. Bremmer and S. W. Lee, "Geometrical optics solution of reflection from arbitrarily curved surface," *Radio Science*, vol. 17, no. 5, pp. 1117–1131, 1982.
- [13] C. A. Balanis, *Advanced Engineering Electromagnetics*. John Wiley and Sons, 1999.
- [14] K. Ng, E. Tameh, and a.R. Nix, "A new hybrid geometrical optics and radiance based scattering model for ray tracing applications," *IEEE International Conference on Communications, 2005. ICC 2005. 2005*, vol. 4, no. C, pp. 2168–2172, 2005.

- [15] S. Reynaud, Y. Cocheril, R. Vauzelle, A. Reineix, L. Aveneau, and C. Guiffaut, "Influence of an Accurate Environment Description for the Indoor Propagation Channel Modelling," *2005 European Conference on Wireless Technologies*, pp. 61–64, 2005.
- [16] L. Tian, V. Degli-Esposti, E. M. Vitucci, X. Yin, F. Mani, and S. X. Lu, "Semi-deterministic modeling of diffuse scattering component based on propagation graph theory," *IEEE International Symposium on Personal, Indoor and Mobile Radio Communications, PIMRC*, vol. 2015-June, pp. 155–160, 2015.
- [17] L. Tian, V. Degli-Esposti, E. M. Vitucci, and X. Yin, "Semi-Deterministic Radio Channel Modeling Based on Graph Theory and Ray-Tracing," *IEEE Transactions on Antennas and Propagation*, vol. 64, no. 6, pp. 2475–2486, 2016.
- [18] M. Ghoraishi, J. Takada, and T. Imai, "Identification of scattering objects in microcell urban mobile propagation channel," *IEEE Transactions on Antennas and Propagation*, vol. 54, no. 11, November 2006.
- [19] K. Rizk, J.-f. Wagen, J. Li, and F. Gardiol, "Lamppost and panel scattering compared to building reflection and diffraction," *COST 259 TD(97)*, 1996.
- [20] K. Guan, B. Ai, M. L. Nicolás, R. Geise, A. Möller, Z. Zhong, and T. Kürner, "On the influence of scattering from traffic signs in vehicle-to-x communications," *IEEE Transactions on Vehicular Technology*, vol. 65, no. 8, August 2016.
- [21] I. Kavanagh, S. Hussain, and C. Brennan, "A Full Wave Propagation Model for Indoor Wireless Communications," *17th Research Colloquium on Communications and Radio Science into the 21st Century*, 2014.
- [22] M. F. Cátedra, J. Pérez, F. Saez De Adana, and O. Gutierrez, "Efficient Ray-Tracing Techniques for Three-Dimensional Analyses of Propagation in Mobile Communications: Application to Picocell and Microcell Scenarios," *IEEE Antennas and Propagation Magazine*, vol. 40, no. 2, pp. 15–27, 1998.
- [23] K. Rizk, J.-F. Wegan, and F. Gardiol, "Two-Dimensional Ray-Tracing Modeling for Propagation Prediction in Microcellular Environments," *IEEE Transactions on Vehicular Technology*, vol. 46, no. 2, pp. 508–518, 1997.
- [24] G. E. Athanasiadou, A. R. Nix, and J. P. McGeehan, "Investigation into the sensitivity of a microcellular ray-tracing model and comparison of the predictions with narrowband measurements," *VTC 98 48th IEEE Vehicular Technology Conference*, vol. 2, pp. 870–874, 1998.
- [25] G. E. Athanasiadou and A. R. Nix, "Investigation into the sensitivity of the power predictions of a microcellular ray tracing propagation model," *IEEE Transactions on Vehicular Technology*, vol. 49, no. 4, pp. 1140–1151, 2000.
- [26] Y. L. C. De Jong, M. H. J. L. Koelen, and M. H. A. J. Herben, "A building-transmission model for improved propagation prediction in urban microcells," *IEEE Transactions on Vehicular Technology*, vol. 53, no. 2, pp. 490–502, 2004.
- [27] I. Rodriguez, H. C. Nguyen, N. T. K. Jorgensen, T. B. Sorensen, and P. Mogensen, "Radio propagation into modern buildings: Attenuation measurements in the range from 800 MHz to 18 GHz," *IEEE Vehicular Technology Conference*, pp. 2–6, 2014.

- [28] A. Asp, Y. Sydorov, M. Kesikastari, M. Valkama, and J. Niemelä, "Impact of modern construction materials on radio signal propagation: Practical measurements and network planning aspects," *IEEE Vehicular Technology Conference*, vol. 2015-Janua, no. January, 2015.
- [29] Y. Du, C. Cao, X. Zou, J. He, H. Yan, G. Wang, and D. Steer, "Measurement and modeling of penetration loss in the range from 2 GHz to 74 GHz," *Globecom Workshops (GC Wkshps), 2016 IEEE*, pp. 0–5, 2016.
- [30] A. Roivainen, V. Hovinen, N. Tervo, and M. Latva-aho, "Outdoor-to-Indoor Path Loss Modeling at 10 . 1 GHz," *Antennas and Propagation (EuCAP), 2016 10th European Conference on*, pp. 8–11, 2016.
- [31] K. Haneda, J. Zhang, L. Tan, G. Liu, Y. Zheng, H. Asplund, J. Li, Y. Wang, D. Steer, C. Li, T. Balercia, S. Lee, Y. Kim, A. Ghosh, T. Thomas, T. Nakamura, Y. Kakishima, T. Imai, H. Papadopoulos, T. S. Rappaport, G. R. Maccartney, M. K. Samimi, S. Sun, O. Koymen, S. Hur, J. Park, C. Zhang, E. Mellios, A. F. Molisch, S. S. Ghassamzadeh, and A. Ghosh, "5G 3GPP-like channel models for outdoor urban microcellular and macrocellular environments," *IEEE Vehicular Technology Conference*, vol. 2016-July, 2016.
- [32] N. Rogers, A. Seville, J. Richter, and D. Ndzi, "A generic model of 1-60 GHz radio propagation through vegetation-final report," *QINETIQ/KI/COM/CR020196/1.0, UK*, no. May, p. 152, 2002.
- [33] R. F. S. Caldeirinha and M. O. Al-Nuaimi, "Microwave propagation modeling and measurement of scattering and absorption inside a canopy using the FDTD technique," *IEEE Transactions on Antennas and Propagation*, vol. 63, no. 1, pp. 280–293, 2015.
- [34] M. A. Weissberger, "An initial critical summary of models for predicting the attenuation of radio waves by trees," *Technical Report ESD-TR-81-101, Department of Defense, Annapolis, USA*, 1982.
- [35] N. C. Goncalves and L. M. Correia, "A propagation model for urban microcellular systems at the UHF band," *IEEE Transactions on Vehicular Technology*, vol. 49, no. 4, pp. 1294–1302, 2000.
- [36] Y. L. C. De Jong and M. H. A. J. Herben, "A Tree-Scattering Model for Improved Propagation Prediction in Urban Microcells," *IEEE Transactions on Vehicular Technology*, vol. 53, no. 2, pp. 503–513, 2004.
- [37] F. Mani and C. Oestges, "A ray based method to evaluate scattering by vegetation elements," *IEEE Transactions on Antennas and Propagation*, vol. 60, no. 8, pp. 4006–4009, 2012.
- [38] K. L. Chee, S. A. Torrico, S. Member, T. Kürner, and S. Member, "Radiowave Propagation Prediction in Vegetated Residential Environments," *IEEE Transactions on Vehicular Technology*, vol. 62, no. 2, pp. 486–499, 2013.
- [39] N. R. Leonor, R. F. S. Caldeirinha, T. R. Fernandes, D. Ferreira, and M. G. S?nchez, "A 2D ray-tracing based model for micro- and millimeter-wave propagation through vegetation," *IEEE Transactions on Antennas and Propagation*, vol. 62, no. 12, pp. 6443–6453, 2014.

- [40] N. Leonor, R. Caldeirinha, T. Fernandes, and S. Manuel, "A feasibility study on the extension of the point scatterer formulation to vegetation media," *Antennas and Propagation (EuCAP), 2015 9th European Conference on*, no. 1, pp. 3–7, 2015.
- [41] B. Goktepe, M. Peter, R. J. Weiler, and W. Keusgen, "The influence of street furniture and tree trunks in urban scenarios on ray tracing simulations in the millimeter wave band," *European Microwave Week 2015: "Freedom Through Microwaves", EuMW 2015 - Conference Proceedings; 2015 45th European Microwave Conference Proceedings, EuMC*, pp. 195–198, 2015.
- [42] T. S. Rappaport, *Wireless Communications: Principles and Practice*, 2002.
- [43] Y. Oda and K. Tsunekawa, "Advanced LOS Path Loss Model in Microwave Mobile Communications," *Antennas and Propagation, 10th International Conference on*, vol. 2, pp. 170–173, 1997.
- [44] H. Masui, M. Ishii, S. Takahashi, H. Shimizu, and T. Kobayashi, "Microwave Propagation Characteristics in an Urban LOS Environment in Different Traffic Conditions," *Antennas and Propagation Society International Symposium, IEEE*, pp. 1150–1153, 2000.
- [45] H. Masui, M. Ishii, K. Sakawa, H. Shimizu, T. Kobayashi, and M. Akaike, "Microwave path-loss characteristics in urban LOS and NLOS environments," *Proc. IEEE 53rd Vehicular Technology Conf. (VTC)*, pp. 395–398, 2001.
- [46] H. Masui, T. Kobayashi, and M. Akaike, "Microwave path-loss modeling in urban line-of-sight environments," *IEEE Journal on Selected Areas in Communications*, vol. 20, no. 6, pp. 1151–1155, 2002.
- [47] G. Hernández-Valdez, F. A. Cruz-Pérez, and D. Lara-Rodríguez, "Sensitivity of the system performance to the propagation parameters in LOS microcellular environments," *IEEE Transactions on Vehicular Technology*, vol. 57, no. 6, pp. 3488–3509, 2008.
- [48] J. Maurer, D. Didascalou, and W. Wiesbeck, "Novel Approach in the Determination of Visible Surfaces in 3D Vector Geometries for Ray-Optical Wave Propagation Modelling," *Vehicular Technology Conference Proceedings, 2000. IEEE 51st*, 2000.
- [49] R. P. Torres, L. Valle, M. Domingo, and S. Loredó, "An efficient ray-tracing method for radio propagation based on the modified BSP algorithm," *Vehicular Technology Conference, 1999. IEEE VTS 50th*, pp. 1967–1971, 1999.
- [50] ———, "An efficient ray-tracing method for enclosed spaces based on Image and BSP algorithm," *Antennas and Propagation Society International Symposium, IEEE*, pp. 416–419, 1999.
- [51] J. Bittner, P. Wonka, and M. Wimmer, "Visibility preprocessing for urban scenes using line space subdivision," *Proceedings - Pacific Conference on Computer Graphics and Applications*, vol. 2001-Janua, pp. 276–284, 2001.
- [52] J. Bittner, J. Prikryl, and P. Slavik, "Exact regional visibility using line space partitioning," *Computers and Graphics (Pergamon)*, vol. 27, no. 4, pp. 569–580, 2003.

- [53] K. H. Ng, E. K. Tameh, and A. R. Nix, "An advanced multi-element microcellular ray tracing model," *1st International Symposium on Wireless Communication Systems 2004*, pp. 438–442, 2004.
- [54] K. H. Ng, E. K. Tameh, A. Doufexi, M. Hunukumbure, and A. R. Nix, "Efficient multielement ray tracing with site-specific comparisons using measured MIMO channel data," *IEEE Transactions on Vehicular Technology*, vol. 56, no. 3, pp. 1019–1032, 2007.
- [55] F. A. Agelet, F. P. Fontan, and A. Formella, "Fast Ray Tracing for Microcellular and Indoor Environments," *IEEE Transactions on Magnetics*, vol. 33, no. 2, pp. 1484–1487, 1997.
- [56] F. A. Agelet, A. Formella, J. M. H. Rabanos, F. I. De Vicente, and F. P. Fontan, "Efficient ray-tracing acceleration techniques for radio propagation modeling," *IEEE Transactions on Vehicular Technology*, vol. 49, no. 6, pp. 2089–2104, 2000.
- [57] M. Iskander and Zhengqing Yun, "Propagation prediction models for wireless communication systems," *IEEE Transactions on Microwave Theory and Techniques*, vol. 50, no. 3, pp. 662–673, 2002.
- [58] S. Y. Seidel, T. S. Rappaport, S. Jain, M. L. Lord, and R. Singh, "Path loss, scattering, and multipath delay statistics in four European cities for digital cellular and microcellular radiotelephone," *IEEE Transactions on Vehicular Technology*, vol. 40, no. 4, pp. 721–730, 1991.
- [59] R. C. Bernhardt, "The Effect of Path Loss Models on the Simulated Performance," pp. 1356–1360, 1989.
- [60] Y. Okumura, E. Ohmori, T. Kawano, and K. Fukuda, "Field strength and its variability in VHF and UHF land-mobile radio service," *Review of the Electrical Communication Laboratory*, vol. 16, no. 9-10, pp. 825–873, 1968.
- [61] M. Hata, "Empirical formula for propagation loss in land mobile radio services," *IEEE Transactions on Vehicular Technology*, vol. 29, no. 3, pp. 317–325, 1980.
- [62] ITU-R, "370.7, VHF and UHF propagation ranging from 30 MHz to 1000 MHz," 1995.
- [63] ———, "529.3, Prediction Methods For the Terrestrial Land Mobile Service in VHF and UHF Bands," 1999.
- [64] A. Medeisis and A. Kajackas, "On the use of the universal Okumura-Hata propagation prediction model in rural areas," *Vehicular Technology Conference Proceedings, 2000. VTC 2000-Spring Tokyo. 2000 IEEE 51st*, vol. 3, pp. 1815–1818 vol.3, 2000.
- [65] L. Akhoondzadeh-Asl and N. Noori, "Modification and tuning of the universal Okumura-Hata model for radio wave propagation predictions," *Asia-Pacific Microwave Conference Proceedings, APMC*, no. 1, pp. 7–10, 2007.
- [66] W. C. Y. Lee, *Mobile Communications Design Fundamentals*. John Wiley and Sons, 1993.
- [67] V. Erceg, S. Member, L. J. Greenstein, S. Y. Tjandra, S. R. Parkoff, A. Gupta, B. Kulic, A. a. Julius, and R. Bianchi, "An Empirically Based Path Loss Model for Wireless Channels in Suburban Environments," *IEEE Journal on Selected Areas in Communications*, vol. 17, no. 7, pp. 1205–1211, 1999.

- [68] J. Walfisch and H. L. Bertoni, "A Theoretical Model of UHF Propagation in Urban Environments," *IEEE Transactions on Antennas and Propagation*, vol. 36, no. 12, pp. 1788–1796, 1988.
- [69] F. Ikegami, S. Yoshida, T. Takeuchi, and M. Umehira, "Propagation Factors Controlling Mean Field Strength on Urban Streets," *IEEE Transactions on Antennas and Propagation*, vol. 32, no. 8, pp. 822–829, 1984.
- [70] D. Har, A. M. Watson, and A. G. Chadney, "Comment on diffraction loss of rooftop-to-street in COST 231-Walfisch-Ikegami model," *IEEE Transactions on Vehicular Technology*, vol. 48, no. 5, pp. 1451–1452, 1999.
- [71] A. P. Garcia, H. Ortega, A. Navarro, and a. H. Rodriguez, "Effect of terrain on electromagnetic propagation in urban environments on the Andean region, using the COST231-Walfisch-Ikegami model and GIS planning tools," *Conference on Antennas and Propagation*, vol. 1, pp. 270–275, 2003.
- [72] I. Gruber and H. Li, "Behavior of ad hoc routing protocols in metropolitan environments," *Vehicular Technology Conference, 2004. VTC2004-Fall. 2004 IEEE 60th*, vol. 5, pp. 3175 – 3180 Vol. 5, 2004.
- [73] T. Schwengler and M. Gilbert, "Propagation models at 5.8 GHz-path loss and building penetration," *RAWCON 2000. 2000 IEEE Radio and Wireless Conference (Cat. No.00EX404)*, pp. 119–124, 2000.
- [74] L. Correia, "A view of the COST 231-Bertoni-Ikegami model," *2009 3rd European Conference on Antennas and Propagation*, pp. 1681–1685, 2009.
- [75] L. E. Vogler, "An attenuation function for multiple knife-edge diffraction," *Radio Science*, vol. 17, no. 6, pp. 1541–1546, 1982.
- [76] S. R. Saunders and F. R. Bonar, "Explicit Multiple Building Diffraction Attenuation Function for Mobile Radio Wave Propagation," *Electronic Letters*, vol. 27, no. 14, pp. 1276–1277, 1991.
- [77] ———, "Prediction of Mobile Radio Wave Propagation Over Buildings of Irregular Heights and Spacings," *IEEE Transactions on Antennas and Propagation*, vol. 42, no. 2, pp. 137–144, 1994.
- [78] K. Bullington, "Radio Propagation at Frequencies Above 30 Megacycles," *Proceedings of the IRE*, pp. 1122–1136, 1947.
- [79] J. Epstein and D. W. Peterson, "An Experimental Study of Wave Propagation at 850 MC," *Proceedings of the IRE*, pp. 595–611, 1953.
- [80] J. Deygout, "Multiple knife-edge diffraction of microwaves," *IEEE Transactions on Antennas and Propagation*, vol. 14, no. 4, pp. 480–489, 1966.
- [81] C. L. Giovaneli, "An Analysis of Simplified Solutions for Multiple Knife-Edge Diffraction," *IEEE Transactions on Antennas and Propagation*, vol. 32, no. 3, pp. 297–301, 1984.
- [82] W. Samuel, "Computation of 10 Knife Edge Diffraction Loss Using Epstein-Peterson Method," *American Journal of Software Engineering and Applications*, vol. 6, no. 1, pp. 1–4, 2017.
- [83] ITU-R, *Recommendation ITU-R P.526-13 (2013) Propagation by diffraction*, 2013.

- [84] C. Tzaras and S. R. Saunders, "Comparison of multiple-diffraction models for digital broadcasting coverage prediction," *IEEE Transactions on Broadcasting*, vol. 46, no. 3, pp. 221–226, 2000.
- [85] N. Deminco and P. Mckenna, "A Comparative Analysis of Multiple Knife-Edge Diffraction Methods," *Proceedings of the International Symposium on Advanced Radio Technologies/ClimDiff*, pp. 65–69, 2008.
- [86] ———, "Presentation Slides - A Comparative Analysis of Multiple Knife-Edge Diffraction Methods," *Proceedings of the International Symposium on Advanced Radio Technologies/ClimDiff*, 2008.
- [87] D. A. Bibb, J. Dang, Z. Yun, and M. F. Iskander, "Computational accuracy and speed of some knife-edge diffraction models," *IEEE Antennas and Propagation Society, AP-S International Symposium (Digest)*, pp. 705–706, 2014.
- [88] T. K. Sarkar, Z. Ji, K. Kim, A. Medouri, and M. Salazar-Palma, "A Survey of Various Propagation Models for Mobile Communication," *IEEE Antennas and Propagation Magazine*, vol. 45, no. 3, pp. 51–82, 2003.
- [89] Z. Yun and M. F. Iskander, "Ray tracing for radio propagation modeling: Principles and applications," *IEEE Access*, vol. 3, pp. 1089–1100, 2015.
- [90] F. Fuschini, E. M. Vitucci, M. Barbiroli, G. Falciasecca, and V. Degli-Esposti, "Ray tracing propagation modeling for future small-cell and indoor applications: A review of current techniques," *Radio Science*, vol. 50, no. 6, pp. 469–485, 2015.
- [91] M. Iskander, "A fast ray tracing procedure using space division with uniform rectangular grid," *IEEE Antennas and Propagation Society International Symposium. Transmitting Waves of Progress to the Next Millennium. 2000 Digest. Held in conjunction with: USNC/URSI National Radio Science Meeting (Cat. No.00CH37118)*, vol. 1, pp. 430–433, 2000.
- [92] Z. Yun, M. Iskander, and Z. Zhang, "Fast Ray Tracing Procedure Using Space Division with Uniform Rectangular Grid," *Electronics Letters*, vol. 36, no. 10, pp. 895–897, 2000.
- [93] J. G. Cleary and G. Wyvill, "Analysis of an algorithm for fast ray tracing using uniform space subdivision," *The Visual Computer*, vol. 4, no. 2, pp. 65–83, 1988.
- [94] Z. Zhang, Z. Yun, and M. Iskander, "A new ray tracing method for propagation models in wireless communication," *IEEE Antennas and Propagation Society International Symposium. Transmitting Waves of Progress to the Next Millennium. 2000 Digest. Held in conjunction with: USNC/URSI National Radio Science Meeting (C, vol. 2)*, pp. 1130–1133, 2000.
- [95] ———, "Ray Tracing Method for Propagation Models in Wireless Communication Systems," *Electronics Letters*, vol. 36, no. 5, pp. 464–465, 2000.
- [96] Z. Yun and M. Iskander, "New computationally efficient 2.5D and 3D ray tracing algorithms for modeling propagation environments," *IEEE Antennas and Propagation Society International Symposium. 2001 Digest. Held in conjunction with: USNC/URSI National Radio Science Meeting (Cat. No.01CH37229)*, pp. 460–463, 2001.

- [97] Z. Yun, Z. Zhang, and M. F. Iskander, "A ray-tracing method based on the triangular grid approach and application to propagation prediction in urban environments," *IEEE Transactions on Antennas and Propagation*, vol. 50, no. 5, pp. 750–758, 2002.
- [98] M. Iskander, "A fast indoor/outdoor ray tracing procedure using combined uniform rectangular and unstructured triangular grids," *IEEE Antennas and Propagation Society International Symposium. Transmitting Waves of Progress to the Next Millennium. 2000 Digest. Held in conjunction with: USNC/URSI National Radio Science Meeting (Cat. No.00CH37118)*, vol. 2, pp. 1134–1137, 2000.
- [99] I. Wald, V. Havran, and I. Wald, "On building fast kd-Trees for Ray Tracing , and on doing that in $O(N \log N)$," *Interactive Ray Tracing 2006, IEEE Symposium on*, pp. 61–69, 2006.
- [100] F. Weinmann, "Adaptive and Automated Multilevel Uniform Space Division for Acceleration of High-Frequency Electromagnetic Simulations [EM Programmer's Notebook]," *IEEE Antennas and Propagation Magazine*, vol. 59, no. 1, pp. 130–138, 2017.
- [101] G. E. Athanasiadou, A. R. Nix, and J. P. McGeehan, "Microcellular ray-tracing propagation model and evaluation of its narrow-band and wide-band predictions," *IEEE Journal on Selected Areas in Communications*, vol. 18, no. 3, pp. 322–335, 2000.
- [102] E. A. Haines and D. P. Greenberg, "The Light Buffer: A Shadow-Testing Accelerator," *IEEE Computer Graphics and Applications*, vol. 6, no. 9, pp. 6–16, 1986.
- [103] F. Saez de Adana, O. Gutierrez Blanco, I. Gonzalez Diego, J. Perez Arriaga, and M. Catedra, "Propagation model based on ray tracing for the design of personal communication systems in indoor environments," *IEEE Transactions on Vehicular Technology*, vol. 49, no. 6, pp. 2105–2112, 2000.
- [104] F. S. de Adana, O. Gutierrez, I. Gonzalez, and M. F. Catedra, "FASPRO: Fast Computer," *3rd IEEE International Conference on Industrial Informatics (INDIN)*, pp. 257–261, 2005.
- [105] C. Saeidi and F. Hodjatkashani, "Modified angular z-buffer as an acceleration technique for ray tracing," *IEEE Transactions on Antennas and Propagation*, vol. 58, no. 5, pp. 1822–1825, 2010.
- [106] V. Degli-Esposti, F. Fuschini, E. M. Vitucci, and G. Falciasecca, "Speed-up techniques for ray tracing field prediction models," *IEEE Transactions on Antennas and Propagation*, vol. 57, no. 5, pp. 1469–1480, 2009.
- [107] V. Degli-Esposti, F. Fuschini, and M. Amorini, "Database simplification for field prediction in urban environment," *IEEE Antennas and Propagation Society International Symposium*, 2004.
- [108] W. M. O'Brien, E. M. Kenny, and P. J. Cullen, "An efficient implementation of a three-dimensional microcell propagation tool for indoor and outdoor urban environments," *IEEE Transactions on Vehicular Technology*, vol. 49, no. 2, pp. 622–630, 2000.

- [109] Z. Yun and M. Iskander, "Efficient Calculation of Field Distribution with High-Resolution Using Ray-Tracing Method," *IEEE Antennas and Propagation Society International Symposium*, 2005.
- [110] C. Saeidi and F. Hodjatkashani, "Efficient Point-to-Area Electromagnetic Field Calculation Using Tube Tracing Method," *Wireless Communications & Signal Processing (WCSP), International Conference on*, pp. 1–5, 2009.
- [111] Z. Lai, N. Bessis, G. d. LaRoche, H. Song, J. Zhang, and G. Clapworthy, "An intelligent ray launching for urban prediction," *3rd European Conference on Antennas and Propagation*, 2009.
- [112] Z. Lai, N. Bessis, G. de la Rausche, P. Kuonen, J. Zhang, and G. Clapworthy, "On the use of an intelligent ray launching for indoor scenarios," *European Conference on ANtennas and Propagation*, 2010.
- [113] Z. Lai, H. Song, P. Wang, H. Mu, L. Wu, and J. Zhang, "Implementation and validation of a 2.5d intelligent ray launching algorithm for large urban scenarios," *6th European Conference on Antennas and Propagation*, 2011.
- [114] G. Liang and H. L. Bertoni, "A new approach to 3-D ray tracing for propagation prediction in cities," *IEEE Transactions on Antennas and Propagation*, vol. 46, no. 6, pp. 853–863, 1998.
- [115] J. P. Rossi and Y. Gabillet, "A mixed ray launching/tracing method for full 3-D UHF propagation modeling and comparison with wide-band measurements," *IEEE Transactions on Antennas and Propagation*, vol. 50, no. 4, pp. 517–523, 2002.
- [116] R. Hoppe, G. Wolfle, and F. Landstorfer, "Accelerated ray optical propagation modeling for the planning of wireless communication networks," *IEEE Radio and Wireless Conference RAWCON 99.*, pp. 159–162, 1999.
- [117] G. Wölfle, R. Hoppe, and F. Landstorfer, "A fast and enhanced ray optical propagation model for indoor and urban scenarios, based on an intelligent pre-processing of the database," *Proceedings of the 10th IEEE . . .*, 1999.
- [118] T. Rautiainen, G. Wolfle, and R. Hoppe, "Verifying path loss and delay spread predictions of a 3D ray tracing propagation model in urban environment," *Proceedings IEEE 56th Vehicular Technology Conference*, vol. 4, pp. 2470–2474, 2002.
- [119] T. Rautiainen, R. Hoppe, and G. Wölfle, "Measurements and 3D ray tracing propagation predictions of channel characteristics in indoor environments," *IEEE International Symposium on Personal, Indoor and Mobile Radio Communications, PIMRC*, pp. 0–4, 2007.
- [120] A. Toscano, F. Bilotti, and L. Vegni, "Fast ray-tracing technique for electromagnetic field prediction in mobile communications," *IEEE Transactions on Magnetism*, vol. 39, no. 3 I, pp. 1238–1241, 2003.
- [121] Y. Wang, S. Safavi-Naeini, and S. K. Chaudhuri, "A hybrid technique based on combining ray tracing and FDTD methods for site-specific modeling of indoor radio wave propagation," *IEEE Transactions on Antennas and Propagation*, vol. 48, no. 5, pp. 743–754, 2000.

- [122] G. A. Schiavone, P. Wahid, R. Palaniappan, J. Tracy, and T. Dere, "Analysis of ultra-wide band signal propagation in an indoor environment," *Microwave and Optical Technology Letters*, vol. 36, no. 1, pp. 13–15, 2003.
- [123] Y. Wang, S. K. Chaudhuri, and S. Safavi-Naeini, "An FDTD/Ray-tracing analysis method for wave penetration through inhomogeneous walls," *IEEE Transactions on Antennas and Propagation*, vol. 50, no. 11, pp. 1598–1604, 2002.
- [124] M. Thiel and K. Sarabandi, "3D-wave propagation analysis of indoor wireless channels utilizing hybrid methods," *IEEE Transactions on Antennas and Propagation*, vol. 57, no. 5, pp. 1539–1546, 2009.
- [125] A. G. Kanatas and P. Constantinou, "A Propagation prediction tool for urban mobile radio systems," *IEEE Transactions on Vehicular Technology*, vol. 49, no. 4, pp. 1348–1355, 2000.
- [126] T. Kürner and A. Meier, "Prediction of outdoor and outdoor-to-indoor coverage in urban areas at 1.8 Ghz," *IEEE Journal on Selected Areas in Communications*, vol. 20, no. 3, pp. 496–506, 2002.
- [127] N. Mataga, R. Zentner, and A. K. Mucalo, "Ray entity based postprocessing of ray-tracing data for continuous modeling of radio channel," *Radio Science*, pp. 217–230, 2014.
- [128] J. Nuckelt, M. Schack, and T. Kurner, "Geometry-Based Path Interpolation for Rapid Ray-Optical Modeling of Vehicular Channels," *9th European Conference on Antennas and Propagation (EuCAP)*, 2015.
- [129] A. M. Cavalcante, M. J. De Sousa, C. D. S. Sales, J. C. W. A. Costa, G. P. S. Cavalcante, and C. R. L. Francês, "Computational parallelization strategy applied in full 3D ray-tracing wireless channel modeling," *SBMO/IEEE MTT-S International Microwave and Optoelectronics Conference Proceedings*, pp. 359–362, 2005.
- [130] A. M. Cavalcante, M. J. De Sousa, J. C. W. A. Costa, C. R. L. Francês, and G. P. Dos Santos Cavalcante, "A new computational parallel model applied in 3D ray-tracing techniques for radio-propagation prediction," *Asia-Pacific Microwave Conference Proceedings, APMC*, vol. 3, pp. 1859–1862, 2006.
- [131] A. M. Cavalcante, M. J. De Sousa, J. C. W. Costa, C. R. L. Francês, G. P. D. S. Cavalcante, and C. Protasio dos S de Souza Sales, "3D ray-tracing parallel model for radio-propagation prediction," *2006 International Telecommunications Symposium, ITS*, pp. 269–274, 2006.
- [132] T. Rick and R. Mathar, "Fast Edge-Diffraction-Based Radio Wave Propagation Model for Graphics Hardware," *2007 2nd International ITG Conference on Antennas*, no. Figure 1, pp. 15–19, 2007.
- [133] J. Tan, Z. Su, and Y. Long, "A Full 3-D GPU-based Beam-Tracing Method for Complex Indoor Environments Propagation Modeling," *IEEE Transactions on Antennas and Propagation*, vol. 63, no. 6, pp. 2705–2718, 2015.
- [134] A. Navarro and D. Guevara, "Applicability of game engine for ray tracing techniques in a complex urban environment," *IEEE Vehicular Technology Conference*, no. 122, 2010.

- [135] A. Navarro, D. Guevara, and N. Cardona, "Using game engines and graphic technologies for ray-tracing in future wireless," *8th European Conference on Antennas and Propagation, EuCAP 2014*, no. EuCAP, pp. 1780–1784, 2014.
- [136] A. Navarro, D. Guevara, and J. Gomez, "Prediction of delay spread using ray tracing and game engine based on measurement," *IEEE Vehicular Technology Conference*, pp. 1–5, 2015.
- [137] A. Navarro, D. Guevara, D. Escalante, W. Cruz, J. Gomez, N. Cardona, and J. Gimenez, "Delay spread in mmwave bands for indoor using Game Engines 3D Ray based Tools," *2016 10th European Conference on Antennas and Propagation, EuCAP 2016*, pp. 1–5, 2016.
- [138] A. Navarro Cadavid, D. Guevara Ibarra, and S. Londono Salcedo, "Using 3-D Video Game Technology in Channel Modeling," *IEEE Access*, vol. 2, pp. 1652–1659, 2014.
- [139] "Wireless Insite User Manual," *Remcom Electromagnetic Simulation Solutions*. [Online]. Available: <https://www.remcom.com/wireless-insite-em-propagation-software>
- [140] R. Hoppe, G. Wölfle, and U. Jakobus, "Wave Propagation and Radio Network Planning Software WinProp added to the Electromagnetic Solver Package FEKO," *2017 International Applied Computational Electromagnetics Society Symposium - Italy (ACES)*, 2017.
- [141] "WinProp, Wave Propagation and Radio Network Planning," *Altair Hyperworks*. [Online]. Available: <http://www.altairhyperworks.com/product/FEKO/WinProp-Propagation-Modeling>
- [142] "WaveSight - Radio Planning Tool, Brochure," *Wavecall Inc.* [Online]. Available: <http://www.wavecall.com/wavesight.html>
- [143] Z. Chen, H. L. Bertoni, and A. Delis, "Progressive and approximate techniques in ray-tracing-based radio wave propagation prediction models," *IEEE Transactions on Antennas and Propagation*, vol. 52, no. 1, pp. 240–251, 2004.
- [144] J. Moreno, M. Domingo, L. Valle, J. R. Pérez, R. P. Torres, and J. Basterrechea, "Design of Indoor WLANs, Combination of a ray-tracing tool with the BPSO method," *IEEE Antennas and Propagation Magazine*, no. December, 2015.
- [145] L. Azpilicueta, M. Rawat, K. Rawat, F. M. Ghannouchi, and F. Falcone, "A ray launching-neural network approach for radio wave propagation analysis in complex indoor environments," *IEEE Transactions on Antennas and Propagation*, vol. 62, no. 5, pp. 2777–2786, 2014.
- [146] D. V. Giri and F. M. Tesche, "Electromagnetic Attenuation through Various Types of Buildings," *Electromagnetic Compatibility (APEMC), Asia-Pacific Symposium on*, 2013.
- [147] Y. L. C. De Jong, M. H. A. J. Herban, J. F. Wagen, and A. Mawira, "Transmission of UHF radiowaves through buildings in urban microcell environments," *Electronic Letters*, vol. 35, no. 9, pp. 743–745, 1999.
- [148] N. J. Thomas, M. J. Willis, and K. H. Craig, "The Relative Importance of Different Propagation Mechanisms for Radio Coverage and Interference Prediction in Urban Scenarios at 2.4, 5.8, and 28 GHz," *IEEE Transactions on Antennas and Propagation*, vol. 54, no. 12, pp. 3918–3920, 2006.

- [149] K. Rizk, R. Valenzuela, and D. Chizhik, "Lateral, Full-3d and Vertical Plane Propagation in Microcells and Small Cells," *48th IEEE Vehicular Technology Conference (VTC)*, pp. 998–1003, 1998.
- [150] J. Bach Andersen, "UTD multiple-edge transition zone diffraction," *IEEE Transactions on Antennas and Propagation*, vol. 45, no. 7, pp. 1093–1097, 1997.
- [151] K. Rizk, R. Valenzuela, D. Chizhik, and F. Gardiol, "Application of the Slope Diffraction Method for Urban Microwave Propagation Prediction," *48th IEEE Vehicular Technology Conference (VTC)*, pp. 1150–1155, 1998.
- [152] C. Tzaras and S. R. Saunders, "An improved heuristic UTD solution for multiple-edge transition zone diffraction," *IEEE Transactions on Antennas and Propagation*, vol. 49, no. 12, pp. 1678–1682, 2001.
- [153] F. S. D. Adana, F. J. Fernández, J. L. Loranca, and R. Kronberger, "Covermap : Computer Tool to Calculate the Propagation in Open Areas Importing Data from GoogleMaps," *Loughborough Antennas and Propagation Conference*, pp. 229–232, 2009.
- [154] Z. Yun, M. F. Iskander, S. Y. Lim, D. He, and R. Martinez, "Radio Wave Propagation Prediction Based on 3-D Building Structures Extracted From 2-D Images," *Antennas and Wireless Propagation Letters*, vol. 6, no. 99, pp. 557–559, 2007.
- [155] Z. Yun, S. Y. Lim, and M. F. Iskander, "Use of geospatial resources for radio propagation prediction in urban areas," *IEEE Antennas and Wireless Propagation Letters*, vol. 8, pp. 587–591, 2009.
- [156] Z. Yun, M. F. Iskander, and S. Y. Lim, "The effect of 3D building reconstruction errors on propagation prediction using geospatial data in cyberspace," *IEEE Antennas and Propagation Society, AP-S International Symposium (Digest)*, pp. 7–10, 2009.
- [157] V. Degli-Esposti, "Ray Tracing Propagation Modelling : Future Prospects," *The 8th European Conference on Antennas and Propagation (EuCAP 2014)*, no. EuCAP, pp. 2232–2232, 2014.
- [158] S. Hussain and C. Brennan, "An image visibility based pre-processing method for fast ray tracing in urban environments," in *2016 10th European Conference on Antennas and Propagation, EuCAP 2016*, 2016.
- [159] —, "An Efficient Ray-Tracing Method Based on Image Visibility Mapping for Propagation Prediction in Urban Environments - TD(16)01070," *COST ACTION (CA15104) in Inclusive Radio Communication Networks for 5G and Beyond (IRACON)*, 2016.
- [160] —, "An Efficient Ray-Tracing Method Based on Image Visibility Mapping for Propagation Prediction in Urban Environments," *Accepted for publication in Radio Science*, 2017.
- [161] —, "An Efficient Ray-Tracing Acceleration Technique for Mobile Receivers in Urban Environments," *Computing and Electromagnetics International Workshop (CEM'17)*, 2017.
- [162] [Online]. Available: <https://stackoverflow.com/questions/217578/how-can-i-determine-whether-a-2d-point-is-within-a-polygon>

- [163] E. Damosso, *COST Action 231 : Digital mobile radio towards future generation systems - Final report*, 1999, no. May.
- [164] S. Hussain and C. Brennan, “An Intra-Visibility Matrix Based Environment Pre-Processing for Efficient Ray Tracing,” in *Antennas and Propagation (EUCAP), 11th European Conference on*, 2017, pp. 2–5.
- [165] ———, “Efficient Pre-Processed Ray-Tracing for a Mobile Transmitter in Urban Environments,” *Submitted to IEEE Transactions on Vehicular Technology*, 2017.
- [166] G. E. Athanasiadou and A. R. Nix, “A novel 3-d indoor ray-tracing propagation model: the path generator and evaluation of narrow-band and wide-band predictions,” *IEEE Transactions on Vehicular Technology*, vol. 49, no. 4, pp. 1152–1168, 2000.
- [167] L. Reichardt, J. Maurer, T. Fügen, and T. Zwick, “Virtual drive: A complete V2X communication and radar system simulator for optimization of multiple antenna systems,” *Proceedings of the IEEE*, vol. 99, no. 7, pp. 1295–1310, 2011.
- [168] J. Maurer, T. Fugen, T. Schafer, and W. Wiesbeck, “A new inter-vehicle communications (IVC) channel model,” *IEEE 60th Vehicular Technology Conference, 2004. VTC2004-Fall. 2004*, 2004.
- [169] S. Santini, S. Bertini, and A. Monorchio, “An acceleration technique for ray tracing simulation based on a shadow volumetric binary and line space partitioning,” *2008 IEEE International Symposium on Antennas and Propagation and USNC/URSI National Radio Science Meeting, APSURSI*, pp. 1–4, 2008.
- [170] A. F. Molisch, F. Tufvesson, J. Karedal, and C. F. Mecklenbräuker, “A survey on vehicle-to-vehicle propagation channels,” *IEEE Wireless Communications*, vol. 16, no. 6, pp. 12–22, 2009.

Appendix A

Publications

Journal

- S. Hussain and C. Brennan, “An Efficient Ray-Tracing Method for Propagation Prediction along a Mobile Route in Urban Environments”, Accepted for publication in Radio Science, DOI:10.1002/2017RS006275, June 2017.
- S. Hussain and C. Brennan, “Efficient Pre-Processed Ray-Tracing for a Mobile Transmitter in Urban Environments”, Submitted for publication in IEEE Transactions on Vehicular Technology, May 2017.

Conference

- S. Hussain and C. Brennan, “An Efficient Ray-Tracing Acceleration Technique for Mobile Receivers in Urban Environments”, Computing and Electromagnetics International Workshop (CEM’17), June 2017.
- S. Hussain and C. Brennan, “Analysis of the Effect of Building Material on Propagation Prediction in Urban Environments”, Research Colloquium on Communications and Radio Science for a Smarter World, March 2017.
- S. Hussain and C. Brennan, “An Intra-Visibility Matrix Based Environment Pre-Processing for Efficient Ray Tracing”, 11th European Conference on Antennas and Propagation (EuCAP), March 2017.
- S. Hussain and C. Brennan, “An Efficient Ray-Tracing Method Based On Image Visibility Mapping For Propagation Prediction In Urban Environments”, COST ACTION (CA15104) in Inclusive Radio Communication Networks for 5G and Beyond (IRACON), May 2016.

-
- S. Hussain and C. Brennan, “An Image Visibility Based Pre-Processing Method for Fast Ray Tracing in Urban Environments”, 10th European Conference on Antennas and Propagation (EuCAP), April 2016.
 - I. Kavanagh, S. Hussain and C. Brennan, “Comparison of 3D Volume Integral Equation and Ray Tracing for Indoor Propagation Modeling”, 10th European Conference on Antennas and Propagation (EuCAP), April 2016.
 - S. Hussain, D. Trinh and C. Brennan, “Mixed Path Loss Model for Urban Environments”, 9th European Conference on Antennas and Propagation (EuCAP), April 2015.
 - D. Trinh, V. Pham, S. Hussain and C. Brennan, “Integral Equation Based Path Loss Modelling for Propagation in Urban Environment”, International Conference on Electromagnetics in Advanced Applications (ICEAA), August 2014.
 - I. Kavanagh, S. Hussain and C. Brennan, “A Full Wave Propagation Model for Indoor Wireless Communications”, 17th Research Colloquium on Communications and Radio Science into the 21st Century, May 2014.